Finding Cepheid Variable Stars in Northern Dwarf Galaxies of the Local Group

Claus A. Gössl

München 2007

Finding Cepheid Variable Stars in Northern Dwarf Galaxies of the Local Group

Claus A. Gössl

Erstgutachter: Prof. Dr. Ralf Bender

Zweitgutachter: Prof. Dr. Harald Lesch

Tag der mündlichen Prüfung: 18. Dezember 2007

Contents

List of Figures

List of Tables

Zusammenfassung

Die vorliegende Arbeit "*Suche nach Cepheid-artigen Veränderlichen Sternen in nördlichen Zwerggalaxien der Lokalen Gruppe*" faßt die Ergebnisse des *VarStarDwarves*-Projektes für alle "blauen", periodisch Variablen Sterne (VS) zusammen. Die Zielsetzung des *VarStarDwarves*-Projekts, das seit 1999 an der Universitäts-Sternwarte München betrieben wird, läßt sich am besten durch ein Zitat aus dem zugrundeliegenden DFG-Antrag (Ho1812) erläutern: "Die Bestimmung der Sternentstehungsgeschichte von Zwerggalaxien (ZG) erlaubt, wesentliche Randbedingungen für die Modelle der Evolution von Galaxien abzuleiten. Eine Grundvoraussetzung hierzu ist die Kenntnis der genauen Distanz der ZG. Die Beobachtung hinreichend großer Sample von Veränderlichen Sternen ermöglicht es, diese Distanzen wesentlich präziser als bisher zu bestimmen. Um diese großen Sample zu erhalten, sollen mit für Microlensing entwickelten Bildverarbeitungsmethoden VS in nahen ZG bis weit unter die bis jetzt erreichten Detektionsgrenzen nachgewiesen werden. Darüberhinaus werden die gefundenen VS auch Hinweise zur stellaren Zusammensetzung und damit zum Entwicklungszustand der ZG geben." Die Ergebnisse für langperiodische, "rote" VS wurden bereits in der Arbeit von Snigula [2006] präsentiert.

Im Rahmen des *VarStarDwarves*-Projekts wurden umfangreiche Modernisierungen und Verbesserungen an den Beobachtungsinstrumenten und dem Umfeld des Observatoriums Wendelstein durchgeführt und darüberhinaus die Entwicklung und der Bau einer neuen, modernen Zweikanal-CCD-Kamera initiiert. Auch diese Aspekte werden hier dokumentiert und die erreichten Fortschritte aufgezeigt (siehe hierzu Kapitel 2.2, 2.3 und 3 sowie die Anhänge A bis C). Diese Dissertation untergliedert sich weiter in eine Einleitung, die neben einer kurzen Vorstellung der mit dem Projekt befaßten Kollegen und ihrer diesbezüglichen Aufgabenbereichen v.a. eine historische Einführung in die Gebiete der Lokalen Zwerggalaxien sowie der "blauen" pulsationsveränderlichen Sterne bietet (Kap. 1), einen Überblick über Kandidatenauswahl und die durchgeführten Beobachtungen (Kap. 2.1, 2.4 und 2.5), sowie eine detaillierte Erläuterung der aufwendigen, z.T. ebenfalls im Rahmen des Projekts entwickelten Datenanalyseverfahren (Kap. 4). Die wesentlichen wissenschaftlichen Ergebnisse der Arbeit sind neue, unabhängige Entfernungsbestimmungen mittels δ Cephei Perioden-Leuchtkraftbeziehungen zu zwei der sechs *VarStarDwarves* Zwerge, die Bestätigung der Entfernung eines weiteren Zwergs, sowie die Entdeckung etlicher weiterer VS-Kandidaten, deren endgültige Bedeutungen erst durch weitere Beobachtungen bestimmt werden können, wobei aber durchaus mit weitreichenden Konsequenzen für das physikalische Verständnis der entsprechenden VS oder ihrer "Muttergalaxie" zu rechnen ist (Kap. 5).

Chapter 1

Introduction

1.1 The *VarStarDwarves* Project – Motivation and Context

This work here is one of two PhD theses summarising the results of the *VarStarDwarves* project (supported by DFG grant Ho1812 and Ho1813). In order to give an overview on the project goals I will quote the formal application for the DFG grant:

"*The determination of the stellar evolution of dwarf galaxies (DG) allows to derive constraints on models of galaxy evolution. One basic requirement is information on the exact distance of the DG. The observation of adequate samples of variable stars (VS) provides the means of improving present distance determinations. To collect those samples we will apply image processing methods which were developed for micro lensing studies to detect VS in nearby DG far beyond current limits. In addition all VS found will indicate the DG stellar content and therefore its evolutionary state. [. . .]*"

The first thesis [Snigula, 2006] presented the results on red Long Period Variables (LPV), i.e. Mirae stars, which are pulsating Asymptotic Giant Branch (AGB) stars. This thesis here will present the results on the shorter period pulsating stars, i.e. classical and Type II δ Cephei stars. The *VarStarDwarves* project also involved the development of a new two-channel CCD camera as well as many upgrades (mostly software) to the existing telescope and CCD camera which are reported in these two theses.

1.2 Overview – The People Involved

The *VarStarDwarves* project involved many people and since it will not be reported elsewhere I will summarise here who did what in the context of the project. The project was started by Ralf Bender, Ulrich Hopp, and Heinz Barwig, the latter two applying for the DFG grants which successively supported me and Jan Snigula. We were both assiduous enough to be rewarded with full positions soon in the course of the project. Ralf Bender was/is the thesis advisor for the two theses originating from the project. The purely technical part of the project involved the building of a new CCD camera for Wendelstein observatory [see Chap. 3 and Goessl et al., 2003] and improvements to the existing observatory infrastructure, its telescope and the current

CCD camera [see Sect. 2.2 and Snigula, 2006]. While I was responsible for the optical design as well as the mechanical draft, and for most of the final mechanical assembling, Wolfgang Mitsch, the electronics engineer for Wendelstein observatory, provided advice in all of these and did everything which involved electronics for the new camera. The complete mechanical design was elaborated by Werner Altmann, an external contractor. Most of the mechanical parts have been manufactured by the USM workshop (Franz Mittermaier and Peter Well). The camera software again was mostly developed by me. I wrote the routines for the motor controller which operates the shutters and the filter sliders and also implemented the camera daemon which provides high level functions for the camera control utilising the daemon model written by Jan Snigula for the WST 80 cm telescope remote control. The graphical user interface (GUI) for the camera was built by Johannes Koppenhöfer and me. All improvements to the observatory infrastructure which involved "switches and wires" were made by Wolfgang Mitsch. While I added many features to the current CCD camera software Jan Snigula provided a remote control daemon and GUIs for the 80 cm telescope. Together we also developed a more reliable software for auto-guiding from scratch (Jan GUI, me daemon).

Until the end of 2005 there have been about 650 nights on Wendelstein and 70 nights at Calar Alto which produced, among others, also observations for the project. Most of the observations were done by USM staff observers, Christoph Ries (46%) and Otto Bärnbantner (15%). Me (13%), Jan Snigula (9%), Silona Wilke (6%), and Arno Riffeser (4%) as well as some occasional observers did the rest. (See Sect. 2.5 and Tab. 2.3).

The preliminary visual inspection of about 37000 raw images as well as the necessary sorting, book keeping and archiving was exclusively done by myself. For 15% of the repeated inspection of the raw reduced images for positional registration I had the help of a student, Silona Wilke.

Together with the "coders" from the WeCAPP [Riffeser et al., 2001] and MUNICS [Drory et al., 2001] team we developed a shell command line oriented image processing and data reduction software. The pipeline relies on a high performance C++ array calculations- and I/O-library LTL [Gössl et al., 2004]: Niv Drory did the conceptional design on it learning from the Blitz++ library [Veldhuizen, 1995]. He also implemented the dynamical arrays and parts of the linear algebra, while I did the other part of the latter, the statistical functions and FITS[1] file I/O. Jan Snigula finally added ASCII file I/O, and Arno Riffeser did extensive testing of the library. The pipeline itself consists of several parts: Firstly, a "standard reduction" part (FITSTools, see Sect. 4.2), implemented by me with support and ideas of Arno Riffeser, and the difference imaging[2] and PSF fitting photometry (MuPipe, see Sect. 4.3) by Arno Riffeser [Gössl and Riffeser, 2002, 2003]. Jan Snigula provided the absolute photometric calibration combining DAOPHOT [Stetson, 1987] photometry of our reference images by Ulrich Hopp with HST photometry [Holtzman et al., 2006] as well as with standard star observations of the Calar Alto data set. [See Sect. 4.4.2 and Snigula, 2006, Chap. 3.] I again did the variability detection and implemented a Lomb [Lomb, 1976, Scargle, 1982] period analysis for the "shorter" periods while Jan Snigula produced a Lafler-Kinman period computation [Lafler and Kinman, 1965] for the "longer" periods and the visualisation by Yorick [Munro, 1995] routines. [See Sect. 4.6 and

---

[1]The **F**lexible **I**mage **T**ransport **S**ystem, see Wells et al. [1981].

[2]An elaborated version of optimal image subtraction (OIS) originally conceived by Alard and Lupton [1998].

Snigula, 2006, Chap. 4.] Completeness simulations finally were mostly implemented by Jan except for the Lomb completeness which was coded by me. [See Sect. 4.6.3 and Snigula, 2006, Chap. 5.]

As can be seen by the long list of prerequisites above it has been a long way before we finally could work our way through to actual science. While Jan Snigula worked on the LPV / AGB stars I concentrated on all types of Cepheid variables. Ulrich Hopp provided advice and controlling as he did for the whole project.

1.3 The Local Group of Galaxies

The Local Group (LG) of galaxies[3] is dominated by two major Spiral Galaxies, our Milky Way Galaxy (MWG) and the Andromeda "Nebula" (M 31)[4]. Actually, membership to the LG can be defined by being bound to their combined gravitational potential[5]. Next in size is the Triangulum Galaxy (M 33)[6], a minor bulge-free Spiral and maybe close enough to be bound to M 31, followed by two Irregular galaxies, the Large and the Small Magellanic Clouds (LMC and SMC)[7], which are the most massive satellites of the MWG. After M 32 has been discovered by Gentil de la Galazière [1765], $\gtrsim$ 40 LG galaxies have been found until now, most of them in the last decades, and there probably still remain in the order of 10 to 20 LG members undiscovered [Mateo, 1998, Grebel, 1999]. All those LG members or member candidates are Dwarf Galaxies (DGs)[8]. Fig. 1.1 and Tab. 1.1 give a census of the LG at the beginning of the *VarStarDwarves* project while Tab. 2.1 in Sec. 2.1 details the selections criteria of the *VarStarDwarves* candidates.

The LGDs were classically divided into dwarf ellipticals (dEs), dwarf spheroidals (dSphs), and dwarf irregulars (dIrrs), but at a closer look this classification scheme now seems to be artificial [Grebel, 1999]: The dEs are compact with dense cores and contain mainly old and intermediate age populations. DSphs follow the same scaling relation as dEs [Ferguson and Binggeli, 1994] but have no dense cores and are in fact the faintest and least massive galaxies of all. They have little or no gas and also no recent star formation. Both former types are usually found near more massive galaxies, while the dIrrs tend to reside in more isolated regions. DIrrs are similar to dSphs, but host unionised gas and have recent or ongoing star formation in addition to underlying older populations. There is no strong dichotomy between the LGDs, there are rather ample transient types. Even more, they "*were found to vary widely in their star formation histories,*

---

[3]As depicted by Hubble [1936].

[4]Already described and depicted by Al Sufi [964], also described by Marius [1614] and Hodierna [1654], and eventually catalogued by Messier [1774].

[5]To actually prove or disprove LG membership by applying this criterion is rather difficult, because it requires exact 3D velocities and locations relative to the LG barycenter as well as the mass of the potential member which are hard to come by as will be discussed below.

[6]Probably found by Hodierna [1654] and rediscovered by Messier [1774].

[7]First preserved mention by Al Sufi [964]; then again mentioned by Vespucci [1503] and by the survivors of the first circumnavigation of the earth [see the account on Magellan's voyage of Pigafetta, 1522]. The Large and the Small Cloud began being called *Magellanic* not until the 19th century.

[8]The "dwarf" status of M 32 is still in dispute because it follows the same scaling relations as normal elliptical galaxies [Ziegler and Bender, 1998].
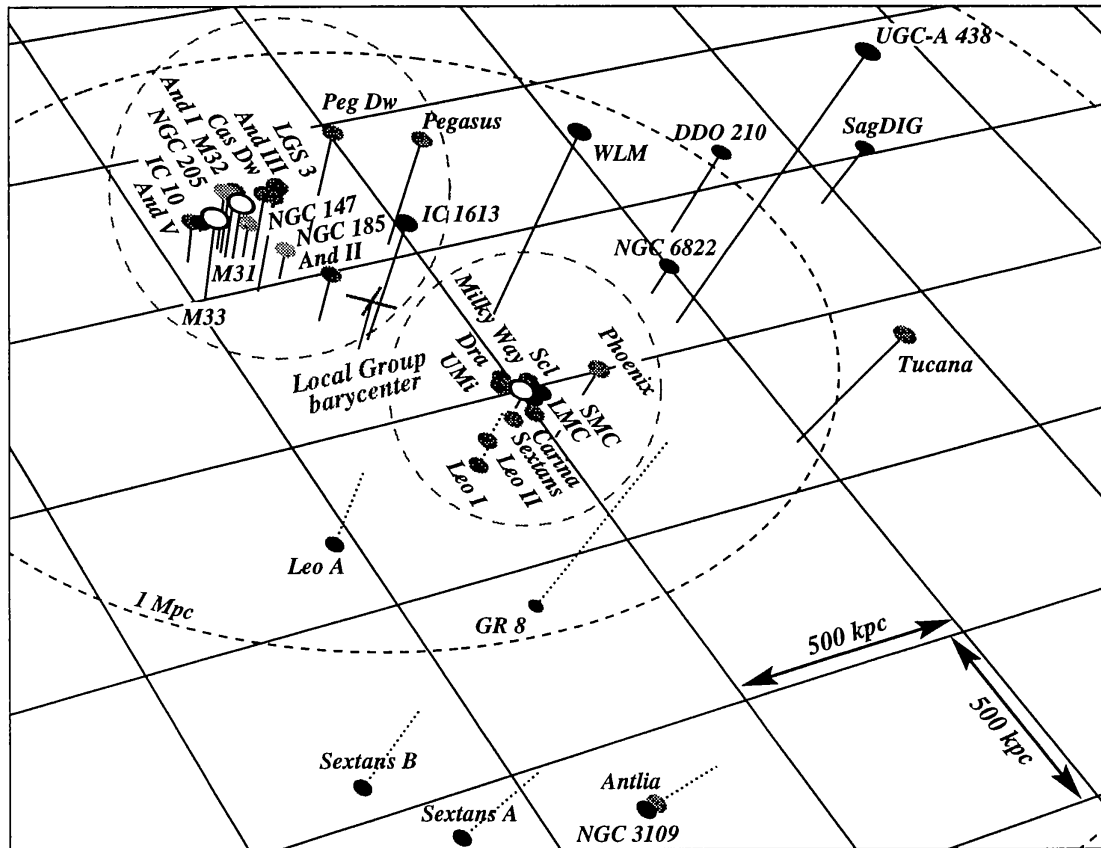
Figure 1.1: Fig. 3 of Grebel [1999]: *"A scaled 3-D representation of the Local Group (LG). The dashed ellipsoid marks a radius of 1 Mpc around the LG barycenter (cross). The underlying grid is parallel to the plane of the Milky Way. Galaxies above the plane are indicated by solid lines and below with dotted lines. The dashed circles enclose the presumed M31/M33 and the Milky Way subsystems. Morphological segregation is evident: the dEs and gas deficient dSphs (light symbols) are closely concentrated around the large spirals (open symbols). DSph/dIrr transition types (e.g. Pegasus, LGS 3, Phoenix) tend to be somewhat more distant. Most dIrrs (dark symbols) are isolated and located at larger distances."* Please note that the projection is misleading: Galaxies above the plane appear to be more distant than galaxies below. Not all galaxies of Tab. 1.1 [Mateo, 1998] are shown.

mean metallicity[9]and enrichment histories, times of their major star formation episodes, fractional distribution of ages and subpopulations. Indeed no two dwarf galaxies are alike, not even if they are of the same morphological type or have similar luminosities." [Grebel, 2001].

---

[9]Since *"metallicity"* is used frequently throughout astrophysical literature and often combined with stellar populations labelled I or II, implicitly referring to metallicity, some explanation shall be given here: Metals in astrophysical terms are all elements heavier than Helium. Stars with about and above solar metallicity as found mostly in the star forming disks of spiral galaxies were called Population I stars whereas stars with well below solar metallicities as found usually in the old MWG globular clusters, its Halo, and in elliptical galaxies were designated Population II stars according to Baade [1944, 1958]. The implicit combination of "recent star forming" with high metallicity is

The LGD type distribution could be interpreted as dIrrs evolving to dSphs near bigger galaxies [Mateo, 1998, Grebel, 2001]. But, because they are more difficult to detect than dIrrs there still may be LG dSphs hiding in the field, and, more important, the proximity to bigger galaxies could also influence the early star formation history of a common dIrr/dSph progenitor [Skillman and Bender, 1995] which would be almost impossible to detect now.

Historically, LG membership was based on the ability to resolve a galaxy into stars (e.g. Baade [1944] or more recently Hoessel et al. [1988]) and to derive a low heliocentric velocity. However, to prove membership at least one reliable distance determination is required. There are two principle distance indicators suitable for the LG: One is to look for absolute features of stellar populations (see Sect. 1.5.1, the HRD), the other utilises period-luminosity relations for variable stars (VS, see Sect. 1.5.3 and 1.5.4). Using intrinsically bright stars helps in observations although bright stars are rare, especially in DGs. Therefore the two main distance indicators for the LG are the TRGB-method (see Sect. 1.5.1[17]) and the classical δ Cephei PLR (see Sect. 1.5.4).

1.4   Local Dwarf Irregular Galaxies

What can we learn from dIrrs and their content of variable stars?

- As far-scattered LG galaxies they trace the LG gravity potential and allow to determine the local Hubble flow [e.g. see Karachentsev, 2005, Karachentsev et al., 2006]. To do so accurate distances are crucial which brings us to the next point:

- The LG dIrrs can be used as calibrators to different distance indicators, i.e. different types of VS and HRD features (see next Sect.). The distant dIrrs are small enough to show negligible depth effects, yet close enough to allow deep photometry. While the MWG, M 31, M 33, and also the LMC trace distance relations with metallicities ranging from above solar to about 0.4 solar the dIrrs allow to investigate a metallicity dependence to well below solar values [i.e. 2% solar in Leo A, Skillman et al., 1989]. Since the LMC, which already has sub-solar metallicity [Dufour, 1984], is still the main calibrator for distances beyond the LG and shows distance modulus inconsistency of 0.15 mag in recent publications [Alves, 2004] it is worthwhile to investigate the whole parameter space accessible.

- Compared to large galaxies, especially Spirals, dIrrs are simple systems. Theories about stellar formation histories utilising different types of stars as tracers can be tested more easily with them.

Therefore, we decided to start *VarStarDwarves* as to establish a census of bright variable stars in some LG dIrrs by applying new techniques, i.e. CCD imaging combined with difference imaging photometry suitable for crowded fields.

---

inadequate for dIrrs which often show recent star formation at very low metallicities. In astrophysics, especially in theory, the composition of stars is usually described in fractions of X = Hydrogen, Y = Helium, and Z = "Metals". Observing astronomers prefer to give logarithmic ratios of a "test" metal content and hydrogen often normalised to solar values and derived of spectroscopic equivalent widths measurements, e.g. the iron abundance "Fe over H": $[Fe/H] = \log_{10}((Fe/H)_*/(Fe/H)_\odot)$.

Table 1.1: A combined selection of Tab. 1 and 2 of Mateo [1998]: *"Name, entries in italics refer to the five giant Local Group galaxies that are not discussed in this review in any detail; a common alternative name; right ascension and declination for epoch J2000.0, respectively; galactic longitude and latitude, respectively; galaxy type following van den Bergh [1994]; subgroup membership within the Local Group; true distance modulus and distance."* Also see Fig. 1.1 for "orientation". This LG census has been the starting point for the *VarStarDwarves* candidates. The selection process will be detailed in Tab. 2.1, Sect. 2.1.

Name	Other Name	RA (2000)	Dec (2000)	l [deg]	b [deg]	Type	Subgroup	$(m-M)_0$ [mag]	Distance [kpc]
WLM	DDO 221	00:01:58	-15:27.8	75.9	-73.6	IrrIV-V	LGC	24.83±0.08	925±40
NGC 55	–	00:15:08	-39:13.2	332.7	-75.7	IrrIV	LGC	25.85±0.20	1480±150
IC 10	UGC 192	00:20:25	+59:17.5	119.0	-3.3	dIrr	M31	24.58±0.12	825±50
NGC 147	DDO 3	00:33:12	+48:30.5	119.8	-14.3	dSph/dE5	M31	24.30±0.12	725±45
And III	–	00:35:17	+36:30.5	119.3	-26.2	dSph	M31	24.40±0.10	760±40
NGC 185	UGC 396	00:38:58	+48:20.2	120.8	-14.5	dSph/dE3	M31	23.96±0.08	620±25
NGC 205	M110	00:40:22	+41:41.4	120.7	-21.1	E5p/dSph	M31	24.56±0.08	815±35
M 32	NGC 221	00:42:42	+40:51.9	121.2	-22.0	E2	M31	24.53±0.08	805±35
M 31	NGC 224	00:42:44	+41:16.1	121.2	-21.6	SbI-II	M31	24.43±	770±
And I	–	00:45:43	+38:00.4	121.7	-24.9	dSph	M31	24.53±0.10	805±40
SMC	NGC 292	00:52:44	-72:49.7	302.8	-44.3	IrrIV-V	MW	18.82±	58±
Sculptor	–	01:00:09	-33:42.5	287.5	-83.2	dSph	MW	19.54±0.08	79±4
LGS 3	Pisces	01:03:53	+21:53.1	126.8	-40.9	dIrr/dSph	M31	24.54±0.15	810±60
IC 1613	DDO 8	01:04:54	+02:08.0	129.8	-60.6	IrrV	M31/LGC	24.22±0.10	700±35
And II	–	01:16:27	+33:25.7	128.9	-29.2	dSph	M31	23.6±0.4	525±110
M 33	NGC 598	01:33:51	+30:39.6	133.6	-31.3	ScII-III	M31	24.62±	840±
Phoenix	–	01:51:06	-44:26.7	272.2	-68.9	dIrr/dSph	MW/LGC	23.24±0.12	445±30
Fornax	–	02:39:59	-34:27.0	237.1	-65.7	dSph	MW	20.70±0.12	138±8
EGB 0427+63	UGCA 92	04:32:01	+63:36.4	144.7	+10.5	dIrr	M31	25.6±0.7	1300±700
LMC	–	05:23:34	-69:45.4	280.5	-32.9	IrrIII-IV	MW	18.45±	49±
Carina	–	06:41:37	-50:58.0	260.1	-22.2	dSph	MW	20.03±0.09	101±5

Table 1.1: A combined selection of Tab. 1 and 2 of Mateo [1998]: *"Name, entries in italics refer to the five giant Local Group galaxies that are not discussed in this review in any detail; a common alternative name; right ascension and declination for epoch J2000.0, respectively; galactic longitude and latitude, respectively; galaxy type following van den Bergh [1994]; subgroup membership within the Local Group; true distance modulus and distance."* Also see Fig. 1.1 for "orientation". This LG census has been the starting point for the *VarStarDwarves* candidates. The selection process will be detailed in Tab. 2.1, Sect. 2.1.

Name	Other Name	RA (2000)	Dec (2000)	l [deg]	b [deg]	Type	Subgroup	$(m-M)_0$ [mag]	Distance [kpc]
Leo A	DDO69	09:59:24	+30:44.7	196.9	+52.4	dIrr	MW/N3109	24.2±0.3	690±100
Sextans B	DDO70	10:00:00	+05:19.7	233.2	+43.8	dIrr	N3109	25.64±0.15	1345±100
NGC 3109	DDO236	10:03:07	-26:09.5	262.1	+23.1	IrrIV-V	N3109	25.48±0.25	1250±165
Antlia	–	10:04:04	-27:19.8	263.1	+22.3	dIrr/dSph	N3109	25.46±0.10	1235±65
Leo I	DDO74	10:08:27	+12:18.5	226.0	+49.1	dSph	MW	21.99±0.20	250±30
Sextans A	DDO75	10:11:06	-04:42.5	246.2	+39.9	dIrr	N3109	25.75±0.15	1440±110
Sextans	–	10:13:03	-01:36.9	243.5	+42.3	dSph	MW	19.67±0.08	86±4
Leo II	DDO93	11:13:29	+22:09.2	220.2	+67.2	dSph	MW	21.63±0.09	205±12
GR 8	DDO155	12:58:40	+14:13.0	310.7	+77.0	dIrr	GR8	25.9±0.4	1510±330
Ursa Minor	DDO199	15:09:11	+67:12.9	105.0	+44.8	dSph	MW	19.11±0.10	66±3
Draco	DDO208	17:20:19	+57:54.8	86.4	+34.7	dSph	MW	19.58±0.15	82±6
Milky Way	–	17:45:40	-29:00.5	0.0	0.0	Sbc	MW	14.52±	8±
Sagittarius	–	18:55:03	-30:28.7	5.6	-14.1	dSph	MW	16.90±0.15	24±2
UKS1927-177	SagDIG	19:29:59	-17:40.7	21.1	-16.3	dIrr	LGC	25.2±0.3	1060±160
NGC 6822	DDO209	19:44:56	-14:48.1	25.3	-18.4	IrrIV-V	LGC	23.45±0.15	490±40
DDO 210	Aquarius	20:46:46	-12:51.0	34.0	-31.3	dIrr/dSph	LGC	24.6±0.5	800±250
IC 5152	–	22:02:42	-51:17.7	343.9	-50.2	dIrr	LGC	26.01±0.25	1590±200
Tucana	–	22:41:50	-64:25.2	322.9	-47.4	dSph	LGC	24.73±0.08	880±40
UKS2323-326	UGCA 438	23:26:27	-32:23.3	11.9	-70.9	dIrr	LGC	25.6±0.5	1320±350
Pegasus	DDO216	23:28:34	+14:44.8	94.8	-43.5	dIrr/dSph	LGC	24.90±0.10	955±50

1.5 "The Variable Star Menagerie"

During its lifetime a star of any mass can become pulsationally unstable at various stages. The classical astronomical classification follows observational quantities which can be derived from broadband photometry in the optical wavebands like absolute brightness, temperature (i.e. colour), period, shape of light curve, and the stellar *vicinity* (e.g. globular cluster, disk of a spiral galaxy etc.). Sometimes a class will be split into subclasses later by concentrating on a previously neglected aspect. A class is often named after the first star found which showed a specific behaviour. The class prototype usually is a nearby star of the galactic solar neighbourhood and might even prove to be not at all physically related with the group labelled by it (e.g. BL Her stars). To complicate things even more the classification boundaries often overlap.

A more physical approach tries to identify the evolutionary phase of a given variable star class or subclass, i.e. its position in the Hertzsprung-Russell-Diagram[10] combined with information on the ranges of masses, ages and metallicities of its members. Following this approach one can learn a lot about the stellar formation history of the *hosts* only by counting the absolute and relative quantities of specific variable stars. The *physical* parameters can be grouped roughly into three mass ranges, two metallicity regimes, and two evolutionary stages, i.e. (close to) main sequence and evolved stars. After a short excursion into stellar evolution following Salaris and Cassisi [2005] and stellar pulsations [Cox, 1974, Gautschy and Saio, 1995, Gautschy, 2003] I will briefly discuss *Period-Luminosity Relations* (PLRs) and summarise the classes of pulsating variable stars which are bright enough to be discovered within the scope of the *VarStarDwarves* project [Fernie, 1969, Madore and Freedman, 1991, Gautschy and Saio, 1996, Becker, 1998, Allen, 2001, Wallerstein, 2002, Sandage and Tammann, 2006].

1.5.1 The Evolution of Single Stars

[Salaris and Cassisi, 2005]

The Main Sequence (MS)

All stars begin their life with Hydrogen core burning on the so called *Zero-Age Main Sequence* (ZAMS, Fig. 1.2) and slowly grow more luminous throughout their main sequence phase. Stars with masses $M_* \gtrsim 1.3\,M_\odot$ (upper main sequence, UMS) have a convective core. They first get cooler until their central Hydrogen drops below $X = 0.05$ which because of deficient fusion causes *overall contraction* at consequently raising temperatures[11]. Again, stars with masses

---

[10]The HRD [Russell, 1913, 1914] plots luminosity vs. temperature of stars. A typical HRD shows a well populated *main sequence* of stars where luminosities increase with temperature corresponding to stars burning hydrogen in their cores. In addition there is usually a vertical sequence of almost constant temperature *evolved* stars which is separated by the *Hertzsprung gap* from the main sequence. (See Fig. 1.2.)

[11]*Rotational mixing* can prolong the main sequence life time of massive stars and therefore lead to crossing evolutionary tracks when comparing rotating with non-rotating stars [i.e. see Walborn and Lennon, 2004, Fig. 1 and 2]. This would cause ambiguities when estimating ages and masses of stars from their position in the HRD alone not only for the main sequence but consequently also for the evolved phases. However, this theory still lacks observational evidence [Lennon, 2007, priv. comm.].
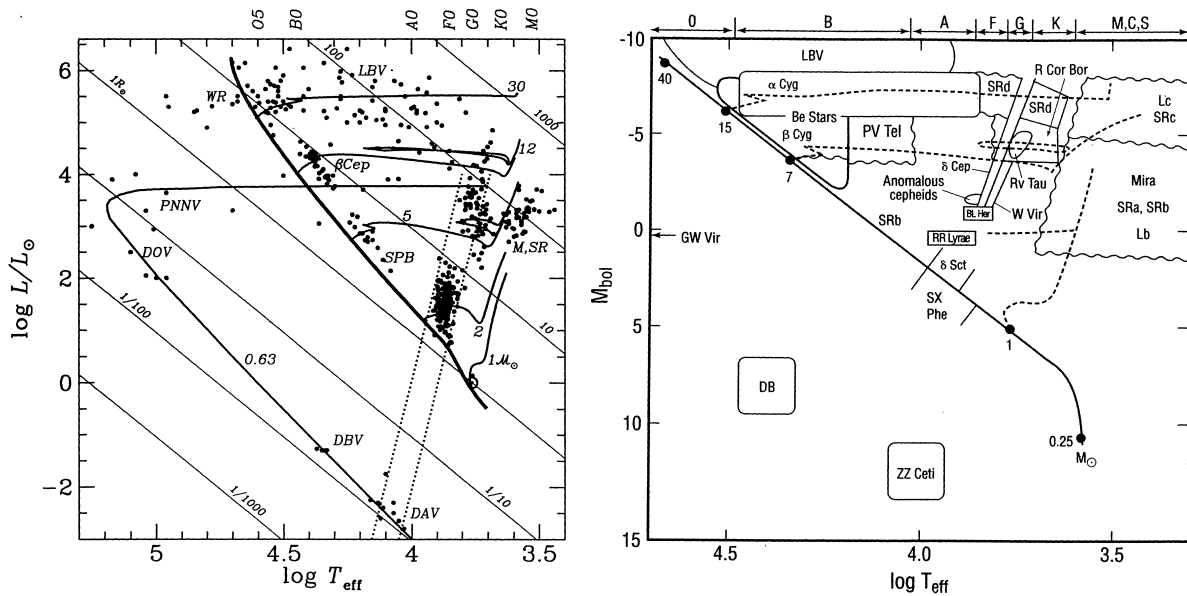
Figure 1.2: Variable Stars in the HRD. Left [Gautschy and Saio, 1995, Fig. 1]: *"HR diagram showing the distribution of types of pulsating variables (dots). The heavy line shows the location of the zero-age main sequence for solar abundances. A number of evolutionary tracks, labelled with the masses in solar units, are included. A post-AGB evolutionary path for a 0.63 $M_\odot$ star is show; it leaves the AGB at constant luminosity and turns later into a white dwarf cooling track. The thin diagonal lines represent loci of constant radius. The classical instability strip and its extrapolation towards the white-dwarf region is indicated by dashed lines. Abbreviations: WR: Wolf-Rayet stars; LBV: luminous blue variables; SPB: slowly pulsating B stars; M: Miras; SR: semiregular variables; PNNV: planetary nebulae nuclei variables; DOV, DBV, DAV: variable DO-, DB-, and DA-type white dwarfs."* Right [Becker, 1998, Fig. 1]: *"The approximate position of various types of pulsating variable stars on a M_{bol} vs. $\log T_{eff}$ H-R diagram. Spectral class boundaries are given at the top of the diagram. The solid curved line represents the Zero-Age Main Sequence corresponding to representative star masses in solar units. The dashed curves are the evolutionary tracks for 1, 7, and 15 $M_\odot$ population I models."* (β Cyg should read as β Cep.)

1.3 $M_\odot \gtrsim M_* \gtrsim 0.4 M_\odot$ (low main sequence, LMS) and radiative cores constantly get hotter. Stars with $M_* \lesssim 0.4 M_\odot$ (very low-mass, VLM) are fully convective but too faint on the main sequence and their maximum age[12] is too young for them to have evolved beyond the main sequence. Therefore they are irrelevant for the *VarStarDwarves* project. Lower metallicity shifts the ZAMS to higher temperatures (and luminosities[13]). After $\sim 80 - 90\%$ of their total life time the central Hydrogen is exhausted and the stars start to enter *Post Main Sequence* phases[14].

---

[12]They live longer than a Hubble time.

[13]But the gain in luminosity does not keep up with the gain in temperature. So a metal poor ZAMS appears to be shifted to the left in the HRD when compared to a solar metallicity one.

[14]The corresponding position in the HRD is the so called *turn-off point* (TO) of a star. The HRD of stars of a range of masses but with identical ages shows a main sequence which stops at an age corresponding to a mass reflecting

The Sub-Giant and the Red Giant Branch (SGB & RGB)

After Hydrogen burning has ceased in the centre of a star it still continues in a shell around the Helium core. *Low mass stars* ($\lesssim$ 2.3 $M_\odot$) have a fractional Helium core below the *Schönberg-Chandrasekhar limit* [Schönberg and Chandrasekhar, 1942] which provides enough pressure to support the overlying envelope. More massive stars have a slowly contracting core until the onset of Helium burning. All stars go through the Sub-Giant phase (SGB) with an expanding, successively cooler envelope at almost constant luminosity[15]. For more massive stars this phase is increasingly shorter resulting in the *Hertzsprung gap* in the HRD. In the subsequent Red Giant phase (RGB) the stars get more luminous at almost constant temperature climbing up a track in parallel to, but "bluer" than, the *Hayashi* track[16]. The RG phase ends for the low mass stars at the Tip of the Red Giant Branch [17] (TRGB) with a series of Helium flashes[18], which finally reach the core, and a drastic drop in luminosity during this short (1 Myr) transition phase. The more massive stars start Helium core burning in a non-degenerate state without any Helium flashes and at a successively younger phase. For very high mass stars the RG phase can completely disappear. (See evolutionary tracks in Fig. 1.2.)

The Helium Core Burning Phase

The Helium core burning phase is the second longest in the life time of a star[19]. The evolutionary paths stars take are determined now by their Helium core mass, their total mass, as well as the abundance of Helium and metallicity in their envelope. These paths can get very complicated when taking into account mixing processes like *convective overshoot*, *induced semi-convection* or *breathing pulses* which are beyond the scope of this simplified review. (Again, see tracks for different masses in Fig. 1.2.)

The Horizontal Branch (HB):   When their Helium flashes finally have completely removed degeneracy from the core low mass stars settle on the *Zero-Age Horizontal Branch* (ZAHB) a more or less horizontal stripe in the HRD. Increasing envelope masses follow a decreasing temperature. The actual position and morphology of the HB depends mostly on Helium abundance and metallicity of the envelope. Roughly speaking, increasing metallicity (Z) successively de-populates the blue part of the HB while with increasing Helium abundance (Y) the HB grows

---

the successive shorter main sequence life time with growing mass and therefore increasingly efficient Hydrogen core burning. All stars of that age brighter than the turn-off point will have evolved to lower temperatures.

[15]The physical reasons why stars become Red Giants are still unclear [e.g. see Chiosi, 1998, Sect. 2.2, last paragraph and references therein]!

[16]Hayashi [1961] described the evolutionary track of the fully convective phase of *Pre-Main Sequence* stars. Those protostars have reached hydrostatic equilibrium and contract on the Kelvin-Helmholtz timescale [Thomson (Lord Kelvin), 1862, Helmholtz, 1871] with dropping luminosity at almost constant temperature.

[17]The TRGB luminosity is for stars below 1.8 $M_\odot$ almost independent of mass/age and only slightly dependent of metallicity and therefore a good indicator for extragalactic distances [Lee et al., 1993].

[18]I.e. phases of unstable nuclear Helium burning because of a thermal runaway processes.

[19]Unless one considers *stellar corpses*, like white dwarfs and neutron stars, as stars still being alive. They, off course, easily outlast the corresponding preceding main sequence phase.

more luminous. The position and extension of the HB therefore is mostly a indicator for the chemical composition of a stellar population.

Blue Loops: Intermediate mass stars perform a *blue loop* in the HRD: Starting from the RGB they first drop in luminosity at almost constant temperature like "retreading" on the RGB[20]. Then they grow again in luminosity but now also in temperature, the ratio depending on mass but also on metallicity, following the increasing energy release of the Hydrogen burning shell which delivers about 80% of the nuclear burning energy at the bluest point of the loop. Subsequently the stars still grow more luminous but start to cool down again to the point where Helium burning contributes about one third of the total energy budget. The loop is closed by a drop in temperature in parallel to its first rise on the loop until the star reaches a point near its starting point on the RGB now with a $\approx 60\%$ energy contribution of Helium core burning. Depending on the chemical composition and the presence of mixing processes mentioned above secondary loops on this path can occur.

Blue Supergiants: Massive stars above $8 - 10\,M_\odot$ ignite Helium in their core before they reach the RGB configuration and are still on their monotonic way to the red on the HRD when they exhaust their core Helium and almost immediately start to ignite carbon in non-degenerate conditions.

The Asymptotic Giant Branch (AGB)

As the Helium in the core gets consumed the stars enter the *Asymptotic Giant Branch* with a first phase of Helium shell burning which closely resembles the RGB phase[21]. Throughout this phase all stars drop in effective temperature and grow in luminosity, again almost in parallel to the Hayashi track[16]. At the onset of Helium shell burning the overlying Hydrogen burning shell extinguishes[22]. Massive stars[23] will eventually ignite their carbon core while low and intermediate mass stars enter the *thermally pulsating AGB phase* (TPAGB). The TPAGB starts when the Helium shell burning dies down because it reaches the Hydrogen/Helium discontinuity with a reignition of the Hydrogen shell. The Helium ashes of the burning Hydrogen shell accrete above the degenerate CO core. When those ashes exceed a critical mass[24] a thermonuclear runaway (thermal flash) expands the Hydrogen shell and thereby throttles its burning. As the runaway dies down quiescent Helium burning commences and lasts until the Helium ashes are spent.

---

[20]At least if they have reached the RGB before they start Helium core burning which strongly depends not only on mass but also on metallicity. If they are still on the SGB they begin the blue loop right where they are thereby only performing only a partial loop.

[21]For low mass stars the resemblance in the effective temperature-luminosity relation is very close, just slightly hotter, i.e. it follows *asymptotically* the RGB.

[22]For stars above $3 - 5M_\odot$ immediately.

[23]The M^{up} limit is given by the largest mass with enough electron degeneracy of the CO core to prevent carbon ignition and depends strongly on the initial chemical composition. It is $\approx 8\,M_\odot$ for solar and extremely low metallicity and minimal with $\approx 4\,M_\odot$ for $Z \approx 0.001$ stars.

[24]I.e. $10^{-3}\,M_\odot$ for a $0.8\,M_\odot$ CO core.

Now the hydrogen shell reignites and the cycle starts over while the star continues to climb up the AGB. Frequent cycles will occur during which high mass loss due to stellar winds and large amplitude pulsations (*Mirae*[49]) prevent even intermediate mass stars to grow a CO core beyond the *Chandrasekhar mass limit* ($\approx 1.4\,M_\odot$) which would ignite carbon. The (TP)AGB lasts about several 10^6 years.

Final stages

Massive stars will go through a short series of successive burning of Carbon (10^3 years) , Neon (years), Oxygen (years), and Silicon (days) before they finally explode as *Type II supernovae*. Lower mass stars will finally leave the tip of their AGB path rapidly getting hotter at constant luminosity as they evolve to the *white dwarf* (WD) phase[25].

1.5.2 Pulsational Instability – The κ-mechanism

Shapley [1914] and Plummer [1914] were the first to argue in favour of a pulsation mechanism in single stars to overcome the growing difficulties of explaining observational properties of some variable stars with a pure "binary picture"[26]. Already Ritter [1879][27] had shown a radially and adiabatically pulsating homogeneous sphere follows

$$P \propto \sqrt{R/g} \propto \sqrt{R^3/M} \Rightarrow P\sqrt{\rho} = Q \quad \text{, with}$$

P = period,	R = radius,
g = surface gravity $\propto M/R^2$,	M = mass of the sphere
ρ = mean density, and	Q = the resulting pulsational constant.

But it was Eddington [1918, 1919, 1926] who developed the basic theory of stellar pulsation. In principle any star can experience radial pulsations, however, it needs an excitation mechanism to continuously drive the pulsation, otherwise it will be damped within short time scales[28]. The most prominent under those excitation mechanisms is the κ-mechanism[29] which is probably the source for all classes of radially pulsating stars. It can occur in any layer of a star where the opacity κ drops with temperature which again is the case within ionisation layers. The most

---

[25]While some stars immediately enter the WD cooling sequence, others "say farewell" with a *self-induced nova*, and some can even recover one last time as a so called *born-again AGB*.

[26]While there still were publications defending the binary hypothesis for Cepheids (see next Sect.) until 1943 Baade [1926] could prove the pulsation premise with a test which was several times improved up to Wesselink [1946]. This method now is known as Baade-Wesselink method for a physical calibration of classical pulsators.

[27]Ritter's work was reviewed by Emden [1907] in his famous "*Gaskugeln*" otherwise, however, completely ignored by the astronomical community.

[28]A few thousand years.

[29]While Eddington already described this *valve-mechanism* he still rejected it as source for stellar pulsations [Eddington, 1941].

important layer[30] is the boundary of He^+ to He^{2+}, nevertheless, it is not the only one[31]. The drop in opacity is due to a decreasing number of free electrons which provide Thomson scattering. The cycle works like follows:

- We start with compressing a stellar atmosphere layer where opacity grows with temperature, i.e. this layer moves inwards. This compression raises the temperature of the layer and therefore also its opacity.

- The increased opacity leads to retained radiation below, i.e. the radiative pressure in the adjacent lower layer increases which, again, drives the layer towards expansion.

- The expanding layer cools decreasing the opacity. Now, the retained radiation can escape quickly

- The radiative pressure below the layer drops. It will again be compressed moving inwards and the cycle starts over.

The working of a κ-mechanism is confined to special regions in the HRD, the instability strips[32]. At present the theory of pulsating stars has matured even beyond semi-analytical non-adiabatic models. It can reproduce the position and extent of the instability regions of many of the variable stars classes depending on physical input parameters. To give only a short summary on latest work in the field would already go beyond the scope of this introduction. Therefore, I will only give a few recent references relating to the variable stars of Sect. 1.5.4: Marconi et al. [2005] on "*Cepheid Pulsation Models at Varying Metallicity and* $\Delta Y/\Delta Z$", Marconi and di Criscienzo [2007] on "*Updated pulsation models for BL Herculis stars*", Fiorentino et al. [2006] on "*Synthetic properties of bright metal-poor variables. I. "Anomalous" Cepheids*", and Miglio et al. [2007] on "*Instability strips of slowly pulsating B stars and* β *Cephei stars [...]*"; W Virginis and RV Tauri stars lack very recent publications, the latest were Bono et al. [1997] on "*Evolutionary scenario for metal-poor pulsating stars. I. Type II Cepheids.*" and Fokin [2001] on "*RV Tauri stars*" in "*Stellar pulsation - Nonlinear Studies*". However, theory is still far from completed: "*We must remember that we do not understand the mechanisms shaping the light curve.*" [Gautschy and Saio, 1996, and still true] to name only one example.

1.5.3 Period-Luminosity Relations

In 1908 Leavitt [1908] discovered the first *Period-Luminosity Relation* (PLR) based on 16 variable stars[33] out of a total of 1777 in the Magellanic Clouds. Successively, in Leavitt and Pickering [1912], she found that the brightness at maximum and at minimum of 25 variable stars in

---

[30]The He^+ ionisation layer as the main origin for the Cepheid pulsations was uncovered by Zhevakin [see 1963, for a extensive list of his references] and Cox and Whitney [1958]. They fought a sort of *Cold Star Wars* over that topic.

[31]E.g. the instability region of β Cephei and SPB stars (see below, Sect. 1.5.4) is due to the *iron opacity bump* [Kiriakidis et al., 1992, Moskalik and Dziembowski, 1992].

[32]The *classical instability strip* for Cepheids has been introduced by Sandage [1958].

[33]With a sufficient number of observed epochs.

the Small Magellanic Cloud follows closely a linear relation with the logarithm of their periods. Hertzsprung [1914] was the first to establish a PLR which can be translated to the modern form

$$\langle M \rangle = a \log_{10} P + b, \quad \text{with} \tag{1.1}$$

M = mean absolute brightness[34] and P = period, using Leavitt's data to determine the slope a and statistical parallaxes[35] of 13 galactic Cepheids for the zero point (ZP) b[36]. Shapley [1918] repeated the work of Hertzsprung but included Globular Cluster (GC) Cepheids which should prove to be fatal: The determination of the PLR ZP was greatly hampered by ignoring interstellar absorption[37] (nowadays often called *reddening*). In addition, effects of galactic rotation were unknown at that time. Together with further systematic errors of the proper motions the zero point derived from local Population I Cepheids[38] was too dim by 1.5 mag. Now, Population II Cepheids[38] are intrinsically fainter by 1.5 visual magnitudes and, being GC members off the galactic plane, suffer only from little interstellar absorption. Therefore later distance determinations to GCs by the use of RR Lyrae stars[39] were in perfect agreement with Cepheid PLR distance moduli [e.g. see Bok and Boyd, 1933]. Thus, the inclusion of GC Cepheids was able to obscure the wrong ZP for almost 40 years until Baade [1954, 1956] actually *rescaled* the universe by almost a factor of two at a meeting during the 1952 IAU meetings in Rome[40]. The astronomical community, having successfully supported Shapley's ZP until then, now leaped at confirming and refining the new ZP[41]. During the next decades observations and theory tried to converge and to actually link empirical period-luminosity-colour relations (PLCRs) with theoretical predictions about the width of the instability strip as well as the dependence of both the ZP and the slope of the PLCR of Classical Cepheids[38]. But the correction for interstellar absorption proved to be very difficult until the advent of modern multi-wavelength photometry including near infrared bands[42]. At the time of the start of the Hubble Space Telescope (HST) key project on the

---

[34] In particular M_V, the absolute V-band (visual band) brightness.

[35] I.e. mean secular parallaxes.

[36] Hertzsprung [1914] in modern form would translate to $\langle M_V \rangle = -0.6 - 2.1 \log P$, which is, mostly because of the big errors of the statistical parallaxes, more than a magnitude brighter than recent PLR determinations. Additionally, a presumably typographical error translated his derived SMC parallax of 0.0001 only to 3000 ly and not 30000 ly.

[37] The existence of interstellar absorption in the galactic plane was not established beyond doubt until Trumpler [1930].

[38] See next Sect.

[39] They populate the cross section of the classical instability strip and the horizontal branch (HB).

[40] Essentially he reported that the new 200-inch Mt. Palomar telescope did not reveal any RR Lyrae stars[39] in M 31 which it should have done if Hubble's Cepheid PLR distance to M 31 was correct. Hubble [1925] had settled the *Great Debate* with the discovery of Cepheids in some of the controversial *nebulae*, i.e. M 31 and M 33, and applying a PLR.

[41] Fernie [1969]: *"The definitive study of the herd instincts of astronomers has yet to be written, but there are times when we resemble nothing so much as a herd of antelope, heads down in tight formation, thundering with firm determination in a particular direction across the plain. At a given signal from the leader we whirl about, and, with equally firm determination, thunder off in a quite different direction, still in tight parallel formation."*

[42] Madore and Freedman [1991]: *"Before we can approach an empirical determination of the coefficients in the PLC relation (or any determination of their variation with metallicity) we must solve the reddening problem. While theory predicts a finite width to the instability strip (with temperature/color being the controlling parameter), and while metallicity is a quantity that is known to be different from galaxy to galaxy (and it is known to vary*

extragalactic distance scale (1990) using PLRs as a measure of the local extragalactic distance scale finally seemed to be firm ground. While theory and observations still struggled to solve the impact of metallicity and Helium abundances one was nevertheless tempted to cite Hubble [1936, on Shapley's PLR]: "*Further revision is expected to be of minor importance.*", meaning only in the order of 0.1 mag. But, again, there now exists profound evidence that the PLRs of the MWG and the LMC differ in slope and ZP at the 0.3 mag level[43]. While those discoveries will ultimately help to lift PLR distances to a new level of accuracy, for now, present day PLR distances should not be taken absolutely but only relative to their calibrator. The study of other PLRs than that of Classical Cepheids has been neglected since Baade [1954] until recent[38].

Historically PLRs were and still are calibrated in the visual optical *V*-band[44]. The addition of *colour* information to derive reddening and temperature first involved the blue *B*-band[45] and later on mostly the optical infrared *I*-band[46]. For *VarStarDwarves* the use of the *V*-band was out of the question[47] as it is not suitable to achieve a high signal-to-noise (S/N) ratio with the instruments and observation sites at hand. Also our interest in red, long-period variables (LPV) led us to invest most of the observations into the red *R*-band[48]. When applying PLRs to our data we were therefore restricted to the rare publications of *R*-band PLRs, but, as will be detailed in the next section, those proved to be adequate for the aim of our survey. To account for the different PLRs for fundamental mode (FM) and first overtone (FO) pulsators we follow Caputo et al. [2004]:

$$\log P_{\text{FM}} = \log P_{\text{FO}} + 0.13 \tag{1.2}$$

More information and literature about recent work on PLRs is detailed in the next Sect. according to the VS types relevant for *VarStarDwarves*.

1.5.4   Bright "Blue" Pulsating Variable Stars

The Mirae[49] stars, i.e. red, long-period variables on the TPAGB in the HRD, within our sample have been already discussed in detail in Snigula [2006] and therefore will be ignored here completely. (The position of subsequent VS types in the HRD is displayed in Fig. 1.2.)

---

systematically within individual galaxies), only when reddening has been accounted for can we go on to look for meaningful correlations of luminosity residuals with intrinsic color and/or metallicity, for instance." In Freedman and Madore [1990] they were convinced to have shown that the impact of metallicity has to be less than 0.13 mag.

[43]See Sandage and Tammann [2006] and references therein.

[44]Centred on 550 nm.

[45]Centred on 450 nm for the $B - V$ colour.

[46]Centred on 850 nm for the $V - I$ colour.

[47]See Sect. 2.4 and 3.1.1 on the choice of filters.

[48]Centred on 650 nm.

[49]o Ceti was the first variable star to be found pulsating later. It was originally discovered by Fabricius [1596], got its first period assessment by Holwarda [1640] and its **mira**culous name by Hevelius [1662]. (Find further details on the history of Mira in Hoffleit [1997].)
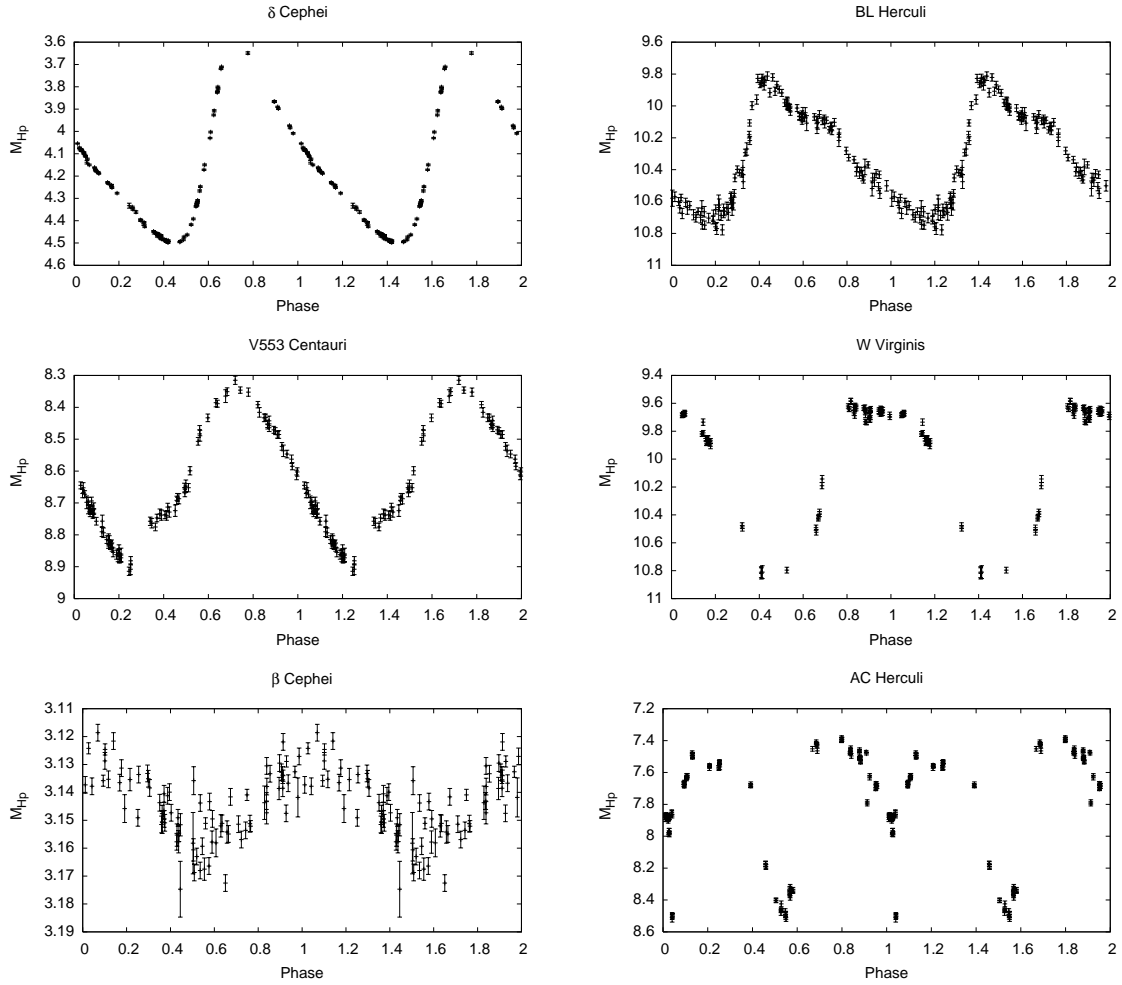
Figure 1.3: Hipparcos [ESA, 1997] photometry light curves of prototype pulsating variable stars.

Classical δ Cephei Stars (CCs)

Goodricke [1786] was the first to report on "*A Series of Observations on, and a Discovery of, the Period of the Variation of the Light of the Star Marked δ by Bayer[50], Near the Head of Cepheus*" which became the prototype of both, all Cepheid variables and the δ Cephei subclass, arguably the most prominent type of all variable stars[51]. Classical δ Cephei stars are intermediate mass, Helium core burning stars crossing the *classical* instability strip of the HRD on their blue loop[52] (see Sect. 1.5.1 and 1.5.2). They have periods from 1 to 130 days, amplitudes from 0.1 to 2

---

[50]Bayer [1603].

[51]Actually, the first δ Cephei type variable star was discovered a month before Goodrike discovered δ Cephei by his friend and neighbour Pigott [1785]: η Aquilae, i.e. at that time still η Antinoi.

[52]See Hofmeister et al. [1964], Lauterborn et al. [1971]. Probably they need masses $M_* > 5M_\odot$ to have the blue loop extending into or crossing the instability strip. But then they might cross the strip even several times.

magnitudes and follow a well defined PLR [Becker, 1998]. Their light curves (Fig. 1.3, top, left) have a steep rise followed by a shallow decline with the exception[53] of the short-period s-Cepheids[54]. From $4\,\mathrm{d} < P < 20\,\mathrm{d}$ there exists a *bump* in the light curve which shift of location with period is known as *Hertzsprung progression*[55]. The most recent PLR calibration in the R-band is that of Madore and Freedman [1991] which also served as the reference for the HST key project on the extragalactic distance scale[56]:

$$M_R = -3.04(\pm 0.17) \cdot (\log P - 1.00) - 4.48(\pm 0.08) \quad [\pm 0.25] \tag{1.3}$$

The photometric precision of *VarStarDwarves* is at about the same level of accuracy as the relation.

Population II Cepheids

The post-main-sequence Population II Cepheids consist of three distinct groups:

BL Herculi stars should actually better be labelled **XX Virginis** after their true metal poor prototype or *above horizontal branch 1* (**AHB1**) stars [Diethelm, 1990]. BL Herculi itself (Fig. 1.3, top, right) is the Population I, metal rich equivalent, but belongs to the same group in terms of evolutionary status. AHB1 stars originate from blue HB stars crossing the instability strip as they evolve towards the AGB[57]. Whatever they are called, they have periods of about 1 to 5 days and amplitudes up to 1.5 mag.
There is a paucity of Type II Cepheids with periods of 5 to 10 days, which is presumably due to the different evolutionary status of the two groups, XX and W Virginis [Gautschy and Saio, 1996].

W Virginis stars are either AGB on a blueward excursion during late Helium shell flashes or already on their final departure from the AGB. Besides being fainter their light curves resemble those of classical δ Cephei stars (Fig. 1.3, centre, right). They have periods of 10 to 35 days and 0.3 to 1.2 mag amplitudes.

---

[53]"**EXCEPTION**, n. A thing which takes the liberty to differ from other things of its class, as an honest man, a truthful woman, etc. '*The exception proves the rule*' is an expression constantly upon the lips of the ignorant, who parrot it from one another with never a thought of its absurdity. In the Latin, '*Exceptio probat regulam*' means that the exception *tests* the rule, puts it to the proof, not *confirms* it. The malefactor who drew the meaning from this excellent dictum and substituted a contrary one of his own exerted an evil power which appears to be immortal." [Bierce, 1906]

[54]With periods of $P \lesssim 7\,\mathrm{d}$ and low amplitude sinusoidal light curves.

[55]This bump is due to an accidental 2:1 ratio of the fundamental mode and the second overtone mode periods [Simon and Schmidt, 1976].

[56]Despite the doubts of the uniformity of the classical Cepheid PLR [Sandage and Tammann, 2006] Rizzi et al. [2007] found the Madore and Freedman [1991] PLRs consistent at the 1% level in average and 0.1 mag per case with distance determinations they have derived for 16 galaxies with the TRGB-method, which they believe to be correct to at least 0.1 mag.

[57]According to theory AHB1 stars should have slowly increasing periods [Sandage et al., 1994] which has been actually observed [Diethelm, 1996].

RV Tauri   stars are most probably AGB stars right at the end of their life getting hotter and crossing the instability strip while they leave the AGB [Jura, 1986]. They show group-defining double-wave light curves whose origin is still controversial (Fig. 1.3, bottom, right, AC Herculi). Their *formal* period is about 30 to 150 days and they have amplitudes up to 5 mag.

Type II PLRs   are not only fainter than their Population I analogue but, according to Sandage and Tammann [2006], also show a different slope[58]. Alcock et al. [1998] selected 30 W Virginis and RV Tauri stars from their MACHO-LMC data base. They are the only ones to give not only a *V*-band PLR but also a PLCR based on *V* and *R*-band data. From their *R*-band data alone I derived

$$M_R = -3.05(\pm 0.29) \cdot (\log P - 1.00) - 2.07(\pm 0.10) \quad [\pm 0.39] \quad . \tag{1.4}$$

Selecting only stars with $V - R < 0.325$, i.e. the bluest and therefore probably least affected by extinction ones, yields

$$M_R = -3.04(\pm 0.25) \cdot (\log P - 1.00) - 2.41(\pm 0.11) \quad [\pm 0.36] \quad . \tag{1.5}$$

(See Fig. 1.4.) Their data indicates a brightening of the PLR at longer periods, i.e. an increasingly steeper slope of the PLR for the longer period RV Tauri. One has to emphasise that different *V*-band PLRs of Type II Cepheids derived so far from theory, Galactic Globular Clusters, and the LMC are barely consistent within their rather huge errors. [See Alcock et al., 1998, , their Tab. 3 and references therein]. Nevertheless, a single PLR for all types of Population II Cepheids is still adequate until better calibrations are available.

Anomalous Cepheids (ACs)

Anomalous Cepheids are short period, low metallicity pulsators, but too bright (and massive) for ordinary XX Virginis stars, although still too low mass for CCs. The last reviews about Cepheids [Gautschy and Saio, 1995, Wallerstein, 2002, Sandage and Tammann, 2006] still assume that they manage to reach their position in the HRD by mass transfer in a binary system. However, Caputo et al. [2004] offers an alternative explanation which would also solve the *AC mystery*, i.e. why ACs are only found in very metal poor Dwarf Spheroidals (and some Dwarf Irregulars) but not in comparably metal poor Galactic Globular Clusters: Referring to Caputo and degl'Innocenti [1995], Castellani and degl'Innocenti [1995] they explain that at low metallicity the ZAHB stops to get cooler with growing mass but starts to get hotter again, leading to a *ZAHB turn-over* and an *upper HB* which intersects the instability strip again. As a group, ACs have periods of 0.8 to 2 days and amplitudes up to 2 mag. Their light curves are more symmetrical than that of both, CCs and Type II Cepheids (Fig. 1.3, centre, left, V553 Centauri). Recent *V*-band PLR determinations [Pritzl et al., 2002, Gallart et al., 2004] indicate that AC PLRs are easily consistent with Madore and Freedman [1991] CC PLRs within the scope of *VarStarDwarves*. In contradiction to theory [Caputo et al., 2004] Pritzl et al. [2002] and Gallart et al. [2004] derive slightly different slopes

---

[58]This statement strongly depends on the selected calibration. Madore and Freedman [1991] and Alcock et al. [1998] PLRs show almost identical slopes!
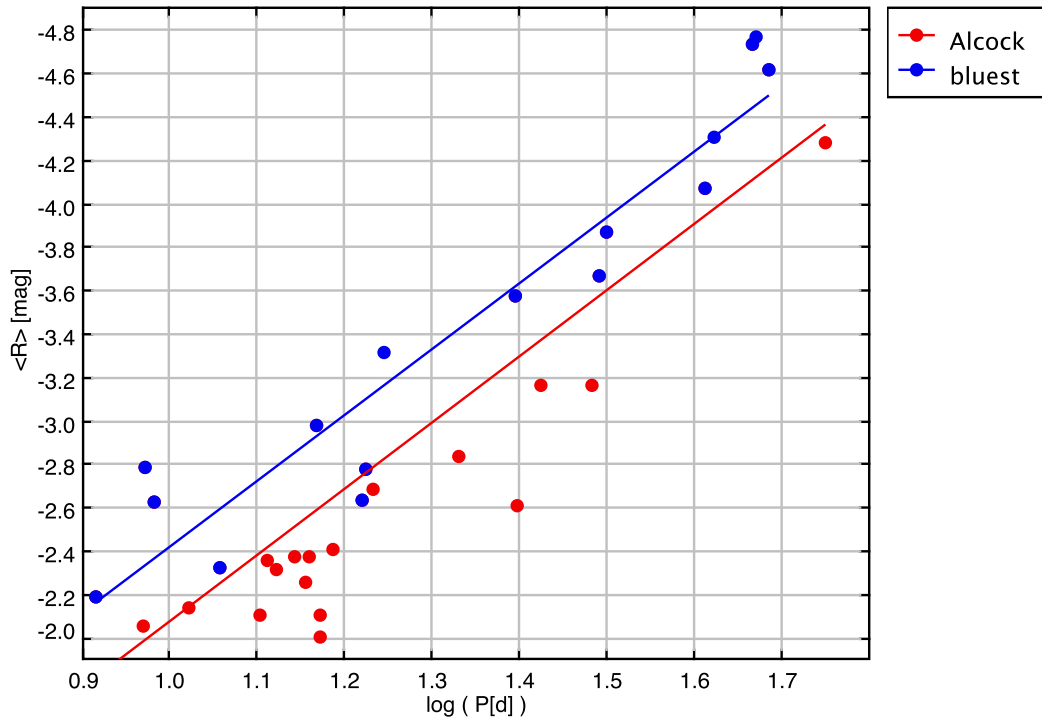
Figure 1.4: Type II Cepheid *R*-band PLR fitted to the data of Alcock et al. [1998] with a LMC distance modulus of $m - M = 18.5$ (Eqn. 1.4). Red & blue: The stars selected by Alcock et al. [1998] for their PLCR; blue: Stars with $V - R < 0.325$.

for their fundamental mode and first overtone mode pulsators. Because there are no *R*-band overtone modes PLRs published at all I will use Eqn. 1.2 nevertheless.

β Cephei and Slowly Pulsating B (SPB) Stars

β Cephei and SPB (or 53 Persei) stars are both main sequence pulsating B-stars (Fig. 1.3, bottom, left). The probability of a B-star falling into the according instability region in the HRD is a function of age and metallicity. Only late B-stars with a sufficient metallicity can become a β Cephei star. They have periods of hours and amplitudes of 0.1 mag. For SPBs either a younger age or an inferior metallicity will suffice. They have periods of about 10 h to several days. Since the *VarStarDwarves* galaxies are all in the low metallicity regime we would not expect to actually find any of those variables[59], but, since they would be detectable in terms of periods, amplitudes, and magnitudes we checked our data without prejudices.

---

[59]There were no β Cephei stars at all known in the metal poor LMC until Pigulski and Kołaczkowski [2002] who found finally 3 out of 27663 B-stars.

Other "blue" Variables

All stars with bolometric magnitudes $M \lesssim -1$ are definitely too faint to be discovered with our survey (see Sect. 4.6.3 and App. D). So RR Lyrae stars[39], the Population I and II Dwarf Cepheids[60], and the pulsating white dwarfs can be neglected here, also.

Non-periodic or eruptive Variables, like all types of *Luminous Blue Variables*[61] (LBVs) or Novae, are too rare to have the chance of appropriate sampling during relevant phases within the *VarStarDwarves* schedule (Sect. 2.5) and therefore have also been excluded from further studies for the time being.

1.5.5 Eclipsing Binaries

While the *VarStarDwarves* data almost certainly contain eclipsing binaries we did not explicitly look for them up to now. In order to derive the binary system parameters which would ultimately yield means of a distance determination to the system one needs high precision spectroscopy in addition to highly accurate photometric data. The DIRECT project [Bonanos et al., 2006] has recently determined a distance modulus to M 33 utilising a detached eclipsing binary[62] (DEB). A DEB bright enough for spectroscopy in the Local Group neighbours[63] will have to be a pair of main sequence, bright B-, if not O-stars. The chances to find such a pair in our sample of DGs are almost zero. Much more promising is the search for semi-detached systems[64] which not only should be much more frequently bright enough but also would provide additional constraints on the system parameters in their light curves, e.g. photometric mass ratios [Kopal, 1959, pp. 490-496]. All suitable candidates will be contained within the Lomb [1976] selected sample of Tab. 4.4 (last column).

---

[60] δ Scuti (or AI Velorum) and SX Phe stars: Stars of spectral classes A-F on the main sequence.

[61] Conti [1984], i.e. P Cygni stars, S Doradus stars, and Hubble-Sandage variables.

[62] See Kuiper [1941], Kopal [1955] for a physically meaningful classification of eclipsing binaries.

[63] Even with a modern 10 m class telescope.

[64] They are also called *Algol* type systems after their prototype β Persei. The variation of Algol (Arabic for "malignant spirit") is most probably known since ancient times and the cause for its ill reputation in astrology. (There are hints of Algol's variation, i.e. related to "Gorgon's eye", even back in Homer's Illiad.) Montanari [1671] systematically observed the variation of Algol between 1668 and 1677 which was another blow to the dogmatic view of the Christian church that the universe was immutable. Goodricke [1784] was the first to interpret the variation as a stellar eclipse.

Chapter 2

Observations

2.1 Candidate Selection

2.1.1 Preselection

Using the compilation of Mateo [1998] we selected the dwarf galaxy candidates to be examined with test observations (Tab. 2.1). The evaluation criteria taken into account were: apparent scale and brightness of the object must be compatible with the instrumentation available, visibility from our observation site, and existence of a young star population to increase the probability of finding δ Cephei stars.

The candidates can be grouped according to their right ascension.

- Pegasus, WLM, IC 10, LGS 3, IC 1613
- EGB 0427+63
- Leo A, Sextans B, Sextans A
- GR 8
- NGC 6822, Aquarius

In order to achieve good sampling the "collision" of best visibilities for the objects should be avoided with the final candidates. Fortunately the candidates accumulate at "winter" right ascensions, were nights at Mt. Wendelstein are significantly longer.

2.1.2 Final Selection

The final selection was done mainly considering the results of the test observations. Furthermore a sufficient distance in right ascension between the individual galaxies and the lack of an already published exhaustive search for variable stars in the objects were mandatory. Finally we had to choose objects which would not interfere too much with the WeCAPP pixellensing project also conducted at Wendelstein observatory [Riffeser et al., 2001, Riffeser, 2006]. So we decided to go for Pegasus, EGB 0427+63, Leo A, GR 8, Aquarius, and, if possible, LGS 3 which does interfere with WeCAPP, but is the only object in this sample doing so.

Table 2.1: Known properties of the dwarf galaxy candidates for test observations at the time of selection. [Mateo, 1998]

WLM -15 δ, 00 h 01 m RA

      pros: strong young stellar population, long night; cons: low declination; additional information: already 15 Cepheids discovered, average distance (within local group).

IC 10 +59 δ, 00 h 20 m RA

      pros: hight declination, long night, only 5-9 Cepheids discovered; cons: low galactic latitude, many foreground stars; additional information: average distance.

LGS 3 (Pisces Dwarf) +22 δ, 01 h 03 m RA

      pros: long night, no Cepheids discovered; cons: weak young stellar population; additional information: average declination and distance.

IC 1613 +02 δ, 01 h 04 m RA

      pros: strong young stellar population; cons: low declination, already 77 Cepheids discovered; additional information: average distance

EGB 0427+63 (UGCA 092) +63 δ, 04 h 32 m RA

      pros: high declination, very long night, no Cepheids discovered; cons: low galactic latitude, many foreground stars, high galactic extinction; additional information: unknown distance.

Leo A (DDO 069, Leo III) +30 δ, 09 h 59 m RA

      pros: long night, high declination, strong young stellar population, only 5 Cepheids discovered; additional information: average distance.

Sextans B +5 δ, 10 h 00 m RA

      pros: long night, strong young stellar population, only 7 Cepheids discovered; cons: low declination, long distance.

Sextans A -4 δ, 10 h 11 m RA

      pros: long night, very strong young stellar population, only 10 Cepheids discovered; cons: very low declination, long distance.

GR 8 (DDO 155) +14 δ, 12 h 58 m RA

      pros: strong young stellar population, only 1 Cepheid discovered; cons: long distance; additional information: average length of night, almost average declination.

NGC 6822 -14 δ, 19 h 44 m RA

      pros: very strong young stellar population, short distance; cons: very low declination; additional information: 13 Cepheids already discovered.

Aquarius Dwarf (DDO 210) -12 δ, 20 h 46 m RA

      pros: strong young stellar population, no Cepheids confirmed; cons: very low declination; additional information: average distance.

Pegasus Dwarf Irregular (DDO 216) +14 δ, 23 h 38 m RA

      pros: strong young population, only 7-10 Cepheids discovered; additional information: average distance, almost average declination.

2.2 Instruments

The bulk of observations aiming at the detection of variable stars with periods of two to several hundred days was carried out with the 80 cm telescope[1] of Wendelstein observatory[2] and the CCD camera MONICA. Additional observations were done with the 1.23 m telescope and its CCD camera at Calar Alto observatory.

2.2.1 The 80 cm Telescope at the Wendelstein Observatory

The Wendelstein 80 cm telescope is a fork-mounted Ritchey-Chrétien system (RC) with a Cassegrain focal station. It has a focal length of $f = 9.9$ m and a primary mirror diameter of $D = 0.8$ m resulting in a f-ratio of $f/D = 12.4$. The free aperture is $A = 0.59$ m^2, and the unvignetted field-of-view diameter $\o = 125$ mm $\approx 0.72°$. The system has a plate scale of 20.8 $''$/mm. [Barwig et al., 2007]

2.2.2 The CCD Camera MONICA

The MOnochromatic Image CAmera (MONICA) is an instrument developed for the 0.8 m telescope of Wendelstein observatory. It was specifically designed to allow high precision narrowband imaging by means of temperature controlled interference filters [Roth, 1993]. Now, it is used almost exclusively for broadband imaging. MONICA is equipped with a Tektronix 1k × 1k CCD which has $24 \times 24 \, \mu$m^2 pixels delivering a pixel scale of 0.5$''$/pixel when mounted on the 80 cm telescope. The broadband filters used for *VarStarDwarves* were Roeser *BV*, Roeser *R*2, and "Johnson" *I* (Fig. 2.1). [Barwig et al., 2007]

2.2.3 The 1.23 m Telescope at the Calar Alto Observatory

The Calar Alto 1.23 m telescope is a German-mounted Ritchey-Chrétien system with a Cassegrain focal station. It has a focal length of $f = 9.8571$ m and a primary mirror diameter of $D = 1.23$ m resulting in a f-ratio of $f/D = 8$. The free aperture is $A = 0.92$ m^2, and the unvignetted field-of-view diameter $\o = 258.1$ mm $\approx 1.5°$. The system has a plate scale of 20.9 $''$/mm. [Marien et al., 1986]
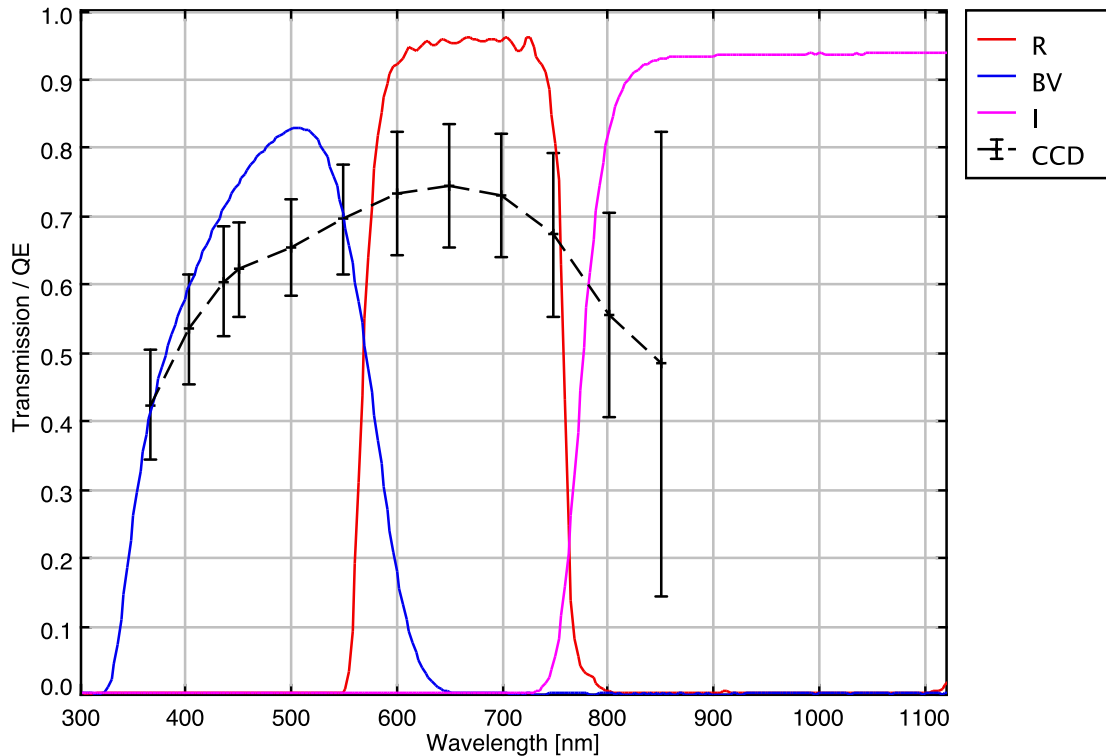
Figure 2.1: The wavelength dependent quantum efficiency (QE) of MONICA's CCD and the transmission of "her" filters used for the *VarStarDwarves* project: CCD Tektronix 1k×1k, 24 μm pixel; Roeser *BV* / 3 mm BG39, Roeser *R*2 / 3 mm OG570 + Calflex_X, "Johnson" *I* / 3 mm RG780. The CCD cutoff *I*-band filter is ill determined, i.e. Johnson not at all.

2.2.4   The 1.23 m CCD Camera

The Calar Alto 123 CCD Camera is equipped with a Site 2k × 2k CCD which has $24 \times 24 \, \mu$m^2 pixels delivering a pixel scale of 0.5″/pixel at the CA 1.23 m telescope. The system is equipped with a motor controlled filter wheel. The filter applied for *VarStarDwarves* were more or less standard Johnson [e.g. 1965] broad band filters *B*, *V*, *R*, and *I* (Fig. 2.2). [Thiele, 2007]

---

[1]"**TELESCOPE**, n. A device having a relation to the eye similar to that of the telephone to the ear, enabling distant objects to plague us with a multitude of needless details. Luckily it is unprovided with a bell summoning us to the sacrifice." [Bierce, 1906] Modern telescopes are usually equipped with the formerly neglected bells.

[2]"**OBSERVATORY**, n. A place where astronomers conjecture away the guesses of their predecessors." [Bierce, 1906] Of course this blasphemy does no longer hold in modern astrophysics which is strict deductive science based on solid findings through unambiguous experiments ... almost. (Those experiments are carried out mostly with telescopes equipped with bells, see footnote 1.)
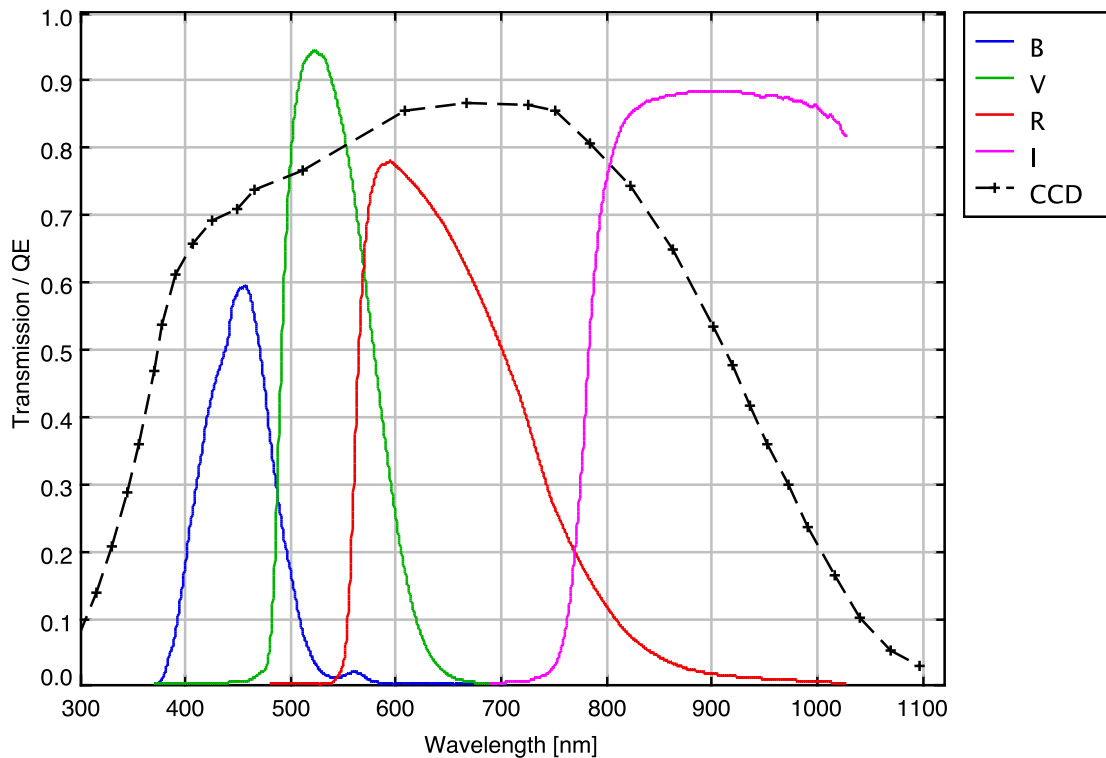
Figure 2.2: The wavelength dependent quantum efficiency (QE) of Calar Alto 1.23 m camera's CCD and the transmission of its filters used for the VarStarDwarves project: CCD Site 2k×2k, 24 μm pixel; Johnson *B* / 1 mm BG12 + 1 mm BG18 + 2 mm GG385, Johnson *V* / 2 mm BG18 + 2 mm GG495, Johnson *R* / 2 mm OG570 + 2 mm KG3, "Johnson" *I* / 3 mm RG780. The CCD cutoff *I*-band filter is the same as MONICA's and therefore also ill determined, i.e. Johnson not at all.

2.3 Improvements to the Observational Performance

Great efforts went into several projects to improve observations at our "home" telescope at Wendelstein Observatory. Besides developing a new CCD camera (Sect. 3) we upgraded the telescope and camera infrastructure to enable remote operation, while aiming for full robotic operation as the final goal.

2.3.1 Dome, Telescope & Environment

Encouraged by the success of simple improvements[3] we[4] continued:

---

[3]I.e. installing a second door in the dome to boost ventilation and shielding MONICA with a Faraday cage from EM radiation of the nearby radio broadcast station [Gössl, 1998, Sect. 2.2.2].

[4]"We" in the following list were mainly Heinz Barwig, Arno Riffeser, Jan Snigula, and me. (And, yes, especially the painting and flooring!)

- A high performance Internet connection now allows immediate access to astronomical Web tools as well as to big storage archiving facilities. It also enables off-site personal to offer service at short notice when encountering software problems. Finally, it is mandatory for remote observations.

- A fibre wired network in addition to uninterruptible power supplies coupled with isolating transformers minimises the damages caused by frequent lightning.

- A *Devil-Linux* [Eng, 2006] based Firewall protects the observatory LAN.

- A temperature and humidity sensor with a network interface has been installed inside the dome.

- A new emergency power generator can overcome 3 days of power outage.

- The installation of webcams in- and outside the dome building and on the telescope improved overall telescope control.

- An EM-shielded electronics laboratory allows on-site maintenance of electronics despite the strong immission of the nearby radio station (≈ 20 V/m in the UHF and VHF bands altogether) and therefore minimises down time.

- To minimise scattered light illumination effects mostly on twilight flat field calibration (Sect. 4.2.6) and "bright time" images[5] we floored the Dome building in black. For the same reasons we also painted the inner side of the dome slit with black colour.

- Air conditioning was installed to improve the "dome-seeing[6]" situation.

- To further improve temperature control we "whitened" the exterior of the telescope building.

- We realigned the telescope mirrors [Lang, 2007] to overcome the well-known problem with RC systems, i.e. decentre coma. Regular mirror alignment control is now part of the maintenance schedule.

- Finally, after the required hard- and software updates had been finished, we relocated the observers from the storey directly below the telescope to a more remote room in order to further decrease the heating of the dome.

The improvements achieved for the local seeing[6] situation are most impressive: Fig 2.3 compares the situation for winter 1997/1998 season [Gössl, 1998], i.e. the first run of the WeCAPP campaign [Riffeser et al., 2001], with 2002, when the *VarStarDwarves* campaign peaked, and

---

[5]Nights with increased skylight background because of moon light.

[6]A temperature gradient between in- and outside the dome blurs astronomical images because of refraction variances in the turbulent temperature boundary layers.

[8]The point spread function (PSF) describes the intensity distribution of a point source in the image plane. Its full width half maximum (FWHM) is a suitable quantity for imaging quality assessment.
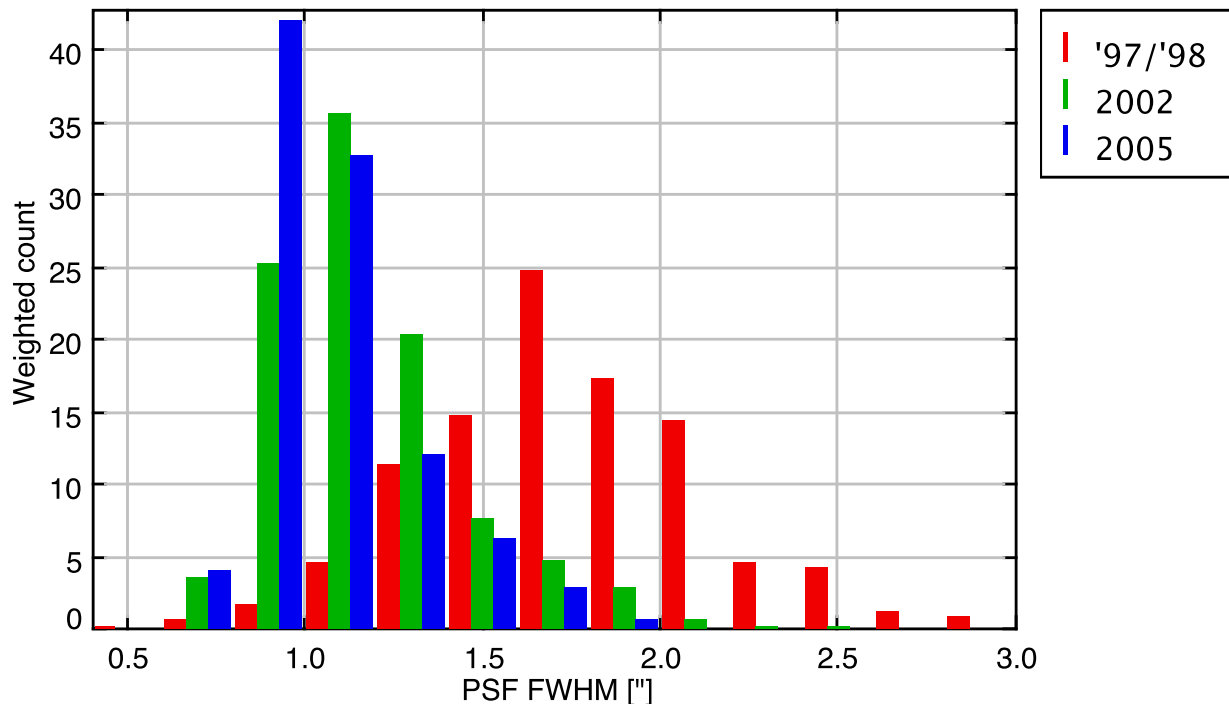
Figure 2.3: Distribution of MONICA / 80 cm WST imaging point spread function (PSF) full width half maximum (FWHM) measurements[8] in the *R*-band for 1997/1998, 2002, and 2005. (Bin size is 0.2″.) The data are all normalised to unity airmass and 100 measurements. In 2005 almost half of the observations had PSF FWHM below 1″ and about 75% were below 1.2″ whereas merely two third were below 1.8″ in the winter of 1997/1998. Note that the Nyquist [1928] rate of MONICA at the Wendelstein 80 cm telescope is ≈ 1″.

2005, the last year with data included in this thesis. The "seeing" statistics mode improved from about 1.7″ in 1997/1998 to about 1.1″ in 2002, and even below 1.0″ in 2005. The huge gain in image resolution translates directly into an improved signal-to-noise ratio (S/N), especially for crowded field photometry. Here, the relation is linear, i.e. the 2005 images excel the '97/98 images by 50%.

The observing environment is being further improved by a webcam based all-sky cloud monitor and by the installation of an additional 40 cm telescope suitable for atmospheric extinction monitoring via standard stars observations [Lang, 2007].

2.3.2 Software – Telescope & Camera Controlling Systems

In the course of my diploma thesis [Gössl, 1998] I deployed a new camera controlling program supporting menu and simple scripting control of all camera features, log file generation, FITS data format images[9], an autofocus function, and already accessing telescope data. We (mainly

---

[9]Wells et al. [1981].

Jan Snigula and me) continued to upgrade the telescope and camera controlling software.

Telescope Control Software

In order to allow remote access to the telescope and to give means for better integration of the observing software the existing telescope software has been expanded and complemented by client / server architecture applications. They communicate utilising an Beck IPC Microcontroller [Bec, 2006] as a relay between the observatory LAN and the telescope's serial interface and hardware switches. The details are given in Snigula [2006, Chap. 7].

Offset guiding – Auto-dither

The offset guiding unit of MONICA is built of a commercial CCD camera (SBIG ST-7) which can be positioned by the same motor controller as the filter wheel of MONICA. A radial translation stage may be rotated by 270 degrees on an azimuth drive. In addition a motor driven adjustable diagonal mirror on the radial stage images a 1:1 subfield onto the guiding camera and allows for focusing as well as for compensation of the focal plane curvature. While the motor controls were already accessible from the MCS [Gössl, 1998, Sect. 2.3.2] the camera and the actual guiding still had to be controlled by a Windows PC. This "solution" was very unstable when encountering rapidly changing observing conditions[10] and also involved very long parallel interface cables which together with the high immission of a nearby radio broadcast station again lead to an unreliable behaviour. Also the field selection for "Windows-"guiding was restricted to three azimuth positions of the camera. Therefore we replaced the Windows PC with a small embedded Linux PC directly attached to MONICA. In order to relay the guiding camera control I wrote a server application for this Linux PC which makes all camera functions available via network and provides a flexible and robust guiding scheme. All server functions and configuration options are detailed in App. A. A graphical user interface based on the cross-platform application development library Qt [Haavard and Chambre-Eng, 2007] can be used to control the guider. This also enables remote control of the guiding unit via Internet. In addition the azimuth position of the camera is directly updated by the MONICA Controlling Software (MCS) allowing to use the complete 270 degrees for guide field selection.

When trying to minimise effects of defective detector pixels and the impact of the S/N ratio of calibration images[11]on the overall S/N ratio of an image stack a technique called "dithering" is the solution: Dithering slightly moves a detector relative to the observed field between subsequent exposures to ensure that the same region of that field is probed by different detector elements. Of course dithering has to be implemented in a manner that it does not interfere with guiding. Actually guiding can even be used to perform the dithering procedure if it can be triggered by the primary camera control system which is exactly the way I went: The MCS has

---

[10]E.g. even small clouds passing by aborted guiding and the commercial guiding software did not allow any changes in the guiding scheme.

[11]See Sect. 4.2.6 for flat field calibration. For actual calculations quantifying differences in S/N of dithered and undithered stacks see Gössl and Riffeser [2002, Sect. 2.2].

Table 2.2: The combined filter throughputs + CCD sensitivity of the 7 MONICA filters relative to the twilight sky without any filter.

filter	no filter	I	R	BV	H_α	V	B	U
throughput τ	1.0	0.2	0.4	0.4	0.05	0.2	0.2	0.05

implemented an auto-dither toggle which, if turned on, triggers dithering during readout of the MONICA CCD.

Automated twilight flat field calibration acquisition

Obtaining a "perfect" flat field calibration image for every night and every filter is mandatory (Sect. 4.2.6). The Tyson and Gal [1993] twilight formula describes the time dependency of the brightness of the twilight sky. After adjusting for the observatory's latitude resulting in a table for the twilight length for every day of the year it can be used to adjust exposure times to achieve flat field images with a more or less constant flux. But full automation requires even more than that: To achieve an optimal flat field series the maximal number of calibration images for a given sequence of filters, which is a complex function of their consecutive throughputs and the CCD sensitivity within that passband in respect to the colour of the sky, has to be predicted beforehand and distributed among them. In addition, images within one filter band have to be dithered by an offset big enough to avoid stars having an impact on a stacked flat field (Sect. 4.2.6).

After implementing the necessary prerequisites[12] I have derived a working scheme by evaluating existing "optimal" flat field series performed by experienced observers. The empirically determined constraining limits for the series are:

- The minimal exposure time is 5 s to minimise systematics caused by the shutter movement.

- The maximal exposure time is 600 s to limit the impact of cosmics and stars on the stacked flat field (Sect. 4.2.6).

- The maximal flux (i.e. the median flux of the flat) is 63488 ADU which is already enough below the saturation level of 65535 ADU.

- The minimal flux is 16384 ADU.

- The "optimal" flux which gives both, enough flux per flat and enough total flats, is about 28672 ADU.

- Multiple filters in a series are sorted due to their throughput (Tab. 2.2), i.e. less throughput corresponds to brighter sky.

---

[12]Telescope offsets controlled by the camera software, date dependent twilight flux prediction for Wendelstein, maximum number of flat fields per filter prediction, automatically constructing the filenames fulfilling the naming convention sky_filter_yymmdd_###.fits, etc.

- A flat field series starts centred on a blank field. Offset the pointing by 20″ in declination and right ascension between every image (flat field dither offset). Change direction of the offset after the every "odd" filter change (first, third, fifth, etc.).

These constraints are applied to the following procedure:

1. Calculate the number n of achievable images per filter:

$$n = \frac{15}{N}\left(1 + \sum_{i=2}^{N} \|T_i - T_{i-1}\|\right) \quad , \text{with} \tag{2.1}$$

N = number of filters in the series,
T_i = relative throughput of a filter band compared with no filter, and
$i = \{U, B, V, H_\alpha, BV, R, I, \text{nofilter}\}$ (Tab. 2.2).

2. Capture $2\,\text{s}$ pre-flat series images with a window readout of the centre 100×100 pixel region[13] until the sky is bright or dim enough to start the series: For dusk the predicted flux for the minimal exposure time must be less than the maximal allowed flux; for dawn[14] the predicted flux for the maximal exposure time must be more than the minimal required flux.

3. Calculate the next exposure time Δt_i with a modified Tyson and Gal [1993] twilight formula:

$$\Delta t_i = \frac{\ln\left(a^{t_i - t_{i-1}} + A\left(\ln a^{\Delta t_{i-1}} - 1\right)\right)}{\ln a} - (t_i - t_{i-1}) \quad , \text{where} \tag{2.2}$$

Δt_{i-1} = the previous exposure time,
$t_i - t_{i-1}$ = the time span elapsed since the previous exposure start,
$A = \text{flux}_{\text{optimal}}/\text{flux}_{i-1}$, the amplification factor needed to derive an optimal flux level considering the flux level of the previous exposure, and
$a = 10^{\kappa/\tau}$, with
$\kappa = 0.094\,\text{min}^{-1}$ the empirical normalisation factor for the exponential twilight brightness law derived by Tyson and Gal, and
τ = actual length of twilight in minutes which has to be determined for the latitude of Wendelstein and every day of the year. If the derived exposure time is beyond the limits reset it to the nearest limit. Start an exposure.

4. During CCD readout move the telescope by the flat field dither offset. If there is an "odd" filter change coming up, reverse offset direction for the next offsets.

---

[13]To reduce the overhead from 90 s for a full image to less than 20 s for the centre 1% window.

[14]"**DAWN**, n. The time when men of reason go to bed. Certain old men prefer to rise at about that time, taking a cold bath and a long walk with an empty stomach, and otherwise mortifying the flesh. They then point with pride to these practices as the cause of their sturdy health and ripe years; the truth being that they are hearty and old, not because of their habits, but in spite of them. The reason we find only robust persons doing this thing is that it has killed all the others who have tried it." [Bierce, 1906] Quot erat demonstrandum: Observing astronomers are men of reason.
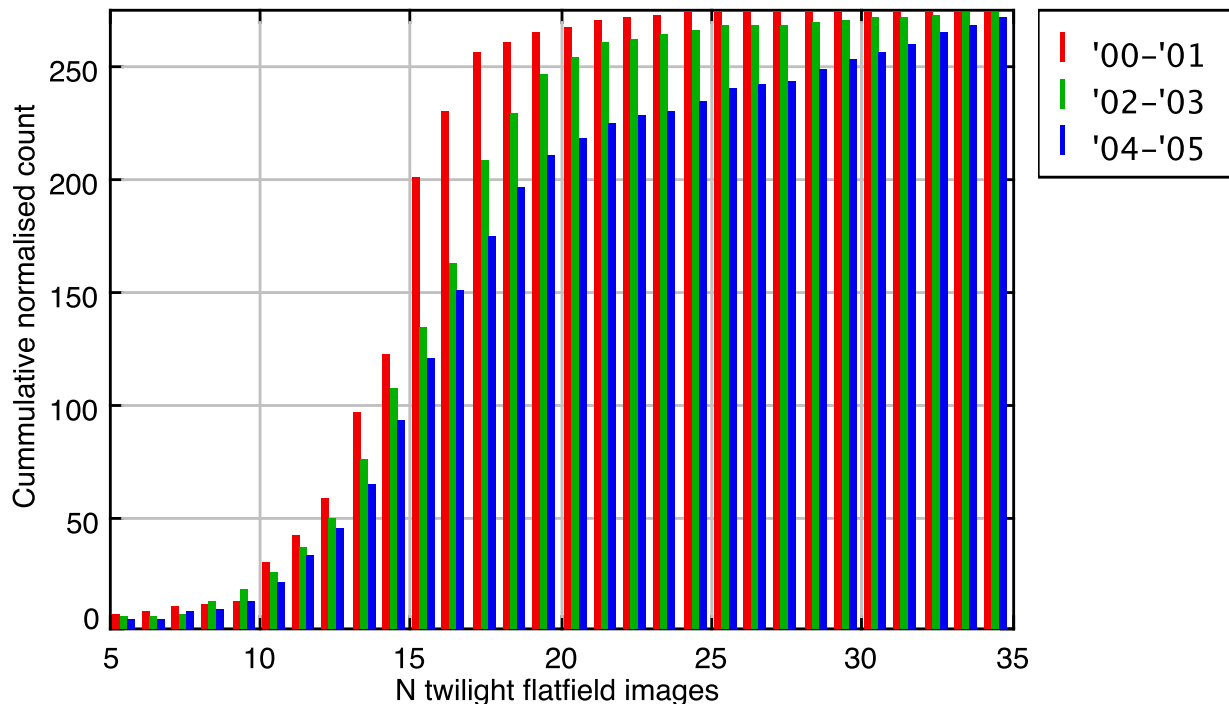
Figure 2.4: The number of flat field calibration images achieved per night has continually increased. First by experience (red to green), then by introducing the auto-flat procedure (green to blue). The cumulative histogram counts the number of twilight flats normalised to the average of 280 clear nights per biennium. The later the histogram saturates or the slower it grows the more flat field images were recorded. Example 1 (blue 250 / 29, green 280 / 29): In '04-'05 for 250 (of 280) nights no more than 29 twilight flat field images could be obtained which implicitly means that for 30 nights more than 29 "flats" were recorded; in '02-'03 no night had more than 29 flats. Example 2 (blue 150 / 16, red 225 / 16): In '04-'05 for 130 (normalised) nights more than 16 "flats" were obtained whereas in '00-'01 only 55 nights surpass 16 "flats".

5. If the current filter is done and there are still filters on the list, select the next filter.

6. Whenever the flux actually was too high before the end of the series or the predicted flux after a filter change would be too high (using the exposure time derived for the previous filter) repeat a pre-flat to readjust the exposure time.

7. Go back to 3, but repeat the last filter in the series just unless the abort conditions for dusk or dawn respectively are met. For dusk: The previous exposure was with maximum exposure time and is below the minimum flux threshold. For dawn: The previous exposure was saturated and the following pre-flat is also saturated.

Fig. 2.4 displays the gain in flat field images per night. (See caption and compare the blue bars to the green and red ones.) The average number of "flats" per twilight increased from 14.34 in '00/'01 over 15.87 in '02/'03 to 17.56 in '04/'05, i.e. by more than 20% overall.
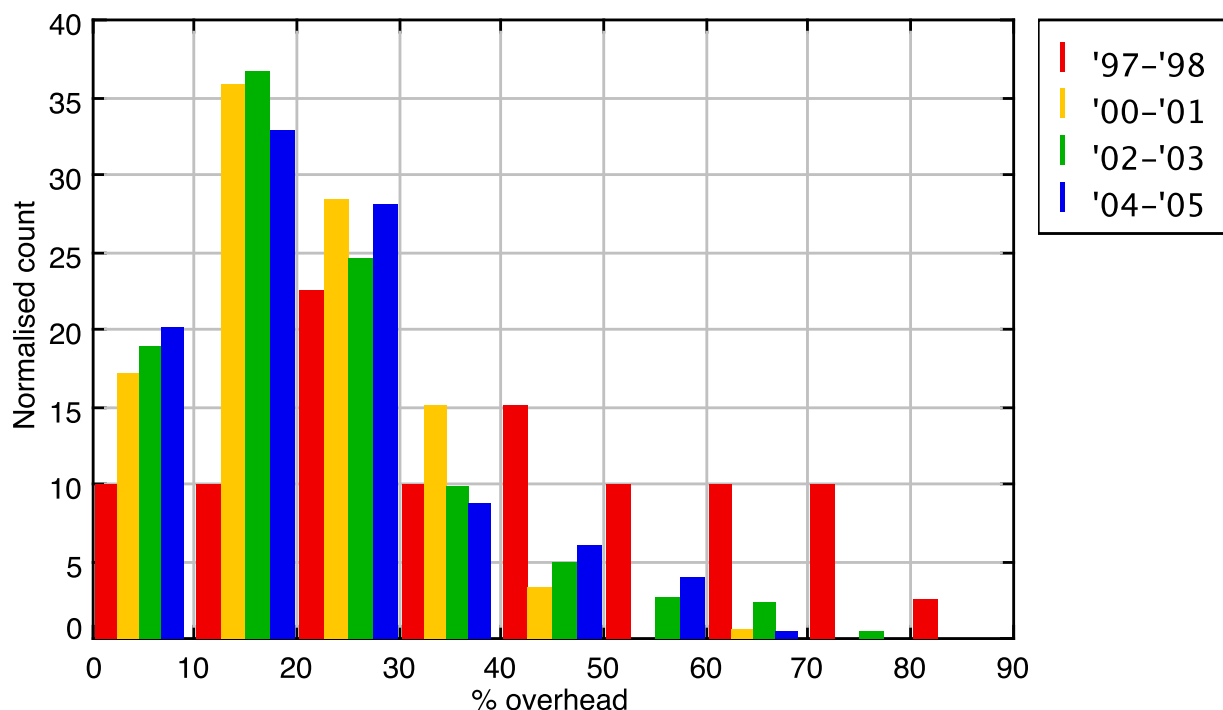
Figure 2.5: The MONICA imaging overhead (excluding pure camera overhead as CCD wipe or CCD readout). The overhead is the percentage of "idle" time of the camera in the span between the first and the last science night sky image of each night. Observations performance has been greatly improved until 2001 and remains on that high level since. In '97/'98 about 50% of the observations had less than 40% overhead (i.e. summing up the four "0, 10, 20, and 30% bins") whereas more than 90% of the observations did so since 2000. The data of 1997/1998 and partially from 2000 had to be put together manually, because no automatic logs were available. Nights with less than 30 minutes "shutter-open" time and guest observers who produced in average more than 50% overhead were ignored. Observation breaks longer than an hour were also put off the record, because they are presumably due to clouds passing through.

2.3.3 Log files, Webcam Movies, and Backups

To replace handwritten observation reports and manual DAT tape archives by more contemporary means I installed additional network services: Instrument and observer log files, logs of the dome environment and the public weather[15] station messages, together with small movies of

---

[15]"**WEATHER**, n. The climate of the hour. A permanent topic of conversation among persons whom it does not interest, but who have inherited the tendency to chatter about it from naked arboreal ancestors whom it keenly concerned. The setting up official weather bureaus and their maintenance in mendacity prove that even governments are accessible to suasion by the rude forefathers of the jungle.

Once I dipt into the future far as human eye could see,
And I saw the Chief Forecaster, dead as any one can be –
Dead and damned and shut in Hades as a liar from his birth,

the terrace and the 80 cm telescope finder webcams are automatically collected and placed on a secure "Intranet" website which also hosts observatory documentation. All data collected is synchronised with a backup system at USM[16] which again runs an automated backup process utilising the LRZ[17] archive centre in Garching. The new services not only allow to evaluate observation performance more easily, they even provide means to automate surveillance procedures (Fig. 2.5, also Fig. 2.3 and 2.4).

2.4 Observational Strategies

The overall observation setup should yield a preferably homogeneous data set. Therefore the decisions to be made during observations should be few and simple to accomplish this requirement with multiple observers and observing conditions. Aiming at a limiting magnitude of ≈ 22.5 and taking into account instrumental overhead as well as the frequency of instrumental and observing artifacts (i.e. satellite trails, cosmics, focus drift, guiding failure etc.) we came up with the following observing strategy:

- A single observations series comprises 10×180 s exposures of one target in one filter.

- Since R-band yields best S/N ratio per time it is our primary filter. Additional filters to derive colours should be pursued only with good observing conditions (i.e. seeing $\leq 1.5''$, sky $\leq 60 \, e^-/s \, arcsec^2$).

- An observations series shall be repeated if the limiting magnitude could not be reached with one run (i.e. seeing $\geq 1.5''$, sky $\geq 60 \, e^-/s \, arcsec^2$), if necessary multiple times.

- All exposures of a single series should be dithered[11] to reduce the impact of pixel systematics and the flat field noise.

- Try to get as many flat field exposures as possible to avoid calibration being the limiting factor.

With a record of unreason seldom paralleled on earth.
While I looked he reared him solemnly, that incandescent youth,
From the coals that he'd preferred to the advantages of truth.
He cast his eyes about him and above him; then he wrote
On a slab of thin asbestos what I venture here to quote –
For I read it in the rose-light of the everlasting glow:
Cloudy; variable winds, with local showers; cooler; snow.

Halcyon Jones" [Bierce, 1906]
    [16]Universitäts-Sternwarte München der Ludwig Maximilians Universität München.
    [17]Leibniz-Rechenzentrum der Bayerischen Akademie der Wissenschaften in Garching bei München.

2.5   Observations – Database

Tab. 2.3 displays the maximum covered time span from 1999 to 2005 and the number of observed nights per filter / site for each of the observed candidates. After data reduction (Sect. 4) nights with very bad observing conditions resulting in significantly lower limiting magnitudes were abandoned whereas nights with many high quality images were split into several epochs (Sect. 5). One epoch is a stack of 10 to 30 three minutes exposures, depending on the observing conditions (seeing, sky etc.). Observations are still continued to expand the detectable period range to even longer periods.

Table 2.3: Maximum time span and number of observed nights per filter and instrument.

| object | Δt [y] | WST - 80 cm | | | CA - 1.23 m | | | |
		BV	R	I	B	V	R	I
Leo A	5.7	46	150	2	13	1	47	29
Pegasus	5.3	21	83	2	–	–	2	–
EGB 0427+63	5.8	61	184	3	14	–	48	29
GR 8	5.2	28	112	1	14	1	49	33
Aquarius	5.5	13	95	1	3	–	10	2
LGS 3	5.1	12	48	2	–	–	–	–

Chapter 3

AMiGo – A New, Two-Channel CCD Camera for Wendelstein Observatory

Tests of the seeing conditions at Mt. Wendelstein displayed a seeing statistics mode of 0.5″ FWHM. The telescope of Wendelstein Observatory is designed to reach an encircled energy distribution of 80% within a 0.6″ diameter over a 100 mm diameter field-of-view (FoV). The CCD-camera employed at present[1] (MONICA) does not comply with those site and telescope characteristics: Its 1k × 1k CCD with 24 μm × 24 μm pixels yields an 8.5′ × 8.5′ FoV with a 2 pixels / ″ scale leading to undersampling even for average observing conditions. We therefore decided to build a new camera which can take full advantage of the current situation, and, at the time, will enable robotic operation. This new instrument was planned to play a major role in the VarStarDwarves project. Unfortunately many problems during the manufacturing phase of the instrument delayed the commissioning until 2007. Nevertheless, the developement and building of the camera being a substantial part of my work and its construction being motivated by my PhD thesis I will give a summary of the overall camera design as presented at the SPIE conference on "*Astronomical Telescopes and Instrumentation 2002*" and published in the corresponding proceedings [Goessl et al., 2003].

3.1   Optical Layout

3.1.1   Design Goals

To specify the design goals for the camera we defined a three-level scheme of favoured characteristics, basic conditions, and acceptable trade-offs.

---

[1]"**PRESENT**, n. That part of eternity dividing the domain of disappointment from the realm of hope." [Bierce, 1906]

Favoured characteristics

The pixel scale of the instrument must be adapted to the optical performance of the telescope and the seeing of the site, which requests at least 2 pixels / 0.6″. If feasible the FOV should be larger than the present one. Using high efficient CCDs and building a multi-channel camera, which also allows simultaneous multi-waveband observations, increases the telescope efficiency tremendously. A photometric shutter enables short exposures without introducing systematic errors (shutter pattern). Therefore it allows a superb twilight flatfield acquisition for every night. Including robotic operation and maintenance features, thereby minimising the need for on-site manpower, will help to guarantee a future for the observatory. Since fund raising for a new 2 m class telescope for Wendelstein observatory was successfull the camera should be able to cope with a 2 m, $f/6$ telescope design without too much image degradation.

Basic design constraints

All basic conditions can be summarized in the need for a compact design: The optics must fit between the focal plane and the telescope flange, which are only 267 mm apart from each other. A massive electro-magnetic shielding for all electronics is mandatory not only because of frequent lightning but moreover to minimize the influence of the intense radio immission of a nearby radio station. The complete instrument (including controllers and EM-shielding) must not exceed a weight of 100 kg. It must apply to the telescope's Cassegrain focus and therefore fit in a volume less then $0.5\,\text{m}^3$.

Acceptable trade-offs

Concessions may be made regarding the filter wave bands: Despite its excellent seeing conditions the observatory site displays only modest transparency and suffers from light pollution of nearby villages. The Hg lines of the street lighting add to the O[I] night-sky line in the V band. The already poor performance of atmospheric cut-off UV band filters, which is mainly due to air pollution, is also hampered by the street lighting, i.e. its UV lines. So the use of both, U and V band filters, should be avoided.

3.1.2   Design Solution

Because of the compactness constraints we decided to go for a two-channel design. The heart of our design solution is a massive dichroic beam splitter cube with two reflection prisms attached so that both beams have their focus in the same image plane (Fig. 3.1 and Fig. C.1, top). This enables us to place both CCD detectors into a single cryostat with one Cryotiger cooling unit, only. We defined the dichroic layer to build two optical channels operating in the spectral range of $400 - 540\,\text{nm}$ and $570 - 900\,\text{nm}$. The camera has three interchangeable filters per channel and two independent photometric shutters. It is equipped with two LORAL/Lesser $2\text{k} \times 2\text{k}$ CCDs with 80% peak quantum efficiency [Deiries et al., 1995, 1996, and Fig. 3.4 here], each displaying the same FOV of $10.7' \times 10.7'$ with a resolution of $0.3''$ per $(15\,\mu\text{m})^2$ pixel.
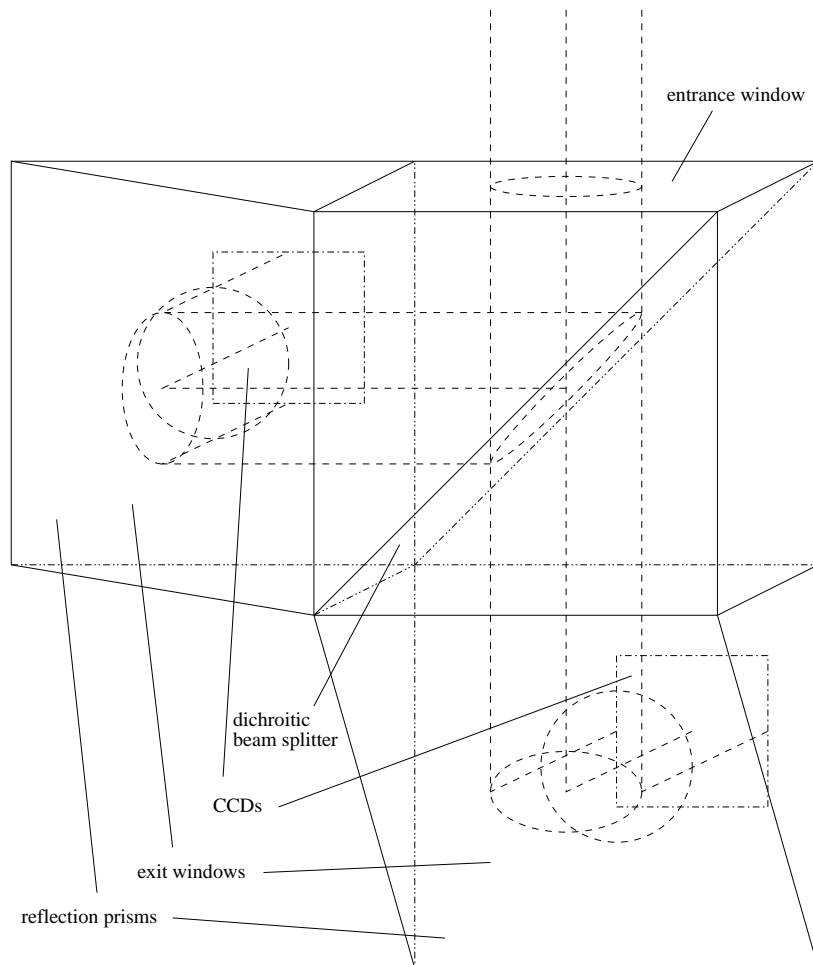
Figure 3.1: Design sketch [2:3] of the dichroic beam splitter. Light falling in from "above" is split within the 80 mm × 80 mm × 80 mm beam splitter cube in a reflected, left side, blue beam and a transmitted, downwards, red beam. Both beams are reflected by adjacent reflections prisms and leave the unit "backwards" to fall on their corresponding 30 mm × 30 mm CCDs resting in the same image plane after a 60 mm gap which holds filters, shutters and cryostat windows. The 160 mm massive glass results in having a wavelength dependent focal length. This can be compensated by filters of an individually matched thickness, which are inserted between the beam splitter and the CCDs. Coordinate definition: x-axis from left to right, y-axis from bottom to top, z-axis from image/CCD to observer plane.

3.1.3 Resulting Optical Parameters

The massive design of the dichroic beam splitter and the reflection prisms elongates the focus distance by 53 mm which gives additional room for the filter and shutter modules. But it also introduces a chromatic error. The thickness of each filter has to be adjusted to compensate for the wavelength dependency of the focus length. Because of the slow f-ratio ($f/12.4$) of the

Table 3.1: AMiGo image quality as derived by raytracing simulation for the SDSS [Fukugita et al., 1996] filter set (Fig. 3.4, bottom). Radii of r.m.s. spot size (top and Fig. 3.2) and 80% polychromatic encircled energy (bottom and Fig. 3.3). Columns: respective filter, radii of airy disk (top) and diffraction limit (bottom), corresponding radii for on optical axis (central field), an average distance to the optical axis, the detector edge, and the detector corner.

field	airy disk	centre 0.0 mm	avg. 10.6 mm	edge 15.0 mm	corner 21.2 mm
filter		r.m.s. spot radius [μm]			
SDSS g	6.5	12.8	12.7	13.3	16.0
SDSS r	8.8	11.2	11.1	11.7	14.6
SDSS i	11.0	10.7	11.3	12.6	16.5
		radius of 80% encircled energy [μm]			
SDSS g	9.2	19.5	18.8	18.6	19.5
SDSS r	12.2	19.4	17.7	16.7	18.6
SDSS i	14.9	18.3	17.8	17.8	20.9

telescope the intra wave band error of a single filter is rather small. Raytracing simulations of the expected image quality for the SDSS [Fukugita et al., 1996] filter set (Fig. 3.4 and Tab. 3.2, bottom) are presented in Fig. 3.2 and Tab. 3.1. Unlike a design using beam splitter plates no offcentre ghosts, astigmatism, or additional coma[2] are inferred. The apertures of the entrance and exit windows are baffled to meet even the demands of an $f/6$ focal ratio of a future 2 m class telescope for Wendelstein observatory without affecting the field illumination, i.e. off-field beams deflected inside the beam splitter unit are masked.

3.1.4 AMiGo Filter sets

The first AMiGo filter set was designed to mimic the standard MONICA (Fig. 2.1) and/or Johnson [1965] filters (Tab. 3.2 and Fig. 3.4 top, photos in Fig. C.1, top.). Using coloured Schott glass filters [Sch, 2004] is cheap but undermines compensating the chromatic focal length because of their very ill defined refractive indices. A second set of filters (Tab. 3.2 and Fig. 3.4 bottom) following the meanwhile standard[3] SDSS system [Fukugita et al., 1996] was specified and ordered as thin film coated fused silica which has a well known refractive index. Its filter thicknesses completely compensate for inter-waveband focal length discrepancies.

---

[2]The astigmatism resulting from a beam splitter plate can be corrected with an additional plate rotated by 45° along the optical axis but with the same inclination angle as the beam splitter plate, but will show coma shaped distortions [Reif et al., 1999, Woche et al., 2000].

[3]For extragalactic science.
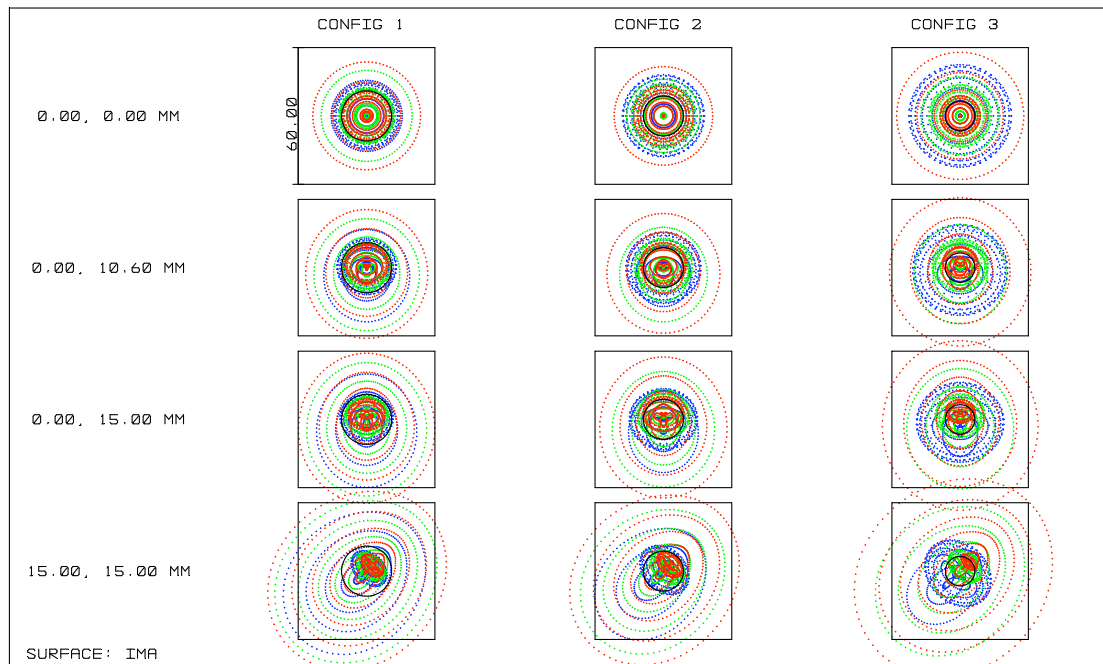
Figure 3.2: Visualisation of AMiGo image quality by raytracing spot diagrams. (See also Tab. 3.1, top.) The focus position of the image plane is adjusted to optimum within the detector area, i.e. minimising r.m.s. spot sizes. Rows: From top to bottom central field (on optical axis), average field (average distance from optical axis), detector edge, detector corner. Columns: From left to right SDSS [Fukugita et al., 1996] i (Config 1), r (Config 2), and g (Config 3) filter cases (Tab. 3.2 and Fig. 3.4, bottom). Colours: blue is short wavelength 50% transmission edge, green is central wavelength, red is long wavelength 50% transmission edge. The black ring show the airy disk. The black box has a side length of $60\,\mu$m correspondig to 4×4 detector pixels.

3.2   Mechanical Design

The optically active parts of the camera are combined to four major units: the cryostat, a filter / shutter unit, the dichroic beam splitter unit and the offset guiding unit. All units together with controllers and computers are mounted on a basement plate, which is suited to be attached to the telescope flange. (See also design drawings Fig. 3.5 and 3.6 as well as photos in Fig. C.1 and C.2.)

3.2.1   Cryostat

The cryostat holds two CCDs placed on two independent, three-axis motorized chip mounts: Six Newfocus Picomotors enable two-axis tilt plus an independent focus adjustment for each CCD. Together with the six axis alignment of the beam splitter unit (Sect. 3.2.3) we have 12 axis alignment for two detectors, so every detector can be aligned independently. Active cooling by a
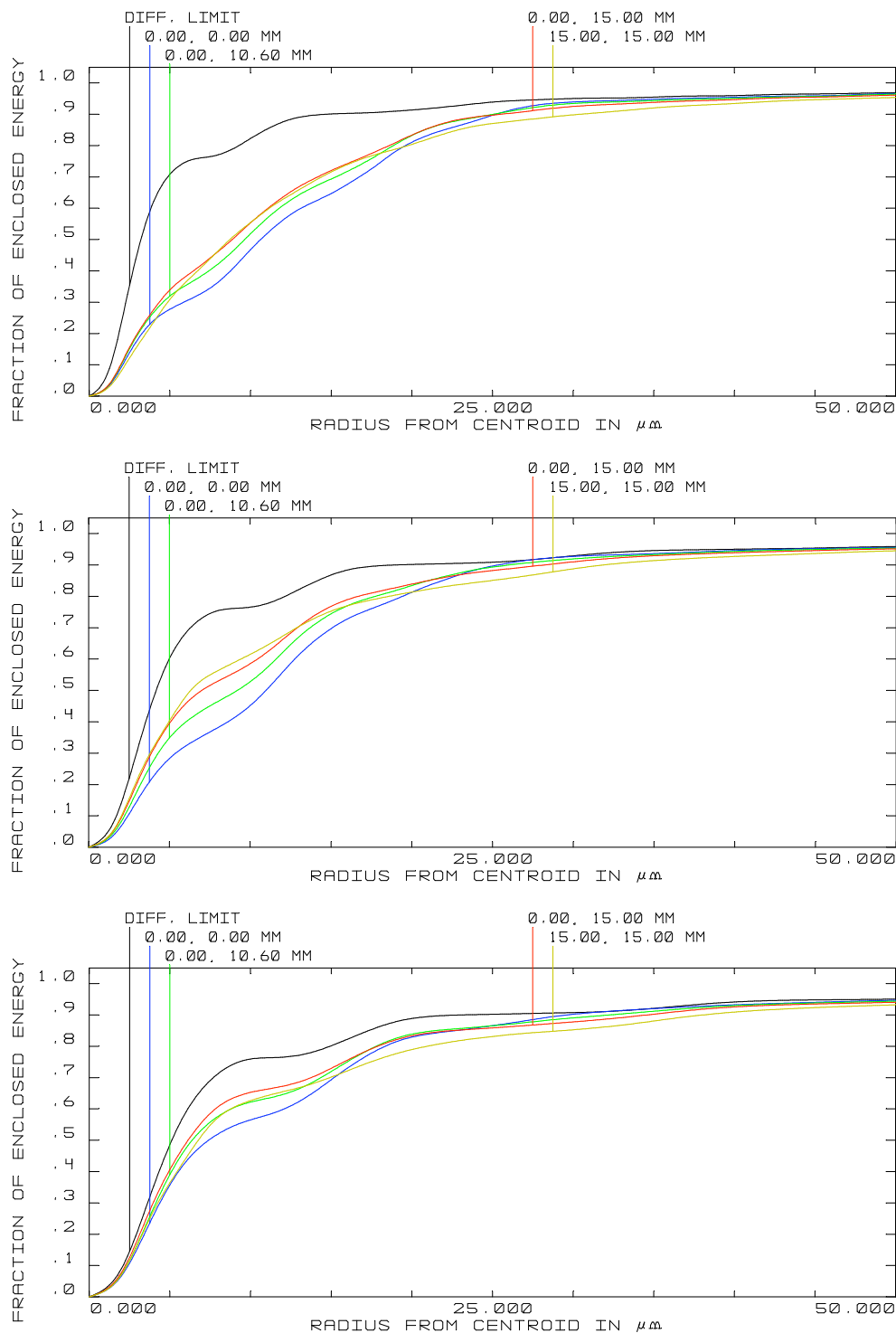
Figure 3.3: Visualisation of AMiGo image quality by raytracing simulation, i.e. polychromatic encircled energy distribution within respective filter band. (See also Tab. 3.1, bottom.) The focus position of the image plane is adjusted to optimum within the detector area, i.e. minimising r.m.s. spot sizes. Rows: From top to bottom SDSS g, r, and i filter cases (Fig. 3.4, bottom). Colours: black corresponds to the diffraction limit, blue to the central field (optical axis), green to an average field (average distance from optical axis), red to the detector edge, and yellow to the detector corner.
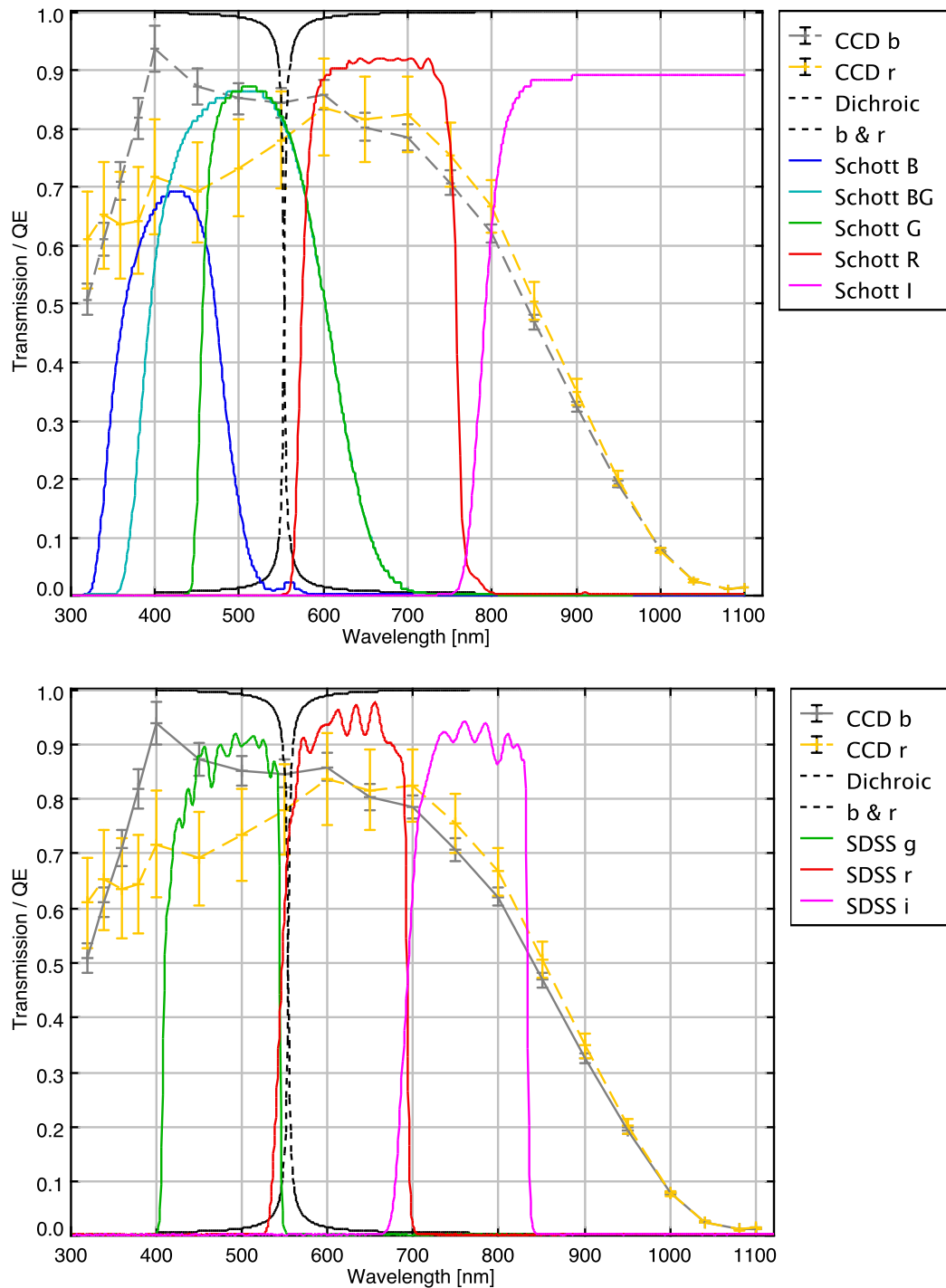
Figure 3.4: Both figures: Wavelength dependent quantum efficiency of the AMiGo LO-RAL/Lesser CCDs [Deiries et al., 1995, 1996]. One CCD (grey) shows clearly superior sensitivity in the blue bands, while the other (yellow) displays only a slightly enhanced response in the red bands. The wavelength characteristics of the dichroic beam splitter are shown as specified. Top: Throughput of the AMiGo Schott coloured glass filters as specified. Bottom: Throughput of the AMiGo SDSS [Fukugita et al., 1996] filter set as measured by its producer. The filters are made of thin coated fused silica and their thickness is adapted for a common focal plane independent of wavelength. (See also Tab. 3.2.)

Table 3.2:   Filter waveband characteristics: Schott coloured glass filters [Sch, 2004], SDSS [Fukugita et al., 1996] filters, and dichroic beam splitter as specified (see also Fig. 3.4). Numbers in brackets give an estimate for the filter characteristics when combined with the beam splitter (B, BG, G) or the CCD (I).

filter name	composition	blue edge [nm]	centre [nm]	red edge [nm]
Schott B	1 mm BG25 + 2 mm BG39	349 (365)	415 (390)	482
Schott BG	1 mm BG39 + 2 mm GG395	390	499 (472)	609 (554)
Schott G	1 BG39 + 3 mm GG455	455	532 (504)	609 (554)
Schott R	2+3 mm OG570 + thin film coatings	573	651	730
Schott I	3+3 mm RG780	789	– (854)	– (920)
Dichroic beam splitter	fused silica + thin film coatings	400 – – 540	554	570 – – 900
SDSS g	3.81 mm fused silica	409	477	546
SDSS r	5.48 mm + thin film	555	623	692
SDSS i	6.0 mm coatings	695	763	831

Cryotiger cooling device provides the operating temperature of 160 K. A turbomolecular vacuum pump is permanently attached to the cryostat via an electromagnetic vacuum valve. A cryopump which has onboard heating resistors to allow cleaning cycles without requiring any additional equipment keeps the vacuum between pumping cycles. Both, active cooling and permanent vacuum control together enable robotic maintenance.

3.2.2   Filter / Shutter Unit

The complete filter / shutter module is only 40 mm thick and can easily be mounted / dismounted without interfering with any of the other units. In this way the instrument needs no optical readjustment in case filters need to be replaced. The unit holds two three-position motorized filter sliders, which are specified to reproduce their position with below μm accuracy. Each of the two shutters has two motorized linear blades to have equivalent opening and closing movements. We expect to achieve full field photometric exposures at a 0.1% systematic error level for exposure times as short as 0.1 s.

3.2.3   Dichroic Beam Splitter Unit

The beam splitter cube / reflection prism module is housed within a six-axes alignment module. Position and position angle have to be manually adjusted once by tuning micrometer screws. The rotational axes cross in one point centred within the beam splitter cube to make the optical adjustment easier. The rotational mount resides within the Cartesian translational mount which again
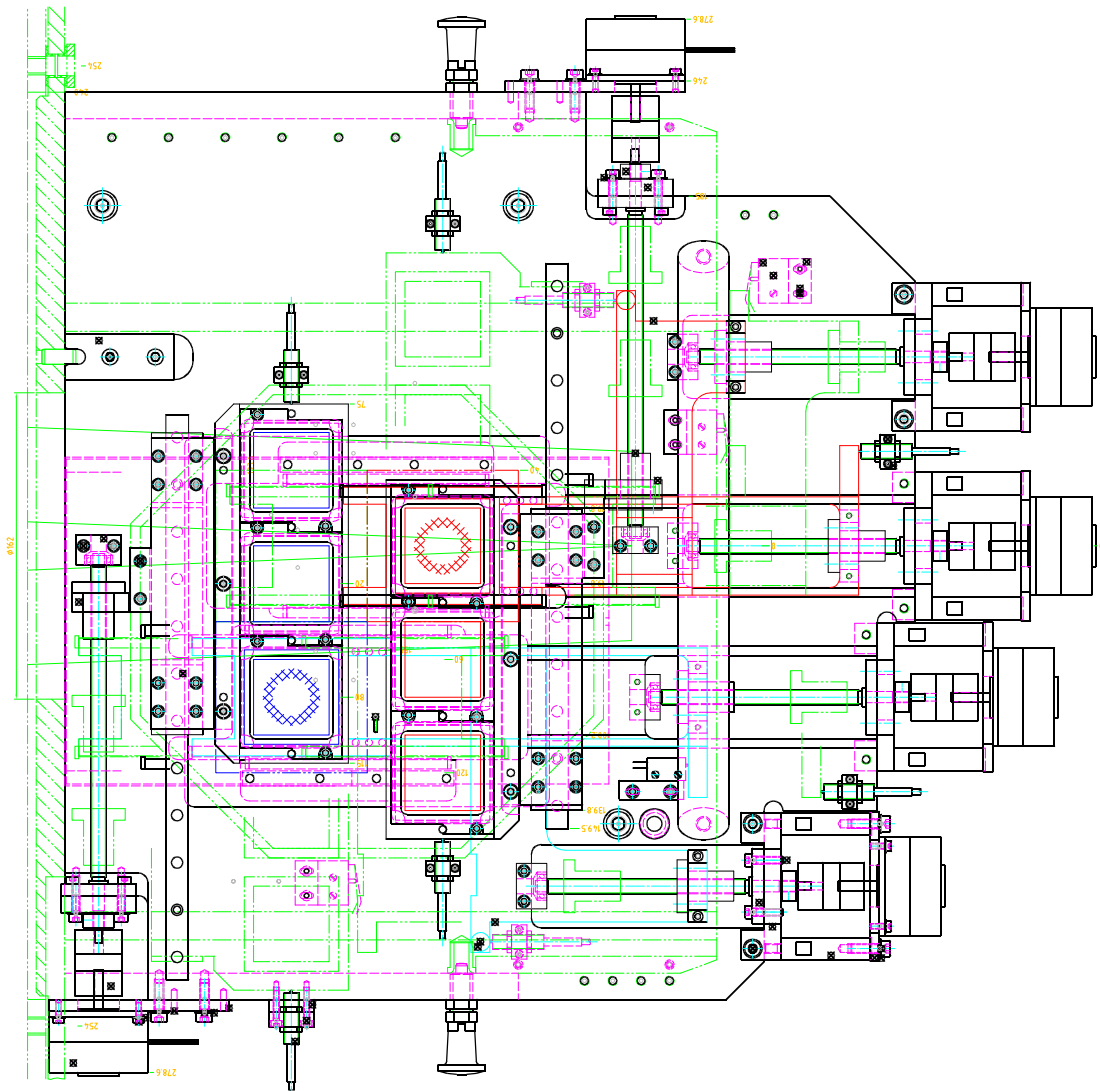
Figure 3.5: Filter / shutter module [1:4]: The design drawing shows a front view of the shutter (background) and filter slider module detailing also the motors and limit switches. The telescope flange side is left on this view.

is oriented along the major axes of telescope and instrument. In this way complex differential effects when adjusting the optics are avoided (Tab. 3.3).

3.2.4 Offset Guiding unit

The offset guide field is deflected by a mirror mounted on the beam splitter unit. The guiding camera rests on a motorized two-axis translation module which enables offset focus adjustment and an one-axis guiding field selection.
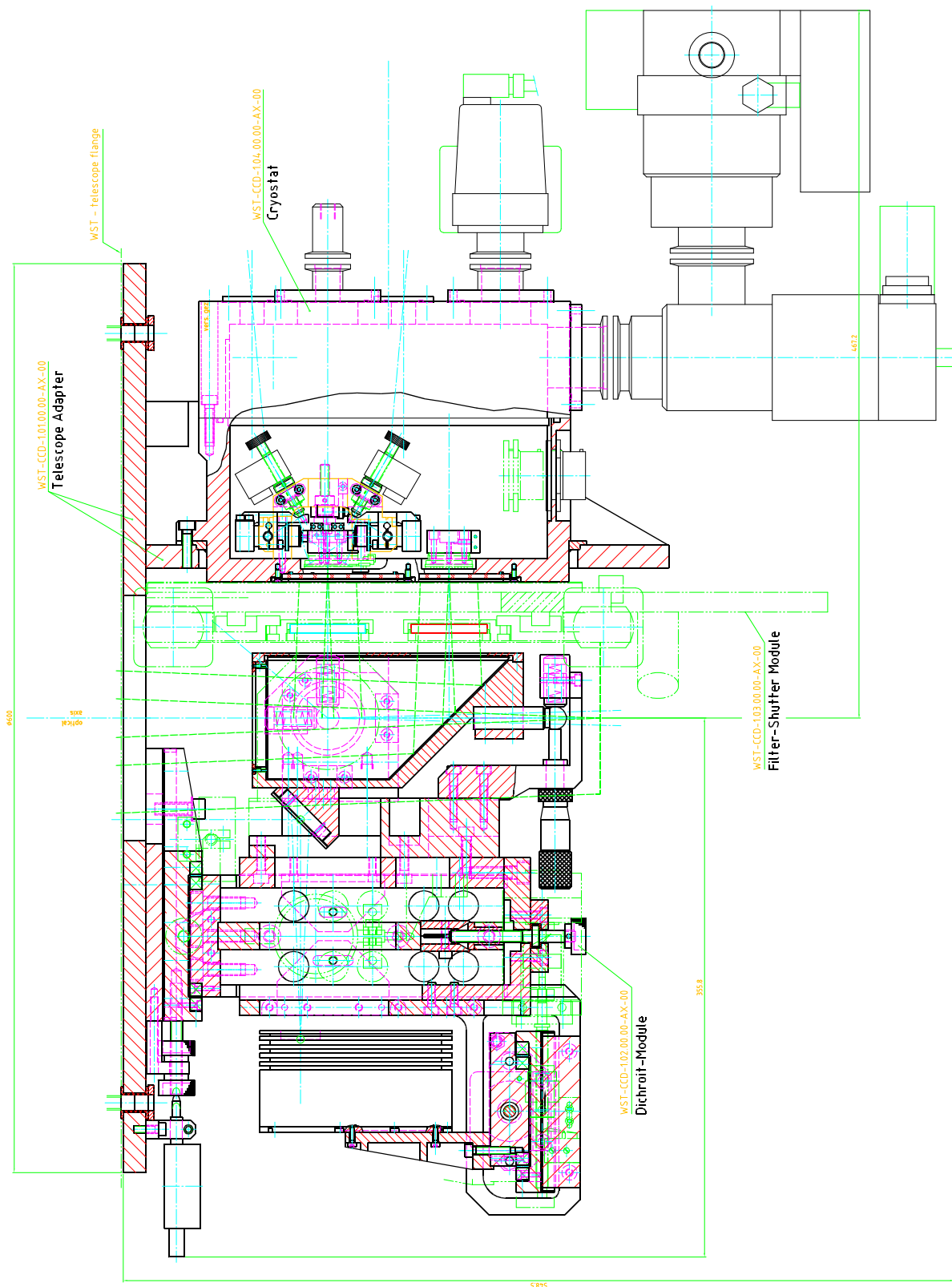
Figure 3.6: Camera overview [1:4]: The beam from the telescope enters left and is split and reflected upwards in the dichroic module, then passing through the filter/shutter module and finally focusing in the cryostat module. The beam for off-field guiding is deflected by a mirror "below" the beam splitter to the guiding camera resting on its mount at the bottom.

Table 3.3: First order adjustment recipe for the dichroic beam splitter unit. See Fig. 3.1 for coordinate definition. The relevant distances for the rotational adjustments are: rotation centre to micrometer adjustment screws = 150 mm, rotation centre to reflection prisms centres = 80 mm, and reflection prism centres to CCDs = 100 mm.

adjustment	lateral			rotational		
by +1 (e.g. μm)	x	y	z	x	y	z
result on CCD				**red**		
x	±0	±0	±0	±0	$\frac{-10}{15}$	$\frac{-10}{15}$
y	±0	+1	−1	$\frac{+20+8}{15}$	±0	±0
z	±0	−1	+1	$\frac{-8}{15}$	±0	±0
result on CCD				**blue**		
x	+1	±0	−1	$\frac{-18+8}{15}$	$\frac{-18-10}{15}$	±0
y	−1	+1	±0	$\frac{+10}{15}$	±0	$\frac{-36+10}{15}$
z	±0	−1	+1	±0	$\frac{+8}{15}$	±0

3.3 Electronic Desgin

3.3.1 CCD Controller

We use the third generation of the Leach and Low [2000] controller. It connects via fiber link to a PCI board which is installed into a PC running the controller software client, which is in our case the camera daemon server (Sect. 3.4.2).

3.3.2 Cryogenic and Motor Controllers

Stepper motors and limit switches for filter slider, shutter blades, and guiding camera movement are controlled by a CyberPak module [Cyb, 2001]. The Picomotors for the CCD alignment are controlled by a separate device driver. The vacuum and cooling devices already provide their own controlling systems. All those systems have serial interfaces which are connected to the camera network. (Sect. 3.3.4.)

3.3.3 Offset Guiding Camera

We use a ST7 CCD camera of SBIG controlled by a small Linux PC as guiding camera. This solution has been well tried and tested with the current camera system (Sect. 2.2.2 and 2.3.2).
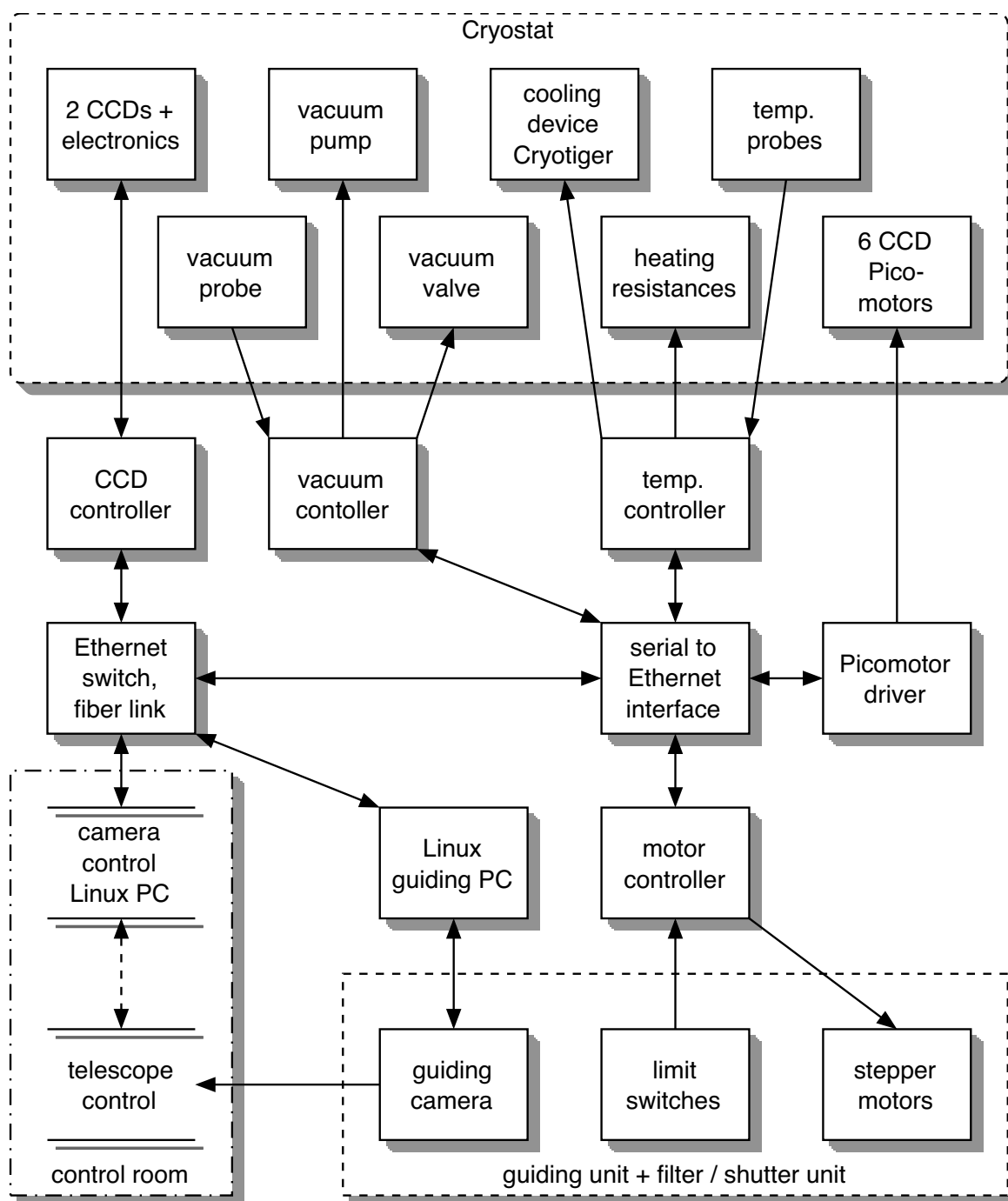
Figure 3.7: AMiGo Control Flowchart (Sect. 3.3.4): Except for the control room box, all components are mounted at the telescope and reside within the EM-shielding. The components are connected to the camera control by a fiber wire link. The camera control, which also holds the main storage unit, can be accessed via Internet.

3.3.4 Network

All Controllers have either Ethernet interfaces, or serial interfaces which are mapped to a Ethernet interface by a Beck IPC Microcontoller. The Ethernet interfaces are combined in a switch which has a fiber link connection to the main camera controlling computer. This Linux PC, which also is connected to the telescope controlling system, holds the main storage device and can be remote controlled via Internet. (See also Fig. 3.7.)

3.3.5 Electro-Magnetic Shielding

To protect the electronics of the camera against frequent lightning and the high radio immission of a nearby radio station it has a massive EM-radiation shielding. The shielding is made of 0.7 mm thick copper plate sheet and conductively connected to the mirror cell. Therefore this Faraday cage has only one major opening for the infalling light beam. Several minor openings are for wiring and a venting system, which is needed to avoid heating of the mirror cell by the camera electrics. An uninterruptible power supply (UPS) and the fiber link connection (Sect. 3.3.4) provide additional safety.

3.4 Controlling Software

The controlling software follows closely the lessons learnt by previous instrument upgrades to MONICA, its offset guiding system and the 80 cm telescope software (TCS). We implement a client / server architecture utilizing programs and libraries already developed for the TCS network [Snigula, 2006, Chap. 7].

3.4.1 Controller interfaces

The CCD controller, connected to proprietary PCI boards of a PC via fiber link, is controlled through device drivers and a software called Voodoo [Streit, 2003]. Voodoo provides low-level C-routines for all controller functions as well as an exemplary Java-GUI.

Two HS-20E Multi-Axis Indexer / Controller of Cyberpak Co. [Cyb, 2001] are controlled via serial interfaces which again are mapped through a Beck IPC device [Bec, 2006] to a TCP/IP socket. The "native" motor controller commands are very cryptic if not incomprehensible. To make things worse some commands do not even work as documented. There are 8 motors altogether which have to be controlled: 2 blades per shutter, 2 filter sliders, guiding focus and field. Since only one Indexer can be active at a time and motors have either to move sequentially or at least with identical stepping we grouped the shutters with one controller and the filter sliders and guiding with the other. This way the camera can take either "*optionally interleaving*" sequential[4] or strictly parallel exposures. Exposures shorter than 5 seconds are accomplished by the two shutter blades forming a slit which moves through the optical beam. Besides exposures

---

[4]Meaning that only one shutter blade can move at a time, but e.g. one channel can make a long exposure while the other takes several short ones.
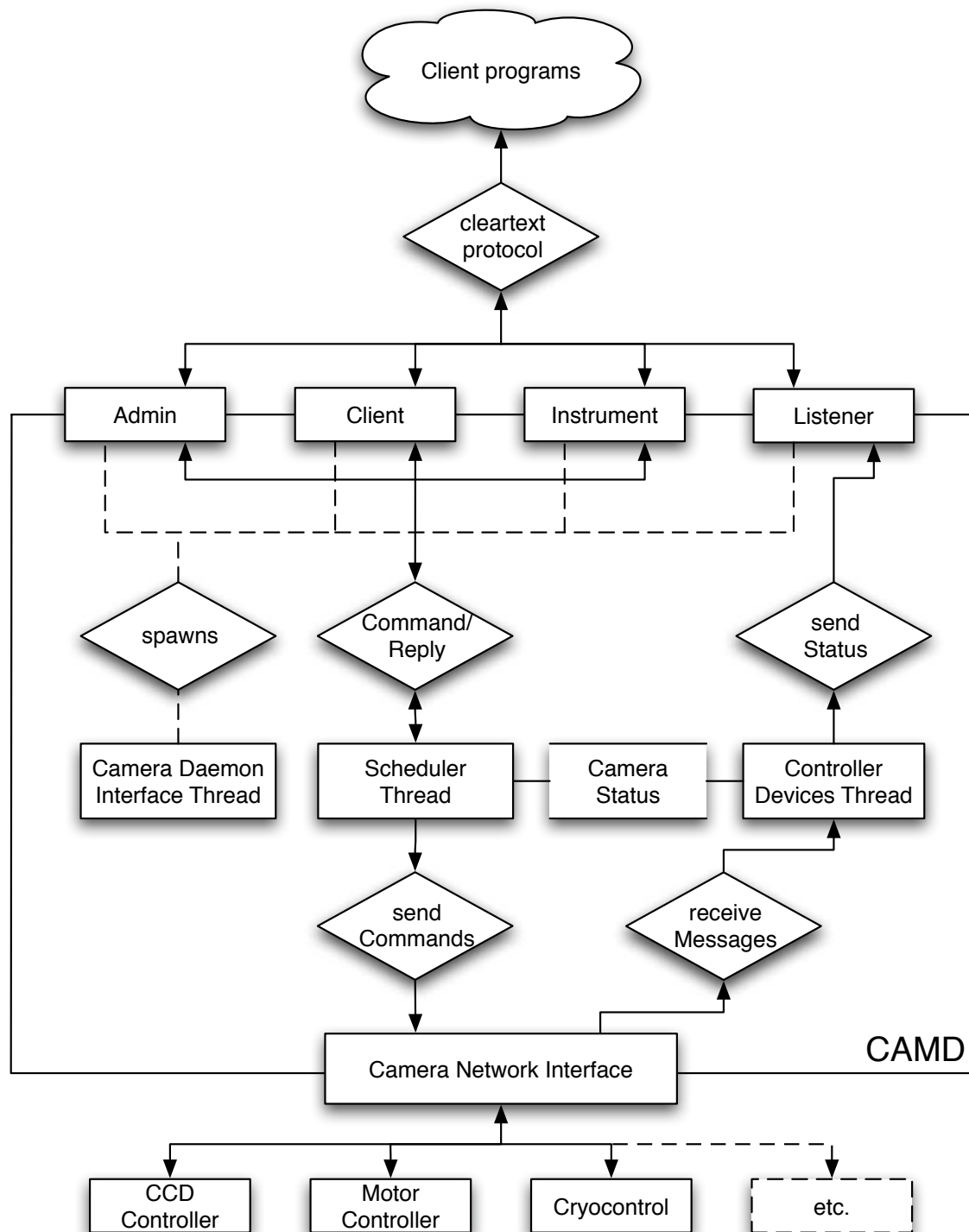
Figure 3.8: AMiGo Server Daemon (camd) overview. Top: Client interfacing; centre: Main threads and status field; bottom: Camera controller interfacing.

(and initialisation) all motors can only move one at a time. For additional information on specific motor controller commands see App. B.1.

The picomotors, vacuum and temperature control serial interfaces come all with their own proprietary protocol. They are relayed through the same Beck IPC device which also handles explicit interface multiplexing.

3.4.2 Server design and interface

The *camera daemon (camd)* follows closely the *TCS daemon (tcsd)* of Snigula [2006, Chap. 7]. The multi-threaded daemon has three principle threads (Fig. 3.8): Those are a main thread which spawns the client interface threads, a scheduler thread which takes care of executing the command queue, and a camera controller devices thread which listens for camera status messages from the different device controllers. The client interface threads supply an access hierarchy provided by separate dedicated IP ports. While *admin* access allows control even to the level of restarting the daemon or disconnecting clients, the user level client access gives only control to the camera functions. Both those access options allow only one client at a time. An additional instrument port offers a distinct subset of the camera functions to give the possibility to trigger commands from other instruments, i.e. the telesope or the guider. Finally, the listener port announces the full camera status every second and allows "unlimited[5]" connection instances. The (human readable!) syntax of all commands and listener messages is summarised in App. B.2. The internal access to the camera status representation structure is controlled by "*mutexes*" which prevent simultaneous read and write access to the same status variable. For the *camd* configuration file options and syntax see App. B.3.

3.4.3 Client design – the GUI

The *camd daemon* already allows easy access to all camera functions, e.g. by an telnet session on the client ports, and it even offers the possibility of scripting observation runs, e.g. via *shell*, *perl* or *python*. Nevertheless, a Graphical User Interface (GUI) is the easiest way to control the functions of an instrument by a computer. Therefore, we built a Qt based [Haavard and Chambre-Eng, 2007] GUI (see Fig. 3.9 for a snapshot). The GUI implements image preview, a status log view, and overall camera control, i.e. binning(s), window(s), exposure time(s), filters etc. It allows to toggle between different modes, i.e. a synchronous and an independent camera channel exposure mode, scripting mode etc. There are already builtin "hooks" for autofocus and autoflat procedures supposedly working similar to those of MONICA (Gössl [1998] and Sect. 2.3.2), but those will be more complicated to implement because of the two channel design.

---

[5]Of course the system operating the daemon and the available network bandwidth limits the real number of possible listener clients.
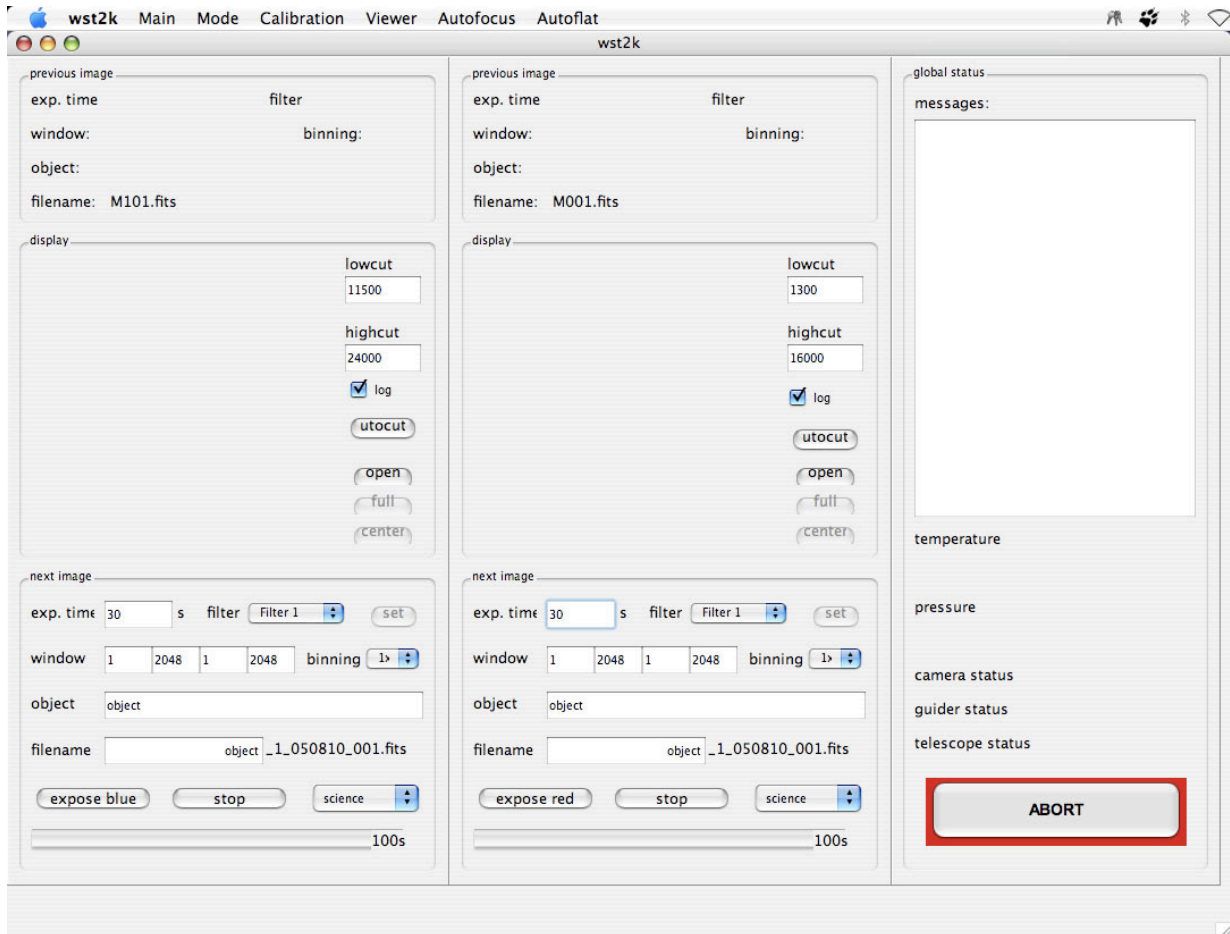
Figure 3.9: Snapshot of the AMiGo GUI: The GUI was coded utilising the Qt library [Haavard and Chambre-Eng, 2007] and therefore is cross-platform deployable. For a detailed description see text.

3.5   Deployment

AMiGo has been mechanically assembled (see also photos Fig. C.2, bottom) and passed preliminary tests of most parts. The motor controllers, camera daemon and GUI work as described above. Unfortunately, as of writing this thesis the camera still waits to see "*first light*". Because of difficulties with the CCDs and their electronics it is currently reengineered to work with a different detector system.

Chapter 4

Data Reduction

4.1 Introduction

All observational data were processed using the techniques described in Gössl and Riffeser [2002, 2003]. Our implementation of these techniques makes heavy use of the LTL [Gössl et al., 2004], a C++ template library for high performance array calculations and data I/O. I will only summarise every step of data reduction detailed in Gössl and Riffeser [2002, 2003] adding differences and improvements accomplished since then, but not dig into all the subtleties, e.g. all the explicit formulas of error propagation; for those I defer the reader to Gössl and Riffeser [2002, 2003].

4.2 Standard Image Processing

4.2.1 $\kappa\sigma$-clipping

Whenever averages of presumably normal distributions have to be calculated, i.e. to correct for additive constants or to divide by normalisation factors, iterative rejection of "outliers" ($\kappa\sigma$-clipping) helps to reduce systematic errors. Asymmetric outliers can be rejected even more effectively by clipping relative to the median (and not the mean) of a sample. Whenever asymmetric outliers are a probable contaminant (e.g. particle events in the overscan region evaluated for the bias level), we apply median clipping, but, as a final iteration, calculate the average.

4.2.2 Bad-Pixel Mask

We mask saturated (and blooming affected) pixels, as well as CCD-defects (hot, cold pixels etc.). While saturated pixels will be flagged as a dominant error the CCD-defects will be corrected later (Sect. 4.2.8).

4.2.3 Bias Correction

We subtract the bias level of individual frames estimated from the overscan region and (for CA 1.23 images) a master bias, i.e. the $\kappa\sigma$-clipped mean image of multiple bias level corrected bias frames. The bias pattern for MONICA/WST (Sect. 2.2.2) images varies over very short timescales (already between two consecutive exposures). This is because of the strong immission from a nearby radio station, so no master bias is applicable there.

4.2.4 Gain

To calculate with more meaningful numbers we multiply the flux [ADU] with the "gain" ($\frac{\text{electrons}_I}{\text{ADU}}$) of the detector system. So we have numbers in units of electrons or detected photons to start with. A propagated error (next paragraph) can now always be compared with a naive $\sqrt{\text{flux}}$ error.

4.2.5 Initial Error Estimate

The initial error estimate $\delta_I(x, y)$ for each pixel (x, y) in every image I is calculated from the pixel's photon noise[1], the bias noise of the image (clipped r.m.s. of the overscan), and the uncertainties of bias level and bias pattern determination.

$$\delta_I(x, y) = \sqrt{\text{counts}_I(x, y) - \text{bias}_I + \sigma_{\text{bias}_I}^2 + \frac{\sigma_{\text{bias}_I}^2}{n_{\text{bias}_I}}} \quad , \text{where} \qquad (4.1)$$

$$
\begin{aligned}
\text{counts}_I \quad &= \quad \text{flux of pixel } (x, y) \text{ in image } I \text{ in } e^-, \\
\text{bias}_I \quad &= \quad \text{bias of the image}, \\
\sigma_{\text{bias}_I} \quad &= \quad \text{we use the } \kappa(= 3)\sigma\text{-clipped r.m.s. of a} \\
& \qquad \text{suitable part of the overscan as an estimation} \\
& \qquad \text{for the bias noise (i.e. readout noise)}, \\
n_{\text{bias}_I} \quad &= \quad \text{number of pixels actually used for the bias} \\
& \qquad \text{determination.}
\end{aligned}
$$

Errors are propagated throughout the complete reduction pipeline with Gaussian error propagation.

4.2.6 Flat field Calibration

The relative sensitivity of resolution elements (pixels) is calibrated by applying a flat field calibration.

Since the time to get twilight flat field calibration images is very limited (< 1h) we also used short timed exposures where the movement time of non-photometric shutters can no longer be

---

[1]**NOISE**, n. A stench in the ear. Undomesticated music. The chief product and authenticating sign of civilization." [Bierce, 1906] With the noise N being the denominator of the signal-to-noise (S/N) ratio civilisation greatly hampers scientific insight as can be seen in the problems of optical astronomy with light pollution or radio astronomy with radio broadcasting.

neglected. Whenever the shutter movement could be proven to have a predictable time dependency, the flat fields were deconvolved from the two-dimensional shutter function as proposed by Surma [1993][2].

To achieve a high signal-to-noise ratio (S/N) for a combined flat field of an epoch we first calculate in each pixel the error weighted mean of normalised and illumination corrected twilight flat fields. After rejecting all 5×5 pixels regions where the centre pixel exceeds this mean by more than 5σ, the final calibration image is built by 3σ clipping of the remaining pixels. The illumination correction is applied twice: Per filter references-of-the-epoch are selected containing as few as possible stars but nevertheless having a comparatively long exposure time. All flat field images of a single epoch are then transformed to the reference illumination pattern by dividing through a 25-parameter 2D polynomial fit to a rigorously clipped flat field/reference ratio. This procedure is repeated adjusting all flat field epochs to an unique illumination pattern in order to minimise illumination effects on the final images.

4.2.7 Cosmic-Ray Rejection

We fit five-parameter (and three-parameter[3]) Gaussians to preselected[4] local maxima of an image. Sources with a full-width-half-maximum (FWHM) along the minor axis of the fit function smaller than a threshold (chosen according to the best, i.e. sharpest, encountered point-spread-function, PSF) and, in addition, an amplitude of the fit function exceeding the expected noise by a certain factor (chosen according to the additional noise i.e. due to crowding) correspond to cosmics[5]. We replace the pixels, where the fit function exceeds the fitted surface constant by more than two times the expected photon noise with the fitted surface constant. Additionally a standard spatial median filter is applied, i.e. we replace pixels which exceed the median of the directly adjacent pixels by more than a suitable factor times the expected noise. In order to mark the "erased" cosmics as a "guess-of-flux" they get the geometric sum of their former error and the proposed naive $\sqrt{e^-}$ noise assigned as new error.

4.2.8 Approximation of bad pixel areas

Bad pixel areas would spread to larger areas after aligning dithered frames to a common positional reference and especially deep stacks, combining many images, would hence look like Swiss cheese. Therefore previously masked bad pixel areas have to be interpolated before alignment and stacking somehow. If all images had the same depth, background and PSF they could

---

[2]See also Riffeser [2006], Sect. 5.5.5.

[3]Most "cosmics" leave a "trail" on the detector. However, there are also many "circular hits", and those yield a singular matrix if centred on a pixel when solving a Levenberg-Marquardt algorithm [Levenberg, 1944, Marquardt, 1963] with too many degrees of freedom. Those cases are re-fit with only surface, amplitude, and "overall" width, neglecting the second width and angular orientation parameter of the five-parameter fit.

[4]Maxima have to exceed the minimum adjacent pixel by a factor depending on their propagated error. They will still be ignored if they have more than four masked neighbours.

[5]Actually, those "cosmics" are mostly due to particle events in the detector itself and its surroundings, and only partly due to real high energy cosmic radiation.

easily be combined. Unfortunately, this is not at all applicable for ground based observations at moderate sites. We therefore replace all bad pixel areas, but saturated ones, with a distance and error weighted linear approximation of the closest neighbours. The fit box is selected as small as possible with the restriction that more than 2/3 of the fit box pixels minus the centre pixel must be valid pixels. Interpolated pixels get comparably large errors assigned derived from the supporting pixels input errors and the quality of the fit. As with the case of cosmics this helps to keep track of "guessed" fluxes and minimises its impact further on.

4.2.9 Astrometric Alignment

To register frames for astrometric alignment suitable sources have to be identified in the DG fields: In a first step the brightest not saturated sources besides those in regions of high crowding have been selected. After going through all the next steps up to convolved difference images and even variability masks (see next Sections) sources with parallaxes and/or proper motion are identified and disregarded. Unfortunately many of the brightest sources are "nearby" and have shown considerable proper motions over the more than five years of observations, especially in the fields at higher galactic latitudes[6], leaving only few suitable sources. The actual cross identification had to be done manually for every frame by pinpointing at least two reference stars.

All frames are then shifted to a common positional reference frame for each observed field: A linear projection proves to be sufficient[7]. To achieve sub pixel alignment without degrading the images we redistribute the flux by fitting a suitable polynomial to the actual flux distribution with integral flux conservation as a side condition as described in Riffeser [2006, Sect. 5.8.6].

We link the references grid to celestial coordinates by identifying USNO stars [Monet, 1996, 1998] and calculating a WCS solution according to the FITS standard [Greisen and Calabretta, 2002, Calabretta and Greisen, 2002].

4.2.10 Signal-to-Noise Optimised Stacks

When building our per-epoch stacks, as outlined in Sect. 2.5, we maximise the S/N ratio by applying individual weights w to the input frames according to

$$w = \frac{f}{(\text{FWHM} \cdot \delta_{\text{sky}})^2} \quad \text{, with} \tag{4.2}$$

$f =$ the flux of a bright and stable "standard" source in the field[8],

FWHM of the position reference PSF, and

$\delta_{\text{sky}} =$ the clipped median of the "error" image.

While f scales with the overall atmospheric and instrumental throughput, i.e. the "signal", the

---

[6]For obvious reasons: While the galactic disk acts almost like a rigid rotator and therefore the "disk" stars more or less corotate with the sun, halo stars follow "random" motions.

[7]Because the image planes of both, Wendelstein 0.8 m and Calar Alto 1.23 m, RC-configuration telescopes can be considered flat and undistorted for the rather small field-of-view of the cameras used.

[8]The method of measurement follows the recipe of Sect. 4.3.2.

product of the image PSF FWHM with the clipped median of the images propagated pixel errors[9] yields a measure of the "noise" for "weak" signals which we are finally looking for[10]. This way, especially when fighting unstable observing conditions, we won sometimes more than half a magnitude over naive stacks. (See Riffeser [2006, Sec. 5.11] for an actual derivation of the formula.)

4.3 Optimal Image Subtraction (OIS)

Alard and Lupton [1998] proposed a method to overcome the difficulties of both, high crowding and changing observing conditions, for differential photometry[11]: When going for time series photometry over more than a few hours ground based observations suffer from variations in atmospheric transparency, skylight background, and the image plane PSF due to atmospheric turbulence ("seeing"). State-of-the-art in the late '90s to deal with those was to apply an iterative PSF deconvolution which also allows for a changing but "smooth" background. This scheme, implemented through packages like DAOPHOT [Stetson, 1987], has been very successful, and still is the "way-to-go" for single epoch photometry. However, differential photometry of highly crowded fields and therefore many blended sources can gain from the information gathered from the best resolving images, as will be explained in the following. Simply put, a best resolving reference frame is convolved by a kernel, which accounts for the PSF variation, to match each "epoch"-stack and then subtracted from them. The remainders show only sources with changing brightness.

4.3.1 Reference Frame

We build common deep reference frames for every DG field following the recipe of Sect. 4.2.10 for the "epoch"-stacks but with additional constraints: Only the best $\sim 10\%$ of the frames, i.e. with the highest weights, are used. Additionally a limit for the FWHM is applied to ensure that a reference frame PSF FWHM is not bigger than any of the individual "epoch"-stacks[12]. Also, frames with saturated cosmics which are still masked "dominant" and occasional badly pointed epochs are dropped not to diminish the field-of-view. The reference frames will also provide the base for absolute photometry and colour-magnitude-diagrams later on as well as for the colour images and finding charts in Chap. 5 and App. G (Fig. 5.1, 5.6, 5.8, 5.14 - 5.17, 5.20 - 5.22, and G.3 - G.6).

---

[9]Which, again, is dominated by the photon noise of the skylight background.

[10]Even if considering bright sources where we are interested even in "faint" variations.

[11]Actually, OIS is only one way to implement difference image analysis [Ciardullo et al., 1990, DIA]. E.g. Tomaney and Crotts [1996] use Fourier convolution as a means to the same end.

[12]Because the successive convolution can not deconvolve!

4.3.2   Photometric Alignment

Our OIS implementation has shown to produce much better results when a photometric alignment of the epoch-stacks to the reference frames is applied beforehand and the convolution kernel normalised to unity (next Sect.). This is due to a partial degeneracy in fitting a 2D additive flat surface (skylight background) and determining the volume of the PSF-convolution kernel in one step which worsens with crowding. We therefore determine the fluxes of well defined, isolated, stable, and bright sources in every stack by Kron [1980] aperture photometry[13]. The median-clipped average ratio of those flux references between an "epoch"-stack and the reference frame supplies the appropriate calibration factor.

4.3.3   Convolution and Subtraction

OIS determines an optimal convolution kernel by decomposing it into a set of orthogonal basis functions and solving for the parameters which provide the least-squares difference of the convolved reference stack and the photometrically adjusted epoch-stacks. To account for PSF variations over the field-of-view the images are subdivided into regions of suitable size. Our latest implementation [Riffeser, 2006, Sect. 5.12.1] utilises three Gaussians of different widths multiplied with polynomials up to sixth order resulting in a 49 parameter kernel and three parameter flat surface. Unlike the Alard and Lupton [1998] OIS we support the least squares calculation by our propagated pixel errors. The results are further improved by masking variable sources detected later on[14] as to ignore for the kernel calculation[15] and repeating the procedure. We save both, the convolved reference frames as well as the resulting difference images.

4.4   Photometric Calibration

4.4.1   Relative Photometry – PSF-Photometry on Difference Images

We first extract the PSF of a suitable, isolated, and bright point source in all the convolved reference frames of every DG field as a preliminary photometric standard. An error weighted fit of these PSFs to every pixel in the according difference frames then yields a measure of the difference flux in units of the preliminary photometric standard[16]. This error weighted fit can be seen as a sort of error-weighted-convolution with the epoch's PSF. This data reduction step also renormalises the propagated error by the reduced χ^2 of this "PSF-fitting convolution" which is necessary because of the correlated noise[17] introduced mostly by the translation procedure

---

[13]We used the software package YODA [Drory, 2003] to perform the photometry.

[14]This includes all the sources of Tab. 4.4, i.e. also the high proper motion or parallactic sources of App. E.2.

[15]But not for the convolution!

[16]Even if any of those "standards" was variable, and most bright sources are variable, at least at the % level, it would not hamper the results because it is always the same reference frame which is being convolved.

[17]Correlated noise is always present when presumably independent pixel "errors" meet again in successive image transformation steps. While the absolute "level" of the errors is compromised by this correlation, the individual, naive propagated errors are still reasonable weights against each other for fits.

(Sect. 4.2.9) but also by OIS. The validity of this renormalisation will come up when checking the level of the cumulative variability mask of Sect. 4.6.1 in the "empty" ($\approx$ constant) regions.

4.4.2 Absolute Photometry – Adopting Photometric Standards

Whenever possible the photometric calibration is conducted using HST data. (Leo A, Pegasus, GR 8, and Aquarius: Holtzman et al., 2006; for Leo A also: Schulte-Ladbeck et al., 2002). A DAOPHOT [Stetson, 1987] catalogue from our observations is positionally cross-correlated with a subsample from the HST catalogue consisting of stars with colours typical for G, K and M giants. The HST $V - I$ colours and V-band magnitudes are then translated into Cousins [Bessell, 1979] R-band magnitudes using the colour tables published by Thé et al. [1990]. The resulting zero-point (ZP) for our R-band catalogue was obtained using a linear fit of the DAOPHOT magnitudes against the converted HST R-band magnitudes. This transformation was performed independently for the WST and the CA dataset[18]. For EGB 0427+63 we had to do an on-site calibration with photometric standard observations. We correlated observations of Leo A, GR 8, and EGB 0427+63 on photometric nights at Calar Alto with observations of NGC 2264 at the same epoch utilising previous measurements of Flaccomio et al. [1999]. Leo A and GR 8 provide an additional check for the validity of the HST calibration scheme[19]. The two photometry schemes differ well below 0.1 mag on average which can be seen as a measure for our systematic photometry error. The details of the absolute photometric calibration build Chap. 3 of Snigula [2006].

4.4.3 Average magnitudes vs. magnitude averages

When listing magnitudes[20] for the variable stars detected (Chap. 5) we give[21] their calibrated brightness as derived from the DG photometric reference image which are close to magnitudes of average fluxes because they are a stack of many randomly selected epochs[22]. Usually[23], average magnitudes are derived directly from the observed light curves. This can only be accomplished if the complete light curve is sampled with an acceptable S/N ratio which is clearly not the case for all of our faint, short-period variable stars (e.g. Fig. H.1 and H.2). Magnitudes derived by Fourier decomposition, despite building on phase binned averages, do not solve this problem.

---

[18]The good overall agreement of both sets can serve as a first indicator for the validity of this calibration approach [see Snigula, 2006, Fig. 3.2].

[19]As shown in Snigula [2006, Fig. 3.4].

[20]"**MAGNITUDE**, n. Size. Magnitude being purely relative, nothing is large and nothing small. If everything in the universe were increased in bulk one thousand diameters nothing would be any larger than it was before, but if one thing remain unchanged all the others would be larger than they had been. To an understanding familiar with the relativity of magnitude and distance the spaces and masses of the astronomer would be no more impressive than those of the microscopist. [...]" [Bierce, 1906]
While the advantage of a unit free of scale is obvious its potential drawback is not, see App. E.3.

[21]Unless explicitly stating differently.

[22]This holds at least for periods up to $\sim$ 200 days with the *VarStarDwarves* sampling. See Snigula [2006, Sect. 4.3].

[23]In literature.

They even tend to be brighter than those from flux averages of the reference frame[24]. To check on this deficiency I made the approximation that the light curve of Cepheid stars can be described by a sawtooth shaped function. I read the maximum magnitude $m_{\mathrm{max}(t=0)}$ from the diagrams of a couple of observed light curves and took the according flux averaged magnitudes $m_{\bar{f}}$ from the DAOPHOT catalogues of the reference frames. The missing minimum magnitude $m_{\mathrm{min}(t=1)}$ can now be calculated from the known $a = m_{\mathrm{max}(t=0)}$ and $m_{\bar{f}}$ by solving

$$\bar{f} = \int_0^1 10^{-0.4(a+t(b-a))} dt \tag{4.3}$$

for $b = m_{\mathrm{min}(t=1)}$ and

$$\bar{m} = \int_0^1 a + t(b-a) dt = \frac{b+a}{2} \quad . \tag{4.4}$$

I found that average flux magnitudes tend to be a few 0.01 mag brighter than magnitude averages. But, this effect is always much less than 0.1 mag for typical Cepheid amplitudes.

4.5   Time Calibration

With the typical stacked exposure time being four times longer than the maximum light travel delay time barycentric effects should be negligible. Nevertheless, I proved the validity of that assumption by comparing Lomb runs (Sect. 4.6.2) on uncorrected and barycentric corrected data sets applying the algorithms of Meeus [1988] as implemented by the *skycalc* program of J. Thorstensen.

4.6   Variable Sources Detection

4.6.1   Preselection – A Cumulative Mask

To find VS candidates and to extract their light curves from the reduced data, we first build a mask frame where we count how often individual difference frames deviate from zero by at least 1σ, utilising the complete per-pixel error propagation of our data reduction pipeline.

This mask still contains information on the noise of the images as well as on the VS candidates which we intend to extract: The ($\kappa\sigma$) clipped median of the cumulative mask corresponds to the number of 1σ outliers, where no variability is present, i.e. ≈ 32 of 100 epochs. The clipped standard deviation of the mask gives the noise of the 1σ-no-variability level. We select as variable star candidates all positions where the level of the mask exceeds its median value by 2 times the noise[25] and, in addition, DAOPHOT photometry of the reference image yielded a detected source within a radius of 1.5 pixels (Tab. 4.4, Col. 1). Then, using these coordinates as input, values and associated errors are read from the PSF-convolved difference images and the light curve data are assembled.

---

[24]I.e. by 0.025 mag on average.

[25]Selecting only positions which exceed this level by 2 times its noise yields a false detection probability for a single pixel of $\approx 5\%$ assuming a normal distribution.

4.6.2 Periodic Sources

The Lomb Algorithm

To search for periodic signals in the extracted difference fluxes we applied the Lomb [1976] algorithm using the interpretation from Scargle [1982] because a discrete Fourier Transform does not work for unevenly sampled data[26]. The power spectrum $P(\omega)$ of the quantity X_j sampled at times t_j, i.e. the Lomb periodigram, is calculated by

$$P_X(\omega) = \frac{1}{2} \left\{ \frac{\left[\sum_j X_j \cos \omega(t_j - \tau) \right]^2}{\sum_j \cos^2 \omega(t_j - \tau)} + \frac{\left[\sum_j X_j \sin \omega(t_j - \tau) \right]^2}{\sum_j \sin^2 \omega(t_j - \tau)} \right\} \quad , \text{with} \qquad (4.5)$$

$$\tan(2\omega\tau) = \left(\sum_j \sin 2\omega t_j \right) \Big/ \left(\sum_j \cos 2\omega t_j \right) \quad . \qquad (4.6)$$

The arbitrary power density can be interpreted as a significance for a peak at frequency n among N test frequencies according to

$$p(\max_n P(\omega_n)) = 1 - [1 - \exp(-P(\omega_n))]^N \qquad (4.7)$$

which contains a *statistical penalty* for the number of test frequencies[27].

Specifically, to find periodic variable stars in our observations I test a logarithmic grid of 23040 periods in the range from 45 minutes (our shortest stacked exposure time) to 1536 days. All sources yielding at least once a Lomb significance ≤ 0.25 were further examined. This limiting p-value was empirically chosen according to the test case of Leo A. It should be strictly enough to get rid of the most unbelievable light curves (clearly variable, but without any convincing period), but still weak enough to at least show up all variables with already known periods, even if the light curve would finally be manually discarded for being too unconvincing to contribute to a period luminosity relation.

The Lomb algorithm is sensitive to all sorts of periodic sources[28] It prefers sinusoidal light curves[29], but is not restricted to that curve shape and can deal even with very noisy data, good sampling provided. The only drawback of the algorithm is its susceptibility to window functions. This again can be minimised by clever sampling [Saunders et al., 2006], but of course only as far as nature allows. Ground based observations (restricted to one observing site) will always

---

[26]Even resampling only works for a well sampled grid but for the bulk of the data we have just sparse sampling.

[27]The more frequencies are tested the higher the probability of a random high power peak gets.

[28]All kinds of pulsating variable stars, but also eclipsing binaries and, in combination with light curves derived from photometry at fixed coordinates, even to parallaxes, see also Sect. 4.2.9 and 4.3.

[29]See Sect. 4.6.3 and App. D.

fight the imprinted signal of the day[30], month and year[31] cycles, i.e. the Lomb power spectrum can be fooled by their window functions. All observing periods (1 d and 1 yr) and their integer fractions as well as non-observing periods (sidereal and/or synodic month, 1 yr) and their integer multiples can lead to artificial power.

Therefore, finding the real period of a VS can get quite complicated because its true period can be superimposed by a window function resulting in "resonance" power in an overtone mode of either the window or the true period or even their beat period. Visual inspection of the light curves always clearly favoured the period of a "smooth" curve, but that did not always be the one with the smallest p-value, i.e. the highest power.

To get rid of the most obvious window functions I disregarded all periods of 1 d ±1%, 1/2 d ±1%, and 1/4 d ±1%, because I had no way of distinguishing real from fake periods. I excluded ambiguous detections by selecting only the most significant Lomb candidate per DAOPHOT match.

The Lafler-Kinman Algorithm

While the Lomb algorithm has shown to be the superior method to detect periods of less than half a year in all of our samples it often gave indistinct solutions for the longer periods. Therefore, Snigula [2006, Sect. 4.2] applied the Lafler and Kinman [1965] algorithm to search for LPVs / Mirae stars. It proved to be less sensitive to the window functions caused by the yearly visibility gaps of our DGs.

4.6.3 Completeness Tests

Completeness tests were performed applying the techniques described in detail in Snigula [2006, Chap. 5]. Since new reference images had been created since, the artificial stars simulation (see below) and the DAOPHOT completeness had to be repeated.

Artificial stars simulation

To build artificial light curves first one or several grids[32] of $\approx$ 1000 test stars in total with adapted flux and PSF are put into each stacked image of an epoch.   This is done for the interesting range of magnitudes (16 mag to 26 mag, 0.1 mag stepping). Then the OIS and PSF-photometry

---

[30]**DAY**, n. A period of twenty-four hours, mostly misspent. This period is divided into two parts, the day proper and the night, or day improper – the former devoted to sins of business, the latter consecrated to the other sort. These two kinds of social activity overlap." [Bierce, 1906] Astronomers manage to employ the former for the latter and vice versa thereby extending the overlap to identity, and rendering this artificial distinction between night and day completely obsolete.

[31]"**YEAR**, n. A period of three hundred and sixty-five disappointments." [Bierce, 1906] In contrast to the above-quoted *cynical year* the *sidereal year* lasts 365 d, 6 h, 9 min, and 9 s (at the epoch J2000.0).

[32]Depending on the apparent size of the dwarf galaxy: The grid may not be too dense to avoid crowding of the artificial sources. The distance of the artificial stars should be large enough that their convolution kernels would not overlap. If one grid with $\approx$ 1000 stars would have been larger than the host galaxy, we did several grids with offsets.

is applied according to Sect. 4.3 and 4.4. Tables giving flux and errors for every test star, epoch and test magnitude are extracted.

Variation mask completeness

Variation mask completeness was checked as detailed in Snigula [2006, Sect. 5.2.2]. The results show that the variation mask has no limiting impact on the recovery of artificial variable sources when compared to either DAOPHOT or Lomb completeness. [See Snigula, 2006, Tab. 5.1, 5.3, 5.5, and 5.7, and top Fig. 5.1, 5.3, 5.5, and 5.7.]

Lomb completeness tests

We tested two sets of light curves, cosine and sawtooth. The former is the easiest for a Lomb algorithm to detect, the latter is more or less the worst case[33]. For the cosine we tested 0.2, 0.6, 1.0, and 1.4 peak-to-peak amplitudes, for the sawtooth, after a first test run, only 0.6, 1.0, and 1.4 (see below, Caveats). All tests cover a magnitude range of 18.0 to 25.0 (0.1 mag steps) and a period range of 0.15 to 129.95 days therefore including the whole range of periods known for Cepheids.

The results of the tests are displayed in Tab. 4.1, Fig. 4.1, showing the cumulative Lomb completeness for Leo A, and the figures of App. D, showing the cumulative Lomb completeness for the rest of our DGs as well as exemplary period resolved Lomb completeness again for Leo A. They can be summarised as follows:

- Completeness is dependent on light curve shape, average magnitude, and amplitude as expected.

- Completeness is nearly independent of the period, but for a slight drop at the shortest periods and around either the sidereal and the synodic month[34].

- No artificial increase in completeness could be seen at the obvious window function periods. Nevertheless any variability still can cause resonance power at the window functions frequencies.

Caveats

The completeness tests can only answer the question asked which is: *What is the probability of an arbitrary star with given average magnitude, amplitude, and period to result in a significant p-value for dwarf galaxy X for the actually observed epochs?* Since the *p*-value is empirically

---

[33]A pure cosine will put all its power into a single fundamental Lomb mode, while a sawtooth will spread power also into many overtones. Cepheid light curves are somewhere in between those extremes.

[34]Since observations with the target within less then 30° from the moon are drowned in moonlight, and therefore are avoided, as are observations during full moon in general, objects with those lunation periods will loose completeness earlier for the phases coinciding a maximum in their light curve and the objects "lunatic" blackout. Since EGB 0427+63 has the largest distance to the ecliptic it also shows the smallest impact due to lunation.

chosen according to the test case of Leo A (see Sect. 4.6.2), the test will only account for stars showing up in the automatically selected sample because of enough power in the Lomb spectrum at its true period. It will not give additional insights about the credibility of its light curve. It will also not tell if the input period would have been the one with most power in the resulting spectrum. And of course the test will not say if the power leading to a "significant" detection is "real" or due to window functions.

The Lomb completeness tests are very time consuming[35]. We therefore had to compromise on the test grid density at various instances:

- Since the magnitude stepping is 0.1 mag the smallest amplitudes detectable are 0.2 mag for cosine light curves. Sawtooth light curves with 0.2 mag amplitudes have 50% of their points at average brightness and 50% of their points equally distributed above and below average which is still consistent with noise, i.e. non-periodicity.

- To bring down calculation time to a tolerable amount only a small region around the input period is tested ($P\pm5\%$). Therefore the tests give no additional information on the influence of window functions at other than the tested period. Since the p-value also depends on the total number of tested periods it had to be renormalised to resemble the original Lomb periodigram setup for the variable sources search (Sect. 4.6.2).

- The flux of the artificial stars can dominate the OIS convolution which will lead to loosing completeness at the "bright" side of the test mostly for small amplitudes and/or sawtooth light curves (e.g. see Fig. 4.1). This is due to the fact that the artificial stars grid has a common magnitude when put into the image yielding an "magnitude instance". The details depend on the convolution grid size, the test star density, and the ratio of test star flux to real objects flux.

- We did not test for periods which are obvious window functions.

DAOPHOT completeness

DAOPHOT completeness tests yield limiting magnitudes for the photometric reference frames (Sect. 4.3.1). Snigula [2006, Sect. 5.2.3] details the parameters and recipe for obtaining those tests. Since Snigula [2006] new reference frames for the Pegasus dwarf and EGB 0427+63 had been obtained and therefore new DAOPHOT completeness tests had to be performed. Tab. 4.2 summarises the results, while Fig. 4.1 and Fig. D.1 to D.4 in App. D display the impact on overall completeness in combination with the Lomb completeness.

Adopted limiting magnitudes

We finally adopted the combined 50% completeness (Lomb $\times$ DAOPHOT) of the 1.4 mag peak-to-peak amplitude cosine as an uniform limiting magnitude. All fainter sources were disregarded (Tab. 4.4, Col. 2).

---

[35]The tests for all of the objects took more than 4 months on a 16 node 1.2 GHz Beowulf cluster.

Table 4.1: Period averaged results from the exhaustive Lomb completeness tests. Columns 1 and 2: Light curve test shape and peak-to-peak amplitude [mag]. Other columns: Magnitude of percentile completeness limit, i.e. percentage of Lomb significance $p \leq 0.25$ light curve recovery, and its standard deviation over the test periods. Boldface: 50% completeness columns and 1.4 mag peak-to-peak amplitude cosine light curve rows.

Leo A		99%	95%	90%	**50%**	10%	5%	1%
cosine	0.2	19.54 ± 0.34	21.09 ± 0.09	21.29 ± 0.05	**21.73 ± 0.05**	22.12 ± 0.04	22.25 ± 0.05	22.50 ± 0.04
cosine	0.6	21.30 ± 0.06	22.44 ± 0.06	22.57 ± 0.05	**22.90 ± 0.02**	23.28 ± 0.04	23.39 ± 0.03	23.62 ± 0.05
cosine	1.0	21.89 ± 0.06	23.00 ± 0.03	23.10 ± 0.04	**23.49 ± 0.04**	23.81 ± 0.04	23.95 ± 0.05	24.19 ± 0.04
cosine	**1.4**	**22.29 ± 0.06**	**23.39 ± 0.03**	**23.50 ± 0.03**	**23.87 ± 0.05**	**24.20 ± 0.02**	**24.33 ± 0.05**	**24.56 ± 0.05**
sawtooth	0.6	19.77 ± 0.21	20.52 ± 0.27	20.92 ± 0.10	**21.49 ± 0.03**	21.92 ± 0.04	22.06 ± 0.05	22.32 ± 0.04
sawtooth	1.0	19.96 ± 0.37	21.48 ± 0.07	21.64 ± 0.07	**22.08 ± 0.04**	22.49 ± 0.03	22.60 ± 0.03	22.87 ± 0.05
sawtooth	1.4	20.68 ± 0.12	21.89 ± 0.06	22.05 ± 0.07	**22.45 ± 0.06**	22.85 ± 0.05	22.99 ± 0.04	23.23 ± 0.05

Pegasus		99%	95%	90%	**50%**	10%	5%	1%
cosine	0.2	19.48 ± 0.14	20.98 ± 0.06	21.12 ± 0.07	**21.50 ± 0.05**	21.90 ± 0.06	22.03 ± 0.06	22.29 ± 0.07
cosine	0.6	21.05 ± 0.08	22.20 ± 0.05	22.32 ± 0.06	**22.67 ± 0.05**	23.02 ± 0.05	23.14 ± 0.06	23.40 ± 0.06
cosine	1.0	21.67 ± 0.07	22.77 ± 0.05	22.88 ± 0.04	**23.22 ± 0.05**	23.58 ± 0.04	23.70 ± 0.05	23.96 ± 0.06
cosine	**1.4**	**22.07 ± 0.07**	**23.16 ± 0.06**	**23.28 ± 0.05**	**23.60 ± 0.04**	**23.97 ± 0.05**	**24.09 ± 0.04**	**24.35 ± 0.06**
sawtooth	0.6	18.90 ± 0.31	20.40 ± 0.41	20.67 ± 0.30	**21.26 ± 0.06**	21.72 ± 0.06	21.86 ± 0.06	22.14 ± 0.07
sawtooth	1.0	19.95 ± 0.16	21.17 ± 0.14	21.36 ± 0.09	**21.82 ± 0.07**	22.25 ± 0.06	22.38 ± 0.05	22.67 ± 0.06
sawtooth	1.4	20.44 ± 0.13	21.57 ± 0.13	21.74 ± 0.09	**22.19 ± 0.06**	22.61 ± 0.06	22.75 ± 0.06	23.03 ± 0.06

EGB 0427+63		99%	95%	90%	50%	10%	5%	1%
cosine	0.2	18.00 ± 0.00	18.00 ± 0.00	18.30 ± 0.02	**19.87 ± 0.05**	21.30 ± 0.02	21.60 ± 0.03	22.03 ± 0.05
cosine	0.6	18.00 ± 0.00	18.70 ± 0.02	19.52 ± 0.04	**21.04 ± 0.05**	22.50 ± 0.02	22.80 ± 0.01	23.20 ± 0.03
cosine	1.0	18.00 ± 0.00	19.30 ± 0.02	20.10 ± 0.01	**21.60 ± 0.01**	23.07 ± 0.05	23.40 ± 0.02	23.78 ± 0.05
cosine	**1.4**	**18.19 ± 0.03**	**19.69 ± 0.03**	**20.50 ± 0.01**	**22.00 ± 0.01**	**23.43 ± 0.05**	**23.79 ± 0.03**	**24.16 ± 0.05**
sawtooth	0.6	18.00 ± 0.00	18.00 ± 0.00	18.06 ± 0.05	**19.61 ± 0.04**	21.06 ± 0.05	21.40 ± 0.03	21.84 ± 0.05
sawtooth	1.0	18.00 ± 0.00	18.00 ± 0.00	18.70 ± 0.02	**20.26 ± 0.05**	21.70 ± 0.02	22.00 ± 0.02	22.43 ± 0.05
sawtooth	1.4	18.00 ± 0.00	18.27 ± 0.05	19.10 ± 0.02	**20.62 ± 0.04**	22.09 ± 0.03	22.40 ± 0.01	22.81 ± 0.03

GR8		99%	95%	90%	50%	10%	5%	1%
cosine	0.2	20.62 ± 0.06	20.82 ± 0.05	20.91 ± 0.04	**21.26 ± 0.05**	21.61 ± 0.04	21.73 ± 0.05	21.99 ± 0.05
cosine	0.6	21.80 ± 0.04	21.99 ± 0.03	22.09 ± 0.03	**22.40 ± 0.02**	22.75 ± 0.05	22.87 ± 0.05	23.11 ± 0.05
cosine	1.0	22.36 ± 0.05	22.56 ± 0.05	22.64 ± 0.05	**22.97 ± 0.05**	23.30 ± 0.03	23.42 ± 0.04	23.68 ± 0.05
cosine	**1.4**	**22.74 ± 0.05**	**22.93 ± 0.05**	**23.02 ± 0.04**	**23.35 ± 0.05**	**23.70 ± 0.03**	**23.81 ± 0.03**	**24.08 ± 0.05**
sawtooth	0.6	20.29 ± 0.08	20.52 ± 0.06	20.64 ± 0.06	**21.00 ± 0.03**	21.41 ± 0.04	21.54 ± 0.05	21.81 ± 0.05
sawtooth	1.0	20.86 ± 0.07	21.09 ± 0.04	21.19 ± 0.04	**21.57 ± 0.05**	21.97 ± 0.05	22.10 ± 0.04	22.36 ± 0.06
sawtooth	1.4	21.23 ± 0.08	21.46 ± 0.06	21.57 ± 0.05	**21.92 ± 0.04**	22.32 ± 0.04	22.46 ± 0.05	22.73 ± 0.05

Aquarius		99%	95%	90%	50%	10%	5%	1%
cosine	0.2	19.43 ± 0.07	20.06 ± 0.06	20.26 ± 0.06	**20.68 ± 0.04**	21.08 ± 0.04	21.22 ± 0.06	21.50 ± 0.02
cosine	0.6	20.65 ± 0.05	21.23 ± 0.05	21.40 ± 0.05	**21.87 ± 0.05**	22.23 ± 0.06	22.42 ± 0.08	22.68 ± 0.06
cosine	1.0	21.24 ± 0.06	21.79 ± 0.04	21.98 ± 0.04	**22.46 ± 0.06**	22.84 ± 0.06	22.95 ± 0.05	23.17 ± 0.05
cosine	**1.4**	**21.62 ± 0.05**	**22.20 ± 0.05**	**22.40 ± 0.05**	**22.83 ± 0.05**	**23.20 ± 0.05**	**23.29 ± 0.03**	**23.54 ± 0.07**
sawtooth	0.6	18.96 ± 0.17	19.62 ± 0.17	19.85 ± 0.14	**20.40 ± 0.06**	20.88 ± 0.05	21.00 ± 0.04	21.34 ± 0.09
sawtooth	1.0	19.63 ± 0.12	20.24 ± 0.11	20.43 ± 0.09	**20.96 ± 0.06**	21.46 ± 0.05	21.56 ± 0.05	21.82 ± 0.06
sawtooth	1.4	20.04 ± 0.13	20.60 ± 0.11	20.79 ± 0.09	**21.32 ± 0.07**	21.78 ± 0.05	21.92 ± 0.06	22.17 ± 0.05

Leo A: 1.4 mag peak–to–peak amplitude, cosine lightcurve

Leo A: 1.4 mag peak–to–peak amplitude, sawtooth lightcurve

Leo A: 1.0 mag peak–to–peak amplitude, cosine lightcurve

Leo A: 1.0 mag peak–to–peak amplitude, sawtooth lightcurve

Leo A: 0.6 mag peak–to–peak amplitude, cosine lightcurve

Leo A: 0.6 mag peak–to–peak amplitude, sawtooth lightcurve

Leo A: 0.2 mag peak–to–peak amplitude, cosine lightcurve

Figure 4.1: Leo A DAOPHOT, period averaged Lomb, and both combined completeness example. Red: DAOPHOT completeness; green: Lomb completeness; black: Combined DAOPHOT and Lomb completeness; solid (green and black): Period averaged completeness; slashed (green and black): Minimal and maximal recovery rate in the period span. For all other DGs see App. D. Loosing completeness on the bright end is due to intrinsics of the test (see text).

Table 4.2: DAOPHOT photometry completeness of the WST *R*-band reference images following Snigula [2006, Sect. 5.2.3]. In accordance with having the highest number of usable single epochs EGB 0427+63 also produced the deepest reference frame.

	99%	95%	90%	50%	10%	5%	1%
Leo A	20.4	21.6	22.1	**23.7**	25.0	25.0	25.0
Pegasus	20.5	21.8	22.2	**23.8**	25.0	25.2	25.6
EGB 0427+63	19.5	22.6	23.4	**24.7**	25.5	25.8	26.0
GR 8	20.8	22.2	22.7	**24.2**	25.3	25.5	25.9
Aquarius	18.9	21.7	22.5	**23.6**	24.4	24.7	25.0

Table 4.3: Combined completeness of DAOPHOT photometry on the *R*-band reference images (Tab. 4.2) and the Lomb simulations on the complete data sets (Tab. 4.1). (See also Fig. 4.1 and all figures of App. D.) Combined 50% completeness was adopted as limiting magnitudes for variable sources to be considered. Despite having the deepest reference frame EGB 0427+63 achieved the worst combined completeness limit. This is due to the significantly infererior single epoch stacks (worst average PSF) for this dwarf and probably caused by a problem with the mirror mount of the 80 cm telescope at "northern", > 60° declinations.

	99%	95%	90%	50%	10%	5%	1%
Leo A	20.0	21.5	22.1	**23.5**	24.0	24.1	24.3
Pegasus	20.2	21.7	22.2	**23.4**	23.8	23.9	24.2
EGB 0427+63	18.0	19.4	20.3	**21.9**	23.3	23.7	24.1
GR 8	20.8	22.2	22.7	**23.2**	23.6	23.7	24.0
Aquarius	18.9	21.4	22.0	**22.7**	23.1	23.2	23.4

4.7   Variable Sources Classification

From here on, I will focus the discussion of data reduction on the major aim of finding classical and Type II Cepheid variables and establishing their periods and magnitudes:

After applying the limiting magnitudes I disregarded all candidates with periods of more than 130 days of the remaining, presumed periodic, variable sources. This upper limit reflects the longest periods known for δ Cephei stars in the Local Group [Groenewegen et al., 2004].

Table 4.4: Breakdown of variable sources detection: Variation mask $> 2\sigma$ and DAOPHOT match within 1.5 pixel radius, (mask threshold and total number of input epochs,) Lomb significance $p \leq 0.25$ corrected for DAOPHOT ambiguities and ignoring 1, 1/2, and 1/4 d periods, period limit $P \leq 130$ d and $m \leq$ limit according to Tab. 4.3.

	mask (thresh./total) $> 2\sigma$ of 1σ var. lvl.	Lomb $p \leq 0.25$	$P(< 130\,\mathrm{d})$ $+m$ limits
Leo A	12656 (47/120)	309	131
Pegasus	11290 (41/94)	525	214
EGB 0427+63	6754 (66/158)	326	40
GR 8	3445 (45/102)	65	16
Aquarius	6573 (39/85)	130	17

In order to quantify a classification scheme, in particular to identify δ Cephei stars, I tested two approaches on Leo A candidates. Firstly, I did a crude template fitting utilising a "typical" real δ Cephei star and adjusting only its magnitude, amplitude and phase shift by adaptive simulated annealing [Ingber, 1993]. The ratio of the fit's r.m.s. and the r.m.s. of a constant curve should yield a means of picking up the most appropriate candidates. Secondly, I applied a four-mode Fourier decomposition using an error weighted Levenberg-Marquardt algorithm [Levenberg, 1944, Marquardt, 1963] to determine the usual mode amplitude ratios and phase differences ($R_{21}, \phi_{21}, \phi_{31}$, see e.g. Simon and Lee 1981), which obey certain rules for different kinds of pulsating variables. Because the S/N ratio of the light curves is too low for most but the brightest stars both methods failed to be conclusive.

Therefore, I finally applied a classification strategy based on a visual inspection of the light curve solutions for every candidate. I distinguished 3 groups of variable sources based on their period: Short periods $P < 1$ d, intermediate periods $1\,\mathrm{d} < P < 10$ d, and long periods $10\,\mathrm{d} \leq P \leq 130$ d (Tab. 4.5). The first group produced mainly light curves either indistinguishable from the remaining short period window functions[36] or with no regular light curve shape. Nevertheless, a few of those candidates had second power peaks yielding believable light curves at longer periods and were therefore added with their longer periods to the according group[37]. The latter two groups were further divided into three subgroups each which reflect the significance of the detection (p-value). Again, second power peaks with believable light curves at different periods were added to the according group and subgroup.

---

[36] 1/3 d, 2/3 d, and $1/N$ d ($N \geq 5$)
[37] Numbers in brackets in Tab. 4.5.

Table 4.5: Variable sources candidates classification: Classification due to period P and significance p (additions because of convincing second power peaks in brackets in the order short, intermediate, and long period first power peak).

Period	$P < 1$ d	1 d$< P < 10$ d			10 d$\leq P \leq 130$ d		
signif. p	all	$< 10^{-4}$	$< 10^{-2}$	< 0.25	$< 10^{-4}$	$< 10^{-2}$	< 0.25
Leo A	61	9 (0, 2, 0)	8 (1, 3, 0)	39 (3, 1, 1)	2	2 (2, 0, 0)	10 (1, 1, 0)
Pegasus	68	5	9	57 (4, 3, 0)	17 (0, 0, 1)	16 (0, 1, 2)	42 (1, 5, 8)
EGB 0427+63	19	–	–	6	–	–	15
GR 8	10	–	–	–	1	– (1, 0, 0)	5
Aquarius	15	–	–	2 (2, 0, 0)	–	–	–

(second power peaks from short, intermed., and long periods)

Chapter 5

Results

The *VarStarDwarves* "Blues"[1]

 Preliminary results of the *VarStarDwarves* project have been published in Snigula et al. [2004, 2006] and Gössl et al. [2006]. The results on Long Period Variable, "red" stars were detailed in Snigula [2006], while the results on shorter period variable, "blue" stars will be reported on here. In App. E, I report about "by-chance" discoveries and missing objects which were beyond the scope of the VarStarDwarves project but for some reason caught the eye of the observer: Sometimes they caused problems with difference imaging like high proper motion and parallactic stars (App. E.2) or small solar system bodies (App. E.1, Tab. E.1). Other objects were interesting because of their physics and their potential as distance indicators like Supernovae (App. E.3).

5.1 Some History – Dwarf Tales

5.1.1 Leo A

The LG dIrr galaxy Leo A (DDO 069, Leo III, UGC 05364)[2] was first mentioned by Zwicky [1942][3]. It had been discovered in a survey with the 18" Schmidt telescope on Palomar Mountain.

---

[1]Twinkle, twinkle little star,   How I wonder what you are. . .

[2]Naming in astronomy is as confusing as can be. In particular, for faint galaxies and/or LG galaxies there exist several schemes: Arbitrary naming by its or after the discoverer(s), after constellation with additional consecutive Roman numerals (modern use only for dSphs) or capital letters (originally for galaxy clusters and now befitting dIrrs), simply by a catalogue number with the catalogue usually named after the observatory which carried out the underlying survey (DDO = David Dunlop Observatory Catalogue of Low Surface Brightness Galaxies, van den Bergh [1959, 1966]; UGC = Uppsala General Catalog of Galaxies, Nilson [1973]; UGCA = Uppsala General Catalog Appendix, Nilson [1974]). I will give here the most common names under which the *VarStarDwarves* objects are known among astronomers.

[3]Mistaking it for a galaxy cluster.

The first distance[4] guess was given by de Vaucouleurs [1975] to $m - M \approx 25.2$ mag. Jacoby and Lesser [1981] derived an upper limit for its distance from an associated Planetary Nebula (PN) $m - M < 27.5 \pm 0.5$ mag. Sandage and Tammann [1982] first gave a distance from the brightest red stars to $m - M = 27.4 \pm 0.3$ mag; Demers et al. [1984] estimated its distance from the brightest blue stars[5] to $m - M = 26.8 \pm 0.4$ mag whereas Sandage [1986] gave, also solely based on the brightest blue stars[6], a distance modulus of $m - M = 26 \pm 1$ mag. Hoessel et al. [1994] derived a first distance based on what they thought were δ Cephei variable stars of $m - M = 26.74 \pm 0.22$ mag confirming the previous estimates. Meanwhile Skillman et al. [1989] had determined the Leo A metallicity as one of the lowest known in the local universe. They derived an oxygen abundance of $12 + \log(\text{O}/\text{H}) = 7.30 \pm 0.05 (\approx 2.4\%$ solar) from a PN in Leo A, a result which was confirmed by van Zee et al. [2006] who additionally measured the oxygen abundance of four H II regions to $12 + \log(\text{O}/\text{H}) = 7.38 \pm 0.10$.

Hubble Space Telescope (HST) observations were needed to call into doubt the Hoessel et al. [1994] Cepheid distance: Tolstoy et al. [1998] derived a distance modulus of $m - M = 24.2 \pm 0.2$ mag from various features in the HST colour-magnitude diagram (CMD)[7]. Their modelling of the CMD suggests a metallicity as low as $Z = 0.0004$ which is consistent with the oxygen abundance measurements. They also claim that Leo A is predominantly young and an underlying old population cannot contribute more than 10% to the total star formation. This was rejected by Schulte-Ladbeck et al. [2002][8] in the sense that Leo A is mainly young only in its centre but has overall an underlying intermediate and even an old population (up to 50% older than 10 Gyr). Thinking of an old population leads them to give $m - M = 24.5 \pm 0.2$ mag from the I-band TRGB and the position of the so called red clump (RC) in the HST CMD. Their proposed star formation history is also strongly supported by our findings of 11 *VarStarDwarves* LPVs [Snigula et al., 2006, Snigula, 2006].

Finally, Dolphin et al. [2002] discovered eight RR Lyrae stars in Leo A and derived from them $m - M = 24.51 \pm 0.12$ mag. This result is also confirmed by our preliminary analysis of three *VarStarDwarves* Leo A δ Cephei stars [Gössl et al., 2006]; they fit a Madore and Freedman [1991] PLR with $m - M = 24.47 \pm 0.10 \pm 0.06_{\text{ZP}}$ mag.

---

[4]"**DISTANCE**, n. The only thing that the rich are willing for the poor to call theirs, and keep." [Bierce, 1906] Many observing astronomers prefer to give distances d not in units of parsecs [pc] but as a distance modulus $m - M = 5 \log(d/10 \, \text{pc})$, especially when derived from the brightness of "standard candles".

[5]They did not find any bright red stars.

[6]He still found bright red stars but now those gave a degenerate solution for distance determination. Sandage emphasised that "*the distance is determined poorly by this method*".

[7]A CMD is the modern observer's equivalent to the HRD. A single waveband's brightness measurement in mag accounts for the luminosity while the colour, i.e. the difference of two wavebands in mag and therefore actually a flux ratio, indicates the temperature.

[8]Again utilising HST observations but this time with some offset from the galaxy centre.

5.1.2 Pegasus Dwarf

The Pegasus Dwarf or Peg DIG (DDO 216, UGC 12613) was discovered in the early 1950s by A.G. Wilson during his work for the Palomar Observatory Sky Survey (POSS)[9] and first referenced by Holmberg [1958]. It shows almost the same early history as Leo A: The first guess by de Vaucouleurs [1975] here was $m - M = 21.2$ mag while the Jacoby and Lesser [1981] PN upper limit yielded $m - M < 29.0 \pm 0.4$ mag. The Sandage and Tammann [1982] red supergiant distance here was $m - M = 28.19 \pm 0.3$ mag. Hoessel and Mould [1982] from a sparsely sampled TRGB and brightest red and blue stars deduced $m - M = 26.1 \pm 0.3$ mag. In contrast, Sandage [1986], after a very thorough discussion, derived only a very vague $25 < m - M < 29 \pm 1$ from brightest red and blue stars. Hoessel et al. [1990], again, were still far off with their presumed δ Cephei distance of $m - M = 26.22 \pm 0.20$ mag; Aparicio [1994] challenged the Hoessel et al. distance as he derived $m - M = 24.9 \pm 0.1$ mag from an I-band TRGB. While Gallagher et al. [1998] concluded an $m - M = 24.4 \pm 0.2$ mag distance modulus, mostly because they adopted a 0.3 mag higher I-band extinction, McConnachie et al. [2005] confirm his result; they give a $m - M = 24.82 \pm 0.07$ mag TRGB distance modulus. Our preliminary δ Cephei distance, $m - M = 24.92 \pm 0.2 \pm 0.06_{ZP}$ [Gössl et al., 2006], is also consistent with those findings.

Aparicio and Gallart [1995], Aparicio et al. [1997] derived a significant old population with oldest stars ≈ 15 Gyrs, several bursts of star formation in recent epochs, and a metallicity as low as $Z = 0.002$ whereas Gallagher et al. [1998] concluded an even lower metallicity of $Z = 0.001$ and most stars forming about $2 - 4$ Gyrs ago[10]. Our findings of 52 LPVs [Snigula et al., 2006, Snigula, 2006] is best explained by the latter star formation history.

5.1.3 EGB 0427+63

EGB 04 27 +63 (UGCA 092) was found by Ellis, Grayson, and Bond [1984] while looking for faint Planetary Nebulae in the POSS. A first CCD photometry by Hoessel et al. [1988] did only yield a lower limit for the distance $m - M > 24.5$ mag. Karachentsev et al. [1997] derived $m - M = 26.25$ mag from the brightest blue stars. It was not until Karachentsev et al. [2006] that its distance was more firmly established from HST data by means of the TRGB method to $m - M = 27.39 \pm 0.18$ mag.

5.1.4 GR 8

GR 8 (DDO 155, UGC 08091) was discovered by G. Reaves [1956] while looking for dwarf galaxy candidates within the Virgo galaxy cluster. Early distance estimates range from 22.5 mag $< m - M < 27.6$ mag [Hodge, 1967, brightest blue stars]. Hodge [1974] gave a variety of distance estimates: They mostly narrowed down the upper limit derived from H II regions to $m - M < 27.0$ mag and gave an average distance of 1 ± 0.5 Mpc[4]. (de Vaucouleurs and Moss [1983] interpreted his results as a median distance of $m - M = 25.5 \pm 0.5$ mag.) de Vaucouleurs [1978]

---

[9]The POSS was conducted with a 48" Schmidt telescope in two photographic bands and is still the largest survey in optical wave bands.

[10]But they find stellar ages up to ~ 8 Gyrs compatible with their data.

also from brightest blue stars and the diameter of H II regions derived $m - M = 25.0 \pm 0.3$ mag. de Vaucouleurs and Moss [1983] got $m - M = 25.25 \pm 0.4$ mag from brightest red and blue stars[11], total magnitude, H II, and H I measurements whereas Hoessel and Danielson [1983] found $m - M = 26.1$ mag from carbon stars but combined this result with Hodge [1974] to derive $m - M = 25.6 \pm 0.8$ mag. Aparicio et al. [1988] obtained $m - M \approx 25.0$, again from bright blue stars, but points out that this distance modulus *"still remains poorly determined "* because of a huge error due to statistical effects as explained by Schild and Maeder [1983] and Greggio [1986]. Skillman et al. [1988] determined the oxygen abundance of GR 8 to be $\sim 3\%$ solar which is confirmed by modern measurements of $\sim 5\%$ solar [van Zee et al., 2006].

Finally, Tolstoy et al. [1995] found a single Cepheid in GR 8 and derived from it a distance modulus of $m - M = 26.75 \pm 0.35$ mag which we recovered in our preliminary results [Gössl et al., 2006, $m - M = 26.45 \pm 0.07 \pm 0.06_{ZP}(\pm 0.25_{PLR})$]. Dohm-Palmer et al. [1998] find this distance consistent with their TRGB estimate from HST CMDs.

5.1.5　Aquarius Dwarf

The Aquarius Dwarf (DDO 210) was first reported on in the DDO survey [van den Bergh, 1959, 1966]. Its LG membership has been based on similarities with other members and an inbound galactocentric velocity [Fisher and Tully, 1975]. Marconi et al. [1990], Greggio et al. [1993] first still considered a $m - M \approx 25$ mag but later conclude that their best fitting model to a CMD has $m - M \approx 28$. Lee et al. [1999] procured $m - M = 24.89 \pm 0.11$ mag from an *I*-band TRGB. McConnachie et al. [2005, 2006] more or less confirm this result by their *I*-band TRGB distance modulus of $m - M = 25.15 \pm 0.08$ mag. However, our *VarStarDwarves* survey failed to detect any LPV in the Aquarius Dwarf [Snigula, 2006] which remains a puzzle if this distance is correct.

5.2　*VarStarDwarves* Data

The observations of Tab. 2.3 did yield 119 (41) Leo A, 78 (0) Pegasus, 158 (45) EGB 0427+63, 102 (49) GR 8, and 85 (10) Aquarius WST (CA) *R*-band epochs suitable for the "Lomb" detection (the consistency check). LGS 3 had only 48 epochs at the end of 2005 and therefore its analysis was deferred until enough data become available. The parameters of the 418 *VarStarDwarves* candidates (Tab. 4.5) will only partly be displayed in the next sections; the longest and/or least relevant tables, finding charts, and additional light curves are shown in App. F, G, and H, respectively.

5.2.1　Leo A – The Test Case

An overview of the VS candidates for Leo A is displayed in the CMD of Fig. 5.2. There is one big caveat[12] to start with: While the *R*-band magnitudes and their errors are reliable the $B - R$ colours

---

[11]In Moss and de Vaucouleurs [1986] they exclude the formerly brightest blue star as a galactic foreground contaminant but do not change their distance estimate.

[12]It applies generally for all subsequent CMDs presented here, i.e. Fig. 5.9, 5.16, and fig. 5.18.

Figure 5.1: Colour composite image of Leo A: Red channel = CA *I*-band reference image, green channel = WST + CA *R*-band reference images, blue channel = CA *B*-band reference image; exponential scaling.

and their errors are not. The according reference frames going into the DAOPHOT photometry combine different epochs for the two filters[13] and therefore the colour should be only interpreted as a hint; the actual colour may be off by almost an amplitude of the VS[14] and the errors for the colours are combined DAOPHOT photometry errors which are known to be a lower limit at best. The CMD background (grey squares) shows the typical features of a young population (upper main sequence and blue loops region, i.e. the "*blue plume*", left centre/top) mixed with an intermediate and maybe old population (RGB, AGB; bulk of data and right top). To allow for a

---

[13]Only 3 epochs for *B*-band CA and the "blue" amplitude is larger than the red one!

[14]LM01 (see below) definitely has this sort of systematic error in colour. The probable location of the instability strip is not at $B - R \approx 1.0$ mag as hinted by the "right" green circles but more at $B - R \approx 0.7$ which is the "green" average colour.
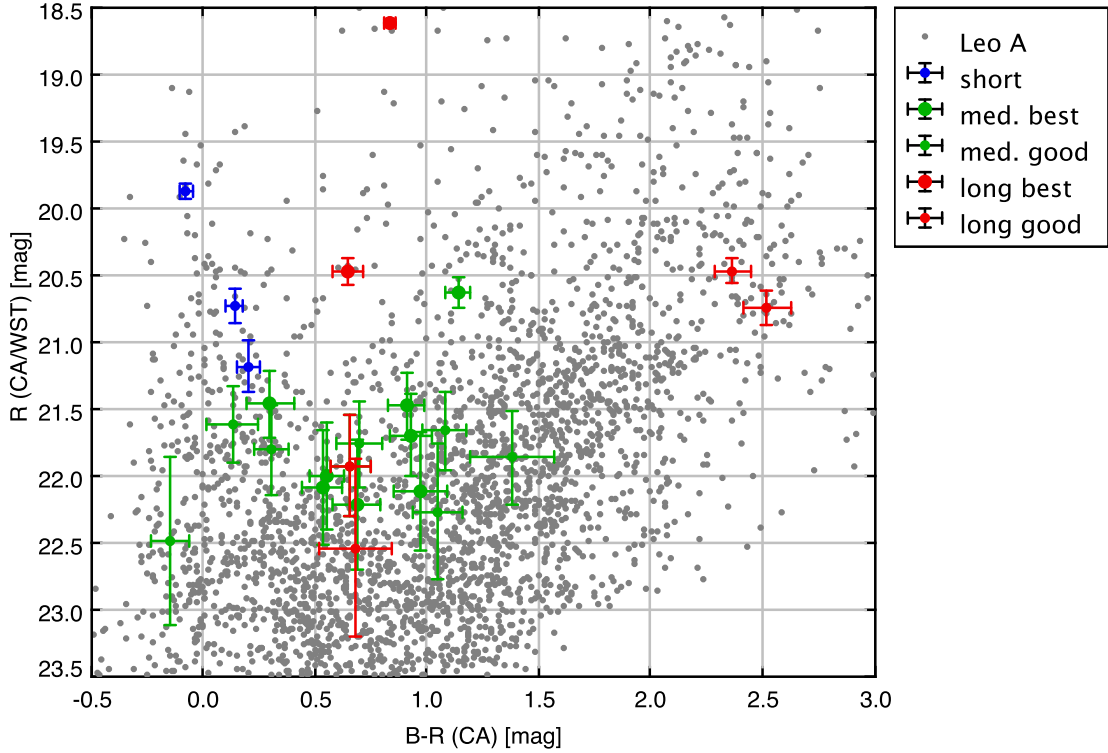
Figure 5.2: Leo A CMD – grey: CA R-band (uncorrected) vs. CA $B - R$ colour (extinction correction after Schlegel et al., 1998, $A_R = 0.055$, $A_B = 0.89$); other colours (VS candidates): WST R-band (uncorrected) and propagated errors vs. CA $B - R$ colour (extinction correction after Schlegel et al., 1998) and DAOPHOT errors (see caveat in text!); blue: $P < 1$ d, $p < 0.25$, Tab. F.1; green: 1 d$< P < 10$ d, $p < 0.01$, Tab. 5.1; red: $P > 10$ d, $p < 0.01$, Tab. 5.2 top. See Fig. G.1 for a CMD indicating all VS candidates.

more easy cross identification of the VS candidates in the successive figures and tables only the $B - R$ colour has been corrected for galactic foreground extinction [Schlegel et al., 1998] but not the R-band brightness.

The photometry and Lomb results of all longer period ($P > 10$ d) candidates and the best and good medium period (1 d$< P < 10$ d, $p < 0.01$) will be shown here (Tab. 5.2 and 5.1), the worse medium period ($0.25 > p > 0.01$) and all short ones ($P < 1$ d) follow in App. F (Tab. F.2 and F.1). Fig. 5.6 is a "special" finding chart for the Leo A candidates discussed here; finding charts displaying all VS candidates grouped by period ranges can be found in App. G.

At least eight, maybe ten, of the LS candidates are due to the diffraction spikes of a bright star in the field[15] (LS9, LS11, LS23, LS34, LS36, LS45, LS51, and LS55, and probably also LS 31 and LS59; Tab. F.1). Some candidates are also probable blends, i.e. they have close location and period (LM40 & LM49 of LM 15, LM50 of LM26, LS39 of LS25; Tab. F.2, 5.1, and F.1).

---

[15]Caused by the secondary mirror mount. Unfortunately, there is no compact, reflective off-axis (free of obstruction) telescope design available so far.
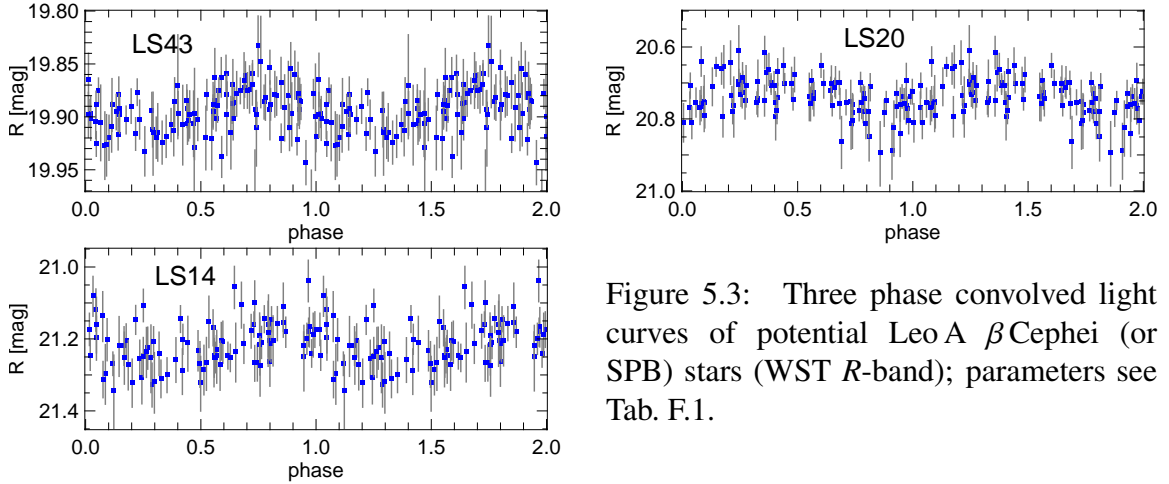
Figure 5.3: Three phase convolved light curves of potential Leo A β Cephei (or SPB) stars (WST R-band); parameters see Tab. F.1.

β Cephei (or SPB) Candidates

Of the three bluest and brightest VS candidates within the "blue plume" which contains the main sequence (Fig. 5.2, blue, $B-R < 0.25$, $R < 21.5$; LS43, LS20, and LS14[16] of Tab. F.1; Fig 5.6 blue LS) at least the brightest one (LS43) shows a promising light curve (Fig. 5.3) and may actually be a β Cephei (or SPB) star. This comes as a surprise as one would not expect to find any β Cephei in hosts with the very low Leo A metallicity. The brightest candidate is certainly adequate ($R = 19.88$ mag) to try a direct metallicity determination with a 10 m-class telescope and is definitely worthy of further investigation[17]. All other short period VS are either too faint (noisy light curve) or too "red" (or both) to be considered here. Some of the bluest Cepheid candidates, discussed in the next paragraph, might also be added here, especially those which display multi-periodic behaviour. LM09, LM16, and LM17 with respective short periods of $P = 0.39, 1.86$, and 0.74 d are the most prominent to mention here. LM02, despite a tempting "Cepheid" colour, has also a convincing alternate period of $P = 0.72$ d and, like all the former, lies with its longer period clearly above a Leo A δ Cephei PLR. If any of this multitude of candidates could be confirmed either the metallicity assessment of Leo A or the pulsation theory for B-stars would have to be revised. Disproved candidates still might be Eclipsing Binaries which would also allow for interesting science from follow-up observations (Sect. 1.5.5).

"Cepheids" with periods 1 d$< P < 10$ d

Tab. 5.1 top and Fig. 5.4[18] show the most promising δ Cephei candidates. The Lomb detection is based solely on the WST data (blue squares), the CA data (red circles) serves only as a consistency check. LM01 and LM03 are so far the longest period δ Cephei stars known in Leo A.

---

[16]With periods $P = 0.095, 0.184,$ and 0.822 d respectively.

[17]Considering that the period of LS43 is smaller than three times the typical exposure stack time span of ~ 45 minutes the signal is thus smoothed, but still large. However, to confirm LS43 photometrically 7 hours straight with a series of ~ 10 minute exposure at a 1.5 m class telescope should suffice.

[18]See Fig. H.1 for the $0.0001 < p < 0.01$ candidates light curves of Tab. 5.1.
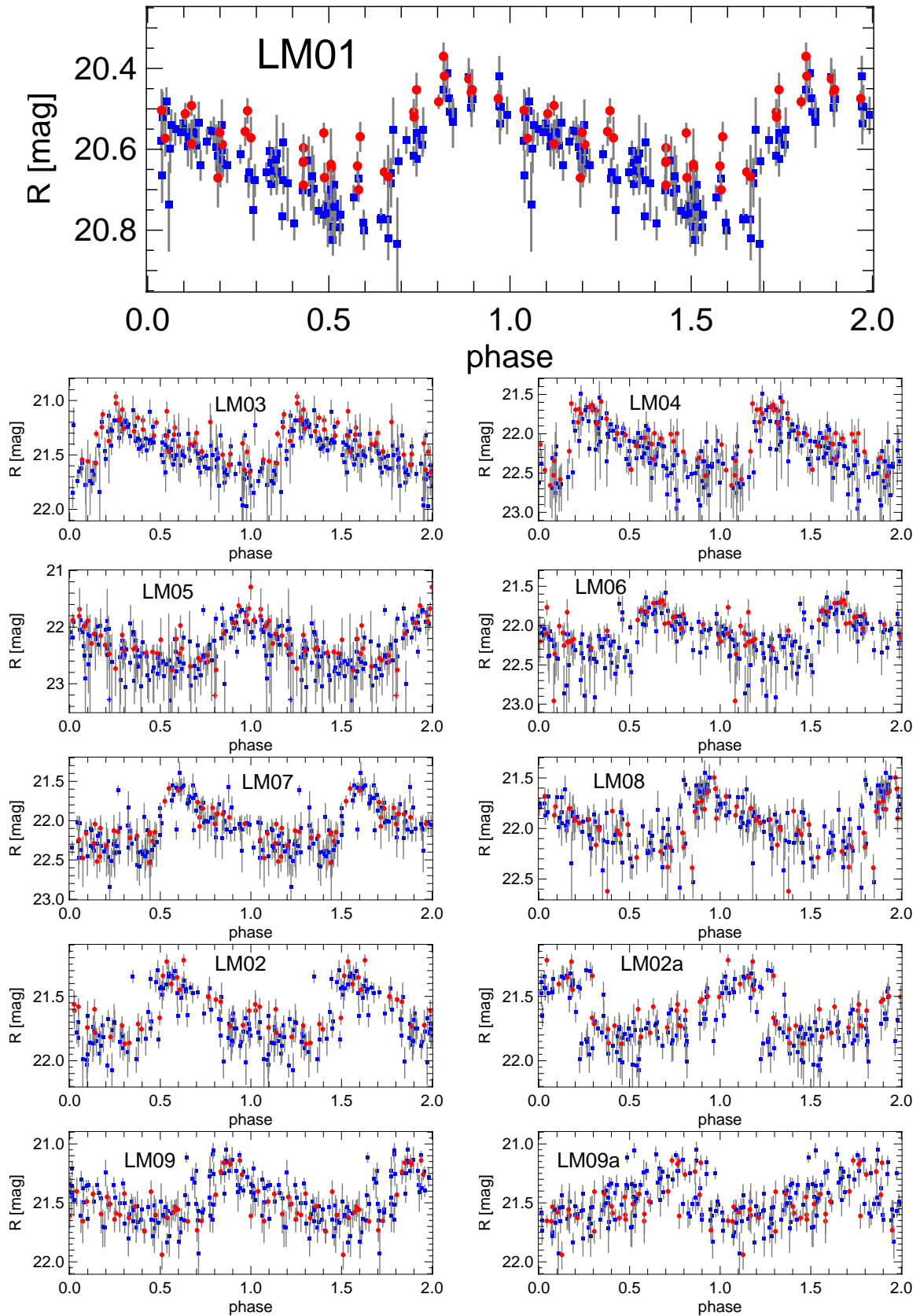
Figure 5.4: Leo A best ($p < 0.0001$, period 1 d$< P < 10$ d) δ Cephei candidates phase convolved light curves. Blue squares: WST data (Lomb detection); red circles: CA data (consistency check); coloured crosses: Data consistent with detection limit at epoch, i.e. $S/N < 1$ at either site; grey: 1σ errors. For additional ($0.0001 < p < 0.01$) light curves see Fig. H.1.

Table 5.1: Parameters of Leo A best and good Cepheid 1 d< P < 10 d period candidates: Short identifier (see Fig. 5.6), IAU compliant identifier, position, most significant Lomb period(s), significance (p-level), flux averaged apparent R-band magnitude, r.m.s. error of R-band magnitude.

| Id	IAU compliant name	RA-2000 [h]	Dec-2000 [deg]	period [d]	signific. [p]	$\langle R_f \rangle$ [mag]
LM01	WST J095928.7+304436	09:59:28.674	+30:44:36.01	6.490	5.12e-12	20.64±0.11
LM02	WST J095925.9+304437	09:59:25.897	+30:44:36.58	1.607	8.65e-08	21.70±0.30
LM02a				2.650	9.35e-05	
LM03	WST J095923.9+304513	09:59:23.925	+30:45:12.92	3.354	1.91e-07	21.48±0.25
LM04	WST J095919.7+304414	09:59:19.692	+30:44:14.21	1.813	1.95e-07	22.22±0.49
LM05	WST J095930.5+304403	09:59:30.456	+30:44:03.10	1.685	3.57e-07	22.28±0.52
LM06	WST J095929.1+304348	09:59:29.122	+30:43:48.44	2.048	1.82e-06	22.12±0.44
LM07	WST J095925.7+304441	09:59:25.669	+30:44:41.49	1.564	2.10e-06	22.09±0.44
LM08	WST J095931.1+304340	09:59:31.136	+30:43:40.04	2.115	5.08e-06	22.01±0.40
LM09	WST J095927.8+304458	09:59:27.765	+30:44:57.61	1.685	2.06e-05	21.47±0.25
LM09a				2.450	8.59e-05	
LM10	WST J095921.1+304457	09:59:21.144	+30:44:57.31	4.008	1.73e-04	21.66±0.29
LM11	WST J095926.9+304501	09:59:26.852	+30:45:01.07	2.429	3.46e-04	21.67±0.29
LM11a				1.690	1.67e-03	
LM12	WST J095932.7+304350	09:59:32.736	+30:43:50.28	2.480	1.06e-03	21.77±0.32
LS01a	WST J095921.5+304442	09:59:21.484	+30:44:42.10	1.020	1.72e-03	21.93±0.38
LM13	WST J095924.3+304342	09:59:24.251	+30:43:41.72	1.943	4.61e-03	22.27±0.51
LM14	WST J095927.4+304357	09:59:27.411	+30:43:56.83	4.529	4.63e-03	21.87±0.35
LM14a				1.280	3.59e-02	
LM15	WST J095923.4+304444	09:59:23.425	+30:44:43.52	4.054	7.08e-03	22.49±0.63
LM15a				1.320	2.61e-02	
LM16	WST J095923.0+304420	09:59:23.040	+30:44:19.51	2.164	7.86e-03	21.81±0.34
LM17	WST J095921.9+304510	09:59:21.869	+30:45:09.55	1.524	8.57e-03	21.62±0.28

In some light curves the CA data are systematically brighter or fainter than the WST data. This is due to the fewer CA reference epochs resulting in a reference image which provides worse magnitude averages than the WST ones (Sect. 4.4.3). Further discussion will follow below when reporting about PLRs.

"Cepheids" with periods 10 d< P < 130 d

Only longer period VS candidates (Tab. 5.2) are bright enough[19] to be considered as Type II Cepheids. LL01 displays a typical RV Tauri light curve (Fig. 5.5) whereas LL02 is already too noisy to decide on a designation. However, both light curves would display rather low amplitudes if they indeed were RV Tauri and would also be more on the "blue" side of the instability strip at least as far as the colours can be trusted[20] (Fig. 5.2, the 2 top left most red circles). LL03, LL06,

---

[19]Compare Tab. 4.3 with the PL diagrams in Fig. 5.7.

[20]See caveat for colours but also Footnote 14 on the location of the instability strip.
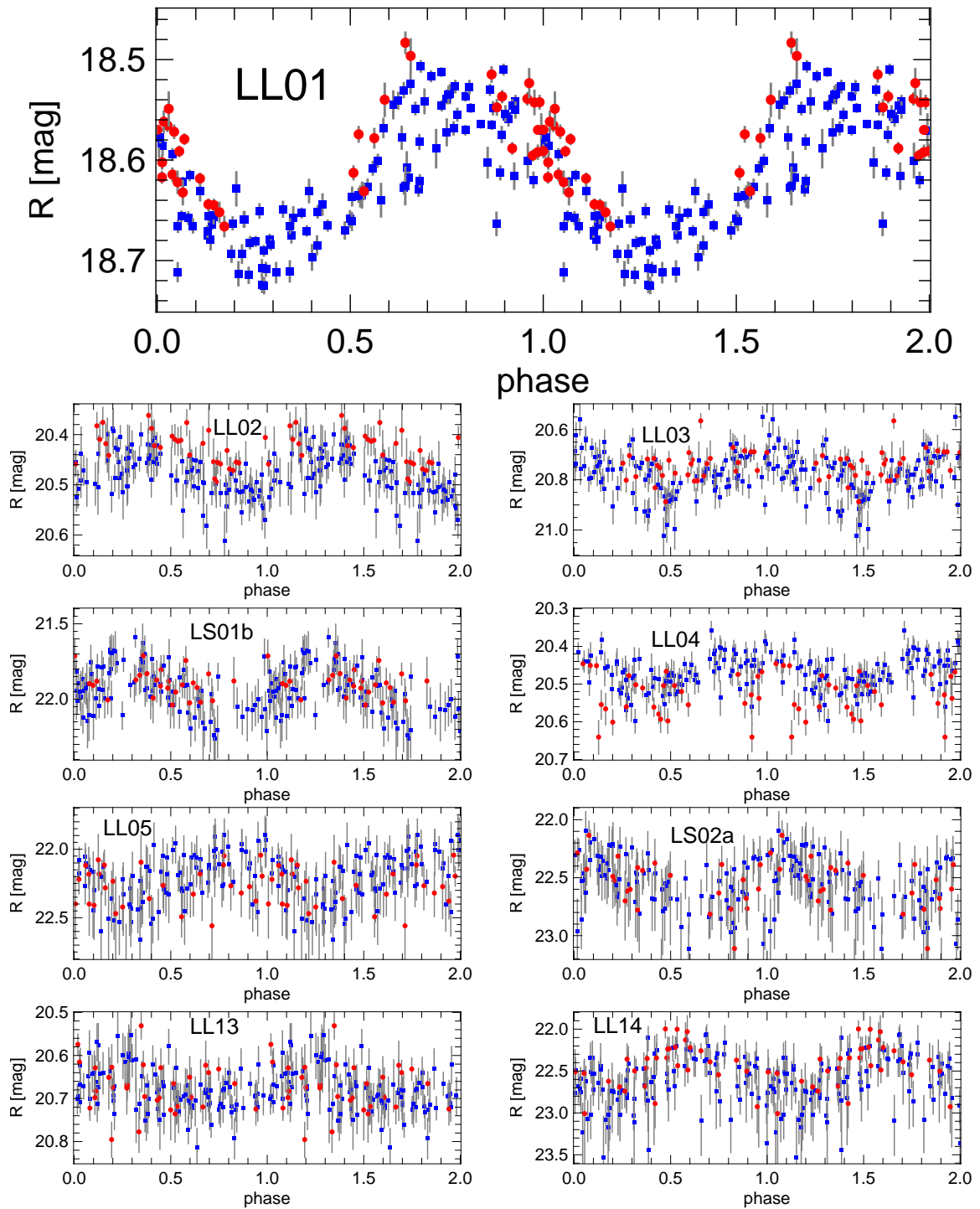
Figure 5.5: Leo A best Type II Cepheid candidates phase convolved light curves. Blue squares: WST data (Lomb detection); red circles: CA data (consistency check); grey: 1σ errors.

Table 5.2: Parameters of Leo A Cepheid $10\,\mathrm{d} \leq P \leq 130\,\mathrm{d}$ longest period candidates: Short identifier (see Fig. 5.6), IAU compliant identifier, position, most significant Lomb period(s), significance (p-level), flux averaged apparent R-band magnitude, r.m.s. error of R-band magnitude.

Id	IAU compliant name	RA-2000 [h]	Dec-2000 [deg]	period [d]	signific. [p]	$\langle R_f \rangle$ [mag]
LL01	WST J095919.3+304516	09:59:19.321	+30:45:15.50	74.529	1.02e-11	18.61±0.02
LL02	WST J095922.9+304512	09:59:22.859	+30:45:12.46	65.446	6.23e-05	20.48±0.10
LL03	WST J095918.9+304422	09:59:18.856	+30:44:21.58	60.231	4.71e-04	20.75±0.13
LS01*b*	WST J095921.5+304442	09:59:21.484	+30:44:42.10	52.600	7.09e-03	21.93±0.38
LL04	WST J095935.5+304225	09:59:35.458	+30:42:25.38	27.829	9.47e-03	20.47±0.10
LL05	WST J095930.7+304506	09:59:30.658	+30:45:06.34	10.391	1.83e-02	22.20±0.48
LL06	WST J095935.4+304450	09:59:35.449	+30:44:50.00	21.498	2.54e-02	20.33±0.09
LS02*a*	WST J095935.0+304334	09:59:34.977	+30:43:33.54	15.830	3.21e-02	22.54±0.66
LL07	WST J095924.9+304352	09:59:24.938	+30:43:52.00	12.639	4.86e-02	23.48±1.56
LL08	WST J095922.5+304232	09:59:22.528	+30:42:31.66	12.022	6.33e-02	23.50±1.59
LL09	WST J095939.4+304405	09:59:39.359	+30:44:05.25	40.163	7.66e-02	22.92±0.93
LL10	WST J095936.0+304609	09:59:36.036	+30:46:09.41	27.122	9.44e-02	21.31±0.21
LL11	WST J095920.2+304446	09:59:20.153	+30:44:45.57	57.912	9.78e-02	19.05±0.03
LL12	WST J095925.9+304627	09:59:25.878	+30:46:27.38	76.713	9.94e-02	23.30±1.32
LS26*a*	WST J095922.9+304431	09:59:22.890	+30:44:31.28	27.370	1.15e-01	22.42±0.59
LL13	WST J095922.6+304435	09:59:22.624	+30:44:34.72	12.033	1.95e-01	20.70±0.12
LL14	WST J095919.8+304445	09:59:19.811	+30:44:44.60	18.920	1.96e-01	22.65±0.72
LM29*a*	WST J095927.6+304454	09:59:27.574	+30:44:54.18	61.940	2.26e-01	18.87±0.02

LL11, LL13 and LM29a are in most respects similar to LL02 but show even less clear light curves; their colour, however, would be more indicative of Mirae[21] stars (Fig. 5.2, red and yellow markers with $B - R \geq 2.0$). The periods of LL04, LL10, and LS16*a* are so close to lunation that they might be caused by the according window function. LS01*b*, LL05, LS02*a*, LL13, and LL14 are the most promising candidates besides LL01 and LL02 for Type II Cepheids in terms of light curve[22] and colour. Further discussion, again, will follow in the PLR paragraph.

Literature cross-references

LM08 and LM04 might be identical to two of four VS candidates suggested by Sandage [1986, Fig. 5] but it is almost impossible to be sure from the poorly printed finding chart alone[23]. Of the Hoessel et al. [1994, Tab. 3] VS candidates probably three, maybe four, match with some of our candidates[23] (Tab. 5.3). However, the *VarStarDwarves* photometry is systematically brighter and the periods do not agree at all. But, since none of the Hoessel et al. [1994] Cepheids could be confirmed later on and their PLR distance was way off this comes as no surprise.

---

[21]In the course of this thesis there will be no further classification, e.g. SRa stars will also be labelled Mirae.

[22]See Fig. 5.5 for their light curves

[23]There is no astrometric solution, not even some arbitrary coordinate system, given in the publication.

Table 5.3: This work's VS candidates cross-correlated with Hoessel et al. [1994], Tab. 3; visual inspection of finding charts (? = doubtful identification, + = probable match).

	this work			Hoessel et al. [1994]		
Id	P [d]	R [mag]	Δ ["]	R [mag]	P [d]	Id
LM02	1.607	21.70±0.30	?	22.68	0.548	V7
LM02a	2.650	21.70±0.30	?			V7
LM07	1.564	22.09±0.44	?			V7
LS01b	52.600	21.93±0.38	+	22.53	2.670	V9
LS48	0.140	22.19±0.48	?			V9
LM10	4.008	21.66±0.29	+	22.29	13.004	V10
LM04	1.813	22.22±0.49	+	22.62	3.417	V13
LS24	0.166	22.72±0.78	?			V13

21 of the 92 Dolphin et al. [2002] VS candidates are within 3.5" radius of *VarStarDwarves* ones[24] (Tab. 5.4). Ten of the 16 clear identifications with $\Delta < 1$" have compatible period solutions ($|P_{VarStarDwarves} - P_{\text{Dolphin}}| \lesssim 1\sigma_{\text{Dolphin}}$). This is very remarkable: The Dolphin et al. [2002] results are based on observations in three consecutive nights with the WIYN 3.5 m on Kitt Peak yielding 23 half hour exposures in the *V*-band aiming at periods less than 2 days. This can be normalised to a total of about 140 hours 1 m aperture exposure. Our 119 half hour *R*-band exposures at the 0.8 m WST telescope have an equivalent of only 38 hours 1 m aperture exposure. While 0.7" seeing is typical for the WIYN observations the 0.8 m WST delivered > 1.4" on average[25]. Therefore, one would expect our data to have at best only 25% of the WIYN data S/N ratio, i.e. to be about 1.5 mag fainter. But, our image processing and data reduction scheme apparently can overcome those odds despite additionally only aiming at periods longer than 2 days with our observational setup. In case of the $P > 2$ d "matches" the WST period solution is definitely superior to the WIYN one because of the larger time line base. Candidates with $\Delta > 1$" are probably mismatches, but for LM43 which may be actually a blend of C2-V28 and C2-V29. In case of LL14 and LS53 I consider the Dolphin et al. [2002] as the better solutions because of their deeper and more densely sampled data. The "true" WST period of LM47 is probably erased because we ignored 0.5 d detections as they are most probable due to a window function. For LM10 and LM53 the case in not settled yet and future observations will have to show which, if any, period solution will prevail.

Leo A VS finding chart

Comparing the distribution of shorter, medium, and longer period candidates over the field[26] shows that the medium periods (LM01-17) are concentrated in the star bursting core of Leo A

---

[24]Dolphin et al. [2002] at least give CCD pixel coordinates which together with their finding charts and some pain I could translate into celestial coordinates.

[25]No airmass correction!

[26]See Fig. 5.6 for a "glimpse", but better compare Fig. G.3, G.4, G.5, and Fig. 4.4 of Snigula [2006].

Table 5.4: This work's VS candidates cross-correlated with Dolphin et al. [2002], Tab. 3, automated list within 3.5" radius. Match column: + = good period match; − = bad period match; d = bad distance (and period) match; b = period mismatch may be caused by variable blending; w = "true" *VarStarDwarves* period maybe lost in erased window function period; Σ = 21: 10 +, 4 −, 5(+1) d, 1 b, 1 w.

	this work			Dolphin et al. [2002]			
Id	P [d]	R [mag]	Δ ["]	R [mag]	P [d]	Id	match
LL08	12.02	23.50±1.59	2.21	23.37±0.03	0.44±0.01	C2-V81	d
LL08				23.36±0.02	0.86±0.03	C2-V81	d
LL11	57.91	19.05±0.03	1.31	22.74±0.02	1.28±0.12	C2-V37	d
LL14	18.92	22.65±0.72	0.08	22.42±0.02	0.47±0.02	C2-V38	-
LM02	1.61	21.70±0.30	0.34	21.96±0.06	1.73±0.23	C2-V42	+
LM04	1.81	22.22±0.49	2.55	23.26±0.08	0.61±0.01	C2-V54	d
LM05	1.69	22.28±0.52	0.67	22.53±0.12	1.46±0.17	C2-V58	+
LM06	2.05	22.12±0.44	0.15	22.14±0.15	2.01+∞	C2-V64	+
LM08	2.12	22.01±0.40	0.05	22.27±0.06	2.13±0.06	C2-V67	+
LM10	4.01	21.66±0.29	0.51	22.88±0.03	1.39±0.15	C2-V25	-
LM11*a*	1.69	21.67±0.29	0.23	22.16±0.16	1.67±0.13	C2-V22	+
LM12	2.48	21.77±0.32	0.42	22.12±0.07	2.29+∞	C2-V63	+
LM14*a*	1.28	21.87±0.35	0.82	22.89±0.26	1.32±0.11	C2-V60	+
LM18	1.40	22.85±0.87	0.17	23.22±0.05	1.47±0.13	C2-V17	+
LM39	1.56	22.15±0.46	0.24	22.67±0.03	1.61±0.05	C2-V43	+
LM43	3.90	22.72±0.78	0.33	23.18±0.05	0.80±0.04	C2-V28	b↓
LM43	3.90	22.72±0.78	2.99	23.07±0.01	0.59±0.02	C2-V29	(d)
LM47	1.02	23.16±1.17	0.30	22.67±0.05	0.51±0.01	C2-V11	w
LM52	1.74	22.84±0.87	1.91	24.78±0.06	0.61±0.02	C1-V03	d
LM53	2.67	22.69±0.75	0.30	22.88±0.07	1.69±0.05	C2-V39	-
LS02	0.94	22.54±0.66	0.10	22.64±0.11	0.93±0.02	C2-V71	+
LS18	0.41	21.63±0.29	3.19	23.08±0.13	0.66±0.02	C2-V45	d
LS53	0.13	22.74±0.79	0.66	23.13±0.04	0.79±0.04	C2-V10	-

while the longer periods show a more diffuse distribution. This can be interpreted as tracing different populations, i.e. medium periods the younger populations in star forming regions and longer periods the older populations of the extended Leo A halo reported by Dolphin et al. [2002].

PLRs and the distance to Leo A

The excellent sample of the Fig. 5.4 δ Cephei candidates allows for the first time to derive a reliable PLR distance to Leo A: Fig. 5.7 shows the VS candidates of Tab. 5.1, F.2, and 5.2 in the context of a Madore and Freedman [1991] PLR (Eqn. (1.3)) shifted to the best fitting distance modulus of LM01, LM03, LM06, and LM08, i.e.

$$\text{Leo A } m - M = 24.48 \pm 0.10(\pm 0.06_{\text{ZP}}) \text{ mag.} \tag{5.1}$$
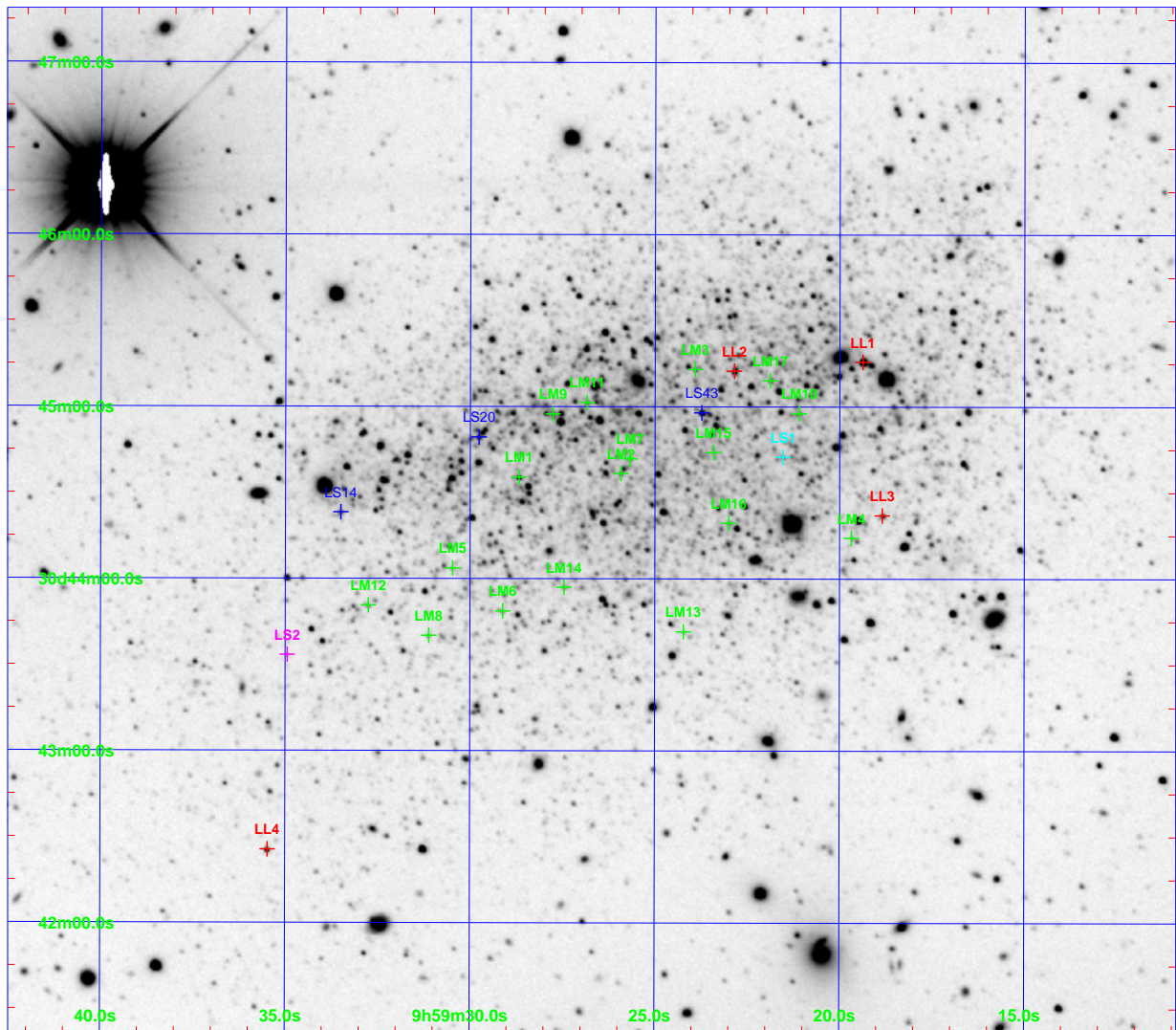
Figure 5.6: Finding chart of selected VS candidates, mostly of Tab. 5.1 and 5.2 but partly also from Tab. F.1. Blue: LS short period pulsating B-star candidates; green: LM most promising δ Cephei candidates; red: LL long period Type II Cepheid candidates. turquoise and purple: Candidates with interesting secondary period solutions.

This result is consistent with both the Schulte-Ladbeck et al. [2002] TRGB_I and the Dolphin et al. [2002] RR Lyrae distance. LM04 and LM05 still perfectly agree with this relation but were not included in the fit because Bauer et al. [1999] report a significant change in the slope of the SMC PLR for periods < 2 d. LM07 coincides with the according Caputo et al. [2004] First Overtone relation (Eqn. (1.2)). LM02 and LM09 (Fig. 5.7, blue diamonds) might either be so called "beat" Cepheids pulsating simultaneously in the Second and First Overtone or the Second Overtone and the Fundamental Mode respectively or SPB stars displaying multiple excited
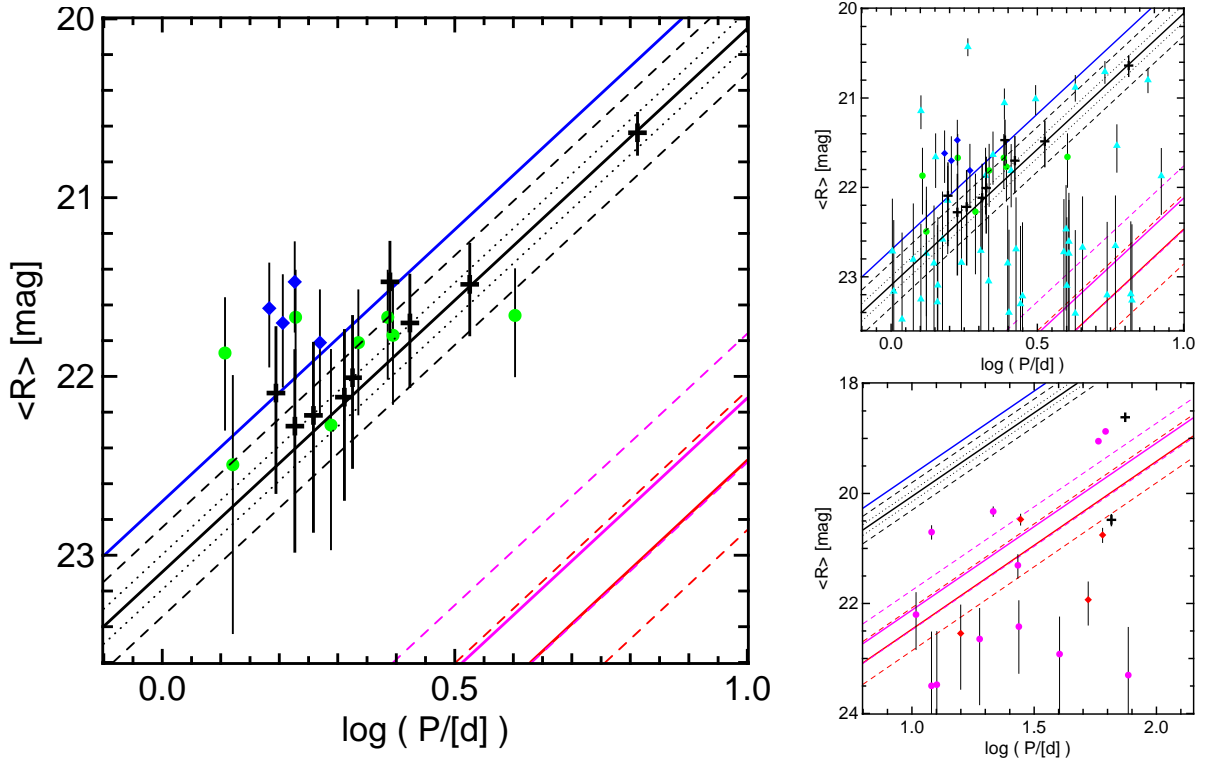
Figure 5.7: Solid black line: *R*-band period-luminosity relation for fundamental mode LMC Cepheids, Eqn. (1.3) [Madore and Freedman, 1991] corrected for galactic extinction [Schlegel et al., 1998, $A_R = 0.055$]. The PLR shown is best-fitting the observed Leo A δ Cephei stars average magnitudes $< R_f >$ and periods of LM01, LM03, LM06, and LM08 (Tab 5.1). The fit is dominated by the longest period star LM01 due to its small error; it yields a distance modulus of $m - M = 24.48 \pm 0.10(\pm 0.06_{ZP})$ mag including random errors and errors of the calibration. LM02 and LM09 were ignored because of their ambiguous period solutions (see text). Other candidates are either too short period ($P < 2$ d) or have less convincing Lomb significances ($p > 0.0001$) to be considered. Dotted black lines show the propagated error of the fit while dashed black lines indicate the error of the PL relation. Solid blue line: First Overtone relation according to Eqn. (1.5). Red and purple lines denote Type II PLRs and their errors (Sect. 1.5.4, Eqn. (1.4) and (1.5)). Black crosses: Highly significant ($p < 0.0001$) VS candidates; blue diamonds: Pulsating B-stars candidates; green circles: Less significant ($0.01 > p > 0.0001$) shorter period ($P < 10$ d) VS candidates; turquoise triangles: Low significant ($0.25 > p > 0.01$) shorter period ($P < 10$ d) VS candidates; red diamonds: Less significant ($0.01 > p > 0.0001$) longer period ($P > 10$ d) VS candidates; purple circles: Low significant ($0.25 > p > 0.01$) longer period ($P > 10$ d) VS candidates.

modes. The probability of a blend is $\sim 3\%$[27] within 21 mag$< R < 22$ mag, therefore, the a priori probability that all of LM02, LM07, and LM09 are not enhanced by blending is $> 90\%$. The

---

[27]I.e. the highest density of stars in the core of Leo A within the brightness range 21 mag$< R < 22$ mag per 2” $\times$ 2” cell.

bluer colour of LM02 together with the low probability of 2/1 beat Cepheids points more towards a SPB star while LM09 has a more suitable "Cepheid" colour; however, the highest significant period yields a typical Cepheid shaped light curve for both cases. Two other SPB candidates (LM16 and LM17) with "blue" colours are also indicated by blue diamonds in Fig. 5.7. Of the remaining $0.01 > p > 0.0001$ candidates (green circles in Fig. 5.7; light curves in Fig. H.1) the most convincing in terms of light curve is LM13 which also lies exactly on the derived PLR. Higher precision and multi-colour photometry with a very dedicated ZP calibration can reduce the PLR distance error but will be only worthwhile if the current tackling of PLR systematic errors concludes an improved solution.

The turquoise triangles Fig. 5.7 illustrate the more or less random distribution of successively less significant candidates. This has to be kept in mind when "grasping at straws" for some other DGs in the *VarStarDwarves* sample. They also show an aggregation of candidates at about 4 d due to an unforeseen window function.

Fig. 5.7 right, bottom shows all candidates with periods $10\,\mathrm{d} < P < 120\,\mathrm{d}$ relative to the Type II Cepheid PL relations derived in Sect. 1.5.4 (Eqn. (1.4) and (1.5)). Of the candidates remaining from the previous discussion (in terms of colour and light curve) LL02, LL05, LS02a, and LL14 are more or less compatible with the (red) PLR but show successively less convincing light curves. However, LL01[28] which is the most clear and interesting case would be too bright by at least one magnitude to be compatible with the ("bluer", i.e. the purple) PLR. The probability for LL01 being a blend is even lower than for the previously discussed medium period candidates. But, Alcock et al. [1998] also see the trends of "brightening", rather small amplitudes and "bluer" colours for the longer period RV Tauri in their MACHO data base[29]. One can speculate that low metallicity might even enhance these trends. So far there are no theoretical models to compare with available. Nevertheless, LL01 is a very interesting star: It may well be both, the most metal poor and most distant, RV Tauri star known so far. And, it is within reach of spectroscopic observations which we intend to do.

Leo A, as a test case, shows the feasibility of our strategy: The overall data reduction scheme and the detection limits applied which are described in the previous Chap. 4 are "conservative" in the meaning of keeping even low significant periodic sources. While this helps identifying interesting objects with either quasi- or multi-periodic behaviour or near to our detection limit the sources to derive reliable PLR distances should be selected with caution, i.e. only those with a high Lomb significance suit[30]. Another lesson learnt already here, but even more with the next galaxy candidate, the Pegasus Dwarf: Already a single "rough" colour helps a lot in identifying both, interesting special cases (e.g. pulsating B-stars) and possible contaminants (e.g. blends or other type of VS). And presumably: More and more precise colours would help even more, i.e. might even allow to disentangle to some degree atmospheric extinction, dust extinction and intrinsic temperature of the source. But, realistically speaking, this is still beyond the capability of our site and equipment.

---

[28] And LL13 if one would be convinced by its light curve.

[29] See also Fig. 1.4.

[30] In our case at least $p < 0.01$ but better $p < 0.0001$.

Figure 5.8: Colour composite image of Peg DIG: Red channel = WST *R*-band reference image, green channel = WST *R*+*b*-band reference images, blue channel = WST *b*-band reference image; exponential scaling.

5.2.2 Pegasus Dwarf – Settled

Our Pegasus Dwarf observations lack CA data and therefore neither include an independent check of the HST based calibration scheme [Snigula, 2006, Tab. 3.1][31] nor "standard" Johnson [1965] $B - R$ colours. The WST "blue" band observations were done with a very broad

---

[31]Therefore, no error estimate for the ZP can be derived, but one has reason to assume that it will not deviate much from the ZP error calculated for Leo A (0.06 mag).
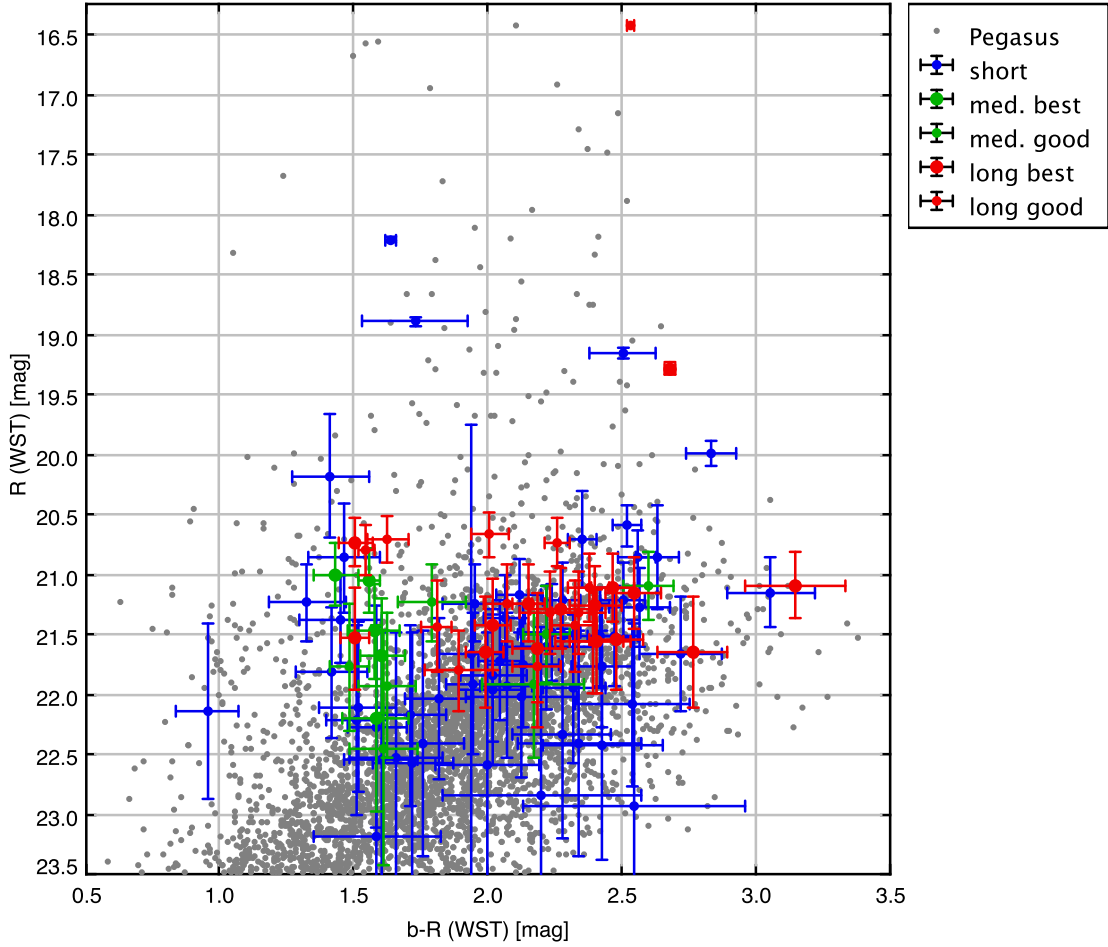
Figure 5.9: Pegasus Dwarf CMD – WST R-band (uncorrected) vs. WST $b - R$ colour (extinction correction after Schlegel et al., 1998, $A_R = 0.176$, $A_B 0.284$); WST R-band propagated brightness errors, WST $b - R$ DAOPHOT colour errors. Please note the discussion of the WST b-band calibration and the derived colour in the text. Blue: $P < 1$ d, $p < 0.25$, Tab. F.3; green: 1 d$< P < 10$ d, $p < 0.01$, Tab. 5.5; red: $P > 10$ d, $p < 0.01$, Tab. 5.6. Fig. G.2 indicates all VS candidates.

BV-filter (Fig. 2.1) which introduces great uncertainties when translated to Johnson [1965] B without colour terms corrections[32]. Also, the zero-point relies on a single night which might have been not as photometric as presumed. Therefore, the $b - R$ colour in Fig. 5.9 should only be interpreted as an "instrumental", relative quantity and actually is at least half a magnitude redder than expected[33]. The CMD of Pegasus (Fig. 5.9) compared to that of Leo A (Fig. 5.2) shows a heavily populated RGB with an about 0.2 mag fainter tip, a blue (main) sequence, however, is hardly discernible. From these observations alone one would derive that Pegasus is slightly further away, has a much more massive intermediate (and maybe also old) population, and much less relatively recent star formation than Leo A.

---

[32]Which, again, would require additional observations in other filter bands.

[33]At least half of this huge colour offset would also be explained if the higher than Schlegel et al. [1998] extinction assumed by Gallagher et al. [1998] was correct.
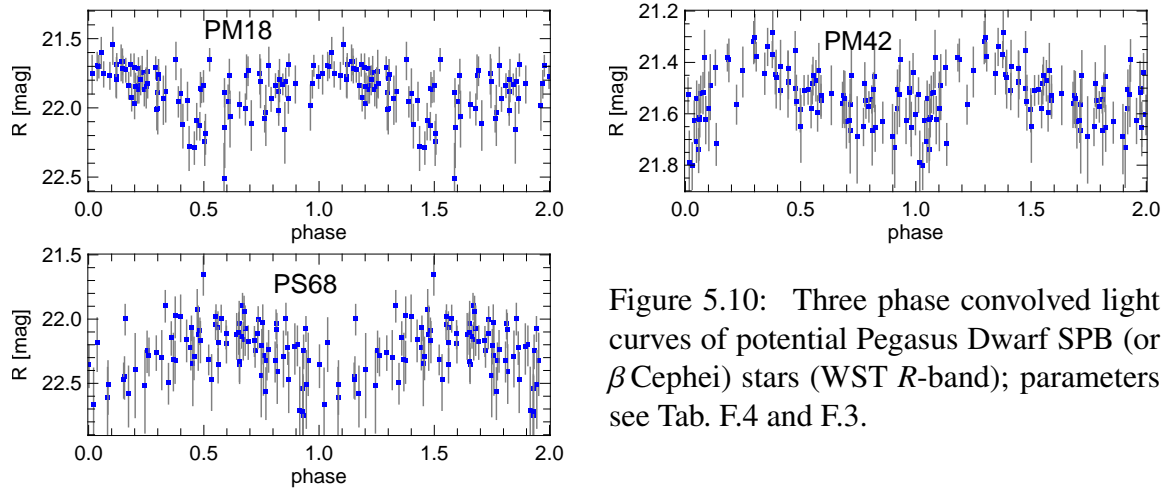
Figure 5.10: Three phase convolved light curves of potential Pegasus Dwarf SPB (or β Cephei) stars (WST R-band); parameters see Tab. F.4 and F.3.

At least 10 of the shorter period (PS) and 5 of the worse intermediate period (PM) candidates are due to diffraction spikes (see Fig. G.6 blue and turquoise). There is also some VS candidate blending which in some cases means that most probably only one candidate is "real" and the other only wrongly cross-correlated with the DAOPHOT source list. Most prominent here are PM02 and PM06 as well as PL01 and PL05; both pairs also show matching periods which also points at a DAOPHOT misidentification (see also Tab. 5.5, 5.6, and Fig. 5.14). Some VS candidates are clearly associated with unresolved background objects[34], but, being unresolved, no further information can be derived for either of them.

SPB (or β Cephei) candidates

The three "bluest" variable stars of Fig. 5.9 PM18, PM42, and PS68 (of Tab. F.4 and F.3, Fig. 5.14) have periods of 2.7, 3.7, and 0.87 days respectively which, together with their suitable brightness and convincing light curves (Fig. 5.10), would qualify them as SPB stars. But, while the metallicity of the Pegasus Dwarf is higher than that of Leo A (Sect. 5.1 and references therein) it is still too low to be consistent with those findings and the predictions of B-star pulsation theory. Unfortunately, the candidates are already too faint to allow for a spectroscopic metallicity determination.

Shorter period "Cepheid" candidates and a new classical δ Cephei PLR distance

Tab. 5.5 gives the parameters of all VS candidates with periods $1\,\mathrm{d} < P < 10\,\mathrm{d}$ and Lomb significance $p < 0.01$ while Fig. 5.11 displays only the candidates with clear and promising light curves. A first PL-diagram which showed also a Madore and Freedman [1991] PLR at a Schlegel et al. [1998] corrected McConnachie et al. [2005] distance temptingly identified several of the

---

[34]PS25, PL54, PM44, and PM 58 are within a background spiral galaxy; PL54 might even be due to a AGN[42] as it sits right on the galaxy core. PM37 and PL65 lie either within a massive Pegasus globular cluster or a background elliptical galaxy. (Again see Fig. G.6 for reference.)

Table 5.5: Parameters of Pegasus best and good δ Cephei 1 d< P < 10 d period candidates: Short identifier (see Fig. 5.14), IAU compliant identifier, position, most significant Lomb period(s), significance (p-level), flux averaged apparent R-band magnitude, r.m.s. error of R-band magnitude.

Id	IAU compliant name	RA-2000 [h]	Dec-2000 [deg]	period [d]	signific. [p]	$\langle R_f \rangle$ [mag]
PM01	WST J232834.7+144444	23:28:34.699	+14:44:43.88	3.458	8.79e-06	21.48±0.40
PM02	WST J232837.3+144346	23:28:37.301	+14:43:45.50	2.642	1.14e-05	22.21±0.78
PM03	WST J232832.7+144516	23:28:32.703	+14:45:15.77	3.889	2.61e-05	21.01±0.26
PM04	WST J232836.2+144402	23:28:36.185	+14:44:02.18	3.712	3.43e-05	21.68±0.48
PM05	WST J232833.7+144428	23:28:33.748	+14:44:27.69	3.188	5.78e-05	21.06±0.27
PM06	WST J232837.3+144346	23:28:37.301	+14:43:46.48	2.640	1.30e-04	21.51±0.41
PM07	WST J232840.6+144423	23:28:40.561	+14:44:23.25	1.654	3.61e-04	21.94±0.60
PM08	WST J232833.5+144435	23:28:33.545	+14:44:35.05	2.367	5.14e-04	21.78±0.52
PM09	WST J232834.4+144402	23:28:34.422	+14:44:02.18	2.252	5.35e-04	21.93±0.60
PM10	WST J232832.3+144520	23:28:32.330	+14:45:19.69	1.013	9.75e-04	21.11±0.28
PM11	WST J232829.1+144531	23:28:29.111	+14:45:31.47	2.465	2.77e-03	22.46±0.98
PM12	WST J232821.0+144747	23:28:20.956	+14:47:47.35	1.675	4.74e-03	23.13±1.80
PM13	WST J232837.7+144416	23:28:37.746	+14:44:16.40	2.472	5.22e-03	21.25±0.32
PM14	WST J232819.8+144546	23:28:19.824	+14:45:45.71	1.057	6.53e-03	22.00±0.64

Tab. 5.5 candidates being consistent with the PLR or the according First Overtone relation but could not explain also many of the candidates which were off the relation. Therefore, I narrowed down the selection criteria to derive a subsample for distance determination not depending on previous knowledge, only selecting sources with a colour within the narrow band of the probable location of the instability strip, a clear light curve, and periods longer than 2 d.

This way following candidates were **not** considered for distance determination: PM03, despite showing a clear Cepheid like light curve, has the bluest colour of the Tab. 5.5 candidates; it is also too bright to be consistent with the finally derived PLR distance. One explanation might be that it actually is a Second Overtone Pulsator but since those are very rare it might more probably be blending with a blue star of similar brightness which also is at odds with statistics[35] but still "possible". PM05 has an almost symmetric light curve which disqualifies it for selection despite its suitable colour. PM06 is most probably a blend of PM02 and also too red to be considered. PM07, PM10, PM12, and PM14 have periods of less than 2 d (PM10 and PM14 are probably still associated with the 1 d window function, PM10 is also too red in addition). Finally, PM09 and PM13 were dropped for red colours (PM13 also shows a very unclear light curve).

---

[35]A similar estimate as in Sect. 5.2.1 yields a blending probability of less than 10% for PM03, i.e. the highest density of stars in the mag range of 21 to 22 is 0.087 per $2'' \times 2''$ cell. This is an upper limit as DAOPHOT does a better job at deblending as is assumed here.
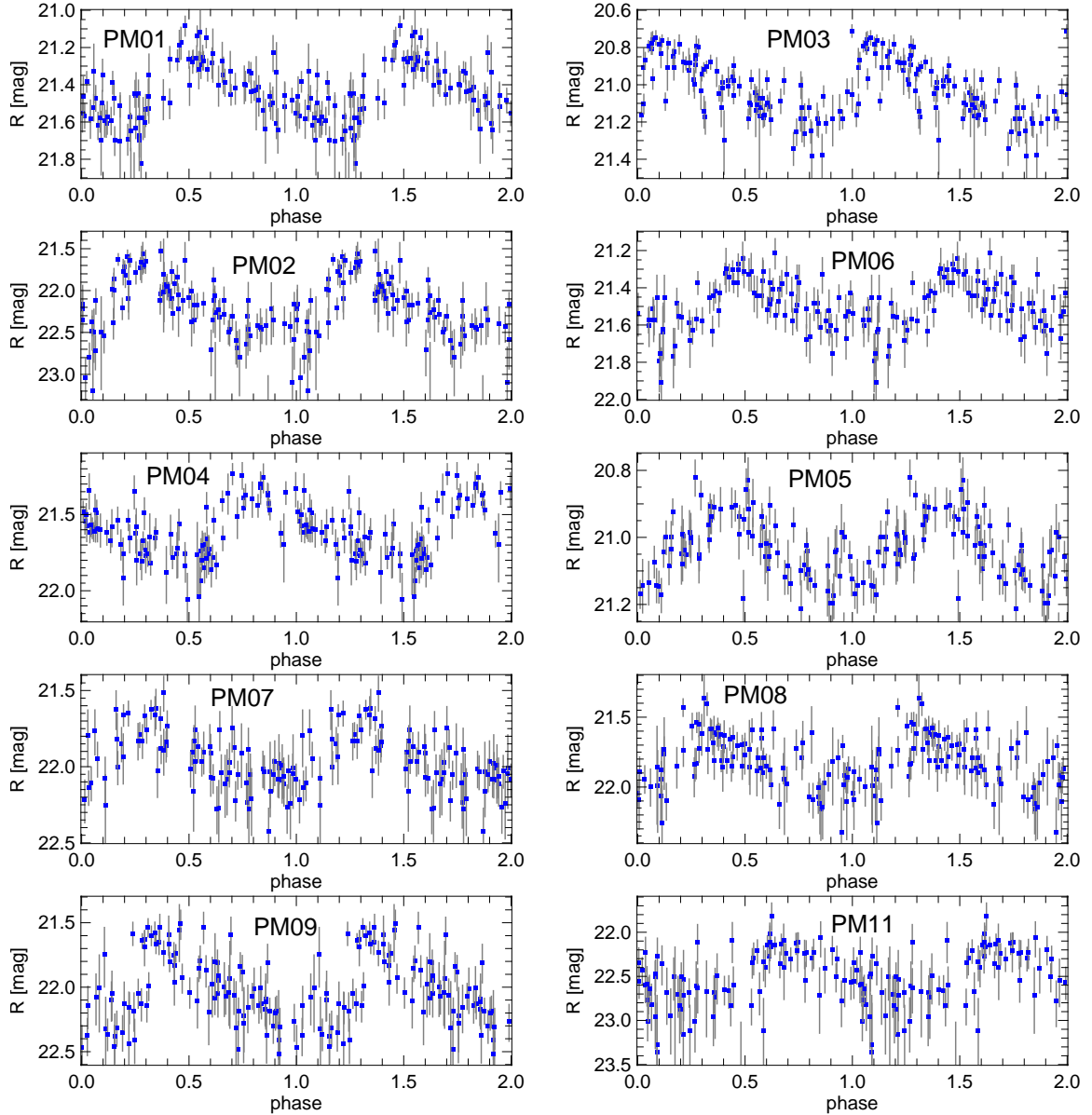
Figure 5.11: Pegasus Dwarf best δ Cephei candidates phase convolved light curves from Tab. 5.5. Blue squares: WST R-band data (Lomb detection). grey: 1σ errors.

This leaves PM01, PM02, PM04, PM08, and PM11 for distance determination. PM01 and PM08 I assume to be First Overtone Pulsators from their suitable brightness offset when compared with the other "distance" candidates and consider them with their according Fundamental period applying Eqn. (1.2). An error weighted fit of a Madore and Freedman [1991] R-band PLR including a Schlegel et al. [1998] extinction of $A_R = 0.176$ yields

$$\text{Pegasus } m - M = 24.72 \pm 0.24 \text{ mag} \tag{5.2}$$

which is perfectly consistent with previous TRGB distances (see references in Sect. 5.1). This
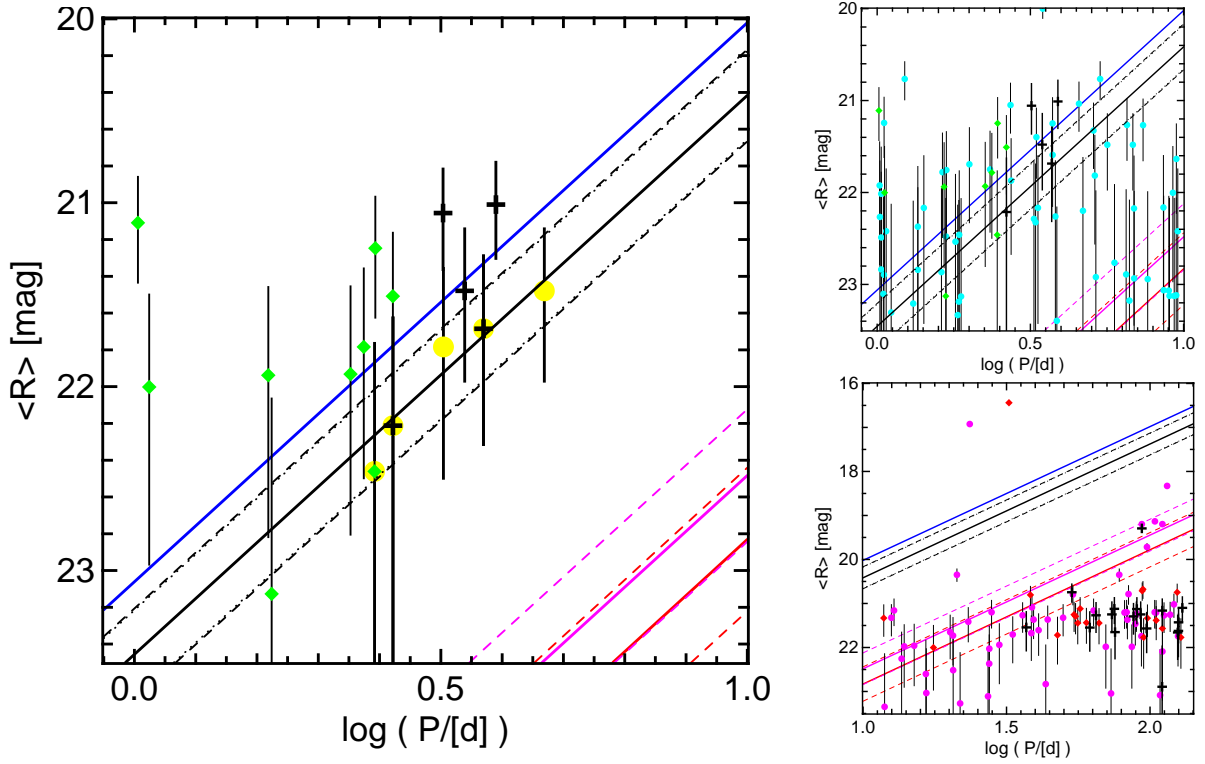
Figure 5.12: Solid black line: *R*-band period-luminosity relation for fundamental mode LMC Cepheids, Eqn. (1.3) [Madore and Freedman, 1991] corrected for galactic extinction [Schlegel et al., 1998, $A_R = 0.176$]. The PLR shown is best-fitting the observed Pegasus Dwarf δ Cephei stars average magnitudes $< R_f >$ and periods of PM01 (FO), PM02, PM04, PM08 (FO), and PM11 (Tab. 5.5). The fit yields a distance modulus of $m - M = 24.72 \pm 0.24$ mag. See text on selection of the candidates contributing to the fit. Dotted black lines show the propagated error of the fit while dashed black lines indicate the error of the PL relation which happen to be almost identical. Solid blue line: First Overtone relation according to Eqn. (1.5). Red and purple lines denote Type II PLRs and their errors (Sect. 1.5.4, Eqn. (1.4) and (1.5)). Black crosses: Highly significant ($p < 0.0001$) VS candidates; green diamonds: Less significant ($0.01 > p > 0.0001$) shorter period ($P < 10$ d) VS candidates; clear yellow circles: Fundamental periods of presumably First Overtone δ Cephei candidates contributing to the PLR distance; underlying yellow circles (two under crosses, one under diamond): Fundamental mode δ Cephei candidates contributing to the PLR distance; turquoise circles: Low significant ($0.25 > p > 0.01$) shorter period ($P < 10$ d) VS candidates; red diamonds: Less significant ($0.01 > p > 0.0001$) longer period ($P > 10$ d) VS candidates; purple circles: Low significant ($0.25 > p > 0.01$) longer period ($P > 10$ d) VS candidates.

result can still be greatly improved by a better resolved and deeper reference image which would provide higher photometric precision. Fig. 5.12 shows PL diagrams of the VS candidates in the light of the newly derived PLR distance.
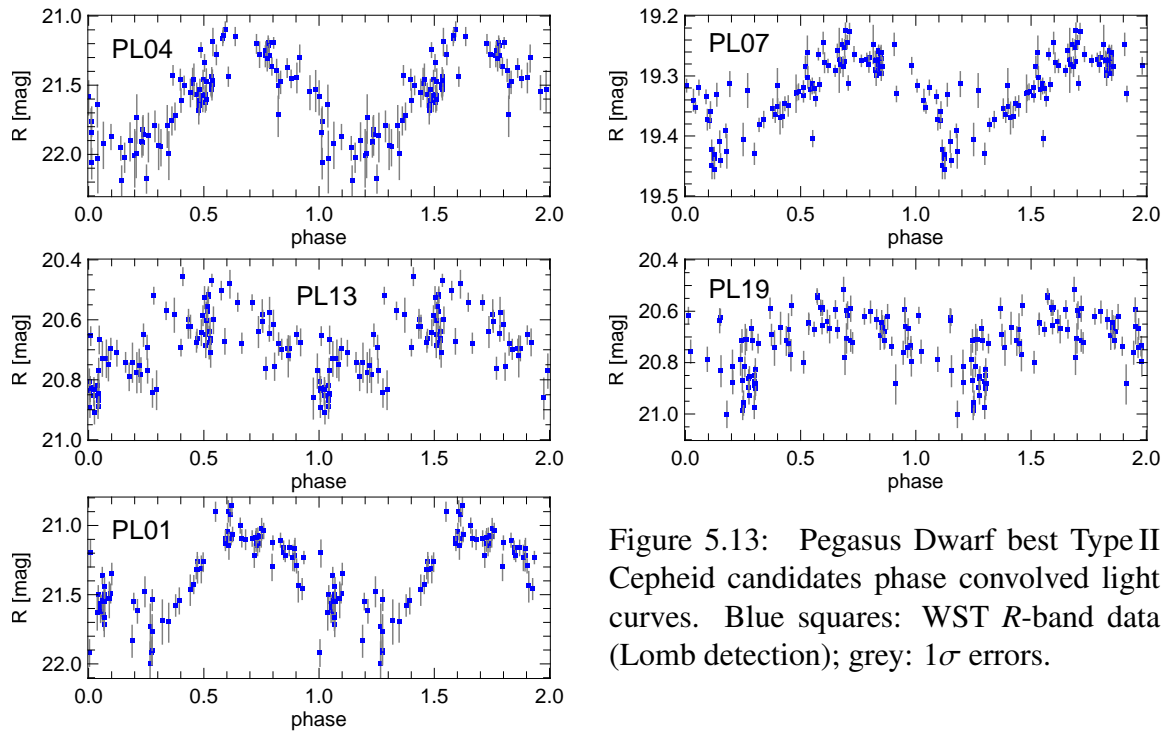
Figure 5.13: Pegasus Dwarf best Type II Cepheid candidates phase convolved light curves. Blue squares: WST *R*-band data (Lomb detection); grey: 1σ errors.

Since the cross-correlation of the wrongly classified variable candidates of Hoessel et al. [1994] for Leo A did not provide any further insight than one has to have sufficient sampling for period assessment and classification I did not repeat this painful exercise for the Hoessel et al. [1990] Pegasus VS candidates which also resulted in a wrong distance determination. However, Aparicio [1994] not only disproves the Hoessel et al. Cepheids but also lists what he presumes to be valid Cepheid candidates from colour and observed variability between two nights but unfortunately fails to give coordinates for them; he also does not provide a proper finding chart but only a diagram displaying positions and brightness of his sample of 1270 stars in Peg DIG. Nevertheless, by comparing this diagram with the Fig. 5.14 finding chart one can surmise that PM02, PM03, PM04, PM05, and PM09 are identical with five of his six δ Cephei candidates. Again, it is most unfortunate that the diagram does not explicitly identify those candidates in the according photometry table, but, since his brightest candidate has $R = 21.36$, which also sets the limit for PM03, and the Aparicio [1994] data had below 0.6″ seeing, the assumption that PM03 is indeed brightened by a "blue blend" is strengthened[36]. For similar reasons one might argue that the photometry of PM09 is hampered by a "red blend".

---

[36]Unless, off course, the according observations exactly met the minimum of the light curve.

Table 5.6: Parameters of Pegasus long δ Cephei $10\,\mathrm{d} \leq P \leq 130\,\mathrm{d}$ period candidates: Short identifier (see Fig. 5.14), IAU compliant identifier, position, most significant Lomb period(s), significance (p-level), flux averaged apparent R-band magnitude, r.m.s. error of R-band magnitude.

Id	IAU compliant name	RA-2000 [h]	Dec-2000 [deg]	period [d]	signific. [p]	$\langle R_f \rangle$ [mag]
PL01	WST J232839.5+144246	23:28:39.462	+14:42:46.13	125.682	1.41e-10	21.43±0.38
PL02	WST J232847.4+144123	23:28:47.382	+14:41:23.19	124.834	6.68e-10	21.66±0.47
PL03	WST J232843.5+144460	23:28:43.549	+14:44:59.53	129.599	1.02e-09	21.10±0.28
PL04	WST J232846.9+144359	23:28:46.896	+14:43:59.17	37.047	1.39e-09	21.54±0.42
PL05	WST J232839.4+144246	23:28:39.429	+14:42:46.13	125.569	1.96e-09	21.62±0.45
PL06	WST J232835.7+144349	23:28:35.742	+14:43:49.43	61.661	5.90e-09	21.55±0.42
PL07	WST J232835.8+144414	23:28:35.847	+14:44:14.44	93.647	5.45e-08	19.29±0.05
PL08	WST J232831.8+144518	23:28:31.754	+14:45:18.22	75.511	7.06e-08	21.65±0.46
PL09	WST J232829.0+144604	23:28:28.980	+14:46:03.85	75.103	7.70e-08	21.12±0.28
PL10	WST J232840.5+144131	23:28:40.537	+14:41:31.08	73.626	2.35e-07	21.25±0.32
PL10*a*				92.760	4.15e-06	
PL11	WST J232835.2+144412	23:28:35.169	+14:44:12.48	110.315	6.33e-07	21.16±0.30
PL12	WST J232836.0+144315	23:28:36.009	+14:43:15.09	89.960	2.13e-06	21.13±0.29
PL13	WST J232830.6+144428	23:28:30.561	+14:44:27.70	53.394	2.79e-06	20.75±0.20
PL14	WST J232840.5+144415	23:28:40.492	+14:44:14.91	97.308	7.70e-06	21.57±0.43
PL15	WST J232835.2+144413	23:28:35.203	+14:44:13.46	110.215	5.08e-05	22.89±1.45
PL16	WST J232835.0+144502	23:28:35.040	+14:45:02.02	87.557	6.73e-05	21.29±0.33
PL17	WST J232837.5+144227	23:28:37.494	+14:42:26.52	64.829	8.77e-05	21.27±0.33
PL18	WST J232842.2+144531	23:28:42.231	+14:45:31.42	110.415	2.66e-04	21.57±0.43
PL19	WST J232838.1+144126	23:28:38.096	+14:41:26.19	38.304	2.76e-04	20.81±0.21
PL20	WST J232831.4+144349	23:28:31.404	+14:43:49.44	60.014	3.57e-04	21.44±0.38
PL21	WST J232824.8+144632	23:28:24.779	+14:46:31.81	124.328	4.32e-04	20.75±0.20
PL22	WST J232842.4+144151	23:28:42.370	+14:41:51.18	105.067	6.10e-04	21.38±0.36
PL23	WST J232834.7+144416	23:28:34.695	+14:44:16.41	97.925	6.57e-04	21.33±0.35
PL24	WST J232837.1+144359	23:28:37.100	+14:43:58.74	93.900	6.62e-04	20.71±0.20
PL25	WST J232837.8+144503	23:28:37.752	+14:45:03.48	66.398	7.39e-04	21.45±0.38
PL25*a*				55.980	2.73e-03	
PL26	WST J232832.3+144615	23:28:32.338	+14:46:15.12	94.966	8.13e-04	21.77±0.52
PL26*a*				128.090	1.28e-03	
PL27	WST J232833.0+144422	23:28:33.035	+14:44:22.30	55.008	1.33e-03	21.29±0.33
PL28	WST J232839.2+144406	23:28:39.236	+14:44:05.60	47.590	2.57e-03	21.72±0.49
PL29	WST J232830.9+144556	23:28:30.911	+14:45:55.99	54.367	2.67e-03	21.25±0.32
PL30	WST J232836.9+144244	23:28:36.920	+14:42:44.18	11.807	6.18e-03	21.33±0.34
PL31	WST J232832.4+144526	23:28:32.365	+14:45:26.07	57.082	6.84e-03	21.12±0.28
PM14*a*	WST J232819.8+144546	23:28:19.824	+14:45:45.71	17.590	7.87e-03	22.00±0.64
PL32	WST J232821.3+144429	23:28:21.273	+14:44:29.19	32.239	9.66e-03	16.44±0.00
PL33	WST J232835.0+144401	23:28:35.032	+14:44:00.71	94.453	9.78e-03	20.68±0.19

Longer period "Cepheid" candidates

Most of the longer period Type II Cepheid candidates of Tab. 5.6 can be classified as "red" LPVs or Mirae[21] stars; PL01 is an typical example of those. However, it is intriguing that the brightness of the bulk of those objects coincides with the TRGB since Mirae stars are thought to be Post-AGB objects. Also, the completeness tests for Peg DIG (Fig. D.1) show that our data is sensitive to lower limits than indicated by the "cloud" of the LPVs in Fig. 5.9 or the peak of the histogram in Snigula [2006], Fig. 4.8. The average amplitude of those LPVs is also smaller (< 1 mag) than one would expect for bona fide Mirae stars[37]. The shape of their light curves is often enough noisy but would still be compatible with RV Tauri or W Virginis. This group does not correlate with a Type II PLR (Eqn. 1.4) but instead intersects it at about 30 d for our $m - M = 24.72 \pm 0.24$ mag distance modulus. The four bluest VS (Fig. 5.9, left most red circles) of Tab. 5.6 coincide with the instability strip indicated by the shorter period (Fig. 5.9, left most green circles) δ Cepheid candidates. Of those three, PL04, PL13, and PL19 are also perfectly consistent with the "redder", Eqn. (1.4) Type II PLR (Fig. 5.12, red line) at our distance. PM14a is also perfectly aligned with the relation but already too faint to give either colours or a clear light curve shape. PL07 (topmost cross in Fig. 5.12, right bottom) partly resembles LL01: It is consistent with the "bluer", Eqn. (1.4) Type II PLR (Fig. 5.12, purple line) and also has a RV Tauri compatible light curve but with a low amplitude. However, its colour would more point towards its classification as a Mira star. But remember, this can very well be due to the caveat for colours raised in the very first paragraph of Sect. 5.2.1 and which is even more true for long periods.

While our data does not provide evidence beyond doubt it indicates that either known variable stars classes have peculiar features in extremely metal poor environments or those environments actually provide us with different types of variable stars.

---

[37]And still small if all were of the smaller than Mira amplitude SRa type which is their clossesest matching classification.
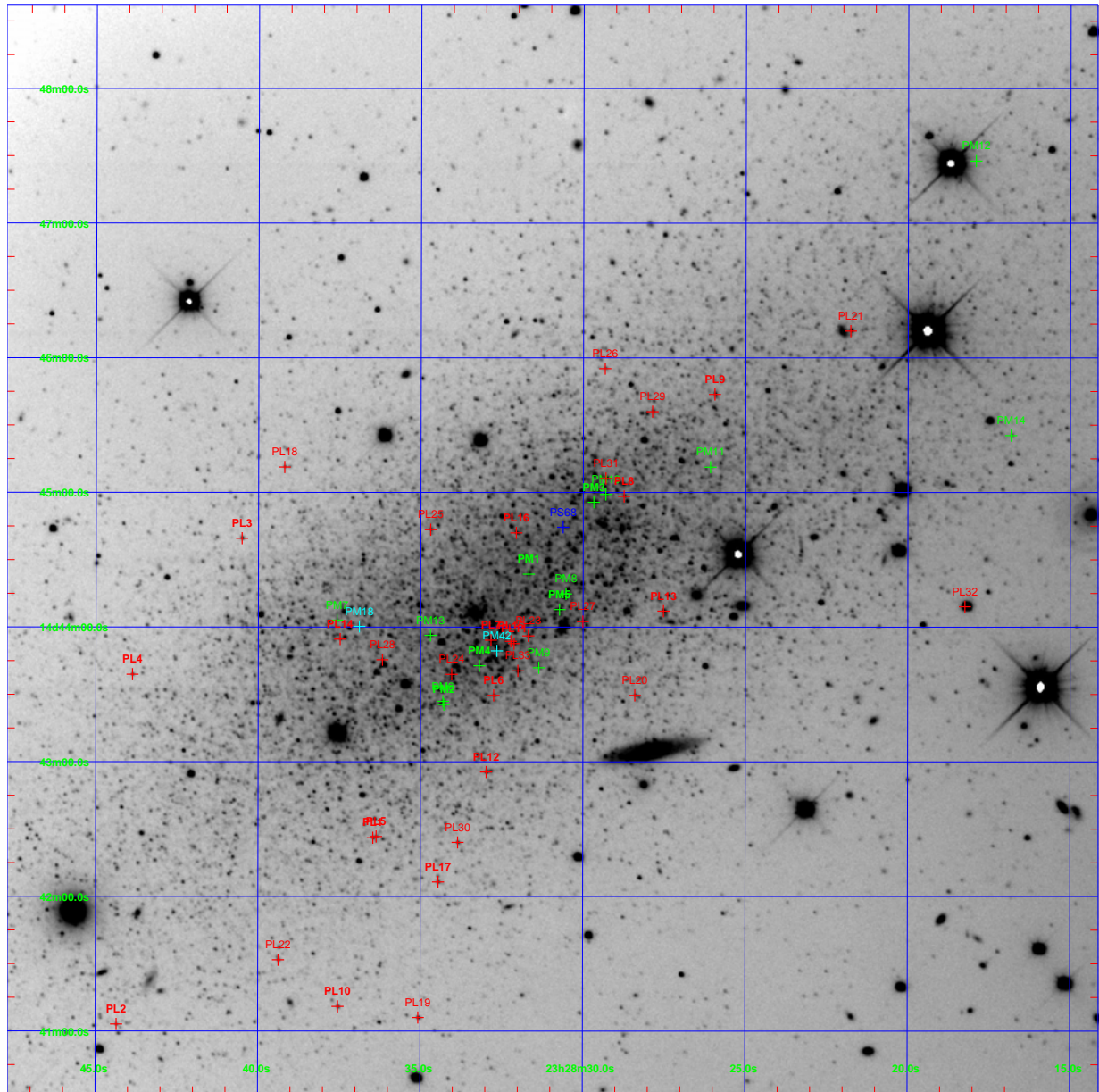
Figure 5.14: Finding chart of selected VS candidates, mostly of Tab. 5.5 and 5.6 but partly also from Tab. F.1. Blue and turquoise: LS and LM short period pulsating B-star candidates; green: LM most promising δ Cephei candidates; red: LL long period Type II Cepheid candidates.

5.2.3   EGB 0427+63 – A Miss

The story on this (most probably not Local Group) Dwarf remains short: It turned out to be beyond the reach of our little telescope, at least for all kinds of Cepheids. Mateo [1998] still lists it with $m - M = 25.6$ which seemed already a hard task to prove by variable stars with
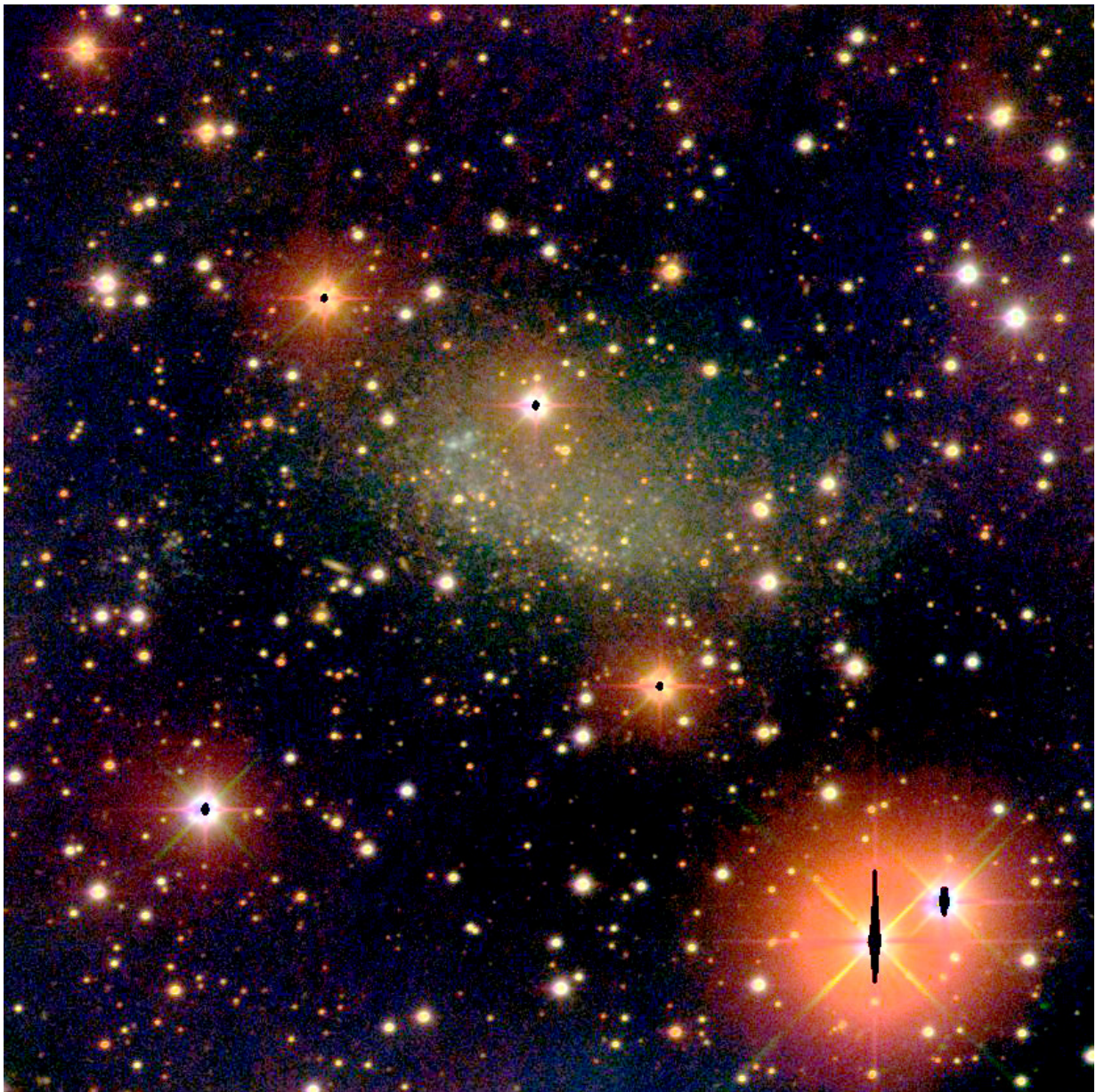
Figure 5.15: Colour composite image of EGB 0427+63: Red channel = CA *I*-band reference image, green channel = WST + CA *R*-band reference images, blue channel = CA *B*-band reference image; exponential scaling.

our equipment, especially when combined with its high galactic extinction [Schlegel et al., 1998, $A_R = 2.118$]. But as it easily showed up with 30 min exposures during test observations and as there was no dwarf competing at its RA (Tab. 2.1) we started observations. Fig. 5.16 shows a finding chart and CMD of this dwarf and the VS candidates (Tab. F.6 and F.7) we found in the vicinity; all stars brighter than ~ 19.5 mag are most likely galactic foreground objects and not at all associated with the dwarf[38]. Also shown is a PL diagram with a extinction corrected Madore and Freedman [1991] R-band PLR at a Karachentsev et al. [2006] distance ($m - M = 27.39 \pm 0.18$ mag). The latter clearly shows that there is nothing to win here for us concerning

---

[38]EGB 0427 has only a galactic latitude of +10.5 deg.
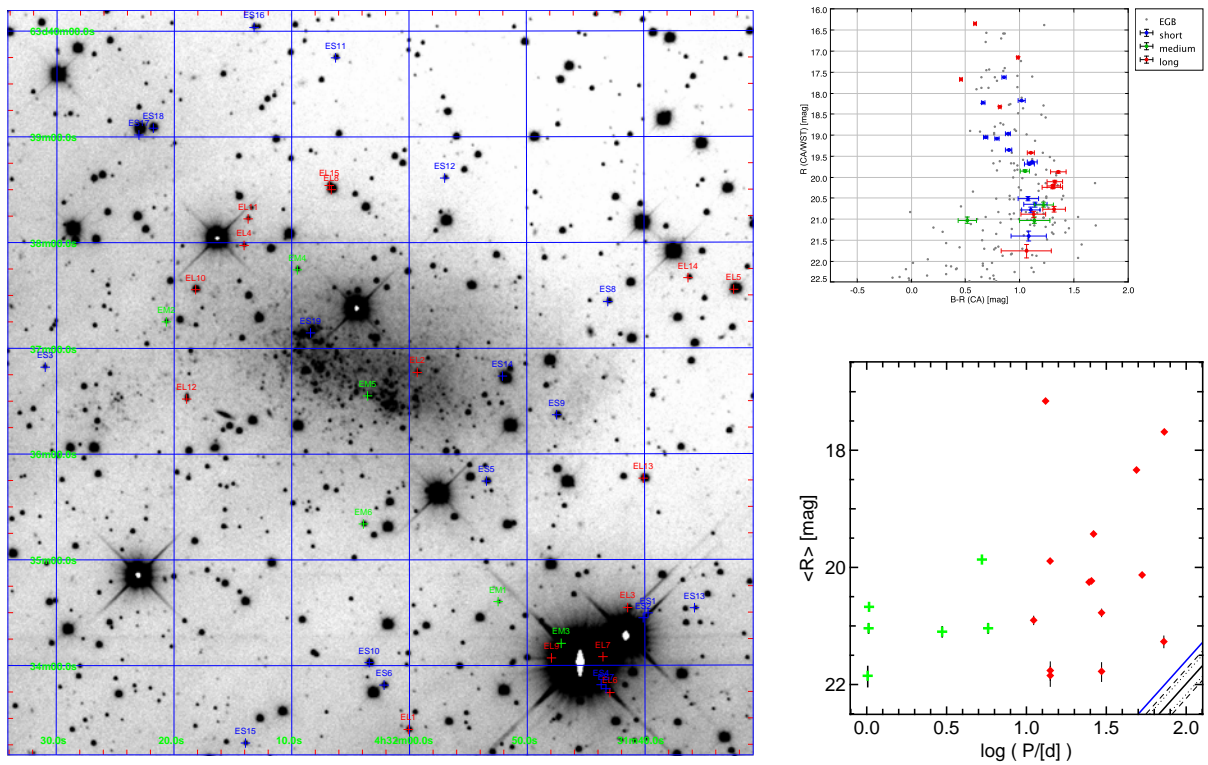
Figure 5.16: EGB 0427+63 finding chart, CM and PL diagrams. Blue markers: short period ($P < 1$ d) VS candidates; green markers: intermediate period (1 d$< P < 10$ d) VS candidates; red markers: long period ($P > 10$ d) VS candidates. CMD grey: CA R-band (uncorrected) vs. CA $B - R$ colour (extinction correction after Schlegel et al., 1998, $A_R = 2.118$, $A_B = 3.419$); CMD other colours: WST R-band (uncorrected) and propagated errors vs. CA $B - R$ colour (extinction correction after Schlegel et al., 1998) and DAOPHOT errors. PL diagram solid black line: R-band period-luminosity relation for fundamental mode LMC Cepheids, Eqn. (1.3) [Madore and Freedman, 1991] corrected for galactic extinction [Schlegel et al., 1998, $A_R = 2.118$] and shifted to the Karachentsev et al. [2006] TRGB distance ($m - M = 27.39 \pm 0.18$ mag); PL diagram dotted black lines: TRGB distance error; PL diagram dashed black lines: PLR error; PL diagram solid blue line: First Overtone relation after Eqn. (1.5).

Cepheids. Nevertheless, EM05 might be a candidate for a variable B-star (leftmost green circle in the CMD), and even more all the LPVs with $R \approx 20$ mag and fainter, $B - R$ colours redder than 1.0, and associated with the dwarf are valid candidates for AGB variable stars (EL02, EL04, EL11, EL12, EL15, and maybe still EL14; Tab. F.7). However, to reasonably apply the same techniques that worked for Leo A and the Pegasus Dwarf with an 80 cm telescope one would require 8 m class telescope observations.

Figure 5.17: Colour composite image of GR 8 (looks as the name says): Red channel = CA *I*-band reference image, green channel = WST + CA *R*-band reference images, blue channel = CA *B*-band reference image; exponential scaling.

5.2.4 GR 8 – Surprise

Fortunately for us GR 8 turned out to be somewhat nearer than EGB 0427+63 and, of course, suffers much less from galactic foreground extinction because of its much higher galactic latitude. Our CMD (Fig. 5.18, left) of this compact looking dwarf indicates very previous star formation, the brightest end of a blue main sequence ("blue plume") is discernible though sparsely populated; the RGB and its tip are still clearly visible. Comparing the R-band TRGB of Leo A (Fig. 5.2 $\sim$ 21.0) with that of GR 8 ($\sim$ 23.0) one would assume a 2 mag greater distance for the latter which perfectly matches the results of our δ Cephei PLR distances (see Sect. 5.2.1 and below). I was able to recover the δ Cephei star previously discovered by Tolstoy et al. [1995, $m_{<r>}$ = 22.12 and P = 16.166 d]. GL01 actually is by far the most significant variable source in the GR 8 field (Tab. 5.7, Fig. 5.19, and Fig. 5.20). GL02 turns out to be a blend of GL01[39]; since it does not match with a blue resolved source it gets the colour of GL01 assigned as this is the closest positional match and still within the matching boundaries[40]. From our measurements I derive a distance modulus of

$$\text{GR 8 } m - M = 26.45 \pm 0.07 \pm 0.06_{\text{ZP}}(\pm 0.25_{\text{PLR}}) \text{ mag.} \tag{5.3}$$

The Tolstoy et al. [1995] "longer" period and fainter brightness explain their larger derived distance modulus ($m - M$ = 26.75 $\pm$ 0.35). GL03, while in agreement with Type II Cepheid PLRs, is actually too red for that kind of VS and falls into the Mira regime in terms of colours. GL05 also coincides with a Type II Cepheid PLR but now is too blue and most probably just caused by a "lunation" window function as GL04 and GL06 suggest. Both are also plotted in the PL diagram (Fig. 5.18) but not associated with GR 8 and lie outside the Fig. 5.20 field of view.

---

[39]Red circle right below the green circle and the black cross in Fig. 5.18, CMD and PL diagram respectively.
[40]The distance is less than 2″.

Table 5.7: Parameters of GR 8 δ Cephei 1 d< P ≤ 130 d period candidates: Short identifier (see Fig. 5.20), IAU compliant identifier, position, most significant Lomb period(s), significance (p-level), flux averaged apparent R-band magnitude, r.m.s. error of R-band magnitude.

Id	IAU compliant name	RA-2000 [h]	Dec-2000 [deg]	period [d]	signific. [p]	$\langle R_f \rangle$ [mag]
GL01	WST J125841.4+141310	12:58:41.407	+14:13:09.63	15.436	8.05e-07	21.47±0.07
GS01a	WST J125841.4+141317	12:58:41.442	+14:13:16.99	56.930	9.26e-03	18.79±0.01
GL02	WST J125841.3+141310	12:58:41.340	+14:13:10.12	15.436	4.28e-02	21.89±0.11
GL03	WST J125835.0+141253	12:58:34.956	+14:12:53.08	56.061	5.40e-02	21.86±0.10
GL04	WST J125839.9+141543	12:58:39.941	+14:15:42.78	29.470	1.25e-01	23.03±0.31
GL05	WST J125838.4+141308	12:58:38.368	+14:13:08.22	29.430	1.86e-01	22.86±0.26
GL06	WST J125854.5+141203	12:58:54.533	+14:12:02.56	29.497	2.17e-01	22.94±0.28

GS04, the bluest VS in the CMD (Fig. 5.18) is a viable β Cephei candidate which, if it could be confirmed, again, would raise the question of either the host's metallicity, the instability region for B-stars or maybe even the main sequence evolution of metal poor B-stars.

GS01*a* comes uncalled for and as a big surprise: Its colour, brightness and light curve denotes it as an α Cygni type variable star, i.e. "*[. . .] quasi-periodic A type supergiants having amplitudes of about 0.1 magnitudes and periods of days to weeks [. . .]*" [Becker, 1998]. Because of their short life time A-giants are already very rare in dwarf galaxies, even in dIrrs. One would expect to more or less "always miss" evolved A-stars in *VarStarDwarves* like galaxies. The finding of such an intrinsically very bright star in a extremely metal poor environment as GR 8 in our "extended neighbourhood" allows to take a closer look on a type of star which contributes most to the light of high redshift star forming galaxies. It also may show if and how the huge stellar wind of this metal poor variant of such a star can affect interstellar feed back and metal enrichment of its environment.
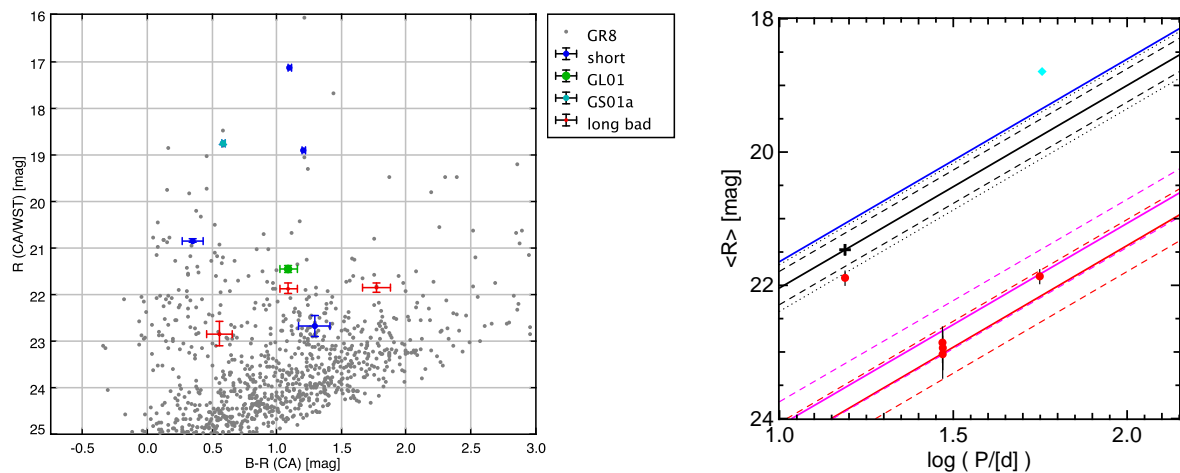
Figure 5.18: GR 8 CM and PL diagrams. Blue: short period $P < 1$ d VS candidates; turquoise: GS01*a* LBV candidate; green: GL01 most promising δ Cephei candidate; red: worse ($p > 0.01$) long period Cepheid candidates. CMD grey: CA R-band (uncorrected) vs. CA $B - R$ colour (extinction correction after Schlegel et al., 1998, $A_R = 0.070$, $A_B = 0.113$); CMD other colours: WST R-band (uncorrected) and propagated errors vs. CA $B - R$ colour (extinction correction after Schlegel et al., 1998) and DAOPHOT errors. PL diagram solid black line: R-band period-luminosity relation for fundamental mode LMC Cepheids, Eqn. (1.3) [Madore and Freedman, 1991] corrected for galactic extinction [Schlegel et al., 1998, $A_R = 0.070$] and shifted to match our GL01 photometry and period assessment ($m - M = 26.45 \pm 0.07 \pm 0.06_{ZP}(\pm 0.25_{PLR})$ mag); PL diagram dotted black lines: TRGB distance error; PL diagram dashed black lines: PLR error; PL diagram solid blue line: First Overtone relation after Eqn. (1.5). PL red and purple lines denote Type II PLRs and their errors (Sect. 1.5.4, Eqn. (1.4) and (1.5)).
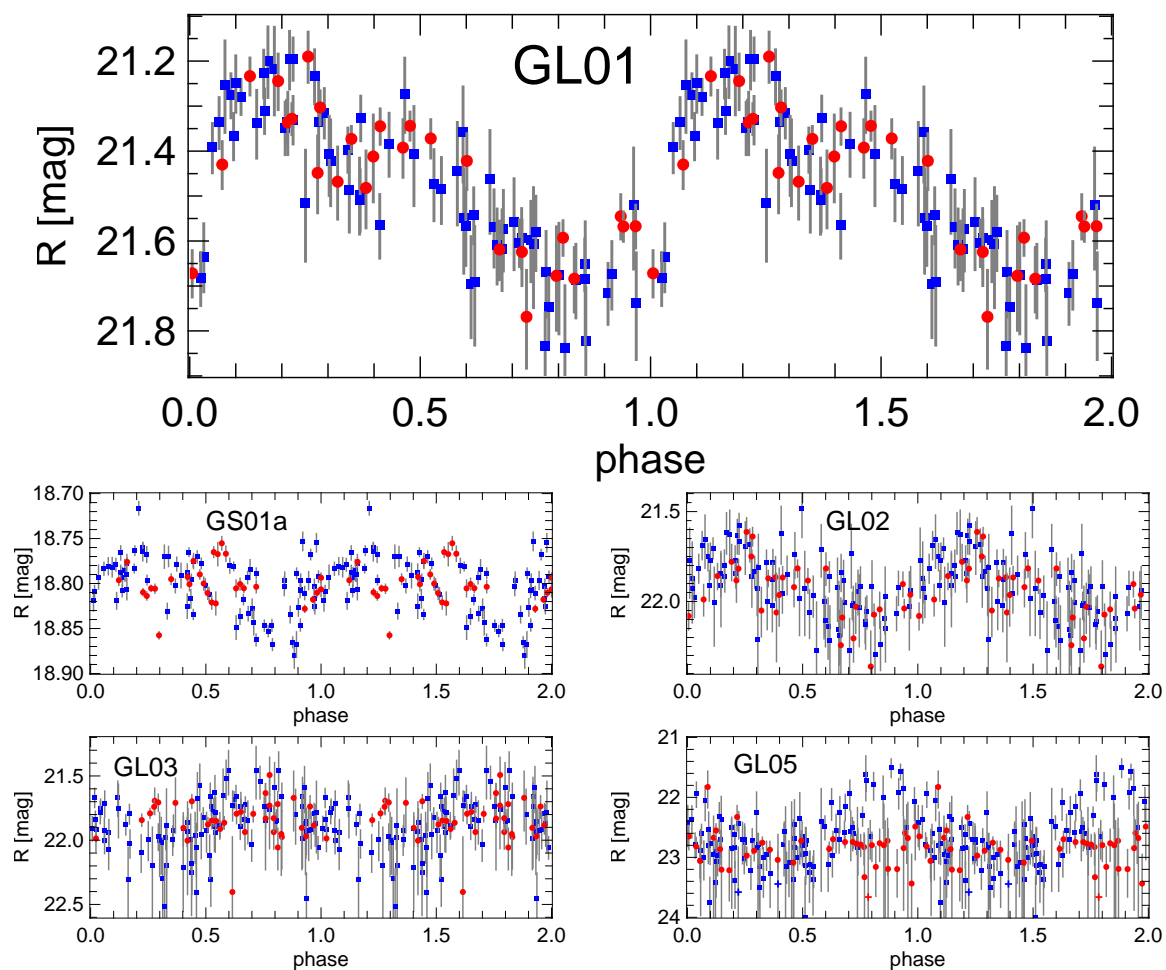
Figure 5.19: GR 8 best VS candidates phase convolved light curves. Blue squares: WST data (Lomb detection); red circles: CA data (consistency check); coloured crosses: Data consistent with detection limit at epoch, i.e. $S/N < 1$ at either site; grey: 1σ errors.
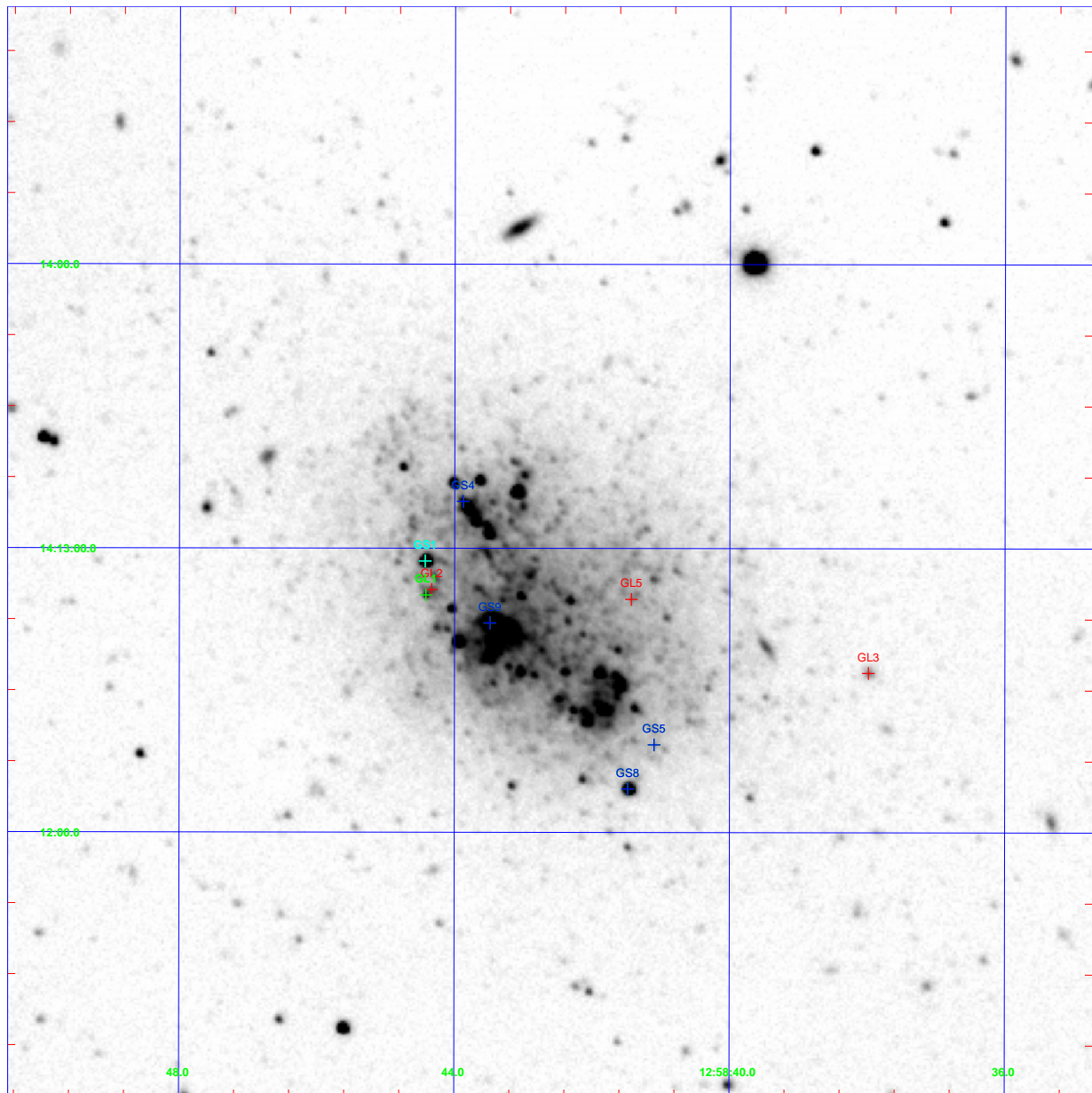
Figure 5.20: Finding chart of selected GR 8 VS candidates (Tab. 5.7 and F.8). Blue: short period $P < 1\,\mathrm{d}$ VS candidates; turquoise: GS01a LBV candidate; green: GL01 most promising δ Cephei candidate; red: worse ($p > 0.01$) long period Cepheid candidates.

Figure 5.21: Colour composite image of the Aquarius Dwarf: Red channel = CA *I*-band refer-
ence image, green channel = WST + CA *R*-band reference images, blue channel = CA *B*-band
reference image; exponential scaling.

5.2.5   Aquarius Dwarf – Mystery still

We do not have any deep enough reference frames[41] besides the *R*-band to build colours and test if there are any candidates for pulsating B-stars among "the usual suspects" in the short period candidates (AS01, AS02, AS12, and AS14 in Tab. F.9 and Fig. 5.22, top). AM02 is consistent with a Madore and Freedman [1991] PLR shifted to the McConnachie et al. [2006] distance ($m - M = 25.15 \pm 0.08$ mag, Fig. 5.22, bottom right). The secondary power peak of AS06*a* gives a solution which may still be consistent with the according First Overtone relation, and AS06 is probably still associated with the dwarf (Fig. 5.22). (AM01 and AS03 are associated with background galaxies and may actually be due to window functions "excited" by AGNs[42].)

Nevertheless, the overall data is inconclusive and suggests a different observing strategy for this galaxy: About six "half" nights randomly spread over two weeks with a 2 m class telescope at a more southern observatory should be sufficient to detect (or confirm) shorter period δ Cephei candidates. The complete absence of any bright longer period stars [Snigula, 2006, Sect. 6.5], however, remains puzzling and either indicates a longer distance or a very strange star formation history[43].

---

[41]Because of the objects low declination and its best visibility during the short summer nights good enough observing conditions were too rare to go for an additional waveband at WST. We also have only very little CA observations. (See also Tab. 2.3.)

[42]Active galactic nuclei.

[43]I.e. a combination of an ancient population which does not produce any bright AGB stars any more and a very young population which still would not produce a sufficiently high amount of AGB stars.

Table 5.8: Parameters of Aquarius δ Cephei 1 d$< P \leq 130$ d period candidates: Short identifier (see Fig. 5.22), IAU compliant identifier, position, most significant Lomb period(s), significance (*p*-level), flux averaged apparent *R*-band magnitude, r.m.s. error of *R*-band magnitude.

Id	IAU compliant name	RA-2000	Dec-2000	period	signific.	$\langle R_f \rangle$
		[h]	[deg]	[d]	[*p*]	[mag]
AM01	WST J204646.4-125219	20:46:46.367	-12:52:18.60	1.033	1.38e-01	18.89±0.02
AS06*a*	WST J204701.4-125041	20:47:01.448	-12:50:40.82	2.030	1.52e-01	22.06±0.38
AM02	WST J204645.3-125036	20:46:45.309	-12:50:35.99	7.408	1.85e-01	21.48±0.22
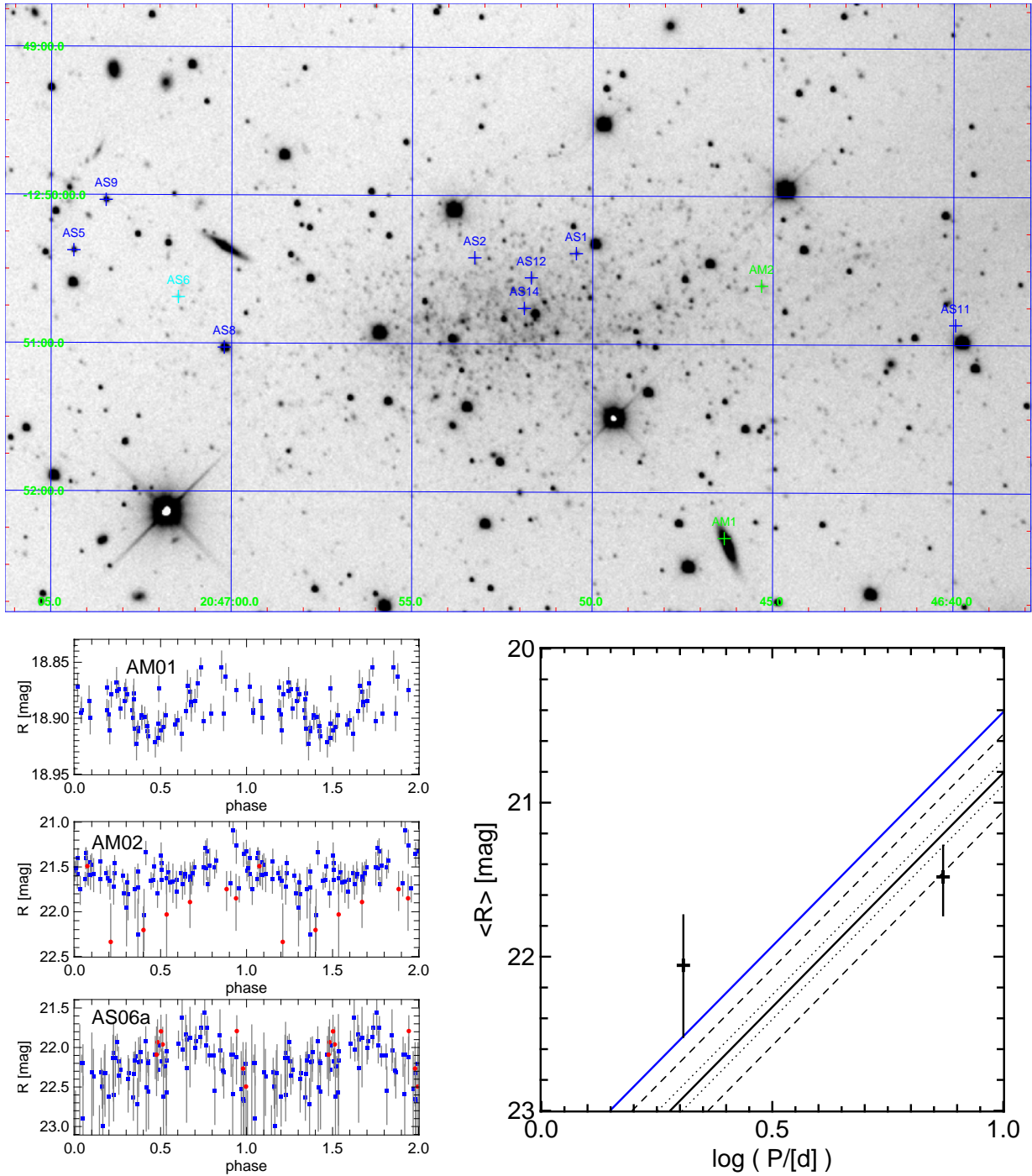
Figure 5.22:   Aquarius Dwarf finding chart, light curves, and PL diagram. Top – Finding chart of VS candidates (Tab. 5.8 and F.9); remaining candidates are outside the FoV of the chart and probably not associated with the dwarf. Bottom left – period $P > 1$ d VS candidates light curves. Bottom right – PL diagram: Solid black line – R-band period-luminosity relation for fundamental mode LMC Cepheids, Eqn. (1.3) [Madore and Freedman, 1991] corrected for galactic extinction [Schlegel et al., 1998, $A_R = 0.137$] and shifted to the McConnachie et al. [2006] TRGB distance ($m - M = 25.15 \pm 0.08$ mag); dotted black lines – TRGB distance error; dashed black lines – PLR error; solid blue line – First Overtone relation after Eqn. (1.5); black crosses – AM02 and AS06a.

5.3 Summary

5.3.1 Status quo

The results regarding "bright, blue" Variable Stars from monitoring of the *VarStarDwarves* DGs for six years can be broken down into the following:

"Firm" results: The finding of four and five unambiguous classical δ Cephei variable stars in Leo A and the Pegasus Dwarf respectively allowed for the first time to establish accurate PLR distances to them (Eqn. (5.1) and (5.2)); they confirm recent TRGB distances by means of a completely independent method. At least another six VS candidates for each dwarf could enhance the δ Cephei samples but would require dedicated deeper, higher resolved, or multi-colour observations. Such observations would also enhance the error margin of the already confirmed samples as they would increase their signal-to-noise ratio and improve the deblending of the highly crowded fields. In GR 8 I was able to recover a previously found δ Cephei star and to derive from it a distance modulus consistent with recent publications (Eqn. (5.3)). The finding of an α Cygni VS in a local dwarf with its very metal poor environment is against all odds and may prove to be of value for astrophysicists, working on hot stars in general, and LBVs in particular, as it is accessible to spectroscopy with very large telescopes, though challenging.

Some speculation: Concerning possible RV Tauri stars in the Pegasus Dwarf, they resemble the Alcock et al. [1998] findings for the LMC RV Tauri which already has much lower than galactic metallicity: The PLR seems to steepen for longer periods and the stars' amplitudes are small compared to galactic, higher metallicity RV Tauri. Looking at the even more metal poor Leo A dwarf this trend seems to progress: Its longest period RV Tauri is even more brighter than expected from a Alcock et al. [1998] PLR and its amplitude significantly smaller. This can be interpreted as follows: For the same period of a RV Tauri, as metallicity decreases also does its amplitude at the same time increasing its R-band brightness. This may very well be explained by just less metals and molecules in the envelope or outer atmosphere of the star or even simply less "dust" in the surrounding, already shed stellar envelope as we look at stars at the very end of their nuclear burning phase.

The finding of bona fide pulsating B-stars candidates in Leo A and Pegasus Dwarf (and possible candidates in GR 8 and EGB 0427+63) is puzzling and would, if they can be confirmed, have some repercussions on theory with three possible scenarios:

1. The main sequence evolution of very metal poor stars after a "zone of avoidance" at about LMC metallicity, again, enters the B-stars instability region.

2. The pulsation theory on B-stars and its derived instability strip is wrong for extremely low metallicity.

3. Unexpectedly and despite their shallow gravity well, isolated DGs, in contrast to DG satellites of bigger galaxies (like the Magellanic Clouds encircling the Milkyway Galaxy), can

retain some of their metals from previous star formation, at least in some regions of recent star formation.

However, the candidates may also turn out to be Eclipsing Binaries which then might allow to derive their system parameters as outlined in Sect. 1.5.5 and, in principle, could provide an independent means of distance determination. Such an eclipsing nature could be tested by looking for strictly periodic radial velocity variations.

5.3.2 Future Prospects

Of course, the questions raised in the previous paragraph "cry" for spectroscopic follow up observations which we have started by looking at the brightest RV Tauri and the brightest β Cephei candidate in Leo A with the 10 m HET telescope and its low-resolution spectrograph to get some hints on both their metallicity. All other candidates will be even more challenging but will be looked at if the brightest ones indicate interesting results.

We plan to share our finding of the α Cygni in GR 8 with specialists working in the field, at the same time looking for other, non-periodic LBVs in our sample which would not have turned up by Lomb periodigrams but will still be visible in the variations mask selected samples. Of course we will at the same time look for other non-periodic or eruptive events.

There is also still existing data waiting to be analysed: We have not touched yet the 2006 and 2007 epochs due to limited resources, and the LGS 3 data right now slowly reach a suitable number of epochs to begin with evaluation for periods. As the quality of our observations (most importantly the images PSF FWHM) still improved over the last two years, higher resolving reference images can be constructed which will most certainly enhance the results of both, the difference photometry of individual epochs and the DAOPHOT deconvolution photometry of the reference.

Furthermore, we are thinking of trying a different approach which so far was not possible due to limited computational and storage resources. If we would build phase binned stacks for the whole range of possible periods before difference imaging we could avoid Lomb periodigrams at all as only sources with periods close to the test period would show up in the variations mask. The former window functions would identify themselves as a largely inhomogeneous sample of phase stacks per period test. This approach would also allow us to attack very short periods in the order of less than half an hour as we can take advantage of the short individual exposures of three minutes.

Due to the long and repeating monitoring we are also on the edge of being able to resolve secular trends of the observed periods. This is of great interest as it would allow an estimate of the "speed of evolution" as stars move through the instability strip, e.g. for metal poor blue loop stars. Also, if the period of RV Tauri stars would always change in the same direction this would finally settle the issue if they really are post-AGB objects.

To conclude, local dwarf galaxies like the *VarStarDwarves* ones and especially their VS content, despite being rather faint objects, still have a "bright" future for observations[44].

---

[44] ... and if they were not all rounded up by some evil "Major Merger" they lived on happily ever after...

Appendix A

Guiding Camera Server

A.1 Commands for the ST7 Guiding Server

All commands are case-insensitive (READ == read == ReAd == . . .) except for **x** and **xx**.

openwindow hostname:displaynumber.screennumber (i.e. deepthought:0.0) Opens server side graphicwindow on hostname. The server must run with tty connected to it. The client must have set "xhost +st7host" (whatever this may be). **This may be a severe security hole, just use with caution.**

closewindow shuts down server side display window

get *item* where *item* can be one of the following

binning	status of binning
ccd	status of imaging and tracking ccd
dither	show selected dither grid spacing
exptime	show selected exposure time [s]
fan	fan status [on/off]
guideangle	show rotation angle of guiding field
guiderate	show guide rate ["/s]
led	led status [on, off, fast blink, slow blink]
relay	show status [on/off] of all 4 relays
save	show server side save file status
shutter	shutter status
temp	show temperature settings

set *item value* where *item* is one of the following

binning #	binning factor: 1, 2 v 3 for imaging ccd
ccd ???	set active ccd, ??? = IMAGING v TRACKING
dither ###.##	set dither grid spacing in arcsec
exptime #####.##	set exposure time in seconds
fan ???	off, on
guideangle ###.##	set rotation angle of guiding field
guiderate ###.##	set guiding rate
led ???	off, slow, fast, on
relay ?? ###.##	turn on relay ?? [X+, X-, Y+, Y-] for ###.## s
save ??	on/off, set server side save file status
shutter ???	open, close, init
temp ???	set temperature control [value in deg C, on, auto, off]

expose start an exposure (darks are automatically determined and subtracted)

autoexpose start an infinite series of exposures, abort with **abort**

check_star [x, y] check star at coordinates x, y and show the results; if no x, y are given, star must be clicked in server side window; if no x, y are present and no server side window open, trying to use old coordinates

focus start focus series with last selected star via check_star (darks will be set on)

autoguide start guiding with last selected star via check_star; guiding will not be started unless a valid star already has been selected with check_star x y (darks will be set on)

abort abort exposure or guiding

dither move to next position on the dither grid

x close connection

xx close connection and end server (camera settings will not be altered)

Responses from server:
    Command accepted: **READY: ...** where ... say what has been done.
    Command denied: **ERROR: ...** where ... tell what specific error has been encountered.

Initialisation message (several strings): returns all hardware info of the camera

Settings messages:

BINNING: # x #	selected binning factor
CCD: [status of both ccds]	
DARK: [on or off]	status of auto dark subtraction
DITHER: ### "	selected dithering grid spacing in arcsec
EXPTIME: ###.# s	selected exposure time in sec
FAN: [on or off]	status of fan
GUIDEANGLE: ###.##	selected rotation of guide field in deg. (0=N)
GUIDERATE: ###.## "/s	selected guide rate in arcsec / sec
LED: [on, slow blink, fast blink or on]	led status
OFFSET: ### x ###	pixel offset of lower left corner
RELAYS: +X = [off or ##.##s], -X = [...], +Y = [...], -Y = [...]	
	status of relays
SAVE: [on or off] (... filename)	server side save option status
SHUTTER: [open, closed, ...]	status of shutter (not sent by exposures!)
SIZE: ### x ###	size of actual window in pixel
TEMP: regulation = [on or off], current = ##.# % of max., fan = [on or off]	
set = ###.# deg C, ccd = ###.# deg C, air = ###.# deg C	
	Temperature settings, 2 seperate strings

Image analysis messages (5 seperate strings each):

MINIMUM: ###	minimum value in image
MAXIMUM: ###	maximum value in image
MEDIAN: ###	median value in image
AVERAGE: ###.##	average value in image
STDDEV.: ###.##	stddev. in image

REFERENCE STAR: sigma of fit = ##.#
position: x = ##.##, y = ##.##
fwhm: x = ##.### (##.### "), y = ##.### (##.### ")
amplitude = ###.##, surface = ###.##
angle = ###.#   or

ACTUAL STAR: sigma of fit = ##.####
position: x = ##.## (d ##.##), y = ##.## (d ##.##)
fwhm: x = ##.### (##.###"), y = ##.### (##.###"); (##.# %)
amplitude = ###.# (###.# %), surface = ###.# (###.# %)
angle = ###.# (d ###.#)

Special messages:

EXPOSING: [dark or image]	type of exposure in progress
READOUT: [dark or image]	type of readout in progress
DOWNLOAD: ##.#%	download status
JPEG: sending image stream	
JPEG: locally saving image to [absolute_path/filename]	
CORRECTION: x = ##.###", y = ##.###"	
azimuth = ##.###", declination = ##.###"	
	movement to be applied in camera and telescope frame, 2 seperate strings

A.2   Guiding camera server configuration file syntax

Syntax of the parameters, their default values and description for the guiding camera server configuration file:

Parameter		value	description
ST7_IPPORT	=	9997	// command and status IP port number
IMAGE_IPPORT	=	9996	// IP port number for server side X11 control
DITHER_IPPORT	=	9995	// IP port number for dither trigger and setting,
	=		// i.e. to be used by main camera control
PARALLEL_PORT	=	1	// parallel interface port number; change to 2 or 3
	=		// if camera is connected not to LPT1
DARK_OK_TEMP_LIMIT	=	15	// [0.1°] temp. range within darks are treated as OK
CCD_WARM	=	80	// temperature offset in 0.1° above which the CCD
	=		// is considered warm so fan can be set off
RELAY_MIN_RESPONSE	=	0.25	// [s] minimal response time for relays
TEL_FOCUS	=	9.9	// [m] focus of telescope
TEL_AREA	=	0.596319	// [m^2] effective mirror area of telescope
FITBOX_SIZE	=	49	// [pixel] initial boxlength for Gaussian centroid fit
	=		// on stars
GUIDEBOX_SIZE	=	81	// [pixel] initial length of window used for guiding
GUIDESTAR_ZOOM	=	4	// zoom factor for display of guidstar
GUIDE_ORIENT	=	-1.0	// -1 v 1, initial orientation of field (mirrored or not)
GUIDE_ANGLE_OFFSET	=	180.0	// constant angular orientation offset
SAVE_FILENAME	=	/home/ftp/guider.jpg	// server side path for image saving

Appendix B

AMiGo Camera Server

B.1 AMiGo motor controller programs

The calls to all programs stored on the CyberPak [Cyb, 2001] motorcontrollers themselves follow below. They can be executed directly over the serial interface, via a telnet session to the IPC relay [Bec, 2006] on the preset port, or by sending a file with the commands through the camera server (App. B.2). Some complex commands, i.e. move guider field / focus to position and slit exposures, are constructed within the server daemon and only call appropriate subroutines.

Shutter control, main routines:

code	description	return message
@0	select shutter control	None
px 0	call initialisation routines and set default behaviour, runs automatically at power up	None
px 1	initialise unit (resets limits and moves to default positions)	*Ready: Shutter Init*
px 10	open blue shutter	*Ready: Shutter b open*
px 11	open red shutter	*Ready: Shutter r open*
px 12	open both shutters (synchronous mode)	*Ready: Shutter s open*
px 20	close blue shutter	*Ready: Shutter b closed*
px 21	close red shutter	*Ready: Shutter r closed*
px 22	close both shutters (synchronous mode)	*Ready: Shutter s closed*

Shutter control, subroutines:

code	description	return message
cal 2	init: power up & test limits	None
cal 3	init: move to default position & power down	None
cal 4	power up blue shutter motors	None
cal 5	power up red shutter motors	None
cal 6	power up all shutter motors	None
cal 7	power down blue shutter motors	None
cal 8	power down red shutter motors	None
cal 9	power down all shutter motors	None
px 13	blue pre-exposure sequence	None
px 14	red pre-exposure sequence	None
px 15	synchronous pre-exposure sequence	None
cal 16	blue pre-exposure subroutine	None
cal 17	red pre-exposure subroutine	None
cal 18	synchronous pre-exposure subroutine	None
px 13	blue post-exposure sequence	*Ready: Shutter b closed*
px 14	red post-exposure sequence	*Ready: Shutter r closed*
px 15	synchronous post-exposure sequence	*Ready: Shutter s closed*
cal 16	blue post-exposure subroutine	*Ready: Shutter b closed*
cal 17	red post-exposure subroutine	*Ready: Shutter r closed*
cal 18	synchronous post-exposure subroutine	*Ready: Shutter s closed*

Filter / guider control, main routines:

code	description	return message
@1	select filter / guider control	None
px 0	call initialisation routines and sets default behaviour, runs automatically at power up	None
px 1	initialises unit (reset limits and move to default positions)	*Ready: Filter/Guider Init*
px 31	move to central guider field position	*Ready: Guider Field*
px 101	select blue filter 1	*Ready: Filter b 1*
px 102	select blue filter 2	*Ready: Filter b 2*
px 103	select blue filter 3	*Ready: Filter b 3*
px 111	select red filter 1	*Ready: Filter r 1*
px 112	select red filter 2	*Ready: Filter r 2*
px 113	select red filter 3	*Ready: Filter r 3*

Filter / guider control, subroutines:

code	description	return message
cal 2	init: power up & test limits	None
cal 3	init: move to default position & power down	None
px 25	move to preset guider focus position power down focus motor	*Ready: Guider Focus*
px 35	move to preset guider field position power down field motor	*Ready: Guider Field*

B.2 Commands for the AMiGo camera server

The AMiGo camera server understands the following set of commands so far (see Sect. 3.4 for additional information):

expose *channel* expose channel [i.e. *blue*, *red* or *sync*]

set exptime *channel duration* set exposure time length to duration [s]

set imagetype *channel type* set imagetype to bias, dark, science or flat

set window *channel region* set window to xStart:xEnd,yStart:yEnd

set binning *channel x-bin y-bin* set binning to x-bin y-bin

uploadMCProgs *filename* send file to motor controller

init shutter initialize shutters of both channels

init filter initialize filter of both channels and guider focus + field

set filter *channel position* sets filter of channel [here only *blue*, *red*] to position [*1*, *2*, or *3*]

set guider focus *position* sets guider focus to position [mm, *0 – 15*]

set guider field *position* moves guider to field position [mm, *-20 – +20*]

help shows help on commands

These commands can be issued on the admin and on the client port. Finished commands return
Ready: [issued command]
on the issuing port. Erroneous commands return a
PROTOCOL error: [Missing parameter . . . ||Unknown command + issued command].

Listener messages

Clients connected to the listener port get the current status every second. The actual messages

syntax also depends on the configuration file syntax.

blue state [idle||active||exposing||readout]
blue progress [0.000000 – 100.000000]
blue exptime [> 0.000000]
blue binning [1 – 64] [1 – 64]
blue window *[1:2048,1:2048]*
blue filterslot [1||2||3]
blue filter [b-slot1||b-slot2||b-slot3]
blue filtername 1 *b-slot1*
blue filtername 2 *b-slot2*
blue filtername 3 *b-slot3*
blue shutter [closed||opening||slit||open||closing]
blue filename *test_b1_070618_001.fits*
red state [idle||active||exposing||readout]
red progress [0.000000 – 100.000000]
red exptime [> 0.000000]
red binning [1 – 64] [1 – 64]
red window *[1:2048,1:2048]*
red filterslot [1||2||3]
red filter [r-slot1||r-slot2||r-slot3]
red filtername 1 *r-slot1*
red filtername 2 *r-slot2*
red filtername 3 *r-slot3*
red shutter [closed||opening||slit||open||closing]
red filename *test_r1_070618_001.fits*
Guider [idle||focussing||moving]

B.3 AMiGo camera server configuration file syntax

Syntax of the parameters, their default values and description for the AMiGo camera server configuration file:

| Parameter	value	description
CAMRELAY_IP	= 195.37.68.95	// IP address of camera relay
CAMRELAY_COM_PORT	= 7999	// COM Port on camera relay
CAMPINRELAY_IP	= 195.37.68.95	// IP address of camera relay
CAMPINRELAY_COM_PORT	= 7998	// COM Port on camera relay
ADMIN_PORT	= 5242	// Port for admin commands
CLIENT_PORT	= 5243	// Port for client commands
LISTEN_PORT	= 5245	// Port for listeners
TCS_IP	= 195.27.68.16	// IP address of TCS daemon
TCS_INSTRUMENT_PORT	= 5244	// Port on TCSD for instrument
TCS_LISTEN_PORT	= 5245	// Port on TCSD for listeners
OBSERVAT	= Wendelstein	// name of observatory for FITS header
TELESCOP	= telescope	// name of telescope for FITS header
INSTRUME	= AMiGo	// name of instrument for FITS header
ORIGIN	= controller	// name of originating device for FITS header
DETECTOR_B	= CCD_blue	// name of blue detector
DETECTOR_R	= CCD_red	// name of red detector
CHANNEL_B	= blue	// name of blue channel
CHANNEL_R	= red	// name of red channel
FILTERNAME_B1	= b-slot1	// filtername of channel blue slot 1
FILTERID_B1	= b1	// filter Id of channel blue slot 1
FILTERNAME_B2	= b-slot2	// filtername of channel blue slot 2
FILTERID_B2	= b2	// filter Id of channel blue slot 2
FILTERNAME_B3	= b-slot3	// filtername of channel blue slot 3
FILTERID_B3	= b3	// filter Id of channel blue slot 3
FILTERNAME_R1	= r-slot1	// filtername of channel red slot 1
FILTERID_R1	= r1	// filter Id of channel red slot 1
FILTERNAME_R2	= r-slot2	// filtername of channel red slot 2
FILTERID_R2	= r2	// filter Id of channel red slot 2
FILTERNAME_R3	= r-slot3	// filtername of channel red slot 3
FILTERID_R3	= r3	// filter Id of channel red slot 3

Appendix C

AMiGo Photos
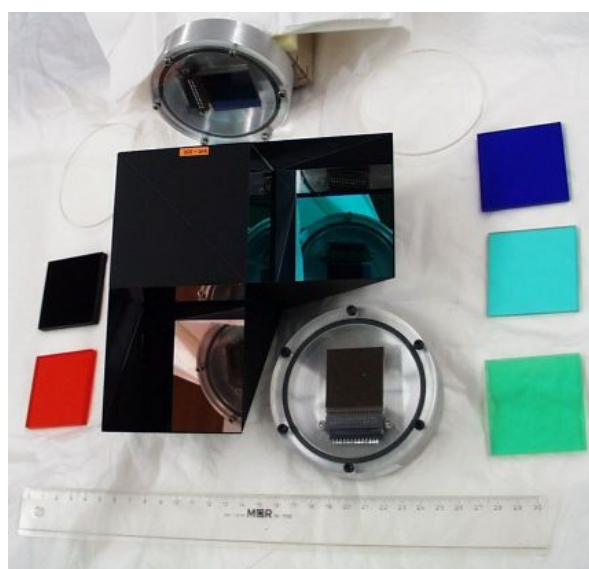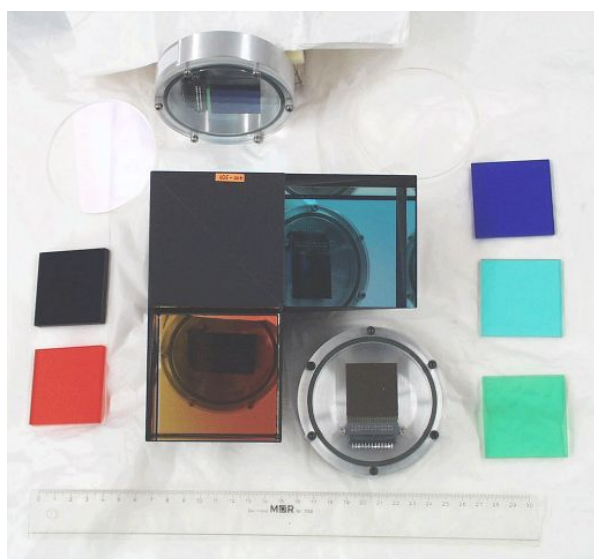
Figure C.1: Top: Dichroic beam splitter, Schott filters and LORAL/Lesser CCDs; bottom: Cryo-stat parts before assembly test and goldening.
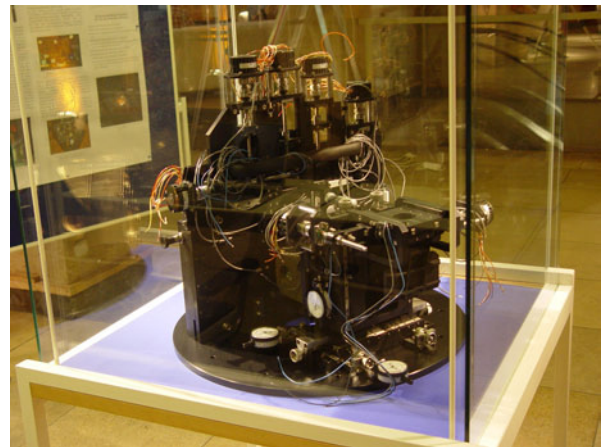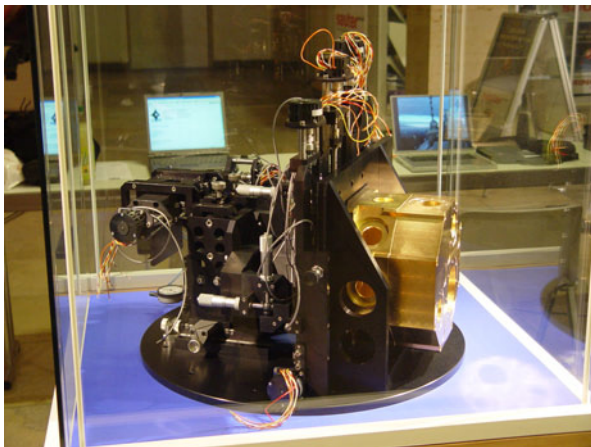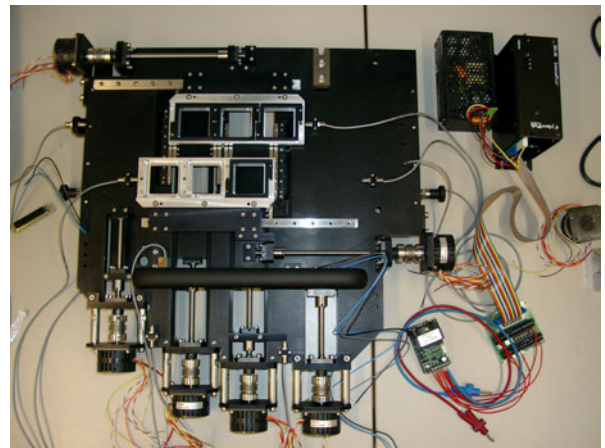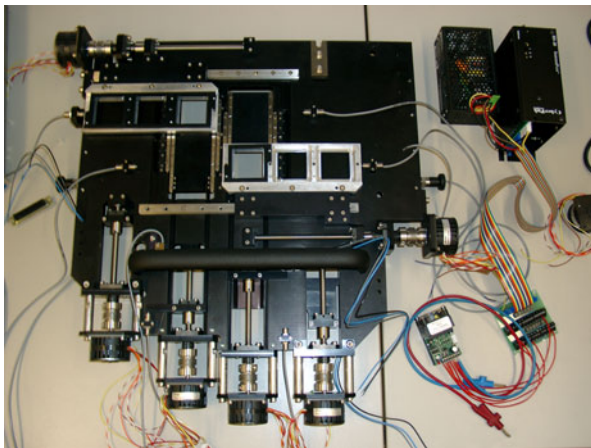
Figure C.2: Top: Dichroic and offset guiding unit mount; centre: Shutter / filter module; bottom: Public exhibition of the instrument at "Lange Nacht der Sterne" 2004 in "Forum der Technik", Deutsches Museum.

Appendix D

Lomb Completeness Test Results

Pegasus: 1.4 mag peak–to–peak amplitude, cosine lightcurve

Pegasus: 1.4 mag peak–to–peak amplitude, sawtooth lightcurve

Pegasus: 1.0 mag peak–to–peak amplitude, cosine lightcurve

Pegasus: 1.0 mag peak–to–peak amplitude, sawtooth lightcurve

Pegasus: 0.6 mag peak–to–peak amplitude, cosine lightcurve

Pegasus: 0.6 mag peak–to–peak amplitude, sawtooth lightcurve

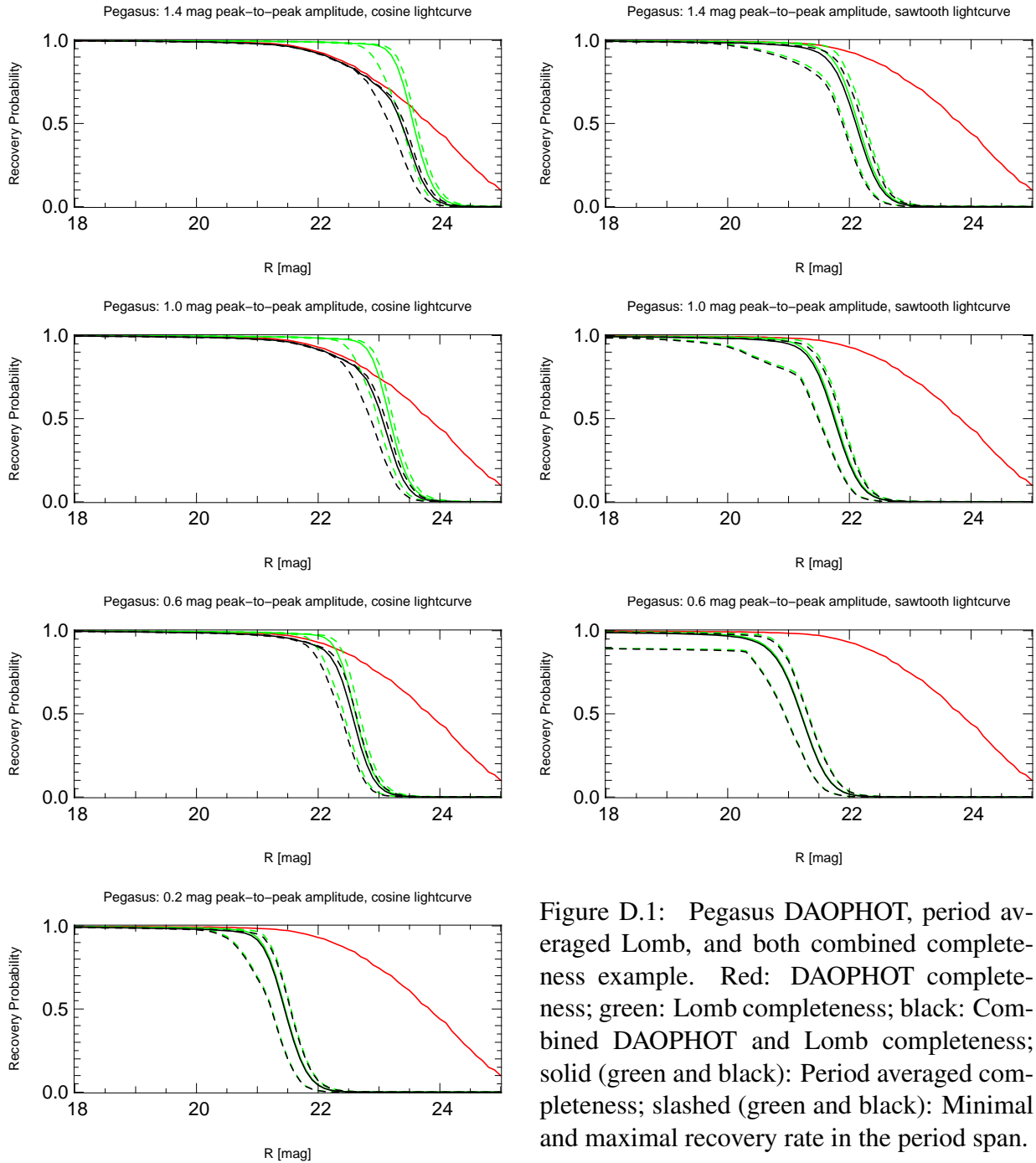Pegasus: 0.2 mag peak–to–peak amplitude, cosine lightcurve

Figure D.1: Pegasus DAOPHOT, period averaged Lomb, and both combined completeness example. Red: DAOPHOT completeness; green: Lomb completeness; black: Combined DAOPHOT and Lomb completeness; solid (green and black): Period averaged completeness; slashed (green and black): Minimal and maximal recovery rate in the period span.

EGB 0427+63: 1.4 mag peak–to–peak amplitude, cosine lightcurve

EGB 0427+63: 1.4 mag peak–to–peak amplitude, sawtooth lightcurve

EGB 0427+63: 1.0 mag peak–to–peak amplitude, cosine lightcurve

EGB 0427+63: 1.0 mag peak–to–peak amplitude, sawtooth lightcurve

EGB 0427+63: 0.6 mag peak–to–peak amplitude, cosine lightcurve

EGB 0427+63: 0.6 mag peak–to–peak amplitude, sawtooth lightcurve

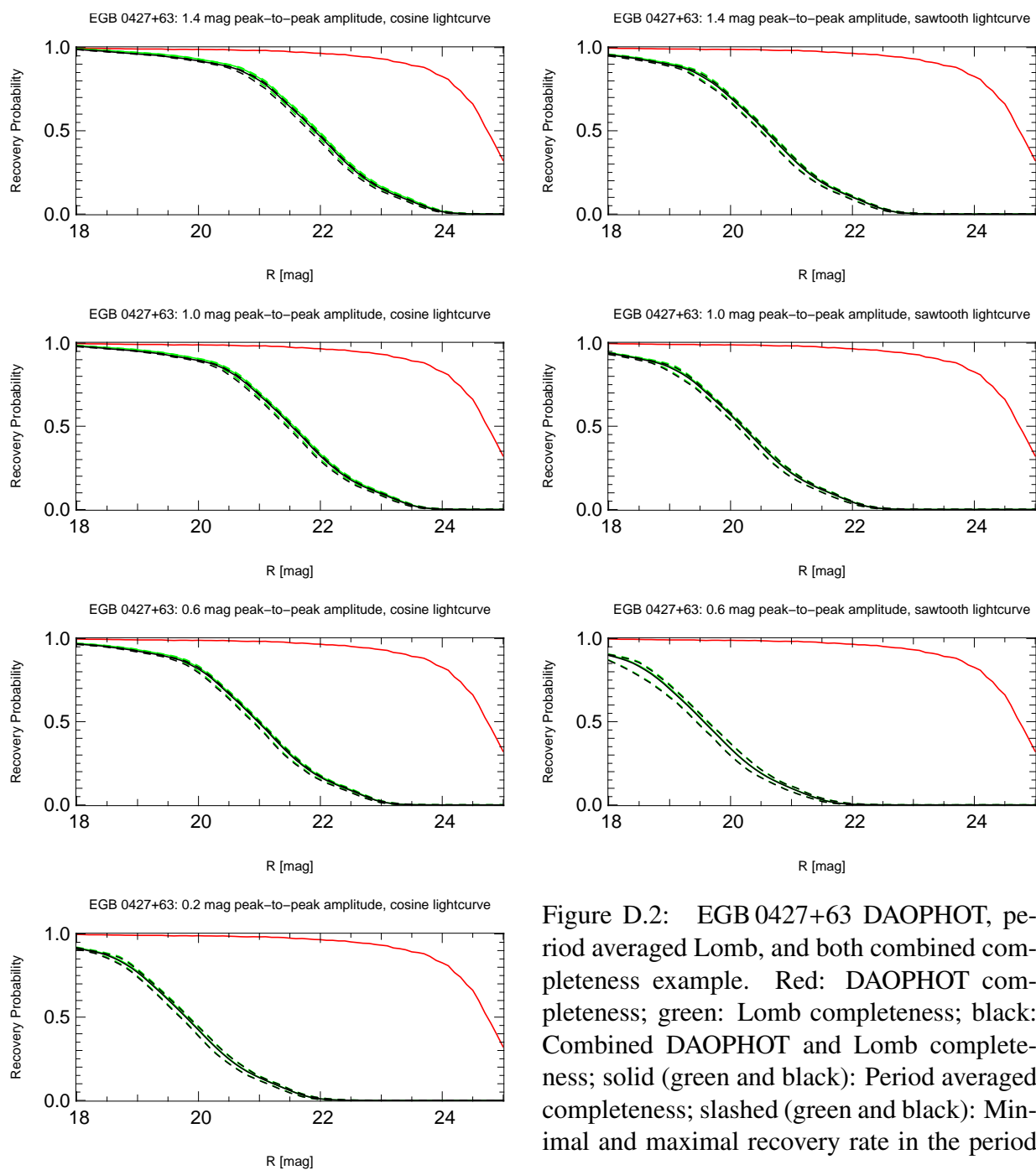EGB 0427+63: 0.2 mag peak–to–peak amplitude, cosine lightcurve

Figure D.2: EGB 0427+63 DAOPHOT, period averaged Lomb, and both combined completeness example. Red: DAOPHOT completeness; green: Lomb completeness; black: Combined DAOPHOT and Lomb completeness; solid (green and black): Period averaged completeness; slashed (green and black): Minimal and maximal recovery rate in the period span.

GR 08: 1.4 mag peak–to–peak amplitude, cosine lightcurve

GR 08: 1.4 mag peak–to–peak amplitude, sawtooth lightcurve

GR 08: 1.0 mag peak–to–peak amplitude, cosine lightcurve

GR 08: 1.0 mag peak–to–peak amplitude, sawtooth lightcurve

GR 08: 0.6 mag peak–to–peak amplitude, cosine lightcurve

GR 08: 0.6 mag peak–to–peak amplitude, sawtooth lightcurve

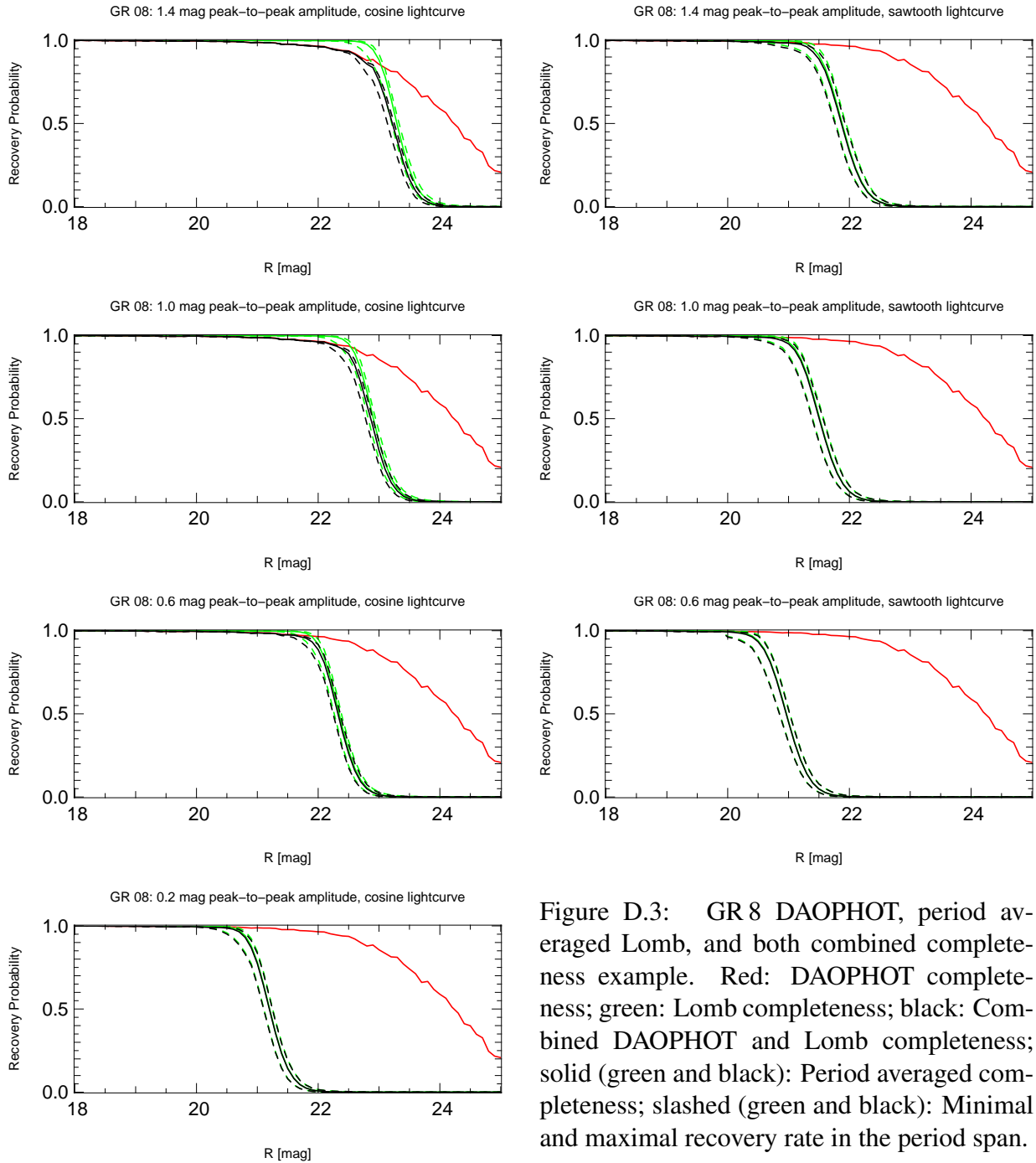GR 08: 0.2 mag peak–to–peak amplitude, cosine lightcurve

Figure D.3: GR 8 DAOPHOT, period averaged Lomb, and both combined completeness example. Red: DAOPHOT completeness; green: Lomb completeness; black: Combined DAOPHOT and Lomb completeness; solid (green and black): Period averaged completeness; slashed (green and black): Minimal and maximal recovery rate in the period span.
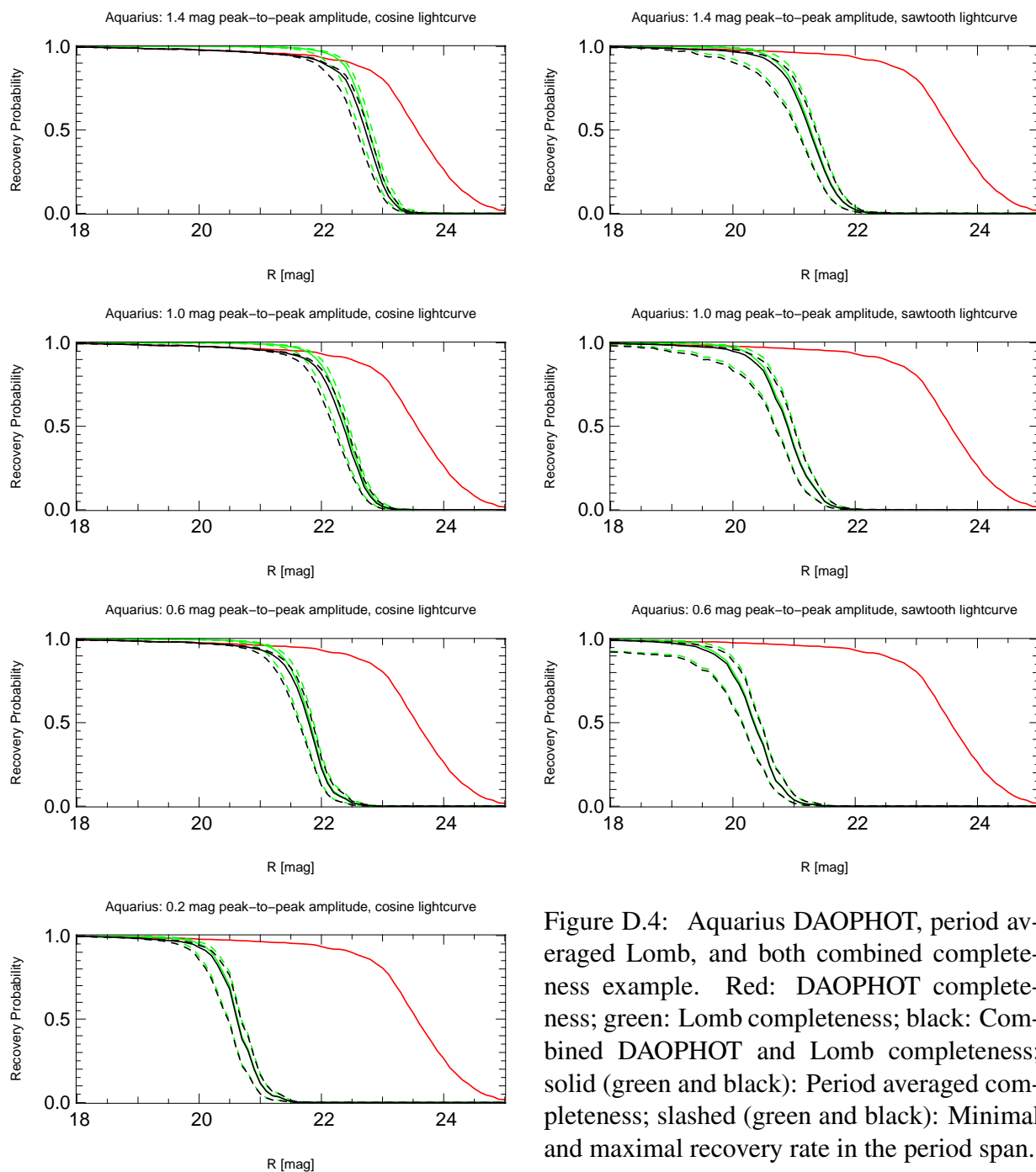
Figure D.4: Aquarius DAOPHOT, period averaged Lomb, and both combined completeness example. Red: DAOPHOT completeness; green: Lomb completeness; black: Combined DAOPHOT and Lomb completeness; solid (green and black): Period averaged completeness; slashed (green and black): Minimal and maximal recovery rate in the period span.
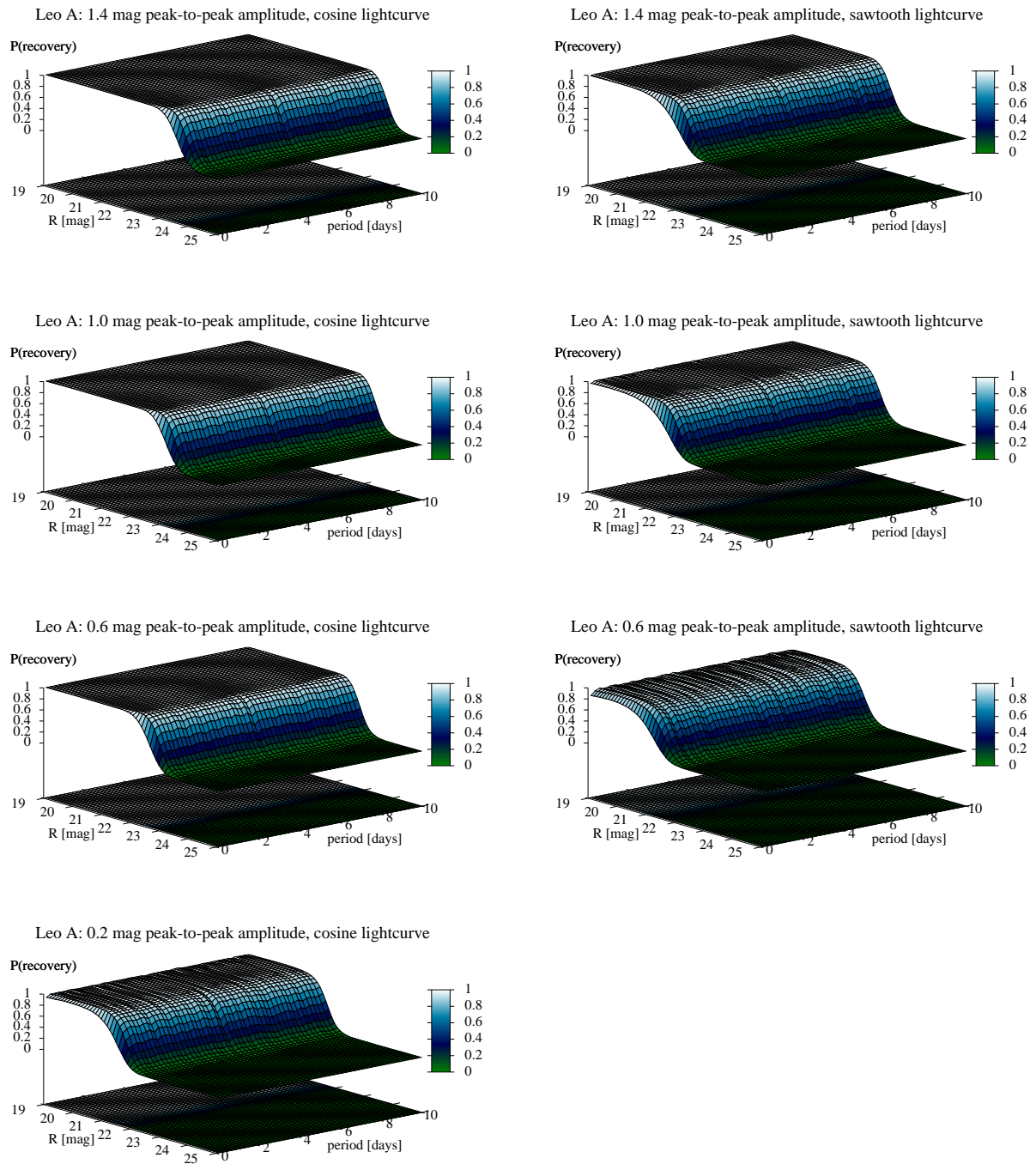
Leo A: 1.4 mag peak-to-peak amplitude, cosine lightcurve

Leo A: 1.4 mag peak-to-peak amplitude, sawtooth lightcurve

Leo A: 1.0 mag peak-to-peak amplitude, cosine lightcurve

Leo A: 1.0 mag peak-to-peak amplitude, sawtooth lightcurve

Leo A: 0.6 mag peak-to-peak amplitude, cosine lightcurve

Leo A: 0.6 mag peak-to-peak amplitude, sawtooth lightcurve

Leo A: 0.2 mag peak-to-peak amplitude, cosine lightcurve

Figure D.5: Leo A Lomb shortest periods completeness.

Leo A: 1.4 mag peak-to-peak amplitude, cosine lightcurve

Leo A: 1.4 mag peak-to-peak amplitude, sawtooth lightcurve

Leo A: 1.0 mag peak-to-peak amplitude, cosine lightcurve

Leo A: 1.0 mag peak-to-peak amplitude, sawtooth lightcurve

Leo A: 0.6 mag peak-to-peak amplitude, cosine lightcurve

Leo A: 0.6 mag peak-to-peak amplitude, sawtooth lightcurve

Leo A: 0.2 mag peak-to-peak amplitude, cosine lightcurve
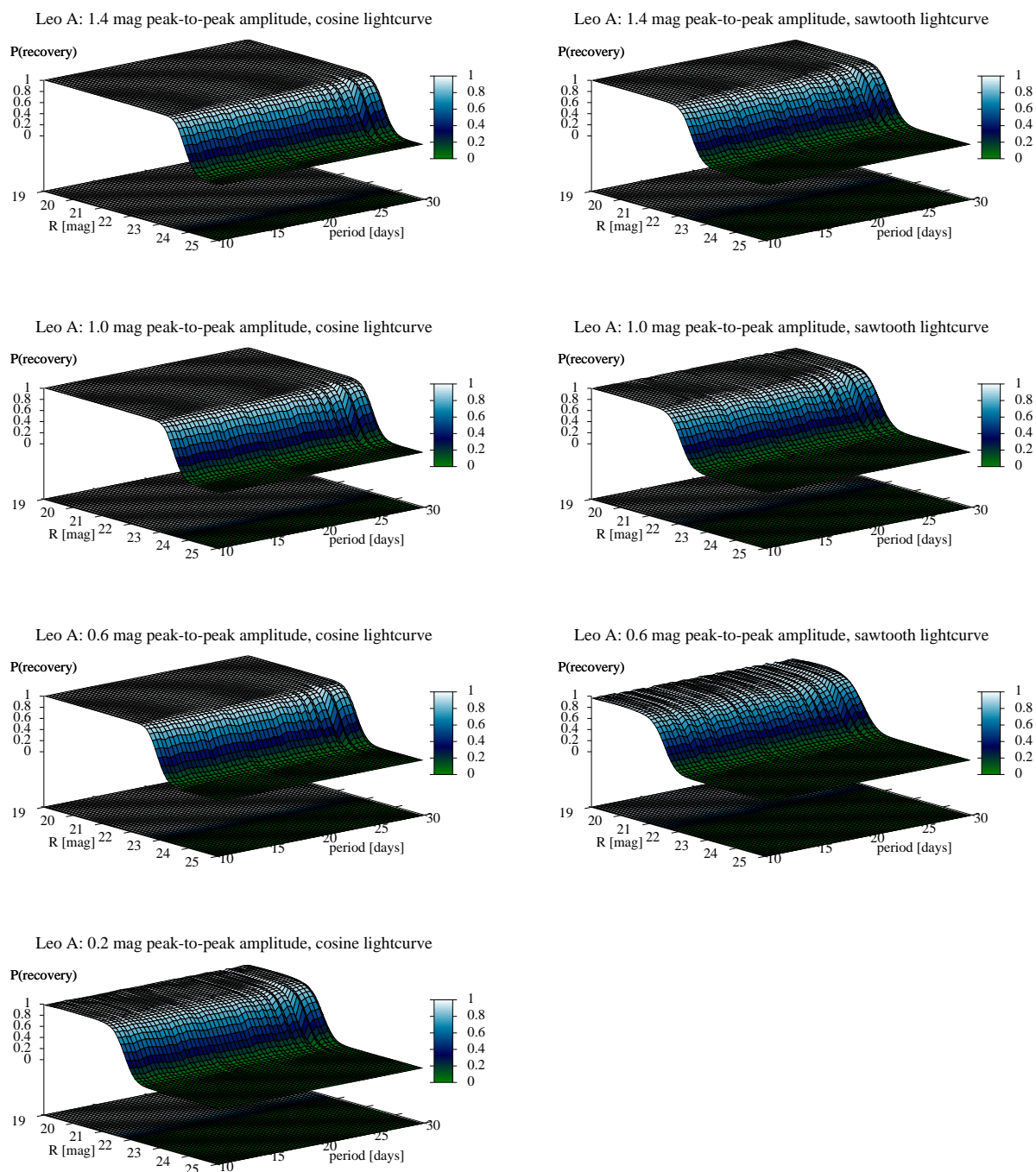
Figure D.6: Leo A Lomb mid-range of periods completeness, including the synodic and sidereal month.

Leo A: 1.4 mag peak-to-peak amplitude, cosine lightcurve
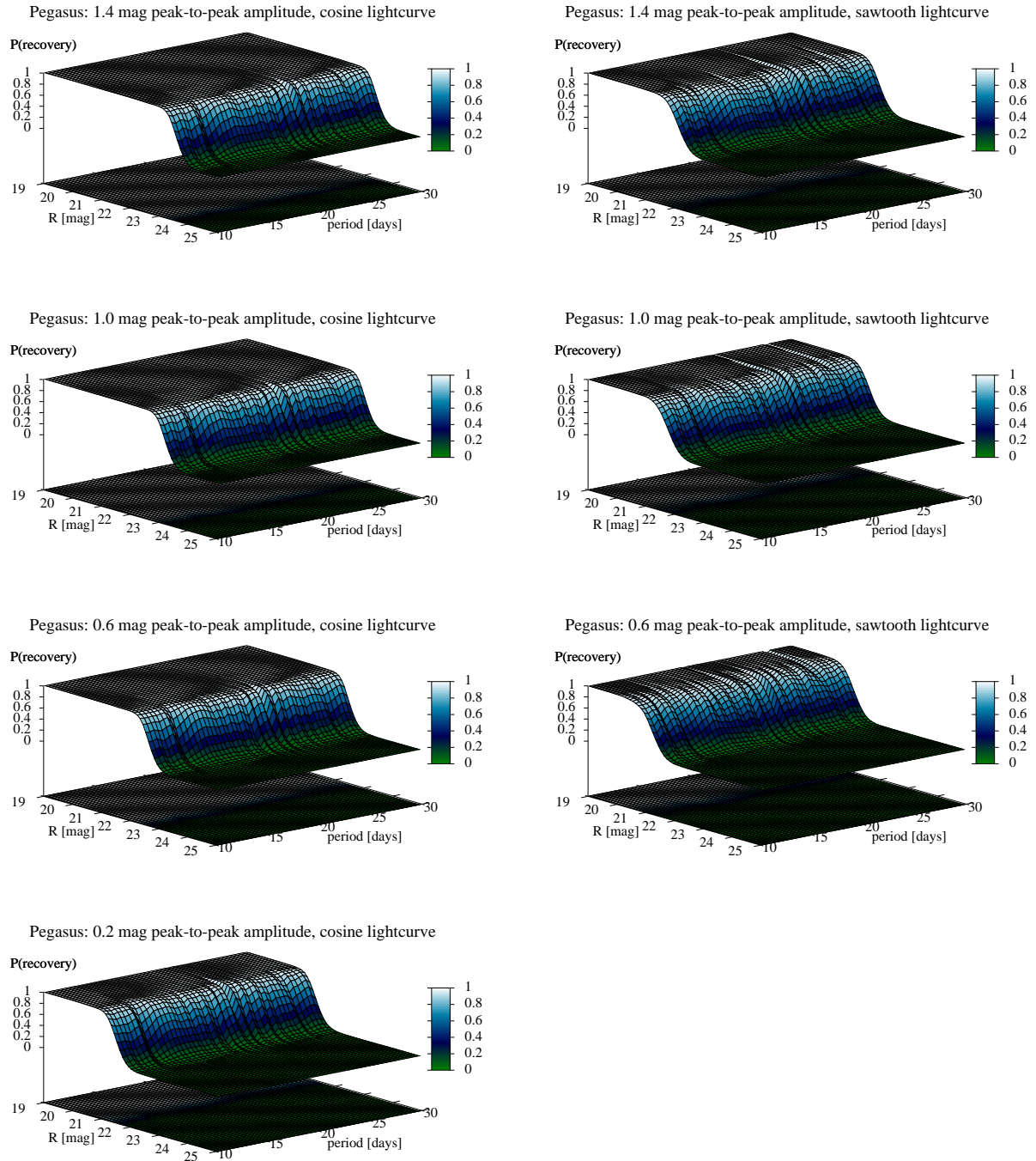
Leo A: 1.4 mag peak-to-peak amplitude, sawtooth lightcurve

Leo A: 1.0 mag peak-to-peak amplitude, cosine lightcurve

Leo A: 1.0 mag peak-to-peak amplitude, sawtooth lightcurve

Leo A: 0.6 mag peak-to-peak amplitude, cosine lightcurve

Leo A: 0.6 mag peak-to-peak amplitude, sawtooth lightcurve

Leo A: 0.2 mag peak-to-peak amplitude, cosine lightcurve
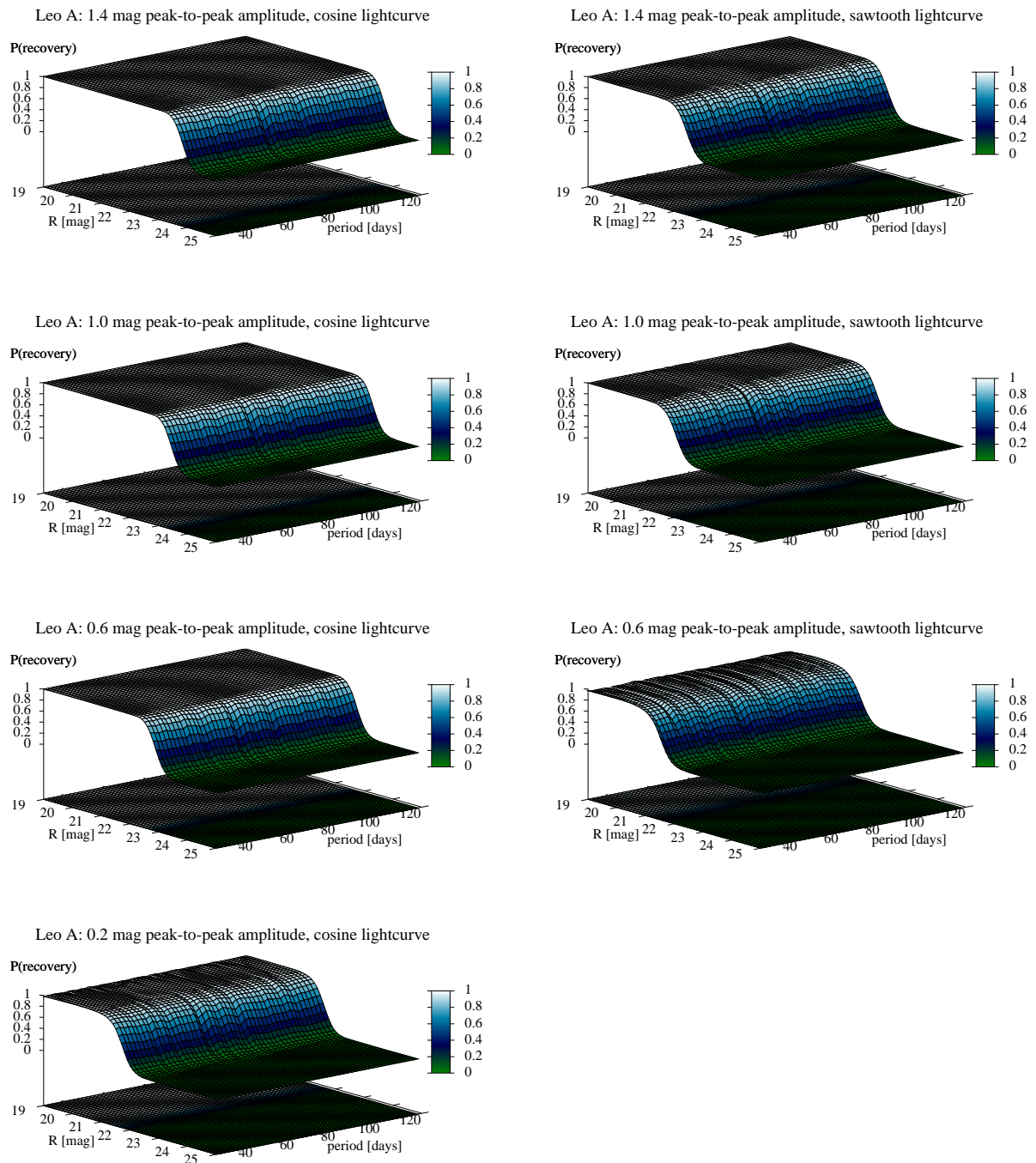
Figure D.7: Leo A Lomb longest periods completeness.

Pegasus: 1.4 mag peak-to-peak amplitude, cosine lightcurve

Pegasus: 1.4 mag peak-to-peak amplitude, sawtooth lightcurve

Pegasus: 1.0 mag peak-to-peak amplitude, cosine lightcurve

Pegasus: 1.0 mag peak-to-peak amplitude, sawtooth lightcurve

Pegasus: 0.6 mag peak-to-peak amplitude, cosine lightcurve

Pegasus: 0.6 mag peak-to-peak amplitude, sawtooth lightcurve

Pegasus: 0.2 mag peak-to-peak amplitude, cosine lightcurve

Figure D.8: Pegasus Dwarf Lomb shortest periods completeness.

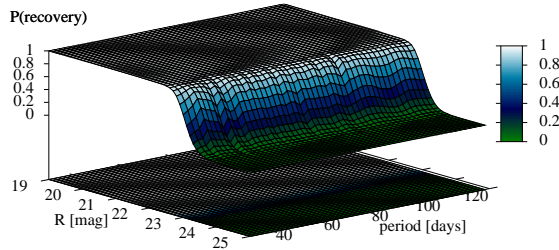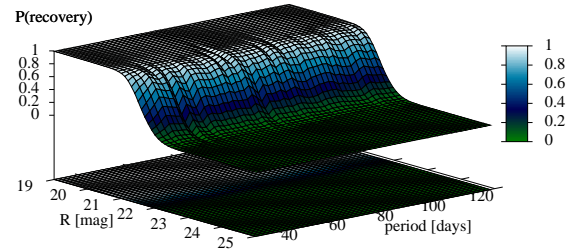Pegasus: 1.4 mag peak-to-peak amplitude, cosine lightcurve

Pegasus: 1.4 mag peak-to-peak amplitude, sawtooth lightcurve

Pegasus: 1.0 mag peak-to-peak amplitude, cosine lightcurve

Pegasus: 1.0 mag peak-to-peak amplitude, sawtooth lightcurve

Pegasus: 0.6 mag peak-to-peak amplitude, cosine lightcurve

Pegasus: 0.6 mag peak-to-peak amplitude, sawtooth lightcurve

Pegasus: 0.2 mag peak-to-peak amplitude, cosine lightcurve

Figure D.9:   Pegasus Dwarf Lomb mid-range of periods completeness, including the synodic and sidereal month.

Pegasus: 1.4 mag peak-to-peak amplitude, cosine lightcurve
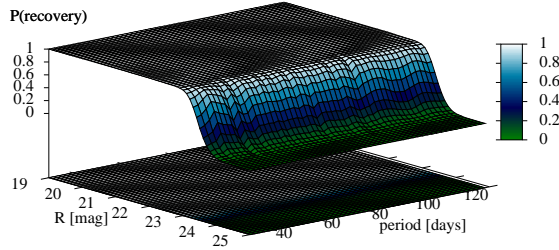
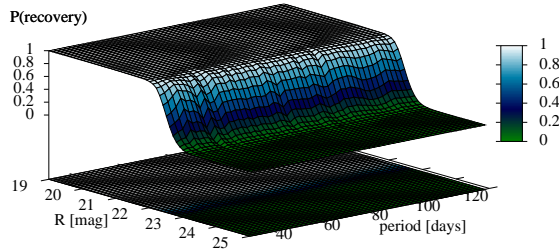Pegasus: 1.4 mag peak-to-peak amplitude, sawtooth lightcurve
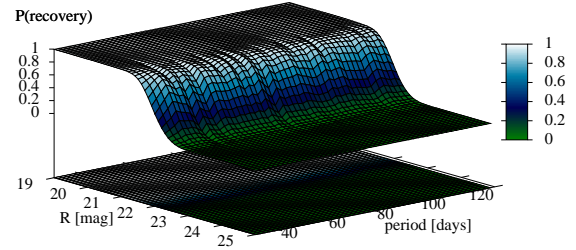
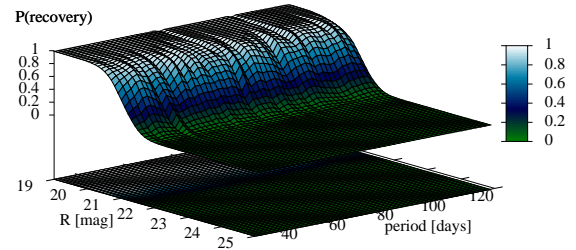Pegasus: 1.0 mag peak-to-peak amplitude, cosine lightcurve

Pegasus: 1.0 mag peak-to-peak amplitude, sawtooth lightcurve

Pegasus: 0.6 mag peak-to-peak amplitude, cosine lightcurve

Pegasus: 0.6 mag peak-to-peak amplitude, sawtooth lightcurve

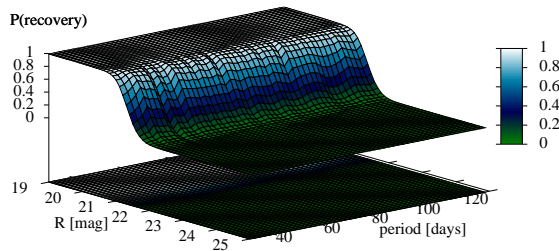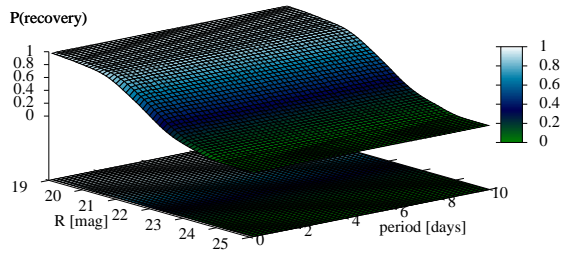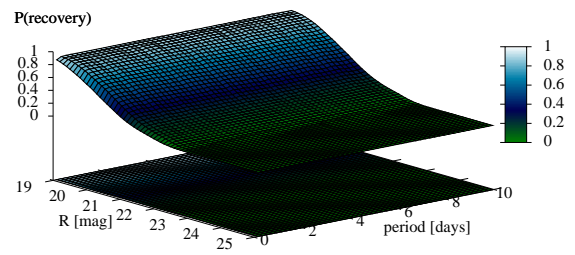Pegasus: 0.2 mag peak-to-peak amplitude, cosine lightcurve

Figure D.10: Pegasus Dwarf Lomb longest periods completeness.

EGB 0427+63: 1.4 mag peak-to-peak amplitude, cosine lightcurve

EGB 0427+63: 1.4 mag peak-to-peak amplitude, sawtooth lightcurve

EGB 0427+63: 1.0 mag peak-to-peak amplitude, cosine lightcurve

EGB 0427+63: 1.0 mag peak-to-peak amplitude, sawtooth lightcurve

EGB 0427+63: 0.6 mag peak-to-peak amplitude, cosine lightcurve

EGB 0427+63: 0.6 mag peak-to-peak amplitude, sawtooth lightcurve

EGB 0427+63: 0.2 mag peak-to-peak amplitude, cosine lightcurve

Figure D.11: EGB 0427+63 Lomb shortest periods completeness.

EGB 0427+63: 1.4 mag peak-to-peak amplitude, cosine lightcurve

EGB 0427+63: 1.4 mag peak-to-peak amplitude, sawtooth lightcurve

EGB 0427+63: 1.0 mag peak-to-peak amplitude, cosine lightcurve

EGB 0427+63: 1.0 mag peak-to-peak amplitude, sawtooth lightcurve
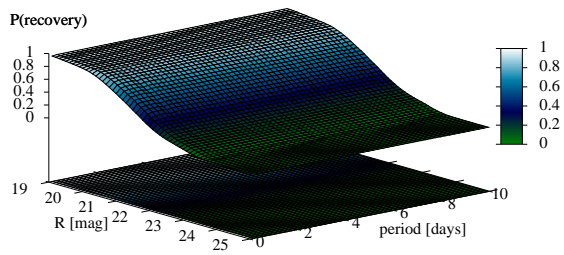
EGB 0427+63: 0.6 mag peak-to-peak amplitude, cosine lightcurve

EGB 0427+63: 0.6 mag peak-to-peak amplitude, sawtooth lightcurve

EGB 0427+63: 0.2 mag peak-to-peak amplitude, cosine lightcurve

Figure D.12: EGB 0427+63 Lomb mid-range of periods completeness, including the synodic and sidereal month.

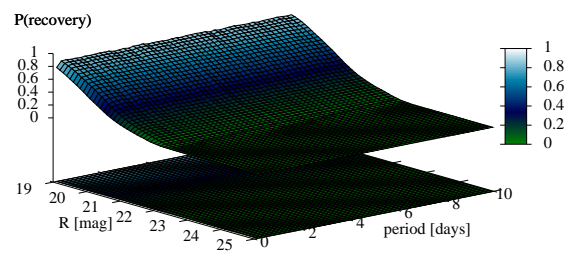EGB 0427+63: 1.4 mag peak-to-peak amplitude, cosine lightcurve

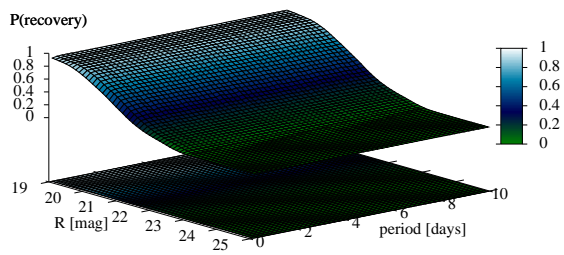EGB 0427+63: 1.4 mag peak-to-peak amplitude, sawtooth lightcurve

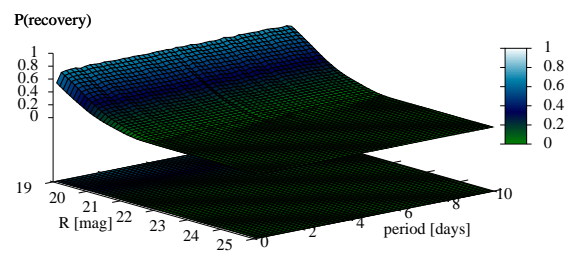EGB 0427+63: 1.0 mag peak-to-peak amplitude, cosine lightcurve
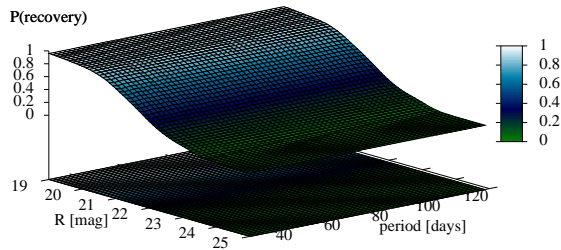
EGB 0427+63: 1.0 mag peak-to-peak amplitude, sawtooth lightcurve

EGB 0427+63: 0.6 mag peak-to-peak amplitude, cosine lightcurve

EGB 0427+63: 0.6 mag peak-to-peak amplitude, sawtooth lightcurve

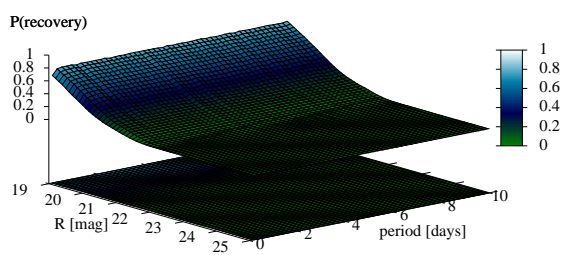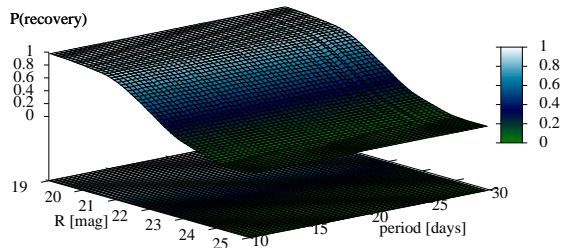EGB 0427+63: 0.2 mag peak-to-peak amplitude, cosine lightcurve
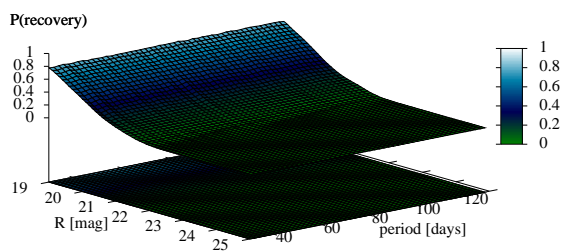
Figure D.13: EGB 0427+63 Lomb longest periods completeness.

GR 08: 1.4 mag peak-to-peak amplitude, cosine lightcurve

GR 08: 1.4 mag peak-to-peak amplitude, sawtooth lightcurve

GR 08: 1.0 mag peak-to-peak amplitude, cosine lightcurve

GR 08: 1.0 mag peak-to-peak amplitude, sawtooth lightcurve

GR 08: 0.6 mag peak-to-peak amplitude, cosine lightcurve

GR 08: 0.6 mag peak-to-peak amplitude, sawtooth lightcurve

GR 08: 0.2 mag peak-to-peak amplitude, cosine lightcurve
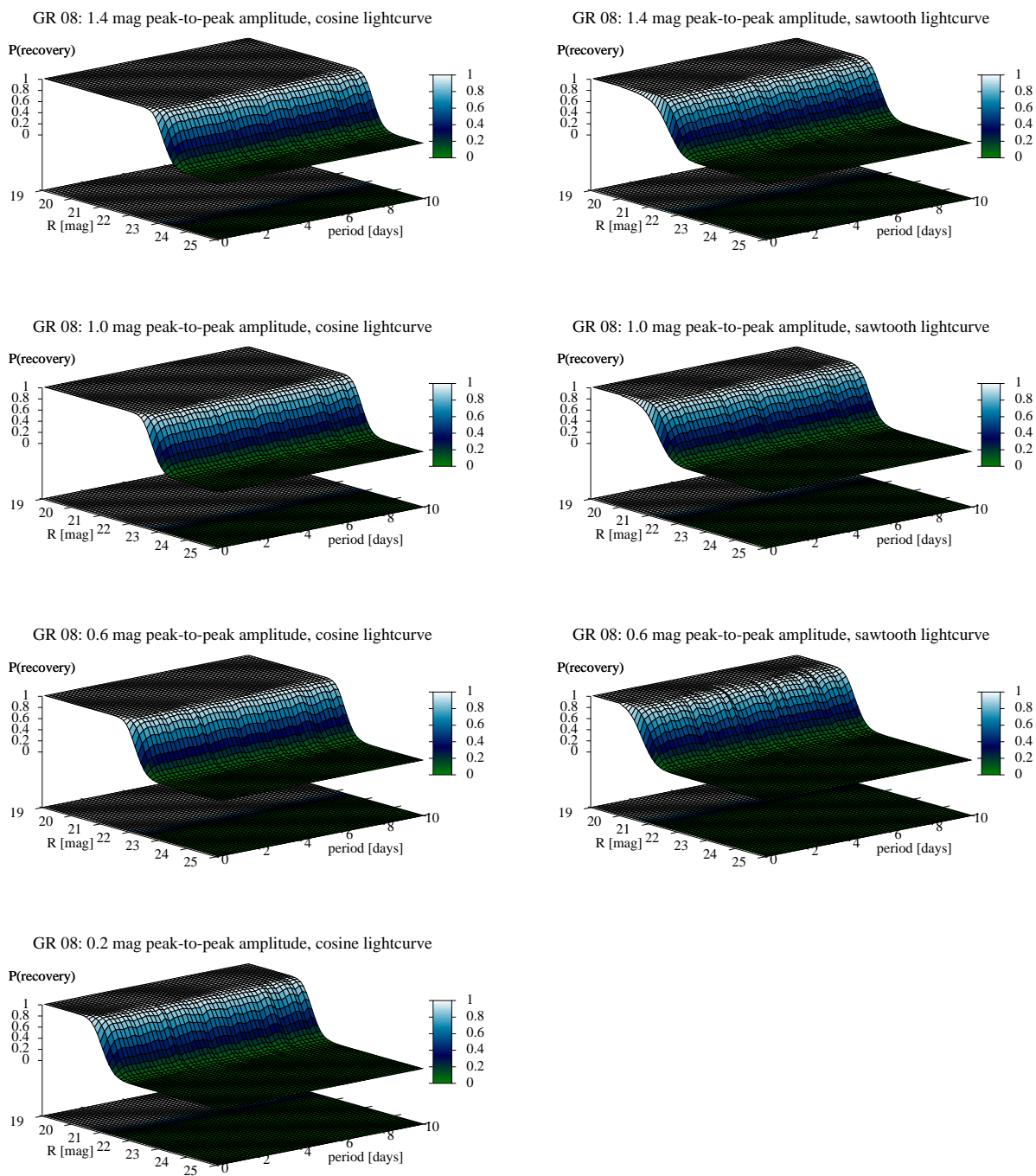
Figure D.14: GR 8 Lomb shortest periods completeness.

GR 08: 1.4 mag peak-to-peak amplitude, cosine lightcurve

GR 08: 1.4 mag peak-to-peak amplitude, sawtooth lightcurve

GR 08: 1.0 mag peak-to-peak amplitude, cosine lightcurve

GR 08: 1.0 mag peak-to-peak amplitude, sawtooth lightcurve

GR 08: 0.6 mag peak-to-peak amplitude, cosine lightcurve

GR 08: 0.6 mag peak-to-peak amplitude, sawtooth lightcurve
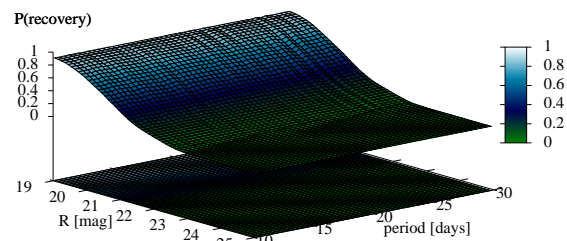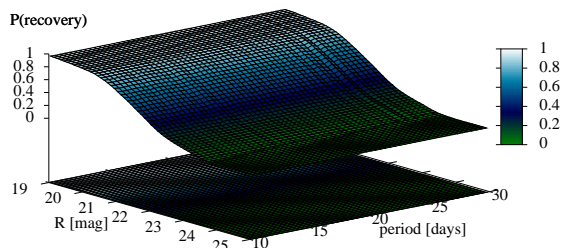

GR 08: 0.2 mag peak-to-peak amplitude, cosine lightcurve
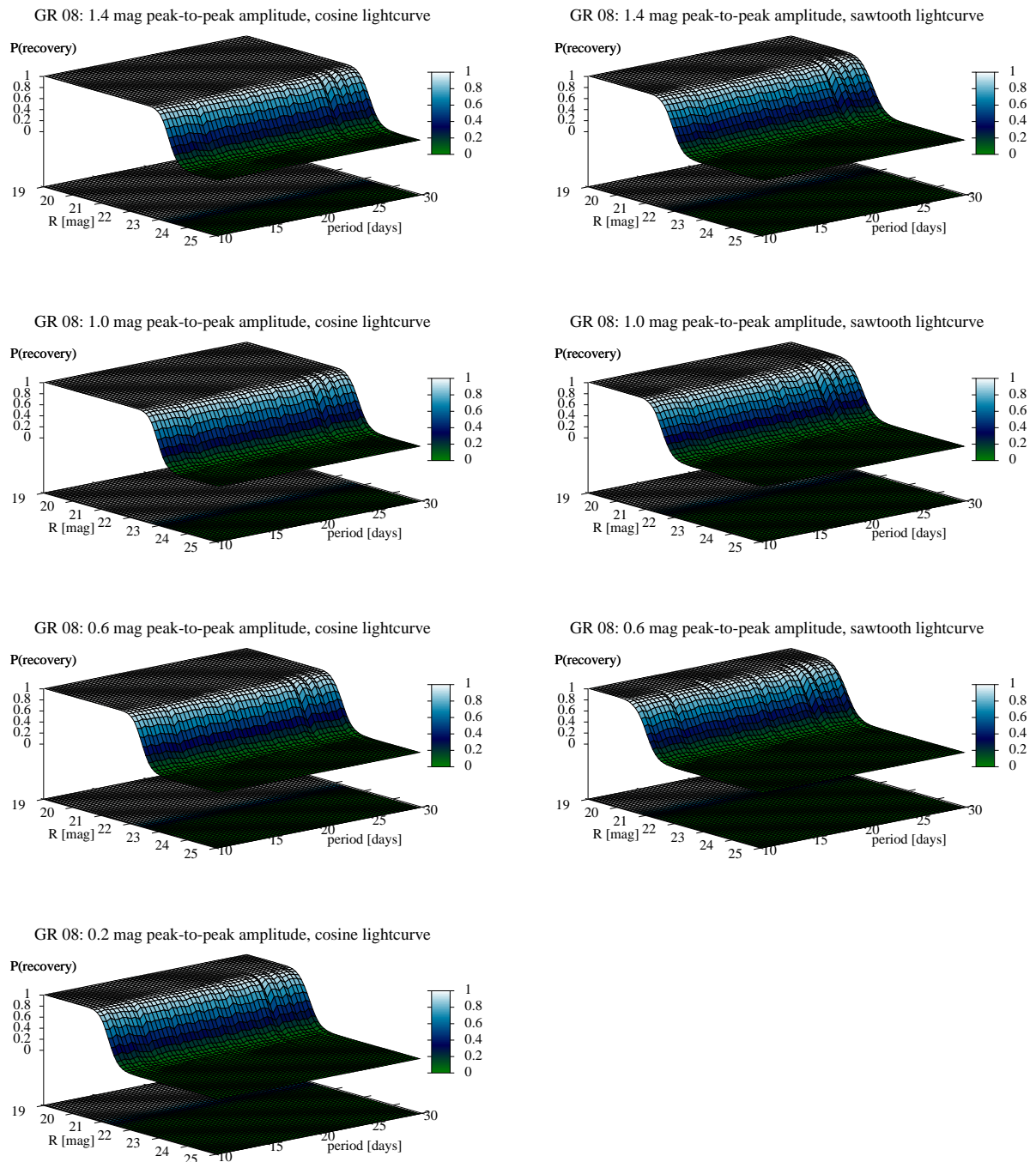
Figure D.15: GR 8 Lomb mid-range of periods completeness, including the synodic and sidereal month.

GR 08: 1.4 mag peak-to-peak amplitude, cosine lightcurve
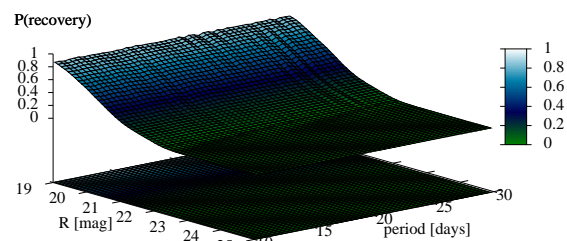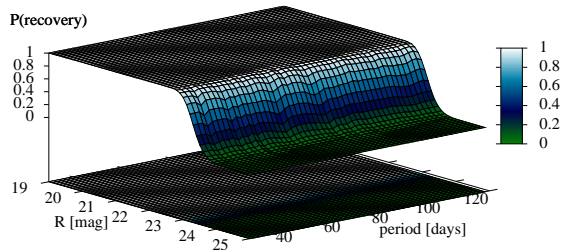
GR 08: 1.4 mag peak-to-peak amplitude, sawtooth lightcurve
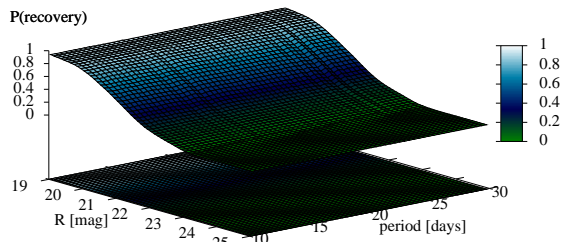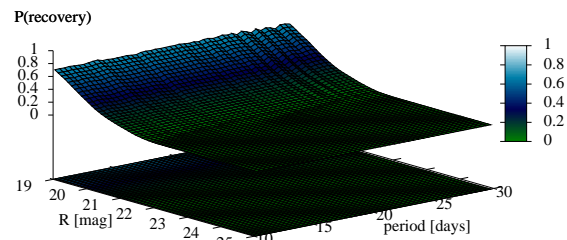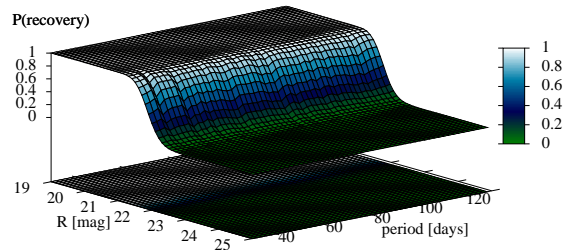
GR 08: 1.0 mag peak-to-peak amplitude, cosine lightcurve
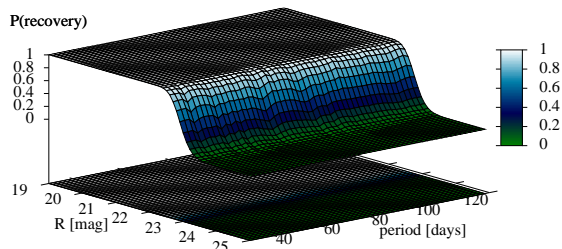
GR 08: 1.0 mag peak-to-peak amplitude, sawtooth lightcurve
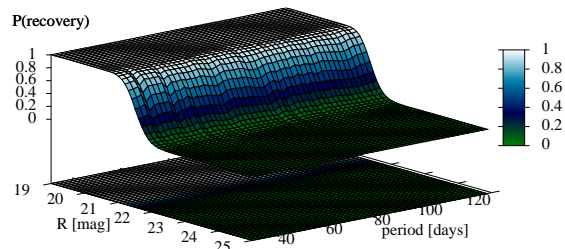
GR 08: 0.6 mag peak-to-peak amplitude, cosine lightcurve
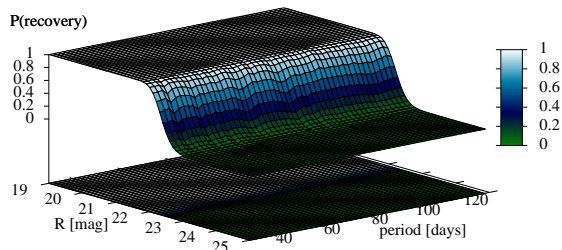
GR 08: 0.6 mag peak-to-peak amplitude, sawtooth lightcurve
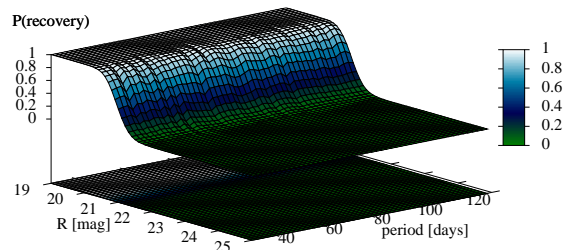
GR 08: 0.2 mag peak-to-peak amplitude, cosine lightcurve
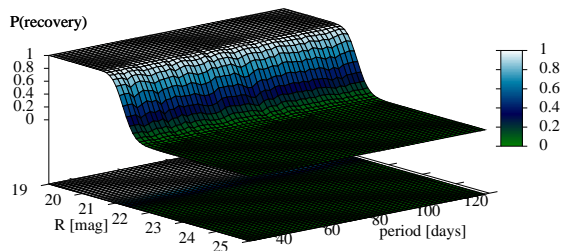
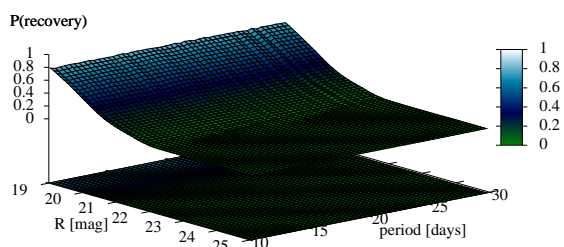Figure D.16: GR 8 Lomb longest periods completeness.

Aquarius: 1.4 mag peak-to-peak amplitude, cosine lightcurve

Aquarius: 1.4 mag peak-to-peak amplitude, sawtooth lightcurve

Aquarius: 1.0 mag peak-to-peak amplitude, cosine lightcurve

Aquarius: 1.0 mag peak-to-peak amplitude, sawtooth lightcurve

Aquarius: 0.6 mag peak-to-peak amplitude, cosine lightcurve

Aquarius: 0.6 mag peak-to-peak amplitude, sawtooth lightcurve

Aquarius: 0.2 mag peak-to-peak amplitude, cosine lightcurve

Figure D.17: Aquarius Dwarf Lomb shortest periods completeness.

Aquarius: 1.4 mag peak-to-peak amplitude, cosine lightcurve

Aquarius: 1.4 mag peak-to-peak amplitude, sawtooth lightcurve

Aquarius: 1.0 mag peak-to-peak amplitude, cosine lightcurve

Aquarius: 1.0 mag peak-to-peak amplitude, sawtooth lightcurve

Aquarius: 0.6 mag peak-to-peak amplitude, cosine lightcurve

Aquarius: 0.6 mag peak-to-peak amplitude, sawtooth lightcurve

Aquarius: 0.2 mag peak-to-peak amplitude, cosine lightcurve
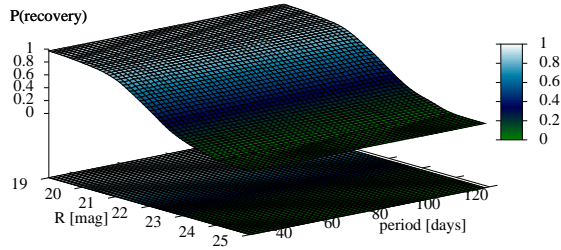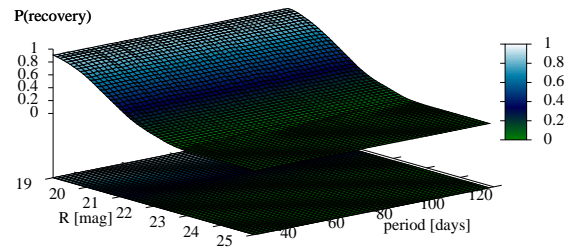

Figure D.18: Aquarius Dwarf Lomb mid-range of periods completeness, including the synodic and sidereal month.

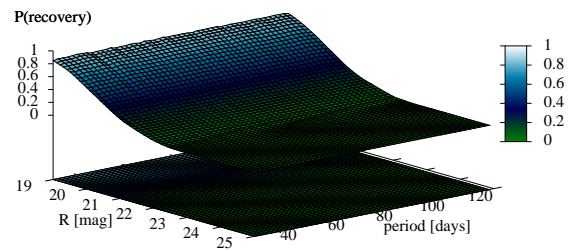Aquarius: 1.4 mag peak-to-peak amplitude, cosine lightcurve

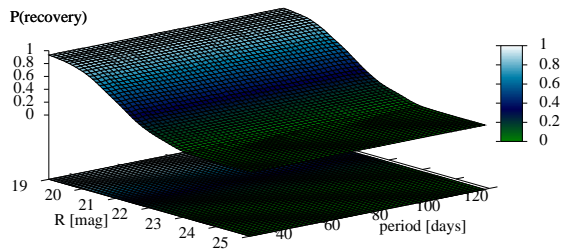Aquarius: 1.4 mag peak-to-peak amplitude, sawtooth lightcurve

Aquarius: 1.0 mag peak-to-peak amplitude, cosine lightcurve

Aquarius: 1.0 mag peak-to-peak amplitude, sawtooth lightcurve

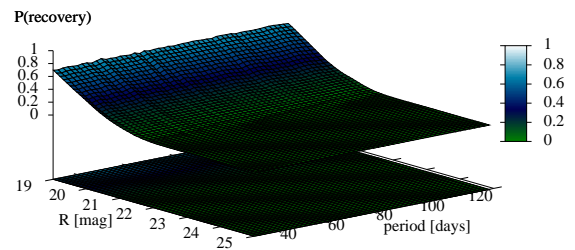Aquarius: 0.6 mag peak-to-peak amplitude, cosine lightcurve

Aquarius: 0.6 mag peak-to-peak amplitude, sawtooth lightcurve

Aquarius: 0.2 mag peak-to-peak amplitude, cosine lightcurve
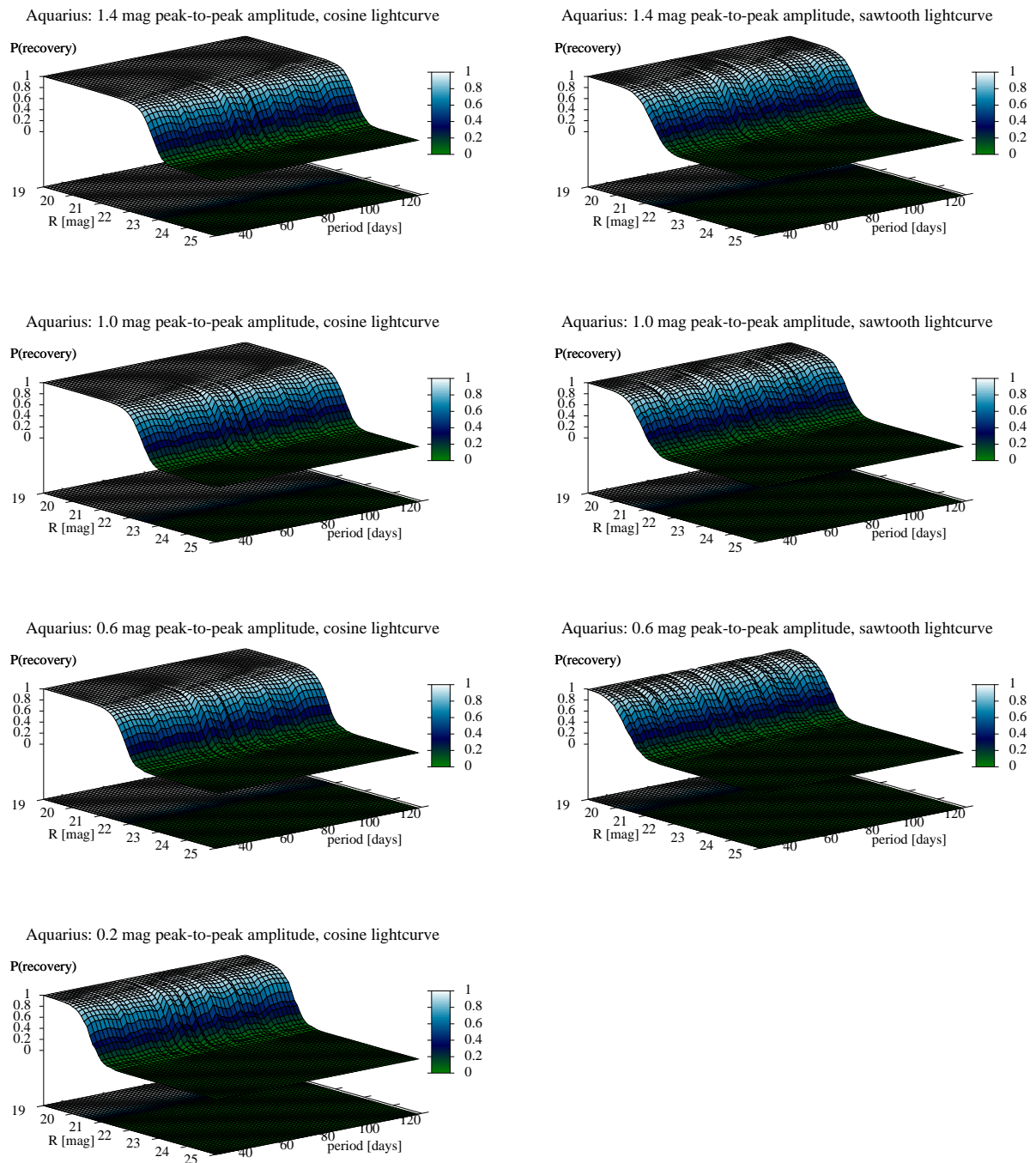
Figure D.19: Aquarius Dwarf Lomb longest periods completeness.

Appendix E

By Chance Discoveries

E.1   Small Solar System Bodies

Table E.1: At the given dates and fields at least 8 detections of a fast moving object are available.

Field	Dates of nights with fast moving objects
Leo A (WST)	2000-01-11, 2000-01-12, 2000-02-27, 2000-02-27, 2000-05-02, 2000-11-30, 2002-02-14, 2002-03-10, 2002-04-02, 2004-12-06, 2005-02-07
Leo A (CA)	2001-02-01, 2001-02-12, 2002-02-01, 2002-02-10, 2002-02-12, 2002-02-14, 2002-02-22, 2002-02-23, 2002-03-21, 2002-03-22, 2002-03-23, 2002-03-23, 2002-04-24
Pegasus (WST)	2000-10-23, 2001-08-01, 2001-08-26, 2003-10-15, 2003-10-15, 2003-10-15, 2004-12-14, 2005-10-08
GR 08	2000-01-31, 2002-04-02
Aquarius	2000-08-23, 2000-08-25, 2001-07-22, 2001-07-27, 2001-07-30, 2001-08-13, 2001-10-17, 2003-09-14, 2003-09-15, 2004-08-08, 2004-10-03, 2005-11-14, 2099-07-17, 2099-07-17

During evaluation of the difference images several Small Solar System Bodies were detected. Since we did not go for any follow-up observations we did not report them to the Minor Planet Center. They are reported in Tab. E.1 only for documentation in case we decide to report the data at a later time. Arcsec astrometry and and 0.2 mag photometry is easily available.

E.2   High Proper Motion and Parallactic Stars

Objects moving more than 0.1 arcsec within the total observed period were detected with difference imaging. If they were bright (< 20 mag) they even had to be flagged for the reference kernel calculation (Sect. 4.3) and of course to be removed from the astrometry reference list

(Sect. 4.2.9). A list of those stars could be easily compiled but was beyond the scope of our project.

E.3   Background SN in the Leo A (CA) field

While we did not explicitly search for eruptive variables I glanced over a list of frequently, highly significant ($> 10\sigma$) outliers which were mostly due to nearby stars (see previous Sect.) and a few very bright Mirae. In case of the rather densely sampled Calar Alto data set this also chanced a Supernova in a background galaxy to show up. Fig. E.1 shows the light curve of the event but more importantly also illustrates one problem with difference photometry, highly crowded fields, and magnitudes: Magnitudes, being the logarithm of a flux ratio, always refer fluxes to some "known" standard. Difference photometry is able to provide changes in flux, and, if properly calibrated, even as an absolute quantity. As convincing a light curve might seem, the apparent mean magnitude (and therefore, of course, also the light curve amplitude) might be no more than a guess or an upper limit because it relies on the photometry of a deconvolved image of blending sources as reference. This has to be taken into account when looking at magnitude light curves built of difference photometry.
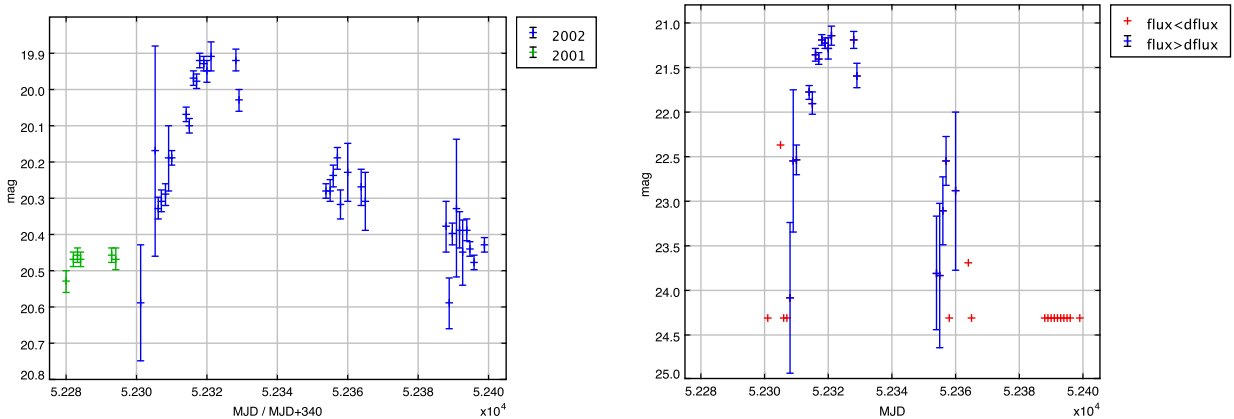
Figure E.1: The *R*-band light curve of a Supernova in a remote background galaxy. Left: Blue – apparent brightness with the local, unresolved galaxy background (≈ 20.45 mag per reference image PSF) as reference over Modified Julian Date MJD = JD − 2400000.5; green – data from previous year added with MJD + 340. Right: Blue – now referencing to zero flux displaying a pure "excess" magnitude; the lower limit (24.3 mag) corresponds to the 1σ noise from the skylight background of the reference image, smaller fluxes are clipped to this value; red – excess flux smaller than flux error resulting in a formally infinite magnitude error.

Appendix F

Periodic Variable Objects Remaining Tables

The parameters of all periodic variable objects of Tab. 4.4 which are not listed in Sect. 5 can be found here.

F.1   Leo A

Table F.1: Parameters of Leo A δ Cephei shortest period candidates: Short identifier (see Fig. G.3), IAU compliant identifier, position, most significant Lomb period(s), significance (p-level), flux averaged apparent R-band magnitude, r.m.s. error of R-band magnitude.

Id	IAU compliant name	RA-2000 [h]	Dec-2000 [deg]	period [d]	signific. [p]	$\langle R_f \rangle$ [mag]	$\delta \langle R_f \rangle$ [mag]
LS01	WST J095921.5+304442	09:59:21.484	+30:44:42.10	0.981	4.65e-05	21.93	0.38
LS02	WST J095935.0+304334	09:59:34.977	+30:43:33.54	0.941	4.09e-04	22.54	0.66
LS03	WST J095922.4+304438	09:59:22.359	+30:44:37.67	0.053	6.39e-03	23.16	1.16
LS04	WST J095922.8+304531	09:59:22.824	+30:45:30.60	0.086	7.31e-03	22.76	0.80
LS05	WST J095937.5+304545	09:59:37.477	+30:45:45.33	0.332	8.95e-03	22.93	0.94
LS06	WST J095925.2+304352	09:59:25.166	+30:43:52.48	0.076	1.42e-02	21.95	0.38
LS07	WST J095916.1+304617	09:59:16.058	+30:46:16.87	0.912	1.53e-02	20.17	0.07
LS08	WST J095926.0+304534	09:59:25.983	+30:45:33.94	0.054	2.79e-02	23.47	1.54
LS09	WST J095937.8+304644	09:59:37.832	+30:46:43.66	0.332	3.92e-02	22.30	0.53
LS10	WST J095921.5+304410	09:59:21.479	+30:44:09.74	0.815	4.58e-02	22.81	0.84
LS11	WST J095941.9+304552	09:59:41.893	+30:45:51.55	0.249	5.16e-02	22.62	0.71
LS12	WST J095932.3+304430	09:59:32.325	+30:44:30.50	0.125	5.31e-02	23.48	1.56
LS13	WST J095932.6+304447	09:59:32.595	+30:44:46.67	0.823	5.86e-02	22.77	0.81
LS14	WST J095933.5+304424	09:59:33.542	+30:44:23.59	0.822	7.22e-02	21.19	0.19
LS15	WST J095911.9+304558	09:59:11.869	+30:45:57.85	0.638	7.48e-02	21.20	0.19
LS16	WST J095917.4+304548	09:59:17.423	+30:45:47.91	0.057	7.70e-02	21.91	0.37
LS17	WST J095929.3+304613	09:59:29.263	+30:46:12.57	0.595	7.73e-02	21.01	0.16
LS18	WST J095932.0+304432	09:59:31.983	+30:44:32.47	0.408	7.88e-02	21.63	0.29

Id	IAU compliant name	RA-2000 [h]	Dec-2000 [deg]	period [d]	signific. [p]	$\langle R_f \rangle$ [mag]	$\delta \langle R_f \rangle$ [mag]
LS19	WST J095924.6+304422	09:59:24.639	+30:44:21.91	0.124	7.93e-02	22.44	0.60
LS20	WST J095929.8+304449	09:59:29.780	+30:44:49.21	0.184	9.04e-02	20.73	0.12
LS21	WST J095922.3+304434	09:59:22.320	+30:44:34.23	0.142	9.14e-02	22.80	0.84
LS22	WST J095917.9+304327	09:59:17.858	+30:43:27.19	0.232	9.45e-02	23.44	1.50
LS23	WST J095941.8+304553	09:59:41.779	+30:45:53.02	0.249	9.46e-02	22.37	0.56
LS24	WST J095919.3+304417	09:59:19.312	+30:44:17.16	0.166	9.65e-02	22.72	0.78
LS25	WST J095922.2+304407	09:59:22.201	+30:44:06.78	0.082	9.91e-02	21.01	0.16
LS26	WST J095922.9+304431	09:59:22.890	+30:44:31.28	0.965	1.04e-01	22.42	0.59
LS27	WST J095929.9+304649	09:59:29.879	+30:46:48.83	0.061	1.07e-01	23.21	1.22
LS28	WST J095914.8+304411	09:59:14.821	+30:44:11.39	0.107	1.17e-01	23.38	1.42
LS29	WST J095930.8+304445	09:59:30.806	+30:44:45.26	0.465	1.20e-01	22.44	0.60
LS30	WST J095925.4+304528	09:59:25.411	+30:45:27.58	0.260	1.25e-01	23.47	1.55
LS31	WST J095938.0+304606	09:59:38.015	+30:46:06.40	0.241	1.29e-01	23.31	1.34
LS32	WST J095925.2+304340	09:59:25.164	+30:43:40.22	0.604	1.32e-01	21.29	0.21
LS33	WST J095913.0+304402	09:59:13.032	+30:44:02.12	0.187	1.34e-01	23.36	1.40
LS34	WST J095936.4+304701	09:59:36.389	+30:47:00.87	0.071	1.35e-01	22.74	0.79
LS35	WST J095927.8+304612	09:59:27.817	+30:46:12.13	0.450	1.36e-01	23.06	1.06
LS36	WST J095941.9+304550	09:59:41.893	+30:45:50.08	0.332	1.36e-01	23.30	1.33
LS37	WST J095925.8+304409	09:59:25.778	+30:44:09.13	0.060	1.41e-01	20.91	0.15
LS38	WST J095931.8+304350	09:59:31.823	+30:43:49.82	0.138	1.43e-01	22.56	0.67
LS39	WST J095922.6+304610	09:59:22.640	+30:46:09.83	0.188	1.44e-01	22.83	0.85
LS40	WST J095922.2+304407	09:59:22.239	+30:44:06.78	0.082	1.49e-01	19.55	0.04
LS41	WST J095927.9+304622	09:59:27.856	+30:46:22.42	0.056	1.50e-01	22.99	0.99
LS42	WST J095922.4+304440	09:59:22.435	+30:44:40.11	0.268	1.52e-01	23.29	1.31
LS43	WST J095923.8+304458	09:59:23.770	+30:44:57.73	0.095	1.54e-01	19.88	0.06
LS44	WST J095916.2+304515	09:59:16.239	+30:45:15.09	0.162	1.85e-01	19.47	0.04
LS45	WST J095936.4+304703	09:59:36.352	+30:47:02.83	0.059	1.89e-01	22.63	0.71
LS46	WST J095918.6+304420	09:59:18.589	+30:44:19.63	0.093	1.89e-01	23.12	1.12
LS47	WST J095916.4+304519	09:59:16.353	+30:45:18.52	0.829	1.92e-01	23.44	1.50
LS48	WST J095921.1+304442	09:59:21.142	+30:44:41.62	0.140	1.99e-01	22.19	0.48
LS49	WST J095918.7+304623	09:59:18.684	+30:46:22.68	0.246	2.00e-01	20.27	0.08
LS50	WST J095927.4+304501	09:59:27.423	+30:45:00.56	0.095	2.02e-01	22.81	0.84
LS51	WST J095941.8+304554	09:59:41.779	+30:45:53.51	0.249	2.06e-01	22.12	0.45
LS52	WST J095932.8+304149	09:59:32.826	+30:41:49.18	0.710	2.12e-01	21.05	0.17
LS53	WST J095930.4+304535	09:59:30.359	+30:45:34.79	0.131	2.13e-01	22.74	0.79
LS54	WST J095920.5+304521	09:59:20.539	+30:45:21.35	0.302	2.14e-01	22.73	0.78
LS55	WST J095916.7+304440	09:59:16.690	+30:44:39.78	0.098	2.21e-01	19.89	0.06
LS56	WST J095931.3+304441	09:59:31.300	+30:44:41.32	0.269	2.30e-01	22.13	0.45
LS57	WST J095920.9+304639	09:59:20.856	+30:46:39.29	0.059	2.32e-01	21.35	0.22
LS58	WST J095924.9+304427	09:59:24.906	+30:44:27.30	0.736	2.44e-01	21.71	0.31
LS59	WST J095937.9+304624	09:59:37.866	+30:46:24.05	0.057	2.46e-01	23.48	1.56
LS60	WST J095915.3+304558	09:59:15.294	+30:45:58.25	0.314	2.46e-01	22.78	0.82
LS61	WST J095921.7+304259	09:59:21.734	+30:42:59.14	0.536	2.47e-01	20.08	0.07

Table F.2: Parameters of Leo A worst δ Cephei 1 d$< P < 10$ d period candidates: Short identifier (see Fig. G.4), IAU compliant identifier, position, most significant Lomb period(s), significance (p-level), flux averaged apparent R-band magnitude, r.m.s. error of R-band magnitude.

Id	IAU compliant name	RA-2000 [h]	Dec-2000 [deg]	period [d]	signific. [p]	$\langle R_f \rangle$ [mag]	$\delta \langle R_f \rangle$ [mag]
LM18	WST J095933.6+304512	09:59:33.627	+30:45:12.13	1.402	1.44e-02	22.85	0.87
LM19	WST J095919.6+304509	09:59:19.624	+30:45:09.12	1.265	2.68e-02	21.14	0.18
LM20	WST J095918.7+304402	09:59:18.662	+30:44:01.98	4.513	3.70e-02	22.67	0.74
LM21	WST J095928.3+304422	09:59:28.253	+30:44:22.29	5.848	3.70e-02	22.65	0.73
LM22	WST J095917.8+304642	09:59:17.812	+30:46:42.32	5.382	5.00e-02	20.71	0.12
LM23	WST J095917.7+304408	09:59:17.712	+30:44:08.37	2.103	5.39e-02	21.87	0.35
LM24	WST J095927.4+304413	09:59:27.414	+30:44:13.00	2.530	5.65e-02	23.40	1.45
LM25	WST J095921.9+304435	09:59:21.902	+30:44:34.74	6.599	6.52e-02	23.19	1.20
LM26	WST J095918.8+304519	09:59:18.827	+30:45:18.94	4.264	6.77e-02	20.88	0.14
LM27	WST J095915.2+304451	09:59:15.208	+30:44:51.09	3.988	7.71e-02	23.10	1.10
LL07a	WST J095924.9+304352	09:59:24.938	+30:43:52.00	1.090	7.74e-02	23.48	1.56
LM28	WST J095934.1+304338	09:59:34.141	+30:43:37.98	2.814	9.07e-02	23.22	1.22
LM29	WST J095927.6+304454	09:59:27.574	+30:44:54.18	1.013	9.26e-02	18.87	0.02
LM30	WST J095920.4+304449	09:59:20.420	+30:44:48.99	2.503	9.73e-02	22.85	0.87
LM31	WST J095920.4+304141	09:59:20.390	+30:41:41.22	6.659	1.21e-01	23.26	1.28
LM32	WST J095921.9+304436	09:59:21.940	+30:44:35.72	2.027	1.26e-01	22.71	0.77
LM33	WST J095915.2+304604	09:59:15.218	+30:46:03.65	1.830	1.35e-01	20.43	0.09
LM34	WST J095918.1+304613	09:59:18.150	+30:46:12.89	1.191	1.35e-01	22.81	0.84
LM35	WST J095933.6+304221	09:59:33.555	+30:42:20.54	1.264	1.43e-01	23.25	1.26
LM36	WST J095939.5+304334	09:59:39.504	+30:43:33.87	2.770	1.48e-01	23.30	1.33
LM37	WST J095919.3+304356	09:59:19.270	+30:43:55.59	5.477	1.52e-01	23.20	1.21
LM38	WST J095923.2+304429	09:59:23.156	+30:44:28.82	3.963	1.52e-01	22.47	0.61
LM39	WST J095925.1+304434	09:59:25.097	+30:44:33.66	1.562	1.56e-01	22.15	0.46
LM40	WST J095923.4+304445	09:59:23.425	+30:44:44.99	4.054	1.63e-01	22.61	0.70
LM41	WST J095926.6+304558	09:59:26.634	+30:45:58.43	2.155	1.65e-01	23.05	1.05
LM42	WST J095912.8+304629	09:59:12.824	+30:46:29.20	1.445	1.66e-01	23.09	1.09
LM43	WST J095932.1+304455	09:59:32.064	+30:44:54.53	3.897	1.67e-01	22.72	0.78
LM44	WST J095929.7+304520	09:59:29.671	+30:45:19.61	5.914	1.78e-01	21.53	0.26
LM45	WST J095929.7+304330	09:59:29.689	+30:43:29.79	1.499	1.84e-01	22.58	0.68
LM46	WST J095926.7+304150	09:59:26.742	+30:41:49.87	1.420	1.88e-01	21.66	0.29
LM47	WST J095926.6+304531	09:59:26.553	+30:45:31.47	1.021	1.88e-01	23.16	1.17
LM48	WST J095935.1+304447	09:59:35.106	+30:44:46.58	7.553	1.90e-01	20.80	0.13
LM49	WST J095923.4+304443	09:59:23.387	+30:44:43.03	4.054	1.92e-01	22.74	0.79
LM49a				1.320	2.27e-01		
LM50	WST J095918.9+304519	09:59:18.865	+30:45:18.94	4.264	1.96e-01	23.41	1.46
LM51	WST J095933.2+304444	09:59:33.203	+30:44:44.20	1.010	2.13e-01	22.71	0.77
LM52	WST J095927.4+304235	09:59:27.397	+30:42:35.44	1.740	2.16e-01	22.84	0.87
LM53	WST J095916.7+304443	09:59:16.728	+30:44:43.21	2.674	2.25e-01	22.69	0.75
LM54	WST J095925.7+304451	09:59:25.709	+30:44:50.81	8.390	2.30e-01	21.87	0.35

Id	IAU compliant name	RA-2000 [h]	Dec-2000 [deg]	period [d]	signific. [p]	$\langle R_f \rangle$ [mag]	$\delta \langle R_f \rangle$ [mag]
LM55	WST J095930.9+304357	09:59:30.949	+30:43:57.20	2.573	2.36e-01	21.81	0.34
LM56	WST J095920.9+304410	09:59:20.870	+30:44:10.25	1.440	2.37e-01	23.28	1.30
LS17a	WST J095929.3+304613	09:59:29.263	+30:46:12.57	3.120	2.53e-01	21.01	0.16
LS18a	WST J095932.0+304432	09:59:31.983	+30:44:32.47	2.230	3.46e-01	21.63	0.29
LS52a	WST J095932.8+304149	09:59:32.826	+30:41:49.18	2.440	3.68e-01	21.05	0.17

F.2   Pegasus

Table F.3: Parameters of Pegasus δ Cephei shortest period candidates: Short identifier (see Fig. G.6), IAU compliant identifier, position, most significant Lomb period(s), significance (p-level), flux averaged apparent R-band magnitude, r.m.s. error of R-band magnitude.

Id	IAU compliant name	RA-2000 [h]	Dec-2000 [deg]	period [d]	signific. [p]	$\langle R_f \rangle$ [mag]	$\delta \langle R_f \rangle$ [mag]
PS01	WST J232834.1+144442	23:28:34.055	+14:44:42.41	0.943	5.25e-03	21.50	0.40
PS02	WST J232830.2+144460	23:28:30.226	+14:44:59.59	0.914	5.45e-03	19.16	0.05
PS03	WST J232831.4+144409	23:28:31.406	+14:44:08.57	0.333	7.18e-03	21.77	0.52
PS04	WST J232834.0+144401	23:28:34.049	+14:44:00.71	0.157	1.06e-02	21.18	0.30
PS05	WST J232824.7+144639	23:28:24.712	+14:46:38.68	0.458	2.61e-02	22.43	0.95
PS06	WST J232826.9+144738	23:28:26.889	+14:47:38.03	0.978	3.67e-02	21.37	0.36
PS07	WST J232838.2+144328	23:28:38.214	+14:43:27.83	0.926	4.09e-02	21.16	0.29
PS08	WST J232850.0+144253	23:28:50.005	+14:42:52.93	0.074	6.09e-02	22.42	0.94
PS09	WST J232841.3+144155	23:28:41.319	+14:41:54.62	0.948	6.14e-02	21.23	0.31
PS10	WST J232821.2+144613	23:28:21.183	+14:46:13.18	0.344	6.20e-02	21.85	0.56
PS11	WST J232849.6+144606	23:28:49.627	+14:46:05.71	0.199	6.52e-02	22.29	0.83
PS12	WST J232827.7+144501	23:28:27.718	+14:45:00.57	0.902	7.05e-02	21.64	0.46
PS13	WST J232843.6+144537	23:28:43.622	+14:45:37.30	0.070	7.43e-02	22.55	1.06
PS14	WST J232821.8+144642	23:28:21.797	+14:46:41.63	0.902	7.64e-02	21.24	0.32
PS15	WST J232825.2+144453	23:28:25.174	+14:44:53.22	0.929	8.36e-02	21.73	0.50
PS16	WST J232833.5+144534	23:28:33.451	+14:45:33.91	0.072	8.37e-02	21.92	0.59
PS17	WST J232829.9+144725	23:28:29.939	+14:47:24.78	0.110	8.70e-02	21.25	0.32
PS18	WST J232831.4+144136	23:28:31.387	+14:41:36.02	0.626	8.75e-02	21.29	0.33
PS19	WST J232839.2+144328	23:28:39.197	+14:43:28.32	0.666	9.17e-02	22.58	1.09
PS20	WST J232841.5+144305	23:28:41.499	+14:43:04.76	0.509	9.41e-02	21.23	0.31
PS21	WST J232835.5+144522	23:28:35.517	+14:45:22.13	0.616	9.85e-02	22.19	0.76
PS22	WST J232819.1+144238	23:28:19.057	+14:42:38.33	0.087	9.93e-02	23.20	1.92
PS23	WST J232849.5+144214	23:28:49.524	+14:42:13.70	0.320	1.04e-01	20.87	0.23
PS24	WST J232829.7+144633	23:28:29.695	+14:46:32.79	0.877	1.10e-01	21.67	0.47
PS25	WST J232831.1+144325	23:28:31.095	+14:43:25.41	0.958	1.10e-01	18.74	0.03
PS26	WST J232818.0+144256	23:28:17.974	+14:42:55.99	0.632	1.19e-01	21.75	0.51
PS27	WST J232840.9+144259	23:28:40.888	+14:42:58.88	0.470	1.24e-01	20.61	0.18
PS28	WST J232838.6+144407	23:28:38.558	+14:44:06.58	0.903	1.30e-01	22.42	0.94

Id	IAU compliant name	RA-2000 [h]	Dec-2000 [deg]	period [d]	signific. [p]	$\langle R_f \rangle$ [mag]	$\delta \langle R_f \rangle$ [mag]
PS29	WST J232817.8+144504	23:28:17.751	+14:45:03.52	0.527	1.37e-01	22.77	1.30
PS30	WST J232821.3+144627	23:28:21.286	+14:46:26.91	0.507	1.38e-01	22.09	0.69
PS31	WST J232818.9+144628	23:28:18.879	+14:46:28.38	0.298	1.38e-01	22.34	0.87
PS32	WST J232831.0+144720	23:28:31.024	+14:47:19.87	0.978	1.41e-01	21.77	0.52
PS33	WST J232833.6+144513	23:28:33.584	+14:45:13.31	0.973	1.42e-01	23.36	2.23
PS34	WST J232834.7+144409	23:28:34.660	+14:44:09.05	0.258	1.46e-01	21.53	0.41
PS35	WST J232834.9+144256	23:28:34.922	+14:42:55.96	0.083	1.48e-01	21.96	0.62
PS36	WST J232848.2+144112	23:28:48.227	+14:41:12.39	0.980	1.51e-01	21.93	0.60
PS37	WST J232829.1+144460	23:28:29.107	+14:44:59.59	0.203	1.53e-01	23.19	1.90
PS38	WST J232832.2+144504	23:28:32.159	+14:45:03.51	0.080	1.57e-01	22.04	0.66
PS39	WST J232819.5+144336	23:28:19.504	+14:43:35.72	0.920	1.58e-01	20.00	0.10
PS40	WST J232818.4+144731	23:28:18.412	+14:47:31.17	0.273	1.59e-01	22.40	0.93
PS41	WST J232821.9+144640	23:28:21.898	+14:46:40.15	0.902	1.62e-01	21.02	0.26
PS42	WST J232827.5+144500	23:28:27.480	+14:45:00.08	0.085	1.63e-01	21.51	0.41
PS43	WST J232817.9+144649	23:28:17.864	+14:46:48.98	0.344	1.66e-01	22.57	1.08
PS44	WST J232848.7+144831	23:28:48.700	+14:48:31.40	0.507	1.68e-01	21.98	0.63
PS45	WST J232835.4+144337	23:28:35.436	+14:43:37.16	0.103	1.76e-01	22.74	1.26
PS46	WST J232823.7+144509	23:28:23.718	+14:45:08.92	0.167	1.83e-01	21.58	0.43
PS47	WST J232842.5+144640	23:28:42.546	+14:46:40.09	0.055	1.85e-01	22.23	0.79
PS48	WST J232840.2+144326	23:28:40.180	+14:43:25.86	0.127	1.86e-01	21.82	0.54
PS49	WST J232825.2+144442	23:28:25.207	+14:44:42.43	0.927	1.87e-01	22.08	0.69
PS50	WST J232828.4+144337	23:28:28.385	+14:43:37.19	0.988	1.95e-01	21.52	0.41
PS51	WST J232825.8+144522	23:28:25.754	+14:45:21.67	0.605	1.98e-01	23.34	2.19
PS52	WST J232822.6+144759	23:28:22.619	+14:47:59.13	0.905	2.01e-01	23.14	1.82
PS53	WST J232831.5+144532	23:28:31.485	+14:45:32.45	0.981	2.05e-01	21.50	0.40
PS54	WST J232823.9+144611	23:28:23.861	+14:46:11.21	0.825	2.05e-01	22.85	1.40
PS55	WST J232844.0+144815	23:28:43.984	+14:48:15.24	0.471	2.06e-01	23.30	2.11
PS56	WST J232823.8+144613	23:28:23.760	+14:46:12.68	0.825	2.07e-01	22.28	0.83
PS57	WST J232821.0+144611	23:28:21.013	+14:46:11.21	0.706	2.08e-01	22.53	1.04
PS58	WST J232846.3+144834	23:28:46.258	+14:48:34.36	0.239	2.08e-01	18.22	0.02
PS59	WST J232821.4+144618	23:28:21.421	+14:46:18.08	0.344	2.14e-01	22.94	1.52
PS60	WST J232820.8+144801	23:28:20.755	+14:48:01.09	0.247	2.15e-01	22.72	1.24
PS61	WST J232850.0+144234	23:28:50.036	+14:42:34.29	0.067	2.16e-01	22.74	1.26
PS62	WST J232819.7+144344	23:28:19.674	+14:43:43.57	0.368	2.20e-01	21.39	0.36
PS63	WST J232830.5+144337	23:28:30.487	+14:43:37.18	0.224	2.26e-01	21.77	0.51
PS64	WST J232822.4+144316	23:28:22.383	+14:43:15.61	0.444	2.26e-01	22.05	0.67
PS65	WST J232823.3+144640	23:28:23.322	+14:46:40.15	0.902	2.37e-01	22.70	1.22
PS66	WST J232821.4+144618	23:28:21.421	+14:46:17.59	0.344	2.41e-01	22.11	0.71
PS67	WST J232830.1+144135	23:28:30.065	+14:41:34.55	0.073	2.46e-01	22.59	1.10
PS68	WST J232833.7+144504	23:28:33.651	+14:45:03.99	0.871	2.48e-01	22.15	0.73

Table F.4: Parameters of Pegasus worst δ Cephei 1 d< P < 10 d period candidates: Short identifier (see Fig. G.6), IAU compliant identifier, position, most significant Lomb period(s), significance (p-level), flux averaged apparent R-band magnitude, r.m.s. error of R-band magnitude.

Id	IAU compliant name	RA-2000 [h]	Dec-2000 [deg]	period [d]	signific. [p]	$\langle R_f \rangle$ [mag]	
PM15	WST J232831.3+144419	23:28:31.340	+14:44:19.36	3.348	1.30e-02	22.17	0.74
PM15a				1.420	7.94e-02		
PM16	WST J232844.6+144653	23:28:44.582	+14:46:52.83	1.031	1.97e-02	22.49	1.00
PM17	WST J232841.9+144323	23:28:41.942	+14:43:23.40	1.853	2.11e-02	22.46	0.98
PM18	WST J232839.9+144420	23:28:39.882	+14:44:20.31	2.736	2.63e-02	21.87	0.57
PM19	WST J232832.4+144428	23:28:32.392	+14:44:28.19	7.374	3.26e-02	21.27	0.33
PM20	WST J232836.2+144353	23:28:36.184	+14:43:53.35	1.848	3.59e-02	23.19	1.91
PM21	WST J232819.1+144407	23:28:19.135	+14:44:06.62	4.556	3.75e-02	21.03	0.26
PM22	WST J232825.3+144556	23:28:25.317	+14:45:56.50	1.021	3.98e-02	22.27	0.82
PM23	WST J232829.1+144446	23:28:29.072	+14:44:45.86	4.694	4.21e-02	22.20	0.77
PM24	WST J232819.7+144403	23:28:19.677	+14:44:03.19	6.888	4.70e-02	22.17	0.75
PM25	WST J232844.5+144653	23:28:44.548	+14:46:53.32	1.031	4.89e-02	22.84	1.38
PM26	WST J232823.4+144144	23:28:23.355	+14:41:43.88	8.949	4.95e-02	23.07	1.71
PM27	WST J232834.0+144505	23:28:33.990	+14:45:05.46	2.335	6.49e-02	21.75	0.51
PM28	WST J232825.7+144305	23:28:25.704	+14:43:05.31	1.053	7.05e-02	22.89	1.46
PM29	WST J232839.2+144251	23:28:39.226	+14:42:51.04	5.172	7.17e-02	22.92	1.49
PM30	WST J232833.8+144309	23:28:33.771	+14:43:08.72	7.635	7.66e-02	22.94	1.52
PM31	WST J232849.7+144506	23:28:49.652	+14:45:05.86	1.031	7.95e-02	22.01	0.65
PM32	WST J232825.2+144633	23:28:25.152	+14:46:33.28	5.341	8.24e-02	20.77	0.20
PM32a				1.230	3.78e-01		
PM33	WST J232832.8+144545	23:28:32.842	+14:45:45.20	1.054	8.61e-02	21.24	0.32
PM34	WST J232843.0+144501	23:28:42.973	+14:45:00.51	1.832	8.77e-02	23.33	2.18
PM35	WST J232832.4+144447	23:28:32.360	+14:44:46.83	8.593	9.68e-02	22.16	0.74
PM36	WST J232833.8+144246	23:28:33.836	+14:42:45.67	8.609	9.69e-02	23.06	1.70
PM37	WST J232848.7+144215	23:28:48.711	+14:42:14.68	1.126	1.06e-01	18.40	0.02
PM38	WST J232845.7+144637	23:28:45.733	+14:46:37.13	3.816	1.10e-01	22.26	0.81
PM39	WST J232837.9+144546	23:28:37.928	+14:45:45.67	1.879	1.18e-01	23.13	1.81
PM40	WST J232830.5+144541	23:28:30.469	+14:45:41.28	1.621	1.20e-01	22.87	1.42
PM41	WST J232822.6+144757	23:28:22.585	+14:47:56.67	6.895	1.21e-01	22.93	1.51
PM42	WST J232835.6+144410	23:28:35.643	+14:44:09.54	3.737	1.22e-01	21.59	0.44
PM43	WST J232833.7+144553	23:28:33.691	+14:45:53.04	9.460	1.23e-01	23.12	1.79
PM44	WST J232830.0+144326	23:28:30.045	+14:43:26.39	2.724	1.26e-01	21.05	0.27
PM45	WST J232818.2+144649	23:28:18.170	+14:46:48.98	1.358	1.30e-01	22.84	1.39
PM46	WST J232818.3+144727	23:28:18.343	+14:47:27.24	8.994	1.34e-01	23.12	1.80
PS08a	WST J232850.0+144253	23:28:50.005	+14:42:52.93	1.070	1.36e-01	22.42	0.94
PM47	WST J232820.0+144338	23:28:20.047	+14:43:37.68	9.224	1.39e-01	22.00	0.64
PM48	WST J232836.9+144415	23:28:36.865	+14:44:14.93	5.082	1.49e-01	21.33	0.34
PM49	WST J232829.6+144400	23:28:29.574	+14:44:00.24	1.048	1.52e-01	23.10	1.76
PM50	WST J232820.2+144156	23:28:20.238	+14:41:55.66	1.111	1.53e-01	23.30	2.12

Id	IAU compliant name	RA-2000 [h]	Dec-2000 [deg]	period [d]	signific. [p]	$\langle R_f \rangle$ [mag]	
PM51	WST J232834.6+144515	23:28:34.635	+14:45:14.78	3.309	1.54e-01	21.40	0.37
PM52	WST J232849.7+144153	23:28:49.657	+14:41:52.60	2.000	1.59e-01	21.69	0.48
PM53	WST J232837.0+144257	23:28:37.024	+14:42:56.94	6.534	1.65e-01	21.27	0.32
PM54	WST J232840.1+144342	23:28:40.080	+14:43:42.05	3.736	1.73e-01	21.25	0.32
PM55	WST J232826.7+144303	23:28:26.652	+14:43:02.85	1.633	1.84e-01	21.78	0.52
PM56	WST J232823.5+144631	23:28:23.457	+14:46:30.83	3.857	1.86e-01	23.40	2.31
PM57	WST J232841.5+144446	23:28:41.547	+14:44:46.30	3.288	1.89e-01	22.32	0.86
PM58	WST J232830.5+144326	23:28:30.485	+14:43:25.90	1.811	1.90e-01	19.81	0.09
PM59	WST J232837.5+144416	23:28:37.475	+14:44:16.40	1.682	1.95e-01	21.76	0.51
PM60	WST J232839.8+144518	23:28:39.755	+14:45:17.70	1.019	1.96e-01	21.92	0.59
PM61	WST J232825.0+144438	23:28:24.969	+14:44:37.52	5.133	1.96e-01	21.82	0.54
PM62	WST J232845.8+144335	23:28:45.808	+14:43:35.15	1.801	2.04e-01	22.54	1.05
PM63	WST J232824.8+144427	23:28:24.764	+14:44:27.22	5.638	2.06e-01	21.48	0.40
PM63a				6.830	2.64e-01		
PM64	WST J232844.7+144104	23:28:44.701	+14:41:04.08	5.949	2.13e-01	22.76	1.29
PM65	WST J232827.5+144455	23:28:27.480	+14:44:55.18	1.678	2.20e-01	22.48	0.99
PM66	WST J232821.1+144647	23:28:21.085	+14:46:46.53	3.248	2.25e-01	22.29	0.83
PM67	WST J232824.3+144613	23:28:24.336	+14:46:13.17	1.358	2.29e-01	22.37	0.90
PM68	WST J232838.4+144410	23:28:38.423	+14:44:10.02	6.493	2.33e-01	22.89	1.45
PM69	WST J232842.2+144444	23:28:42.157	+14:44:43.84	6.656	2.33e-01	23.18	1.89
PM70	WST J232849.3+144110	23:28:49.345	+14:41:10.42	1.311	2.33e-01	23.21	1.94
PM71	WST J232830.1+144452	23:28:30.123	+14:44:52.23	9.316	2.47e-01	23.12	1.80
PS12a	WST J232827.7+144501	23:28:27.718	+14:45:00.57	9.470	3.06e-01	21.64	0.46
PS39a	WST J232819.5+144336	23:28:19.504	+14:43:35.72	3.470	3.34e-01	20.00	0.10
PS28a	WST J232838.6+144407	23:28:38.558	+14:44:06.58	9.570	3.35e-01	22.42	0.94

Table F.5: Parameters of Pegasus worst long δ Cephei 10 d$\leq P \leq$ 130 d period candidates: Short identifier (see Fig. G.6), IAU compliant identifier, position, most significant Lomb period(s), significance (p-level), flux averaged apparent R-band magnitude, r.m.s. error of R-band magnitude.

Id	IAU compliant name	RA-2000 [h]	Dec-2000 [deg]	period [d]	signific. [p]	$\langle R_f \rangle$ [mag]
PL34	WST J232817.9+144509	23:28:17.853	+14:45:08.92	27.517	1.01e-02	22.37±0.90
PL35	WST J232823.1+144312	23:28:23.060	+14:43:11.69	103.795	1.27e-02	21.20±0.31
PL36	WST J232835.7+144414	23:28:35.746	+14:44:13.95	125.173	1.35e-02	21.74±0.50
PL36a				93.310	1.50e-02	
PL37	WST J232842.7+144425	23:28:42.730	+14:44:24.71	86.419	1.66e-02	21.98±0.63
PL37a				70.120	2.06e-02	
PL38	WST J232827.9+144243	23:28:27.904	+14:42:43.23	39.285	1.66e-02	21.37±0.36
PL38a				44.000	2.61e-02	
PL39	WST J232833.6+144528	23:28:33.552	+14:45:28.03	111.869	1.82e-02	21.27±0.33
PL40	WST J232824.7+144616	23:28:24.675	+14:46:16.12	29.845	2.21e-02	21.94±0.60
PL41	WST J232843.8+144238	23:28:43.834	+14:42:37.77	121.116	2.22e-02	21.02±0.26

Id	IAU compliant name	RA-2000 [h]	Dec-2000 [deg]	period [d]	signific. [p]	$\langle R_f \rangle$ [mag]
PL42	WST J232840.9+144343	23:28:40.894	+14:43:43.02	40.895	2.36e-02	21.61±0.44
PL43	WST J232825.2+144453	23:28:25.208	+14:44:52.73	20.605	3.16e-02	22.52±1.03
PL44	WST J232835.8+144423	23:28:35.849	+14:44:22.78	21.237	3.24e-02	20.35±0.14
PL44a				78.110	1.03e-01	
PL45	WST J232827.0+144256	23:28:26.957	+14:42:55.98	21.791	3.48e-02	23.27±2.06
PL46	WST J232834.8+144536	23:28:34.841	+14:45:35.87	53.854	3.80e-02	20.80±0.21
PL47	WST J232831.1+144329	23:28:31.096	+14:43:29.33	110.415	3.84e-02	22.09±0.69
PL48	WST J232825.8+144525	23:28:25.788	+14:45:25.10	81.495	3.87e-02	21.21±0.31
PL48a				104.970	5.80e-02	
PL49	WST J232829.0+144557	23:28:29.013	+14:45:57.47	38.774	4.28e-02	21.09±0.28
PL50	WST J232835.9+144316	23:28:35.907	+14:43:15.58	88.871	4.90e-02	21.46±0.39
PL51	WST J232822.6+144421	23:28:22.594	+14:44:21.34	103.983	5.34e-02	19.13±0.05
PL52	WST J232831.8+144451	23:28:31.750	+14:44:51.24	89.555	5.76e-02	21.25±0.32
PL52a				117.510	1.05e-01	
PL53	WST J232824.9+144605	23:28:24.911	+14:46:04.83	16.614	6.16e-02	23.04±1.66
PS09a	WST J232841.3+144155	23:28:41.319	+14:41:54.62	89.640	6.54e-02	21.23±0.31
PL54	WST J232831.0+144325	23:28:30.994	+14:43:24.92	23.539	6.60e-02	16.92±0.01
PL55	WST J232843.9+144231	23:28:43.867	+14:42:30.90	15.071	7.09e-02	21.96±0.62
PL56	WST J232834.1+144458	23:28:34.057	+14:44:57.61	28.043	7.97e-02	21.20±0.31
PL56a				82.870	8.46e-02	
PL57	WST J232849.8+144247	23:28:49.834	+14:42:47.05	49.787	8.72e-02	21.32±0.34
PL58	WST J232833.2+144519	23:28:33.178	+14:45:19.20	12.554	8.94e-02	21.32±0.34
PM19a	WST J232832.4+144428	23:28:32.392	+14:44:28.19	35.980	1.01e-01	21.27±0.33
PL59	WST J232838.0+144611	23:28:37.999	+14:46:10.68	84.148	1.13e-01	20.79±0.21
PS24a	WST J232829.7+144633	23:28:29.695	+14:46:32.79	38.580	1.20e-01	21.67±0.47
PL60	WST J232826.8+144628	23:28:26.847	+14:46:28.38	20.118	1.26e-01	21.65±0.46
PL61	WST J232847.3+144154	23:28:47.284	+14:41:54.09	13.629	1.40e-01	22.25±0.81
PL62	WST J232835.9+144502	23:28:35.854	+14:45:01.53	108.390	1.42e-01	23.08±1.73
PL63	WST J232836.3+144648	23:28:36.275	+14:46:47.97	11.887	1.43e-01	23.35±2.21
PL64	WST J232830.0+144414	23:28:29.983	+14:44:13.97	23.264	1.45e-01	21.41±0.37
PL65	WST J232848.6+144210	23:28:48.609	+14:42:10.27	97.572	1.47e-01	19.72±0.08
PL66	WST J232837.5+144229	23:28:37.528	+14:42:28.97	27.541	1.61e-01	22.03±0.65
PL67	WST J232824.6+144548	23:28:24.604	+14:45:48.16	16.555	1.64e-01	22.60±1.11
PL68	WST J232831.2+144543	23:28:31.215	+14:45:43.24	114.680	1.67e-01	18.33±0.02
PL69	WST J232825.1+144650	23:28:25.086	+14:46:49.96	33.229	1.69e-01	21.70±0.49
PL70	WST J232833.6+144546	23:28:33.554	+14:45:46.18	13.914	1.82e-01	21.98±0.62
PL71	WST J232824.5+144843	23:28:24.456	+14:48:43.27	27.257	1.91e-01	23.11±1.77
PL72	WST J232838.1+144430	23:28:38.121	+14:44:29.64	93.604	2.11e-01	19.20±0.05
PL72a				110.410	3.11e-01	
PL73	WST J232843.9+144230	23:28:43.934	+14:42:30.41	63.583	2.17e-01	21.16±0.29
PS07a	WST J232838.2+144328	23:28:38.214	+14:43:27.83	12.820	2.24e-01	21.16±0.29
PL74	WST J232839.9+144334	23:28:39.944	+14:43:34.20	43.307	2.33e-01	22.83±1.37
PL75	WST J232834.1+144603	23:28:34.133	+14:46:03.34	73.130	2.41e-01	23.04±1.67

Id	IAU compliant name	RA-2000 [h]	Dec-2000 [deg]	period [d]	signific. [p]	$\langle R_f \rangle$ [mag]
PS15*a*	WST J232825.2+144453	23:28:25.174	+14:44:53.22	20.580	3.25e-01	21.73±0.50
PS06*a*	WST J232826.9+144738	23:28:26.889	+14:47:38.03	83.390	3.35e-01	21.37±0.36

F.3   EGB 0427+63

Table F.6:   Parameters of EGB 0427+63 VS short and medium period candidates: Short identifier (see Fig. 5.16), IAU compliant identifier, position, most significant Lomb period(s), significance (*p*-level), flux averaged apparent *R*-band magnitude, r.m.s. error of *R*-band magnitude.

Id	IAU compliant name	RA-2000 [h]	Dec-2000 [deg]	period [d]	signific. [p]	$\langle R_f \rangle$ [mag]
ES01	WST J043139.7+633430	04:31:39.682	+63:34:30.11	0.249	1.97e-03	21.80±0.16
ES02	WST J043140.1+633428	04:31:40.124	+63:34:27.66	0.332	3.07e-03	21.31±0.10
ES03	WST J043231.0+633649	04:32:30.986	+63:36:49.16	0.195	2.15e-02	20.79±0.06
ES04	WST J043143.7+633349	04:31:43.661	+63:33:49.44	0.137	3.54e-02	19.37±0.02
ES05	WST J043153.5+633544	04:31:53.480	+63:35:44.36	0.141	6.99e-02	19.06±0.01
ES06	WST J043202.2+633349	04:32:02.240	+63:33:48.63	0.432	9.00e-02	19.09±0.01
ES07	WST J043143.2+633347	04:31:43.221	+63:33:46.98	0.249	1.05e-01	21.03±0.08
ES08	WST J043143.1+633726	04:31:43.086	+63:37:25.80	0.200	1.27e-01	19.66±0.02
ES09	WST J043147.4+633622	04:31:47.443	+63:36:22.08	0.132	1.32e-01	18.98±0.01
ES10	WST J043203.4+633402	04:32:03.413	+63:34:02.38	0.985	1.32e-01	18.25±0.01
ES11	WST J043206.3+633945	04:32:06.260	+63:39:45.34	0.227	1.45e-01	19.70±0.02
ES12	WST J043157.0+633837	04:31:56.985	+63:38:37.09	0.225	1.50e-01	20.67±0.06
ES13	WST J043135.8+633432	04:31:35.788	+63:34:32.01	0.258	1.55e-01	21.42±0.11
ES14	WST J043152.1+633645	04:31:52.072	+63:36:44.69	0.108	1.55e-01	18.20±0.01
ES15	WST J043213.8+633316	04:32:13.842	+63:33:15.79	0.789	1.72e-01	20.52±0.05
ES16	WST J043213.1+634002	04:32:13.113	+63:40:02.03	0.200	1.85e-01	20.00±0.03
ES17	WST J043223.1+633901	04:32:23.056	+63:39:00.69	0.212	1.94e-01	21.65±0.14
ES18	WST J043221.9+633905	04:32:21.878	+63:39:05.11	0.473	1.99e-01	17.64±0.00
ES19	WST J043208.3+633709	04:32:08.328	+63:37:09.33	0.554	2.22e-01	21.85±0.17
EM01	WST J043152.4+633436	04:31:52.391	+63:34:36.15	1.014	3.20e-02	21.85±0.17
EM02	WST J043220.7+633716	04:32:20.690	+63:37:15.70	1.027	1.33e-01	21.04±0.08
EM03	WST J043147.1+633413	04:31:47.107	+63:34:12.55	2.966	1.97e-01	21.10±0.09
EM04	WST J043209.6+633745	04:32:09.578	+63:37:45.14	1.034	1.99e-01	20.67±0.06
EM05	WST J043203.5+633633	04:32:03.475	+63:36:33.00	5.753	2.38e-01	21.04±0.08
EM06	WST J043203.9+633520	04:32:03.922	+63:35:20.39	5.264	2.44e-01	19.87±0.03

Table F.7:   Parameters of EGB 0427+63 longer period VS candidates: Short identifier (see Fig. 5.16), IAU compliant identifier, position, most significant Lomb period(s), significance (*p*-level), flux averaged apparent *R*-band magnitude, r.m.s. error of *R*-band magnitude.

Id	IAU compliant name	RA-2000 [h]	Dec-2000 [deg]	period [d]	signific. [*p*]	$\langle R_f \rangle$ [mag]
EL01	WST J043200.0+633324	04:32:00.039	+63:33:23.60	26.314	1.21e-02	19.43±0.02
EL02	WST J043159.4+633646	04:31:59.428	+63:36:46.23	29.537	3.19e-02	21.78±0.16
EL03	WST J043141.4+633433	04:31:41.371	+63:34:32.59	14.066	3.58e-02	19.89±0.03
EL04	WST J043214.0+633759	04:32:13.995	+63:37:58.89	29.537	5.81e-02	20.77±0.06
EL05	WST J043132.3+633733	04:31:32.339	+63:37:32.99	15.256	7.13e-02	16.36±0.00
EL06	WST J043143.0+633345	04:31:43.001	+63:33:45.02	72.505	8.11e-02	21.27±0.10
EL07	WST J043143.5+633405	04:31:43.509	+63:34:05.14	14.098	1.07e-01	21.76±0.16
EL08	WST J043206.7+633830	04:32:06.706	+63:38:30.27	13.175	1.40e-01	17.16±0.00
EL09	WST J043148.0+633405	04:31:47.990	+63:34:04.71	14.098	1.64e-01	21.85±0.17
EL10	WST J043218.1+633734	04:32:18.116	+63:37:33.86	48.874	1.79e-01	18.34±0.01
EL11	WST J043213.6+633813	04:32:13.627	+63:38:13.12	11.099	1.99e-01	20.90±0.07
EL12	WST J043218.9+633632	04:32:18.921	+63:36:31.55	52.986	2.03e-01	20.13±0.03
EL13	WST J043140.1+633546	04:31:40.100	+63:35:45.67	72.965	2.39e-01	17.69±0.00
EL14	WST J043136.2+633740	04:31:36.237	+63:37:40.42	25.531	2.46e-01	20.23±0.04
EL15	WST J043206.7+633832	04:32:06.705	+63:38:32.24	24.681	2.48e-01	20.25±0.04

F.4   GR 08

Table F.8:   Parameters of GR 08 *δ* Cephei shortest period candidates: Short identifier (see Fig. 5.20), IAU compliant identifier, position, most significant Lomb period(s), significance (*p*-level), flux averaged apparent *R*-band magnitude, r.m.s. error of *R*-band magnitude.

Id	IAU compliant name	RA-2000 [h]	Dec-2000 [deg]	period [d]	signific. [*p*]	$\langle R_f \rangle$ [mag]
GS01	WST J125841.4+141317	12:58:41.442	+14:13:16.99	0.983	5.94e-03	18.79±0.01
GS02	WST J125837.6+141554	12:58:37.578	+14:15:54.12	0.102	2.32e-02	20.14±0.02
GS03	WST J125827.2+141141	12:58:27.250	+14:11:41.10	0.329	5.49e-02	20.73±0.04
GS04	WST J125840.8+141329	12:58:40.836	+14:13:29.27	0.164	5.85e-02	20.87±0.04
GS05	WST J125838.1+141238	12:58:38.061	+14:12:37.80	0.196	8.08e-02	22.70±0.23
GS06	WST J125833.3+141043	12:58:33.320	+14:10:42.57	0.887	9.52e-02	21.66±0.09
GS07	WST J125836.9+141620	12:58:36.940	+14:16:19.66	0.064	1.10e-01	22.92±0.28
GS08	WST J125838.5+141228	12:58:38.465	+14:12:28.47	0.414	1.37e-01	18.93±0.01
GS09	WST J125840.4+141303	12:58:40.427	+14:13:03.27	0.899	1.94e-01	17.16±0.00
GS10	WST J125836.5+141023	12:58:36.491	+14:10:23.36	0.409	2.14e-01	22.99±0.29

F.5   Aquarius

Table F.9:   Parameters of Aquarius δ Cephei shortest period candidates: Short identifier (see Fig. 5.22), IAU compliant identifier, position, most significant Lomb period(s), significance (p-level), flux averaged apparent R-band magnitude, r.m.s. error of R-band magnitude.

Id	IAU compliant name	RA-2000 [h]	Dec-2000 [deg]	period [d]	signific. [p]	$\langle R_f \rangle$ [mag]
AS01	WST J204650.4-125023	20:46:50.445	-12:50:23.04	0.250	6.51e-04	20.94±0.13
AS02	WST J204653.2-125025	20:46:53.230	-12:50:25.16	0.200	9.84e-03	22.26±0.46
AS03	WST J204657.3-124658	20:46:57.252	-12:46:57.84	0.250	1.89e-02	20.14±0.06
AS04	WST J204653.5-124719	20:46:53.458	-12:47:19.21	0.143	2.05e-02	22.12±0.40
AS05	WST J204704.4-125022	20:47:04.370	-12:50:21.84	0.333	2.30e-02	19.39±0.03
AS06	WST J204701.4-125041	20:47:01.448	-12:50:40.82	0.398	2.71e-02	22.06±0.38
AS07	WST J204652.4-125437	20:46:52.354	-12:54:36.81	0.510	5.83e-02	18.98±0.02
AS08	WST J204700.2-125102	20:47:00.238	-12:51:01.85	0.332	7.14e-02	16.74±0.00
AS09	WST J204703.5-125002	20:47:03.500	-12:50:01.68	0.539	7.97e-02	19.13±0.03
AS10	WST J204638.8-124724	20:46:38.763	-12:47:24.25	0.062	8.00e-02	19.17±0.03
AS11	WST J204639.9-125052	20:46:39.904	-12:50:51.86	0.082	9.83e-02	22.62±0.64
AS12	WST J204651.7-125033	20:46:51.719	-12:50:32.92	0.108	1.34e-01	21.74±0.28
AS13	WST J204647.4-124716	20:46:47.386	-12:47:15.93	0.967	1.85e-01	21.44±0.21
AS14	WST J204651.9-125046	20:46:51.884	-12:50:45.69	0.171	1.95e-01	21.21±0.17
AS15	WST J204705.7-124819	20:47:05.661	-12:48:19.25	0.224	2.09e-01	19.52±0.04

Appendix G

Additional CMDs & Finding Charts
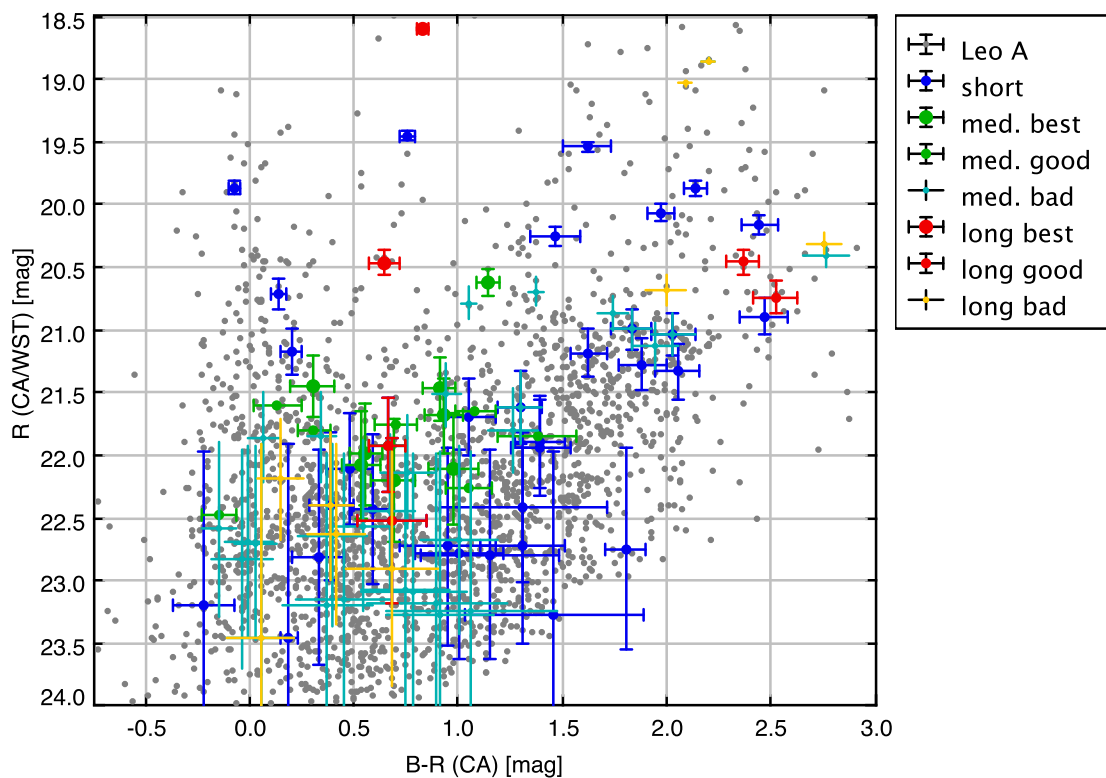
Figure G.1: Leo A CMD (all VS candidates)– grey: CA R-band (uncorrected) vs. CA $B - R$ colour (extinction correction after Schlegel et al., 1998, $A_R = 0.055$, $A_B = 0.89$); other colours (VS candidates): WST R-band (uncorrected) and propagated errors vs. CA $B - R$ colour (extinction correction after Schlegel et al., 1998) and DAOPHOT errors; blue: $P < 1$ d, $p < 0.25$, Tab. F.1; green: 1 d$< P < 10$ d, $p < 0.01$, Tab. 5.1; turquoise: 1 d$< P < 10$ d, $0.25 > p > 0.01$, Tab. F.2; red: $P > 10$ d, $p < 0.01$, Tab. 5.2 top. yellow: $P > 10$ d, $0.25 > p > 0.01$, Tab. 5.2 bottom.
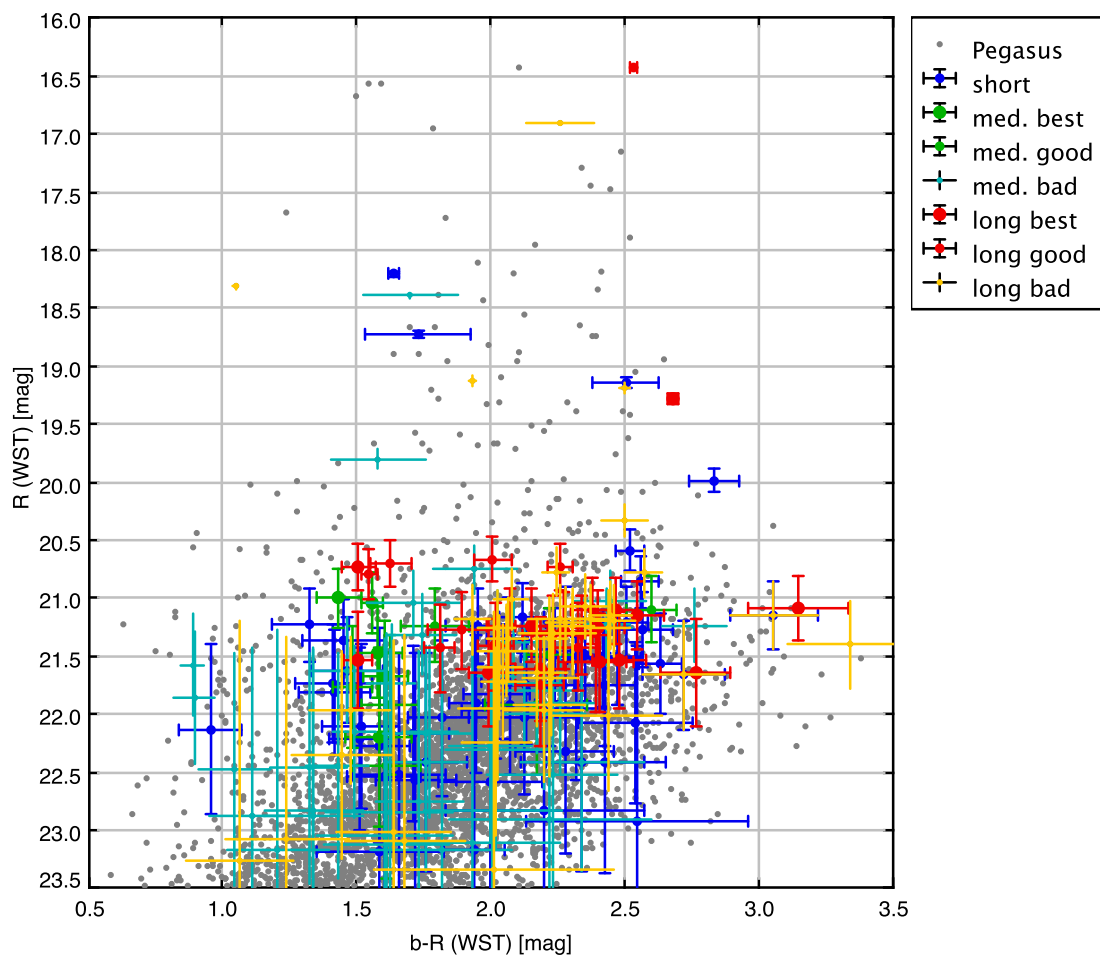
Figure G.2:   Pegasus Dwarf CMD (all VS candidates) – WST R-band (uncorrected) vs. WST $b-R$ colour (extinction correction after Schlegel et al., 1998, $A_R = 0.176$, $A_B 0.284$); WST R-band propagated brightness errors, WST $b - R$ DAOPHOT colour errors. Please note the discussion of the WST b-band calibration and the derived colour in the text. Blue: $P < 1$ d, $p < 0.25$, Tab. F.3; green: 1 d$< P < 10$ d, $p < 0.01$, Tab. 5.5; turquoise: 1 d$< P < 10$ d, $0.25 > p > 0.01$, Tab. F.4; red: $P > 10$ d, $p < 0.01$, Tab. 5.6; yellow: $P > 10$ d, $0.25 > p > 0.01$, Tab. F.5.
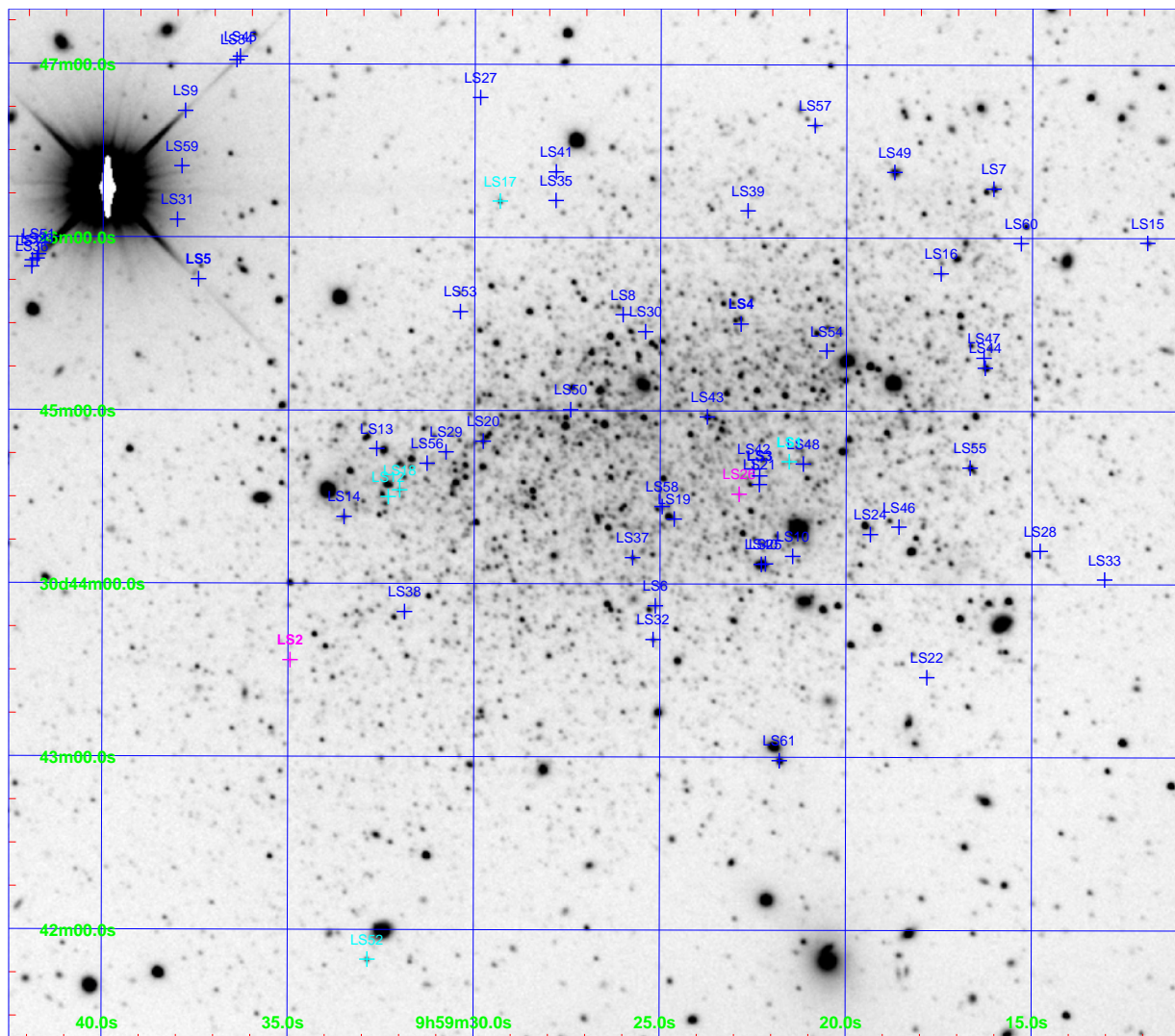
Figure G.3: Finding chart of shortest period $P < 1\,\mathrm{d}$ VS candidates of Tab. F.1. Bold: high Lomb significance $p < 0.01$; blue: LS short period pulsating B-star candidates; cyan and magenta: Candidates with interesting secondary period solutions.
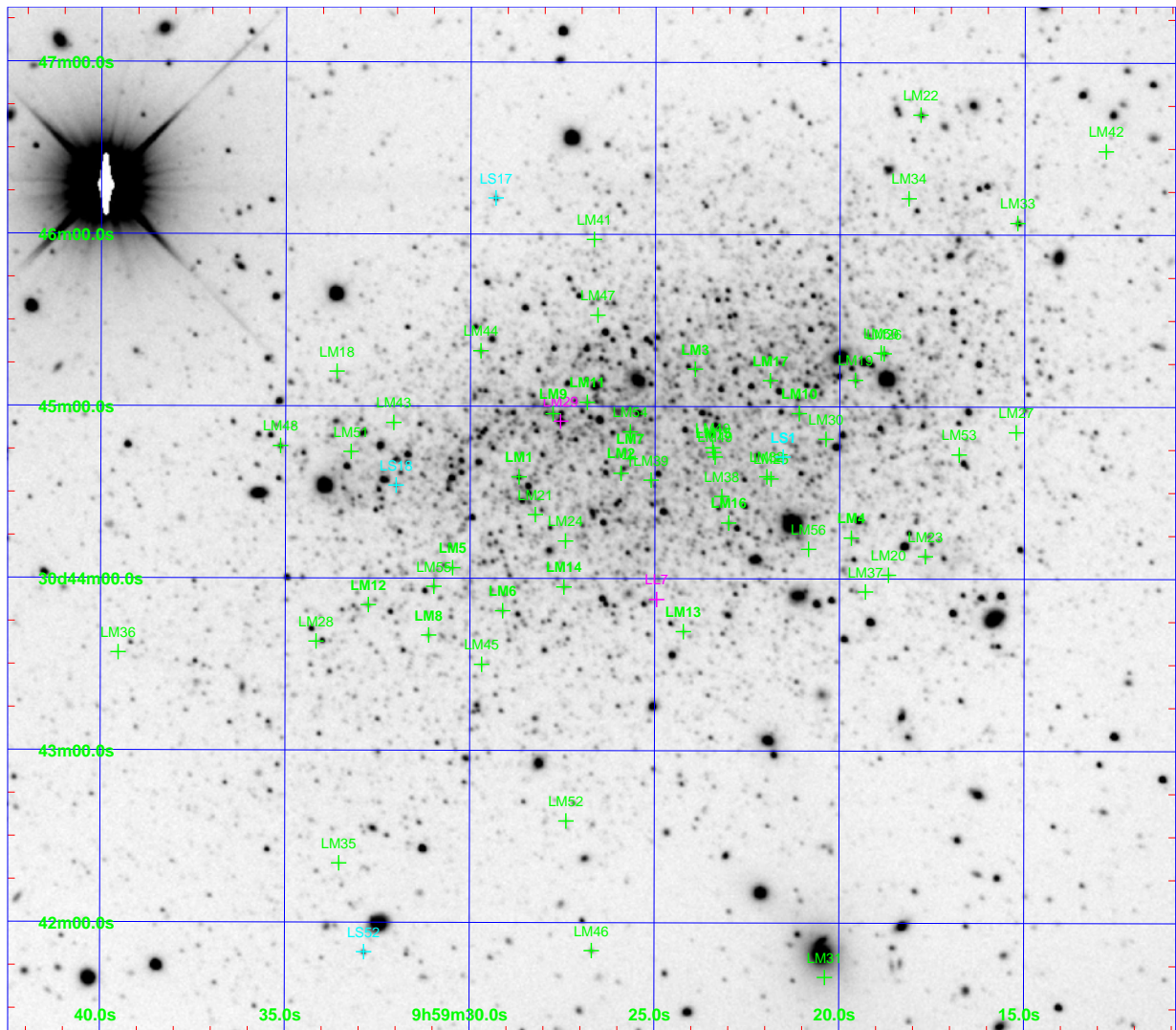
Figure G.4: Finding chart of 1 d< *P* < 10 d candidates, mostly of Tab. 5.1 and F.2 but partly also from Tab. F.1. Bold: high Lomb significance *p* < 0.01; green: LM promising δ Cephei candidates; cyan and magenta: Candidates with interesting secondary period solutions.
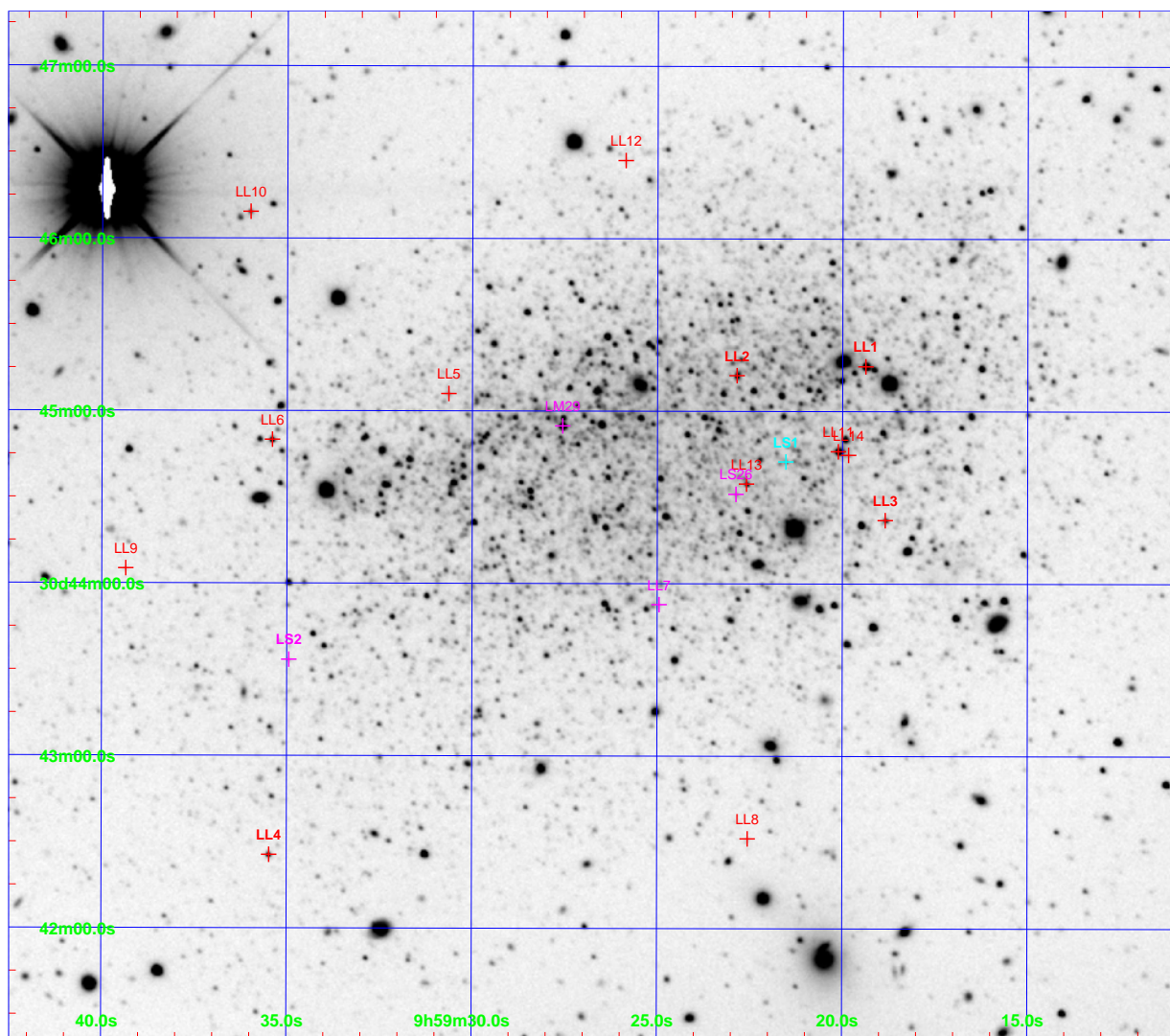
Figure G.5:   Finding chart of longer period $P > 10\,\mathrm{d}$ VS candidates, mostly of Tab. 5.2 but partly also from the others. Bold: high Lomb significance $p < 0.01$; red: Longer period Type II Cepheid or Mirae candidates. cyan and magenta: Candidates with interesting secondary period solutions.
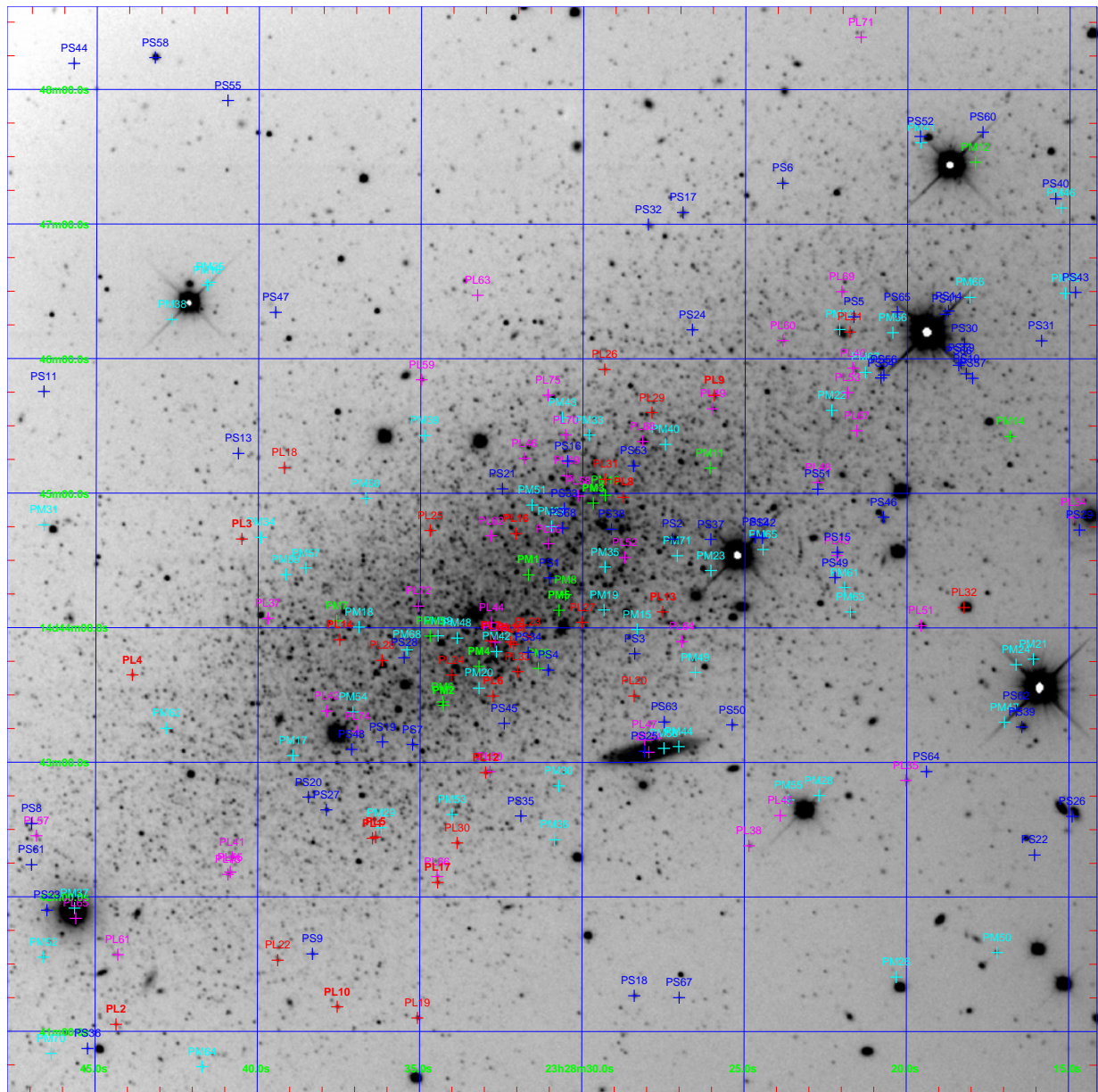
Figure G.6: Finding chart of all Pegasus Dwarf VS candidates. Bold: High Lomb significance $p < 10^{-4}$ for PM and PL candidates; blue: PS short period $P < 1$ d candidates (Tab. F.3); green: Good PM 1 d$< P < 10$ d VS candidates with $p < 0.01$ (Tab. 5.5) cyan: Bad PM 1 d$< P < 10$ d VS candidates with $p > 0.01$ (Tab. F.4); red: Good longer period Type II Cepheid or Mirae candidates with $p < 0.01$ (Tab. 5.6); magenta: Bad longer period Type II Cepheid or Mirae candidates with $p > 0.01$ (Tab. F.5).

Appendix H

Additional Light Curves
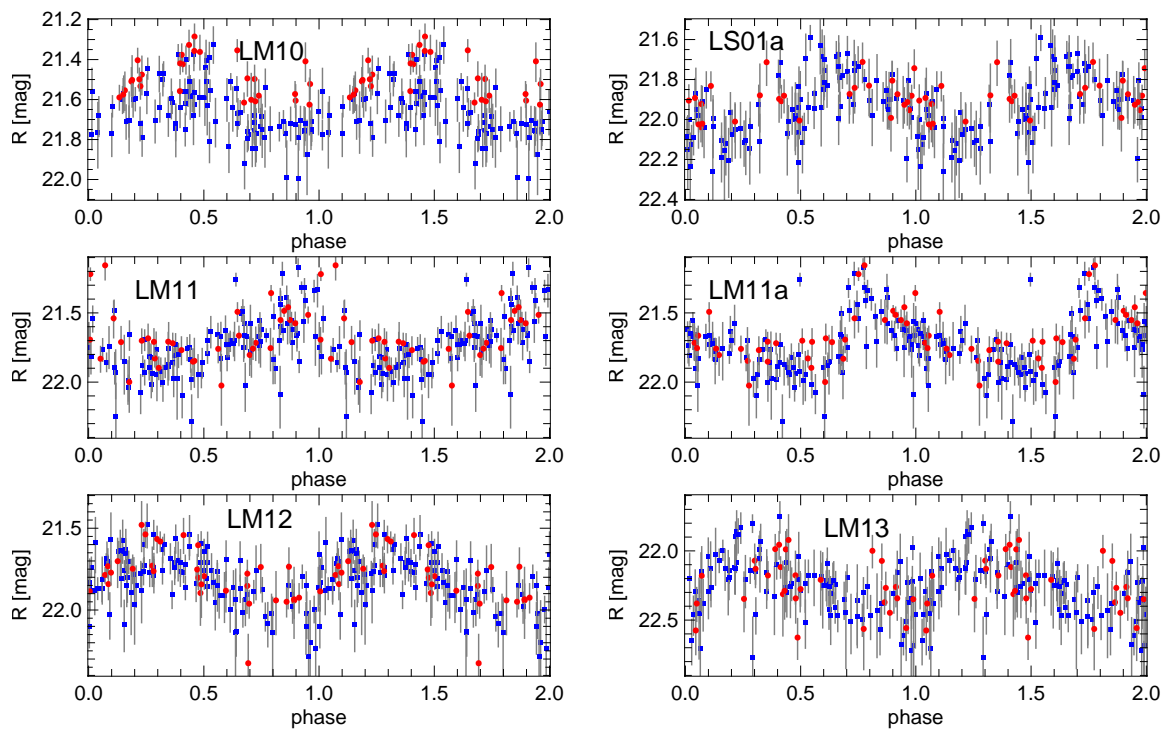
Figure H.1: Leo A 2nd best δ Cephei candidates phase convolved light curves a. Blue squares: WST data (Lomb detection); red circles: CA data (consistency check); coloured crosses: Data consistent with detection limit at epoch, i.e. $S/N < 1$ at either site; grey: 1σ errors.
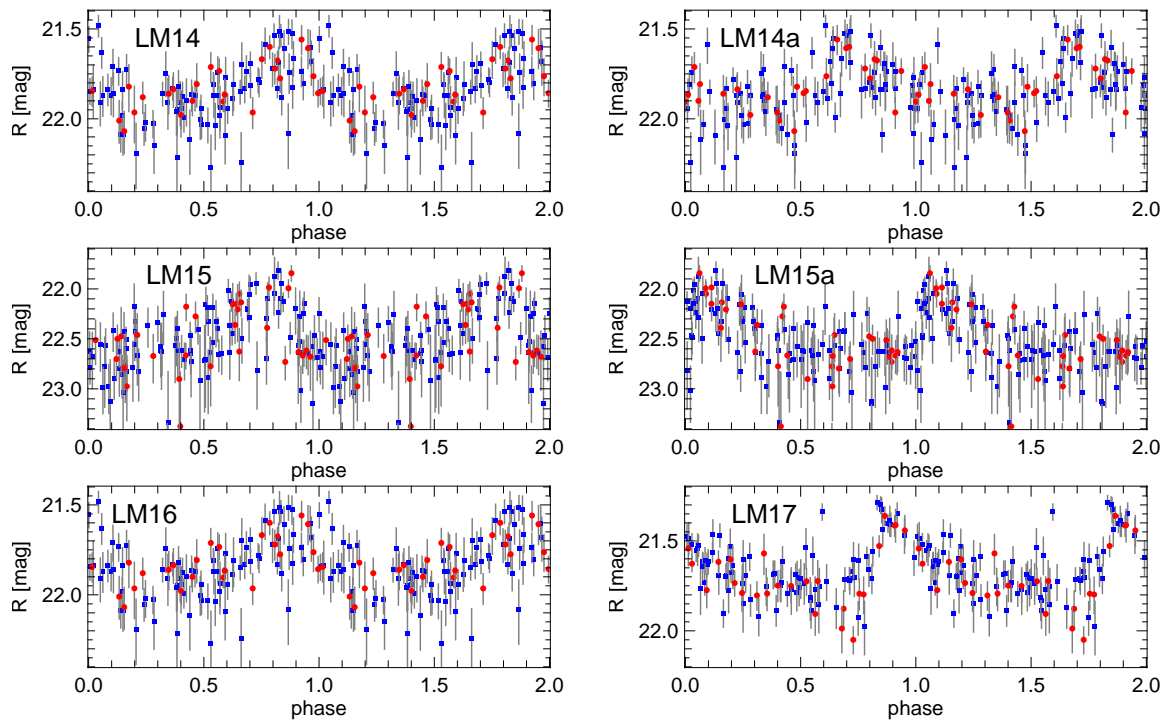
Figure H.2: Leo A 2nd best δ Cephei candidates phase convolved light curves *b*. Blue squares: WST data (Lomb detection); red circles: CA data (consistency check); coloured crosses: Data consistent with detection limit at epoch, i.e. $S/N < 1$ at either site; grey: 1σ errors.

Bibliography

Abd al Rahman Al Sufi. *Kitab al-Kawatib al-Thabit al-Musawwar (Book of Fixed Stars)*. Isfahan (Persia), 964.

C. Alard and R. H. Lupton. A Method for Optimal Image Subtraction. ApJ, 503:325, August 1998.

C. Alcock, R. A. Allsman, D. R. Alves, T. S. Axelrod, A. Becker, D. P. Bennett, K. H. Cook, K. C. Freeman, K. Griest, W. A. Lawson, M. J. Lehner, S. L. Marshall, D. Minniti, B. A. Peterson, K. R. Pollard, M. R. Pratt, P. J. Quinn, A. W. Rodgers, W. Sutherland, A. Tomaney, and D. L. Welch. The MACHO Project LMC Variable Star Inventory. VII. The Discovery of RV Tauri Stars and New Type II Cepheids in the Large Magellanic Cloud. AJ, 115:1921–1933, May 1998.

N. Allen. The Cepheid Distance Scale: A History. `http://www.institute-of-brilliant-failures.com/`, 2001.

D. R. Alves. A review of the distance and structure of the Large Magellanic Cloud. *New Astronomy Review*, 48:659–665, July 2004.

A. Aparicio. The distance to the Pegasus Dwarf Irregular Galaxy: an open question. ApJ, 437: L27–L30, December 1994.

A. Aparicio and C. Gallart. The Stellar Content of the Pegasus Dwarf Irregular Galaxy. AJ, 110: 2105, November 1995.

A. Aparicio, J. M. Garcia-Pelayo, and M. Moles. CCD Photometry of Resolved Dwarf Irregular Galaxies - Part Three - GR:8. A&AS, 74:375, September 1988.

A. Aparicio, C. Gallart, and G. Bertelli. The Star Formation History of the Pegasus Dwarf Irregular Galaxy. AJ, 114:669–679, August 1997.

W. Baade. Über eine Möglichkeit, die Pulsationstheorie der δ Cephei-Veränderlichen zu prüten. *Astronomische Nachrichten*, 228:359, November 1926.

W. Baade. The Resolution of Messier 32, NGC 205, and the Central Region of the Andromeda Nebula. ApJ, 100:137, September 1944.

W. Baade. A Revision of the Extra-Galactic Distance Scale. In P. Th. Oosterhoff, editor, *VIIIth General Assembly - Transactions of the IAU Vol. VIII B, 397-98*. Cambridge University Press, 1954.

W. Baade. The Period-Luminosity Relation of the Cepheids. PASP, 68:5, February 1956.

W. Baade. Galaxies and their Stellar Populations. (A Review of the Present State of Affairs). *Ricerche Astronomiche*, 5:3, 1958.

H. Barwig, C.G. Gössl, W. Mitsch, and A. Riffeser. Das Wendelstein-Observatorium. `http://www.wendelstein-observatorium.de`, 2007.

F. Bauer, EROS Collaboration, C. Afonso, J. N. Albert, C. Alard, J. Andersen, R. Ansari, É. Aubourg, P. Bareyre, J. P. Beaulieu, A. Bouquet, S. Char, X. Charlot, F. Couchot, C. Coutures, F. Derue, R. Ferlet, C. Gaucherel, J. F. Glicenstein, B. Goldman, A. Gould, D. Graff, M. Gros, J. Haissinski, J. C. Hamilton, D. Hardin, J. de Kat, A. Kim, T. Lasserre, É. Lesquoy, C. Loup, C. Magneville, B. Mansoux, J. B. Marquette, É. Maurice, A. Milsztajn, M. Moniez, N. Palanque-Delabrouille, O. Perdereau, L. Prévot, C. Renault, N. Regnault, J. Rich, M. Spiro, A. Vidal-Madjar, L. Vigroux, and S. Zylberajch. A slope variation in the period-luminosity relation for short period SMC Cepheids. A&A, 348:175–183, August 1999.

J. Bayer. *Uranometria: omnium asterismorum continens schemata, nova methodo delineata, aereis laminis expressa.* Christophorus Mangus, Augsburg, 1603.

IPC@CHIP® RTOS Documentation. Beck IPC GmbH, Pohlheim-Garbenteich, 2006.

S. A. Becker. The Variable Star Menagerie. In P. A. Bradley and J. A. Guzik, editors, *ASP Conf. Ser. 135: A Half Century of Stellar Pulsation Interpretation*, page 12, 1998.

M. S. Bessell. UBVRI photometry. II - The Cousins VRI system, its temperature and absolute flux calibration, and relevance for two-dimensional photometry. PASP, 91:589–607, October 1979.

A. Bierce. *The Devil's Dictionary*. Project Gutenberg, 1906.

P. F. Bok and C. D. Boyd. Proper Motions of Forty Three Cluster Type Variables. *Harvard College Observatory Bulletin*, 893:1–6, October 1933.

A. Z. Bonanos, K. Z. Stanek, R. P. Kudritzki, L. M. Macri, D. D. Sasselov, J. Kaluzny, P. B. Stetson, D. Bersier, F. Bresolin, T. Matheson, B. J. Mochejska, N. Przybilla, A. H. Szentgyorgyi, J. Tonry, and G. Torres. The First DIRECT Distance Determination to a Detached Eclipsing Binary in M33. ApJ, 652:313–322, November 2006.

G. Bono, F. Caputo, and P. Santolamazza. Evolutionary scenario for metal-poor pulsating stars. I. Type II Cepheids. A&A, 317:171–177, January 1997.

M. R. Calabretta and E. W. Greisen. Representations of celestial coordinates in FITS. A&A, 395:1077–1122, December 2002.

F. Caputo and S. degl'Innocenti. HB morphology and age indicators for metal-poor stellar systems with age in the range of 1 to 20 Gyr. A&A, 298:833, June 1995.

F. Caputo, V. Castellani, S. Degl'Innocenti, G. Fiorentino, and M. Marconi. Bright metal-poor variables: Why "Anomalous" Cepheids? A&A, 424:927–934, September 2004.

V. Castellani and S. degl'Innocenti. Dwarf spheroidals and the evolution of not-too-old Population II stars. A&A, 298:827, June 1995.

C. Chiosi. Fundamentals of Stellar Evolution Theory: Understanding the HRD. In A. Aparicio, A. Herrero, and F. Sánchez, editors, *Stellar astrophysics for the local group: VIII Canary Islands Winter School of Astrophysics*, page 1, 1998.

R. Ciardullo, P. Tamblyn, and A. C. Phillips. A search for novae in M 31 globular clusters. PASP, 102:1113–1119, October 1990.

P. S. Conti. Basic Observational Constraints on the Evolution of Massive Stars. In A. Maeder and A. Renzini, editors, *Observational Tests of the Stellar Evolution Theory*, volume 105 of *IAU Symposium*, page 233, 1984.

J. P. Cox. Pulsating stars. *Reports of Progress in Physics*, 37:563–698, 1974.

J. P. Cox and C. Whitney. Stellar Pulsation.IV. a Semitheoretical Period-Luminosity Relation for Classical Cepheids. ApJ, 127:561, May 1958.

High Stepper^{TM} Multi-Axis and IndexerPlus^{TM}. CyberPak Co., Lombard, IL, 2001.

G. de Vaucouleurs. Nearby groups of galaxies. *Social Studies of Science*, 9:557, 1975.

G. de Vaucouleurs. The extragalactic distance scale. IV - Distances of nearest groups and field galaxies from secondary indicators. ApJ, 224:710–717, September 1978.

G. de Vaucouleurs and C. Moss. The magellanic irregular galaxy DDO 155. ApJ, 271:123–132, August 1983.

S. Deiries, O. Iwert, and Hummel E. *Chip Characteristics for Lora/Lesser ml2k3ebBI W 15-2*. ESO Garching, December 1995.

S. Deiries, O. Iwert, and Hummel E. *Chip Characteristics for Lora/Lesser ml2k3ebBI W 15-3*. ESO Garching, January 1996.

S. Demers, E. J. Kibblewhite, M. J. Irwin, P. S. Bunclark, and M. T. Bridgeland. Leo A - Color-magnitude diagram of its brightest stars. AJ, 89:1160–1165, August 1984.

R. Diethelm. Physical parameters of pulsating variables with periods between one and three days. II - Fundamental parameters. A&A, 239:186–192, November 1990.

R. Diethelm. Period changes of AHB1 variables. A&A, 307:803–806, March 1996.

R. C. Dohm-Palmer, E. D. Skillman, J. Gallagher, E. Tolstoy, M. Mateo, R. J. Dufour, A. Saha, J. Hoessel, and C. Chiosi. The Recent Star Formation History of GR 8 from Hubble Space Telescope Photometry of the Resolved Stars. AJ, 116:1227–1243, September 1998.

A. E. Dolphin, A. Saha, J. Claver, E. D. Skillman, A. A. Cole, J. S. Gallagher, E. Tolstoy, R. C. Dohm-Palmer, and M. Mateo. Variable Stars in Leo A: RR Lyrae Stars, Short-Period Cepheids, and Implications for Stellar Content. AJ, 123:3154–3198, June 2002.

N. Drory. Yet another object detection application (YODA). Object detection and photometry for multi-band imaging data. A&A, 397:371–379, January 2003.

N. Drory, G. Feulner, R. Bender, C. S. Botzler, U. Hopp, C. Maraston, C. Mendes de Oliveira, and J. Snigula. The Munich Near-Infrared Cluster Survey - I. Field selection, object extraction and photometry. MNRAS, 325:550–562, August 2001.

R. J. Dufour. The composition of H II regions in the Magellanic Clouds. In S. van den Bergh and K. S. D. Boer, editors, *Structure and Evolution of the Magellanic Clouds*, volume 108 of *IAU Symposium*, pages 353–360, September 1984.

A. S. Eddington. The problem of the Cepheid variables. MNRAS, 79:2, November 1918.

A. S. Eddington. On the pulsations of a gaseous star. MNRAS, 79:177–189, January 1919.

A. S. Eddington. *The Internal Constitution of the Stars*. The Internal Constitution of the Stars, Cambridge: Cambridge University Press, 1926, 1926.

A. S. Eddington, Sir. On the cause of Cepheid pulsation. MNRAS, 101:182, 1941.

G. L. Ellis, E. T. Grayson, and H. E. Bond. A search for faint planetary nebulae on Palomar sky survey prints. PASP, 96:283–286, April 1984.

R. Emden. *Gaskugeln*. Teubner, Leipzig, 1907.

Devil-Linux Documentation. Engine Solutions, 2006.

ESA. The Hipparcos and Tycho Catalogues (ESA 1997). *VizieR Online Data Catalog*, 1239:0, February 1997.

D. Fabricius. Letter to Tycho Brahe. See Wolf [1877]., 1596.

H. C. Ferguson and B. Binggeli. Dwarf elliptical galaxies. A&A Rev., 6:67–122, November 1994.

J. D. Fernie. The Period-Luminosity Relation: A Historical Review. PASP, 81:707, December 1969.

G. Fiorentino, M. Limongi, F. Caputo, and M. Marconi. Synthetic properties of bright metal-poor variables. I. "Anomalous" Cepheids. A&A, 460:155–166, December 2006.

J. R. Fisher and R. B. Tully. Neutral hydrogen observations of DDO dwarf galaxies. A&A, 44: 151–171, November 1975.

E. Flaccomio, G. Micela, S. Sciortino, F. Favata, C. Corbally, and A. Tomaney. BVRI photometry of the star-forming region NGC 2264: the initial mass function and star-forming rate. A&A, 345:521–530, May 1999.

A. B. Fokin. *RV Tauri stars*, pages 103–136. Stellar pulsation - Nonlinear Studies, 2001.

W. L. Freedman and B. F. Madore. An empirical test for the metallicity sensitivity of the Cepheid period-luminosity relation. ApJ, 365:186–194, December 1990.

M. Fukugita, T. Ichikawa, J. E. Gunn, M. Doi, K. Shimasaku, and D. P. Schneider. The Sloan Digital Sky Survey Photometric System. AJ, 111:1748, April 1996.

J. S. Gallagher, E. Tolstoy, R. C. Dohm-Palmer, E. D. Skillman, A. A. Cole, J. G. Hoessel, A. Saha, and M. Mateo. A Wide Field Planetary Camera 2 Study of the Resolved Stellar Population of the Pegasus Dwarf Irregular Galaxy (DDO 216). AJ, 115:1869–1887, May 1998.

C. Gallart, A. Aparicio, W. L. Freedman, B. F. Madore, D. Martínez-Delgado, and P. B. Stetson. The Variable-Star Population in Phoenix: Coexistence of Anomalous and Short-Period Classical Cepheids and Detection of RR Lyrae Variables. AJ, 127:1486–1501, March 2004.

A. Gautschy. The history of radial stellar pulsation theory. Technical report, ETH Zürich, Zürich, 2003.

A. Gautschy and H. Saio. Stellar Pulsations Across The HR Diagram: Part 1. ARA&A, 33: 75–114, 1995.

A. Gautschy and H. Saio. Stellar Pulsations Across the HR Diagram: Part 2. ARA&A, 34: 551–606, 1996.

G.-J.-H.-J.-B. Le Gentil de la Galazière. Remarques sur les Étoiles Nebuleuses. [Remarks on the Nebulous Stars.]. *Mémoires de l'Académie Royale des Sciences. Année M.DCCLIX. [Memoirs of the Royal Academy of Sciences. For the year 1759.]*, pages 453–471, 1765.

C. A. Goessl, W. Mitsch, W. Altmann, U. Hopp, and H. Barwig. Two-channel, robotic CCD-camera. In *Instrument Design and Performance for Optical/Infrared Ground-based Telescopes. Edited by Iye, Masanori; Moorwood, Alan F. M. Proceedings of the SPIE, Volume 4841, pp. 648-655 (2003).*, pages 648–655, March 2003.

J. Goodricke. On the Periods of the Changes of Light in the Star Algol. In a Letter from John
    Goodricke, Esq. to the Rev. Anthony Shepherd, D. D. F. R. S. Professor of Astronomy at
    Cambridge. *Philosophical Transactions Series I*, 74:287–292, 1784.

J. Goodricke. A Series of Observations on, and a Discovery of, the Period of the Variation of
    the Light of the Star Marked δ by Bayer, Near the Head of Cepheus. In a Letter from John
    Goodricke, Esq. to Nevil Maskelyne, D. D. F. R. S. and Astronomer Royal. *Philosophical
    Transactions Series I*, 76:48–61, 1786.

C. A. Gössl. Optimierung einer CCD-Kamera zur Beobachtung von Pixellensing in M 31. Mas-
    ter's thesis, Ludwig-Maximilians-Universität München, 1998.

C. A. Gössl and A. Riffeser. Image reduction pipeline for the detection of variable sources in
    highly crowded fields. A&A, 381:1095–1109, January 2002.

C. A. Gössl and A. Riffeser. Image Reduction Pipeline for the Detection of Variable Sources
    in Highly Crowded Fields. In *ASP Conf. Ser. 295: Astronomical Data Analysis Software and
    Systems XII*, page 229, 2003.

C. A. Gössl, N. Drory, and J. Snigula. LTL - The Little Template Library. In *ASP Conf. Ser. 314:
    Astronomical Data Analysis Software and Systems (ADASS) XIII*, page 456, 2004.

C. A. Gössl, J. Snigula, and U. Hopp. Using delta Cep stars to study northern dwarf irregular
    galaxies of the Local Group . *Memorie della Societa Astronomica Italiana*, 77:299, 2006.

E. K. Grebel. Evolutionary Histories of Dwarf Galaxies in the Local Group. In P. Whitelock
    and R. Cannon, editors, *The Stellar Content of Local Group Galaxies*, volume 192 of *IAU
    Symposium*, page 17, January 1999.

E. K. Grebel. Dwarf Galaxies in the Local Group and in the Local Volume (Invited Talk). In
    K. S. de Boer, R.-J. Dettmar, and U. Klein, editors, *Dwarf galaxies and their environment*,
    page 45, 2001.

L. Greggio. The brightest stars in galaxies - A theoretical simulation. A&A, 160:111–115, May
    1986.

L. Greggio, G. Marconi, M. Tosi, and P. Focardi. Star formation in dwarf irregular galaxies -
    DDO 210 and NGC 3109. AJ, 105:894–932, March 1993.

E. W. Greisen and M. R. Calabretta. Representations of world coordinates in FITS. A&A, 395:
    1061–1075, December 2002.

M. A. T. Groenewegen, M. Romaniello, F. Primas, and M. Mottini. The metallicity dependence
    of the Cepheid PL-relation. A&A, 420:655–663, June 2004.

N. Haavard and E. Chambre-Eng. Qt. `http://doc.trolltech.com`, 2007.

C. Hayashi. Stellar evolution in early phases of gravitational contraction. PASJ, 13:450–452, 1961.

H. Helmholtz. *Der Ursprung der Sonnenenergie*. Heidelberg, 1871.

E. Hertzsprung. Über die räumliche Verteilung der Veränderlichen vom δ Cephei-Typus. *Astronomische Nachrichten*, 196:201, January 1914.

J. Hevelius. *Historiola Mirae Stellae*. Johannes Hevelius (Jan Hewelcke), 1662.

P. W. Hodge. The Nature of the Remarkable Galaxy G. R. 8. ApJ, 148:719, June 1967.

P. W. Hodge. The Radial Velocity and Distance of GR8. PASP, 86:645, October 1974.

G. B. Hodierna. *De systemate orbis cometici, deque admirandis coeli characteribus (About the systematics of the cometary orbit, and about the admirable objects of the sky)*. Palermo, 1654.

J. G. Hoessel and G. E. Danielson. Photometry of resolved galaxies. III - GR 8. ApJ, 271:65–69, August 1983.

J. G. Hoessel and J. R. Mould. Photometry of resolved galaxies. I - The Pegasus dwarf irregular. ApJ, 254:38–49, March 1982.

J. G. Hoessel, A. Saha, and G. E. Danielson. Deep CCD observations of nearby dwarf galaxy candidates. PASP, 100:680–682, June 1988.

J. G. Hoessel, M. J. Abbott, A. Saha, A. E. Mossman, and G. E. Danielson. Variable stars in the Pegasus dwarf galaxy (DDO 216). AJ, 100:1151–1158, October 1990.

J. G. Hoessel, A. Saha, J. Krist, and G. E. Danielson. Variable stars in the Leo A dwarf galaxy (DDO 69). AJ, 108:645–652, August 1994.

D. Hoffleit. History of the Discovery of Mira Stars. *Journal of the American Association of Variable Star Observers (JAAVSO)*, 25:115–136, 1997.

E. Hofmeister, R. Kippenhahn, and A. Weigert. Sternentwicklung III. Die Helium-brennende Phase und die Cepheidenstadien eines Sterns von 7.0 Sonnenmassen. Mit 6 Textabbildungen. *Zeitschrift fur Astrophysik*, 60:57, 1964.

E. Holmberg. A photographic photometry of extragalactic nebulae. *Meddelanden fran Lunds Astronomiska Observatorium Serie II*, 136:1, 1958.

J. A. Holtzman, C. Afonso, and A. Dolphin. The Local Group Stellar Populations Archive from the Hubble Space Telescope WFPC2. ApJS, 166:534–548, October 2006.

J. F. Holwarda. *Panselènos ekleiptikè diaugazousa : id est dissertatio astronomica quae occasione ultimi lunaris anni 1638 deliquii manuductio sit ad cognoscendum: I. Statum astronomiae, II. Novorum phenomenoon exortum*. PhD thesis, Franekerae : typis Idzardi Alberti ... & Ioannis Fabiani Theuring, 1640.

E. P. Hubble. Cepheids in Spiral Nebulae. *Popular Astronomy*, 33:252, 1925.

E. P. Hubble. Realm of the Nebulae. *Yale University Press*, 1936.

L. Ingber. Adaptive Simulated Annealing (ASA). Technical report, Caltech Alumni Association, Pasadena, CA, 1993.

G. H. Jacoby and M. P. Lesser. Distances to nearby galaxies derived from planetary nebulae. AJ, 86:185–192, February 1981.

H. L. Johnson. Interstellar Extinction in the Galaxy. ApJ, 141:923, April 1965.

M. Jura. RV Tauri stars as post-asymptotic giant branch objects. ApJ, 309:732–736, October 1986.

I. Karachentsev, I. Drozdovsky, S. Kajsin, L. O. Takalo, P. Heinamaki, and M. Valtonen. Revised photometric distances to nearby dwarf galaxies in the IC 342/Maffei complex. A&AS, 124: 559–571, September 1997.

I. D. Karachentsev. The Local Group and Other Neighboring Galaxy Groups. AJ, 129:178–188, January 2005.

I. D. Karachentsev, A. Dolphin, R. B. Tully, M. Sharina, L. Makarova, D. Makarov, V. Karachentseva, S. Sakai, and E. J. Shaya. Advanced Camera for Surveys Imaging of 25 Galaxies in Nearby Groups and in the Field. AJ, 131:1361–1376, March 2006.

M. Kiriakidis, M. F. El Eid, and W. Glatzel. Heavy element opacities and the pulsations of Beta Cepheid stars. MNRAS, 255:1P–5P, March 1992.

Z. Kopal. The classification of close binary systems. *Annales d'Astrophysique*, 18:379, January 1955.

Z. Kopal. *Close binary systems*. The International Astrophysics Series, London: Chapman & Hall, 1959, 1959.

R. G. Kron. Photometry of a complete sample of faint galaxies. ApJS, 43:305–325, June 1980.

G. P. Kuiper. On the Interpretation of β Lyrae and Other Close Binaries. ApJ, 93:133, January 1941.

J. Lafler and T. D. Kinman. An RR Lyrae Star Survey with Ihe Lick 20-INCH Astrograph II. The Calculation of RR Lyrae Periods by Electronic Computer. ApJS, 11:216, June 1965.

F. Lang. Inbetriebnahme des 40 cm Wendelstein Teleskops zur Novae – Suche in M 31. Master's thesis, Ludwig-Maximilians-Universität München, 2007.

D. Lauterborn, S. Refsdal, and A. Weigert. Stars with Central Helium Burning and the Occurrence of Loops in the H-R Diagram. A&A, 10:97, January 1971.

R. W. Leach and F. J. Low. CCD and IR array controllers. In *Proc. SPIE Vol. 4008, p. 337-343, Optical and IR Telescope Instrumentation and Detectors, Masanori Iye; Alan F. Moorwood; Eds.*, pages 337–343, August 2000.

H. S. Leavitt. 1777 variables in the Magellanic Clouds. *Annals of Harvard College Observatory*, 60:87–108, 1908.

H. S. Leavitt and E. C. Pickering. Periods of 25 Variable Stars in the Small Magellanic Cloud. *Harvard College Observatory Circular*, 173:1–3, March 1912.

M. G. Lee, W. L. Freedman, and B. F. Madore. The Tip of the Red Giant Branch as a Distance Indicator for Resolved Galaxies. ApJ, 417:553, November 1993.

M. G. Lee, A. Aparicio, N. Tikonov, Y.-I. Byun, and E. Kim. Stellar Populations and the Local Group Membership of the Dwarf Galaxy DDO 210. AJ, 118:853–861, August 1999.

D. J. Lennon. private communication, 2007.

K. Levenberg. A Method for the Solution of Certain Non-Linear Problems in Least Squares. *Quart. Appl. Math.*, 2:164–168, 1944.

N. R. Lomb. Least-squares frequency analysis of unequally spaced data. Ap&SS, 39:447–462, February 1976.

B. F. Madore and W. L. Freedman. The Cepheid distance scale. PASP, 103:933–957, September 1991.

G. Marconi, P. Focardi, L. Greggio, and M. Tosi. DDO 210 - The actual appearance of a 'ghost' irregular galaxy. ApJ, 360:L39–L41, September 1990.

M. Marconi and M. di Criscienzo. Updated pulsation models for BL Herculis stars. A&A, 467: 223–227, May 2007.

M. Marconi, I. Musella, and G. Fiorentino. Cepheid Pulsation Models at Varying Metallicity and $\Delta Y/\Delta Z$. ApJ, 632:590–610, October 2005.

K. H. Marien, U. Graser, J. Solf, U. Hopp, and U. Thiele. Astronomie mit digitalen Detektoren am Observatorium Calar Alto. *Mitteilungen der Astronomischen Gesellschaft Hamburg*, 67: 422, 1986.

S. Marius. *Mundus Iovialis anno M.DC.IX Detectus Ope Perspicilli Belgici (The Jovian World, discovered in 1609 by means of the Dutch Telescope)*. Lauer, Ansbach, 1614.

D. Marquardt. An Algorithm for Least-Squares Estimation of Nonlinear Parameters. *SIAM J. Appl. Math.*, 11:431–441, 1963.

M. L. Mateo. Dwarf Galaxies of the Local Group. ARA&A, 36:435–506, 1998.

A. W. McConnachie, M. J. Irwin, A. M. N. Ferguson, R. A. Ibata, G. F. Lewis, and N. Tanvir. Distances and metallicities for 17 Local Group galaxies. MNRAS, 356:979–997, January 2005.

A. W. McConnachie, N. Arimoto, M. Irwin, and E. Tolstoy. The stellar content of the isolated transition dwarf galaxy DDO210. MNRAS, 373:715–728, December 2006.

J. Meeus. *Astronomical formulae for calculators*. Richmond, Virginia: Willmann-Bell, —c1988, 4th ed. (enl. + rev.), 1988.

C. Messier. Tables des Nebuleuses, ainsi que des amas d'Etoiles, que l'on decouvre parmi les Etoiles fixes sur l'horizon de Paris; observes a l'Observatoire de la Marine (Table of nebulae and star clusters, which have been discovered between the fixed stars over the horizon of Paris; observed at the Observatory of the Marine). *Memoires de l'Academie des Sciences for 1771*, 1774.

A. Miglio, J. Montalbán, and M.-A. Dupret. Instability strips of slowly pulsating B stars and β Cephei stars: the effect of the updated OP opacities and of the metal mixture. MNRAS, 375: L21–L25, February 2007.

D. G. Monet. The 491,848,883 Sources in USNO-A1.0. In *Bulletin of the American Astronomical Society*, volume 28 of *Bulletin of the American Astronomical Society*, page 905, May 1996.

D. G. Monet. The 526,280,881 Objects In The USNO-A2.0 Catalog. In *Bulletin of the American Astronomical Society*, volume 30 of *Bulletin of the American Astronomical Society*, page 1427, December 1998.

G. Montanari. *Sopra la sparizione d'alcune stelle ed altre novità celesti*. Bologna. in F. Bianchini: 1737, Astronomicae ac geographicae observationes selectae. . . , Verona, p. 268, 1671.

P. Moskalik and W. A. Dziembowski. New opacities and the origin of the Beta Cephei pulsation. A&A, 256:L5–L8, March 1992.

C. Moss and G. de Vaucouleurs. The brightest star in the Magellanic irregular galaxy DDO 155. PASP, 98:1282–1286, December 1986.

D. H. Munro. Using the Yorick interpreted language. *Computers in Physics*, 9:609–615, November 1995.

P. Nilson. Uppsala General Catalogue of Galaxies, 1973, Acta Universitatis Upsalienis, Nova Regiae Societatis Upsaliensis, Series v: a Vol. *Nova Acta Regiae Soc. Sci. Upsaliensis Ser. V*, page 0, 1973.

P. Nilson. "Catalogue of Selected Non-Ugc Galaxies", 1974, Uppsala Observatory Report no. In *UGCA*, page 0, 1974.

H. Nyquist. Certain topics in telegraph transmission theory. *Trans. AIEE*, 47:617–644, April 1928.

A. Pigafetta. Relazione del primo viaggio intorno al mondo (report on the first voyage around the world). (Partly published in Paris in 1525, the entire manuscript was not published until the late 18th century), 1522.

E. Pigott. Observations of a New Variable Star. In a Letter from Edward Pigott, Esq. to Sir H. C. Englefield, Bart. F. R. S. and A. S. *Philosophical Transactions Series I*, 75:127–136, 1785.

A. Pigulski and Z. Kołaczkowski. Early-type variables in the Magellanic Clouds. I. beta Cephei stars in the LMC bar. A&A, 388:88–99, June 2002.

H. G. Plummer. Note on the velocity of light and Doppler's principle. MNRAS, 74:660, June 1914.

B. J. Pritzl, T. E. Armandroff, G. H. Jacoby, and G. S. Da Costa. The Dwarf Spheroidal Companions to M31: Variable Stars in Andromeda VI. AJ, 124:1464–1485, September 2002.

G. Reaves. Dwarf galaxies in the Virgo cluster. AJ, 61:69–76, March 1956.

K. Reif, K. Bagschik, K. S. de Boer, J. Schmoll, P. Mueller, H. Poschmann, G. Klink, R. Kohley, U. Heber, and U. Mebold. BUSCA: a telescope instrumentation for simultaneous imaging in four optical bands. In *Proc. SPIE Vol. 3649, p. 109-120, Sensors, Cameras, and Systems for Scientific/Industrial Applications, Morley M. Blouke; George M. Williams; Eds.*, pages 109–120, April 1999.

A. Riffeser. *Gravitational microlensing towards the Andromeda galaxy: A search for dark matter in M31*. PhD thesis, Ludwig-Maximilians-Universität München, 2006.

A. Riffeser, J. Fliri, C. A. Gössl, R. Bender, U. Hopp, O. Bärnbantner, C. Ries, H. Barwig, S. Seitz, and W. Mitsch. WeCAPP - Wendelstein Calar Alto pixellensing project I. Tracing dark and bright matter in M 31. A&A, 379:362–373, November 2001.

A. Ritter. Untersuchungen über die Höhe der Atmosphäre und die Constitution gasförmiger Weltkörper, Teil 5. *Annalen der Physik*, 244:157–183, August 1879.

L. Rizzi, R. B. Tully, D. Makarov, L. Makarova, A. E. Dolphin, S. Sakai, and E. J. Shaya. Tip of the Red Giant Branch Distances. II. Zero-Point Calibration. ApJ, 661:815–829, June 2007.

M. Roth. *CCD-Spektrophotometrie Planetarischer Nebel*. PhD thesis, Ludwig-Maximilians-Universität München, 1993.

H. N. Russell. "Giant" and "dwarf" stars. *The Observatory*, 36:324–329, August 1913.

H. N. Russell. Relations Between the Spectra and Other Characteristics of the Stars. *Popular Astronomy*, 22:275–294, May 1914.

M. Salaris and S. Cassisi. *Evolution of Stars and Stellar Populations*. Wiley, 2005.

A. Sandage. Current Problems in the Extragalactic Distance Scale. ApJ, 127:513, May 1958.

A. Sandage. The brightest stars in nearby galaxies. VII - The Pegasus and Leo A Im V dwarfs. AJ, 91:496–506, March 1986.

A. Sandage and G. A. Tammann. Steps toward the Hubble constant. VIII - The global value. ApJ, 256:339–345, May 1982.

A. Sandage and G. A. Tammann. Absolute Magnitude Calibrations of Population I and II Cepheids and Other Pulsating Variables in the Instability Strip of the Hertzsprung-Russell Diagram. ARA&A, 44:93–140, September 2006.

A. Sandage, R. Diethelm, and G. A. Tammann. The P-L relation for RR Lyrae-like stars with 0.8d less than P less than 3d. A&A, 283:111–120, March 1994.

E. S. Saunders, T. Naylor, and A. Allan. Optimal placement of a limited number of observations for period searches. A&A, 455:757–763, August 2006.

J. D. Scargle. Studies in astronomical time series analysis. II - Statistical aspects of spectral analysis of unevenly spaced data. ApJ, 263:835–853, December 1982.

H. Schild and A. Maeder. The relation between the luminosity of the brightest blue star and the luminosity of its parent galaxy. A&A, 127:238–240, October 1983.

D. J. Schlegel, D. P. Finkbeiner, and M. Davis. Maps of Dust Infrared Emission for Use in Estimation of Reddening and Cosmic Microwave Background Radiation Foregrounds. ApJ, 500:525, June 1998.

M. Schönberg and S. Chandrasekhar. On the Evolution of the Main-Sequence Stars. ApJ, 96: 161, September 1942.

Glasfilter-Katalog. Schott AG, 2004.

R. E. Schulte-Ladbeck, U. Hopp, I. O. Drozdovsky, L. Greggio, and M. M. Crone. The Oldest Stars of the Extremely Metal-Poor Local Group Dwarf Irregular Galaxy Leo A. AJ, 124: 896–914, August 2002.

H. Shapley. On the Nature and Cause of Cepheid Variation. ApJ, 40:448, December 1914.

H. Shapley. Studies based on the colors and magnitudes in stellar clusters. VI. On the determination of the distances of globular clusters. ApJ, 48:89–124, September 1918.

N. R. Simon and A. S. Lee. The structural properties of Cepheid light curves. ApJ, 248:291–297, August 1981.

N. R. Simon and E. G. Schmidt. Evidence Favoring Nonevolutionary Cepheid Masses. ApJ, 205:162–164, April 1976.

E. D. Skillman and R. Bender. The Dwarf Galaxy Star Formation Crisis (Invited paper). In M. Pena and S. Kurtz, editors, *Revista Mexicana de Astronomia y Astrofisica Conference Series*, volume 3 of *Revista Mexicana de Astronomia y Astrofisica, vol. 27*, page 25, December 1995.

E. D. Skillman, J. Melnick, R. Terlevich, and M. Moles. The extremely low oxygen abundance of GR 8 - A very low luminosity dwarf irregular galaxy. A&A, 196:31–38, May 1988.

E. D. Skillman, R. C. Kennicutt, and P. W. Hodge. Oxygen abundances in nearby dwarf irregular galaxies. ApJ, 347:875–882, December 1989.

J. Snigula, C. Gössl, U. Hopp, and H. Barwig. Variable star monitoring in local group dwarf irregular galaxies. In D. W. Kurtz and K. R. Pollard, editors, *ASP Conf. Ser. 310: IAU Colloq. 193: Variable Stars in the Local Group*, page 70, May 2004.

J. Snigula, C. Gössl, and U. Hopp. Toward a census of variable stars in northern local group dwarf irregular galaxies . *Memorie della Societa Astronomica Italiana*, 77:344, 2006.

J. M. Snigula. *Long Period Variables in Local Group Dwarf Galaxies*. PhD thesis, Ludwig-Maximilians-Universität München, 2006.

P. B. Stetson. DAOPHOT - A computer program for crowded-field stellar photometry. PASP, 99:191–222, March 1987.

S. Streit. *Voodoo and Device Driver Programmer's Reference Manual*. Astronomical Research Cameras, Inc., San Diego State University, February 2003.

P. Surma. Shutter-free flatfielding for ccd detectors. å, 278:654–658, November 1993.

P. S. Thé, D. Thomas, C. G. Christensen, and B. E. Westerlund. VRI photometric properties of M-type giants. PASP, 102:565–573, May 1990.

U. Thiele. Calar Alto Observatory. `http://www.caha.es`, 2007.

W. Thomson (Lord Kelvin). On the Age of the Sun's Heat. *Macmillan's Magazine*, 5:288–293, March 1862.

E. Tolstoy, A. Saha, J. G. Hoessel, and G. E. Danielson. Variable stars in the dwarf galaxy GR 8 (DDO 155). AJ, 109:579–587, February 1995.

E. Tolstoy, J. S. Gallagher, A. A. Cole, J. G. Hoessel, A. Saha, R. C. Dohm-Palmer, E. D. Skillman, M. Mateo, and D. Hurley-Keller. Wide Field Planetary Camera 2 Observations of Leo A: A Predominantly Young Galaxy within the Local Group. AJ, 116:1244–1262, September 1998.

A. B. Tomaney and A. P. S. Crotts. Expanding the Realm of Microlensing Surveys with Difference Image Photometry. AJ, 112:2872, December 1996.

R. J. Trumpler. Preliminary results on the distances, dimensions and space distribution of open star clusters. *Lick Observatory Bulletin*, 14:154–188, 1930.

N. D. Tyson and R. R. Gal. An exposure guide for taking twilight flatfields with large format ccds. AJ, 105:1206–1212, March 1993.

S. van den Bergh. A catalogue of dwarf galaxies. *Publications of the David Dunlap Observatory*, 2:147–150, 1959.

S. van den Bergh. Luminosity classifications of dwarf galaxies. AJ, 71:922–926, November 1966.

S. van den Bergh. The outer fringes of the local group. AJ, 107:1328–1332, April 1994.

L. van Zee, E. D. Skillman, and M. P. Haynes. Oxygen and Nitrogen in Leo A and GR 8. ApJ, 637:269–282, January 2006.

T. Veldhuizen. Using C++ template metaprograms. *C++ Report*, 7(4):36–43, May 1995. ISSN 1040-6042. Reprinted in C++ Gems, ed. Stanley Lippman.

Amerigo Vespucci. Letter to Lorenzo di Pier Francesco de Medici. Lisbon, 1503.

N. R. Walborn and D. J. Lennon. A Comparison of O Spectral Types with Nonrotating and Rotating Evolutionary Models. In A. Maeder and P. Eenens, editors, *Stellar Rotation*, volume 215 of *IAU Symposium*, page 512, June 2004.

G. Wallerstein. The Cepheids of Population II and Related Stars. PASP, 114:689–699, July 2002.

D. C. Wells, E. W. Greisen, and R. H. Harten. FITS - a Flexible Image Transport System. A&AS, 44:363, June 1981.

A. J. Wesselink. The observations of brightness, colour and radial velocity of δ Cephei and the pulsation hypothesis (Errata: 10 258, 310). Bull. Astron. Inst. Netherlands, 10:91, January 1946.

M. F. Woche, U. Laux, and J. Papamastorakis. Dichroic beam splitter for convergent beams. In *Proc. SPIE Vol. 4008, p. 930-933, Optical and IR Telescope Instrumentation and Detectors, Masanori Iye; Alan F. Moorwood; Eds.*, pages 930–933, August 2000.

R. Wolf. *Geschichte der Astronomie*. München, R. Oldenbourg, 1877.

S. A. Zhevakin. The Incorrectness of Cox and Whitney's Simplified Criterion for the Pulsational Instability of a Star. *Soviet Astronomy*, 7:142, August 1963.

B. L. Ziegler and R. Bender. M 32-like galaxies: still very rare. M 32 analogues do not exist in the Leo group. A&A, 330:819–822, February 1998.

F. Zwicky. On the Large Scale Distribution of Matter in the Universe. *Physical Review*, 61: 489–503, April 1942.

Acknowledgements

Curriculum Vitae

Persönliche Daten

Name: Claus Alexander Gössl
Gebursdatum: 4. März 1971
Geburtsort: Altötting
Familienstand: Ledig
Anschrift: Bad-Kissingen-Str. 58, 81671 München

Ausbildung

1977 - 1981   Grundschule in Unterneukirchen
1981 - 1990   König-Karlmann-Gymnasium in Altötting
1991 - 1998   Studium der Physik and der Ludwig-Maximilians-Universität Müenchen
1997 - 1998   Diplomarbeit an der Universitäts-Sternwarte München über "*Optimierung einer CCD-Kamera zur Beobachtung von Pixellensing in M 31*"
1998   Diplom in Physik, LMU München
1998 - 2007   Promotion in Astronomie an der LMU München über Variable Sterne in Zwerggalaxien der Lokalen Gruppe

Berufliche Tätigkeit

1990 - 1991   Wehrdienst
1998 -   Wissenschaftlicher Angestellter an der LMU München, Instrumentenentwicklung für optische Teleskope, Entwicklung von Datenreduktions- und Bildverarbeitungssoftware